



HAL
open science

Enhanced adhesives for the encapsulation of flexible organic photovoltaic modules

Patrick Mark Boldrighini

► **To cite this version:**

Patrick Mark Boldrighini. Enhanced adhesives for the encapsulation of flexible organic photovoltaic modules. Other. Université Blaise Pascal - Clermont-Ferrand II, 2015. English. NNT : 2015CLF22586 . tel-02003628

HAL Id: tel-02003628

<https://theses.hal.science/tel-02003628>

Submitted on 1 Feb 2019

HAL is a multi-disciplinary open access archive for the deposit and dissemination of scientific research documents, whether they are published or not. The documents may come from teaching and research institutions in France or abroad, or from public or private research centers.

L'archive ouverte pluridisciplinaire **HAL**, est destinée au dépôt et à la diffusion de documents scientifiques de niveau recherche, publiés ou non, émanant des établissements d'enseignement et de recherche français ou étrangers, des laboratoires publics ou privés.

DOCUMENT CONFIDENTIEL

UNIVERSITE BLAISE PASCAL

U.F.R. Sciences et Technologies

ÉCOLE DOCTORALE DES SCIENCES FONDAMENTALES

THESE

présentée pour obtenir le grade de

DOCTEUR D'UNIVERSITE

Spécialité : Chimie-Physique

Par :

BOLDRIGHINI, Patrick Mark

**Enhanced adhesives for the encapsulation
of flexible organic photovoltaic modules**

Soutenue le 30 Juin, 2015 devant la commission d'examen :

Rapporteurs :

Lionel FLANDIN	Professeur des Universités	Université Savoie Mont Blanc
Bernard RATIER	Professeur des Universités	Université de Limoges, XLIM

Membres du jury :

Philippe BOUTINAUD	Professeur des Universités	ENSCCF
Stéphane CROS	Ingénieur-Chercheur	CEA-LITEN
Jean-Luc GARDETTE	Professeur des Universités	Université Blaise Pascal
Manuel HIDALGO	Ingénieur-Chercheur	Arkema Group
Sandrine THERIAS	Directrice de Recherche	CNRS, ICCF

Thesis of Patrick Boldrighini

Enhanced adhesives for
encapsulation of flexible organic
photovoltaic modules

DOCUMENT CONFIDENTIEL

Remerciements

It has truly been a unique experience, unlike anything I had ever done, to come to France and work towards my PhD. I have had such an amazing experience both in and out of the lab while getting to immerse myself in the wonderful French culture. I was also fortunate enough to work in two excellent labs with two excellent groups of people. It is thanks to all of the incredible people I met here that I was able to complete this thesis and create so many great memories.

I first need to thank Stéphane Cros for being my advisor and guiding me through all of the trials and tribulations I faced in and out of the lab. Likewise, Manuel Hidalgo was instrumental with his wealth of expertise and great discussions of the NFL. My great advisors in Clermont-Ferrand, Jean-Luc Gardette and Sandrine Thérias, were invaluable with their encouraging advice and taught me so much about photo-chemistry.

I owe a special thanks to one of my best friends, Dr. Balthazar LeZinzin for telling me about a new project they were working on at INES and helping me to acclimate to a new culture. Go Caps!

Though I spent far less time there than I could have, all the amazing people in Clermont-Ferrand made it my home-away-from-home. I was taken aback by how willing Agnes, Pierre-Olivier and Claire were to help me with great discussions. Above all, the amazing welcome my colleagues gave to a random guy from another lab who spoke weird French was beyond all expectation and really made me feel like a part of the group. Thank you so much Isa, Jenia, Anthony (both of you!), Gigi, Alexis, Camille, Ahmedou, Claire and Romain.

Another special thanks to the interns who worked so well despite having the misfortune of dealing with my confusing guidance and protocols written in shorthand English. Diane, Charlotte and Léo: you were great!

At INES, I have so many people to thank who have made such a big impact on me both in and out of the lab. I was lucky to work under great supervisors like Solenn, Rémi and Stéphane G. who supported my work and gave me freedom to pursue my project. Thank you Matthieu for putting up with me as a neighbor in the office and at home! Muriel, thanks for listening to all my crazy ideas and helping so much with so many different things! Thank you also to Noella and Nathalie for all your help. From making me cells to helping fix my broken

equipment and so much more, I owe a huge thank you to Florance, Pascal, Caroline, Nathalie and Marion!

L'équipe barrière was the best team to be a part of. Arnaud thanks for being a great friend and Allez Metz! Fab, bravo for keep the lab lively with your songs, and along with Clément S., providing plenty of laughter. Aurélie, thanks for being an awesome friend and colleague throughout all your different labs.

My fellow doctoral students were always there to share in both the good times and the pain of writing a thesis. Mélodie, Guillaume, Bruno and Clément, thanks for all the awesome fun times keeping the lab lively with your smiles and pranks! The new guys too, Sacha and Lukas, you were always there to hang out and keep me sane.

All of the great people who have come through the LMPO over the years all helped me immensely both with my work and after work. Mathieu S. you were a great roommate when I arrived and always kept things chill. Boris and Gaëlle were some of the coolest people I've ever worked with. It was an absolute pleasure to work with wonderful people like Celine and Mathilde. My buddies from Disa, Gabriel and Julien, it was awesome to have cool colleagues to share the lab with! And even those students who didn't get to spend too long at INES, you were all really cool and kept work fun! Thanks Mikel, Lucille, Anaïs, Maéva and Sophie.

Last but not least, I had so much help from other labs. I want to thank everyone in LMPV for being such awesome neighbors and labmates! In particular I want to thank Marion and Julien for not only always being open for discussions and letting me use your equipment, but also for being my friends. Dominique thanks for putting up with me always speaking English when I was meeting with you and Manuel. I also want to thank my CEA colleagues from DTNM, and in particular Julia, for constantly bailing me out when my equipment was broken. Thank you so much! A big thank you also to Arkema and Sartomer for helping me out so much with materials and advice. Thank you Pierre G. and Catherine L. for taking time out of your schedules to help a student like myself.

Thank you again to all of you and to anyone I may have missed. You made this difficult task of earning a PhD not only possible, but fun! You were all so welcoming to me even in the beginning when I didn't speak French very well. I could not have done this without you. Thank you for making this the best experience of my life!

Table of Contents

Introduction	5
Chapter 1: Background	9
Introduction	9
Organic Photovoltaic Technologies.....	9
How OPV Devices Function.....	9
Degradation Mechanisms	13
Similar Technologies	17
Permeation Mechanisms and Encapsulation Materials	21
Permeation Mechanisms in Materials.....	21
Encapsulation Processes	32
Adhesives.....	38
Permeation Measurement	48
Chapter 2: Experimental Procedures and Testing.....	57
Raw Materials.....	57
Barrier Films	57
Adhesives.....	58
Nanoparticles.....	61
Materials Preparation.....	63
MAM Pressure Sensitive Adhesives.....	63
UV Curing Acrylates.....	64
Corona Treatment	66
Coating.....	67
Lamination and Encapsulation Methods	68
Aging Conditions.....	70
Accelerated Moisture	71
Accelerated Photo-Aging	71
Experimental Techniques	72
Spectroscopic Techniques	72
Thermo-mechanical Testing.....	73
Microscopy	75
Other Testing.....	76

Chapter 3: Development and Optimization of the Optical Calcium Test.....	81
Introduction	81
Sample Geometry	82
Advantages of Modified Sample Geometry.....	82
Limitations of Modified Sample Geometry	83
Modeling and Analysis.....	84
Image Analysis.....	85
Orthogonal Permeation	86
Lateral Permeation Measurement.....	91
Interfacial Permeation	93
Identification of Permeation Pathways Using Reference Materials	94
Design of Experiment	94
Orthogonal vs. Lateral Permeation.....	95
Influence of Adhesive Thickness	96
Influence of Surface Treatment	97
Conclusions	100
Chapter 4: Adhesive Characterization.....	103
Introduction	103
MAM PSAs	104
Structure of MAM Block Co-Polymers.....	104
Thermo-Mechanical and Optical Properties	106
Permeation	111
UV Cure Acrylates	113
Formulation of the Adhesives.....	113
Comparison of Thermo-Mechanical and Optical Properties	119
Permeation	122
Comparison of Adhesive Chemistries	124
Conclusions	129
Chapter 5: Nanocomposites.....	131
Introduction	131
Overview of Particles	131
Phyllosilicates	131
Zeolites.....	132
Comparison of Properties: Neat vs. Phyllosilicate vs. Zeolite	136
Thermo-mechanical and Optical Properties.....	137

Permeation	140
Conclusions	145
Chapter 6: Encapsulation of Organic Photovoltaic Cells.....	147
Introduction	147
Encapsulation Processes	148
Accelerated Humidity Testing.....	149
Reference PSA	149
Comparison of Different Adhesives.....	151
UV Curing Nanocomposites	154
Conclusions	157
Chapter 7: Photostability.....	159
Introduction	159
MAM PSAs	159
Degradation Kinetics: Photo-oxidation and Photolysis.....	159
Effect of Nanoparticles	164
Changes to Properties.....	167
UV Curing Acrylates	170
Degradation Kinetics: Photo-oxidation and Photolysis.....	170
Changes to Properties.....	172
Conclusions	174
Conclusions and Perspectives.....	177
References	184

Introduction

Renewable energy sources have become one of the most important initiatives facing mankind today. Greenhouse gas emissions and geopolitical concerns have created a strong need for the replacement of fossil fuels in energy production, with renewable sources being particularly promising. The abundant energy produced by the sun is an especially interesting solution to this problem since capturing only a small portion of the sunlight which reaches Earth could easily meet global energy demand as illustrated in Figure I.1.¹ Accordingly, the amount of solar photovoltaic capacity has risen rapidly in recent years from 3.7 GW globally in 2004 to 100 GW globally in 2012.² This has corresponded well to the development of less expensive photovoltaic panels which convert sunlight directly into electricity.² However, the energy and time intensive processes for the production of silicon based photovoltaics limit how inexpensive these devices can become. To drastically decrease the cost of photovoltaic devices, new technologies are needed.

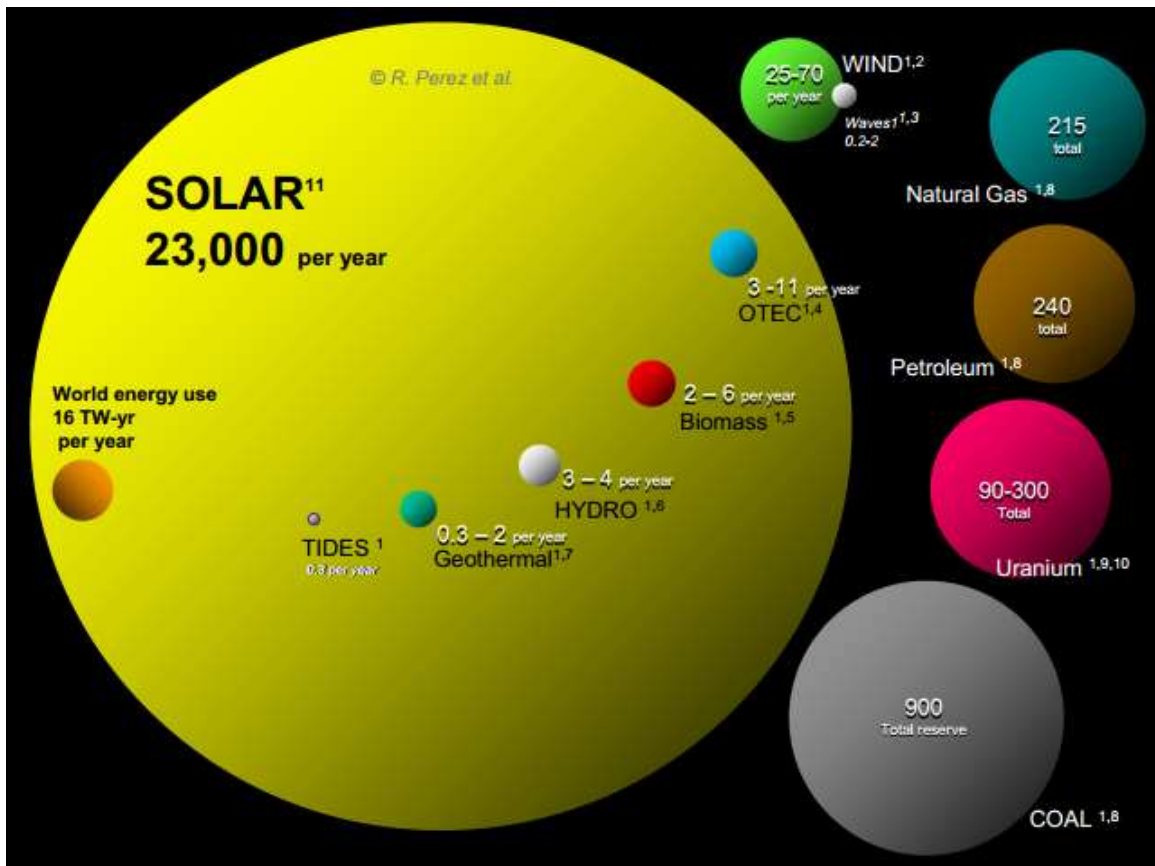


Figure I.1 The total possible energy reserves for various sources are shown compared to the total global yearly energy use from 2009 (orange circle). For non-renewable sources, the total recoverable reserves are shown. For renewable sources, the maximum possible energy which could potentially be captured is shown.¹

While many different photovoltaic technologies have been developed as competitors to silicon-based systems, organic photovoltaic (OPV) devices represent a particularly interesting alternative. These devices use organic molecules and polymers as the semi-conducting light absorber material in place of silicon. These devices tend to operate best when the active layer materials are on the order of hundreds of nanometers in thickness. This, combined with the ability of organic materials to be solubilized in solvents, allows for devices to be printed at relatively low temperatures using evaporative deposition techniques or solvent-based inks.³ The thin, non-brittle nature of these active layer materials also allows for devices to be flexible. This flexibility enables the use of low-cost production techniques, such as roll-to-roll processing.³⁻⁵ Thin active layers also cause less material to be used. This combination of low-cost, low-temperature processing and low material usage creates the potential for OPV devices to be much less expensive and with much shorter energy payback times than their silicon-based counterparts.

OPV devices also have several other advantages which increase their utility. By printing devices on flexible foils, the final devices are much thinner and light-weight than silicon modules. Their flexible nature also allows for more creative deployment of the modules onto both curved surfaces and other flexible materials. The ability to print devices also create the possibility for unique custom shapes, further opening the new options for the deployment of the modules. These attributes also combine to make OPV modules ideal for many smaller niche applications such as chargers for devices or for incorporation into other devices such as smart textiles. OPV technologies also often exhibit less loss of power conversion efficiency at sharp angles of incidence and in low light conditions compared to silicon based modules.⁶ This eliminates the need for expensive solar tracking mounts and makes OPV modules potentially interesting for indoor applications where the illumination is not as intense.

OPV devices do have several drawbacks however. Traditionally, the largest obstacles to large-scale implementation of OPV devices have been their relatively low power conversion efficiencies (PCE)⁷ and short device lifetimes.⁸⁻¹⁰ The problem of low PCE has been the focus of much research and lab scale cells have now surpassed 12% PCE.¹¹ This has been achieved primarily through development of better active layer materials and device architectures such as tandem cells. While this PCE is still low compared to other solar technologies, it has become sufficiently high for OPV devices to become commercially viable. Devices fabricated using industrial scale methods are often not as efficient as those at the lab scale,^{3-5,12,13} but the large

number of companies currently in or preparing to shortly enter industrial scale production indicates that this loss of PCE is not drastic enough to prevent their commercialization.^{11,14–23}

The problem of short device lifetimes remains however. This problem stems from the sensitivity of many OPV materials to light, oxygen, water, and combinations thereof.^{8–10,24} As a result, much research has been performed to develop more stable OPV materials and high gas-barrier encapsulation materials. This has increased the achievable device lifetimes for OPV devices, but much work remains to reach the level of long-term device stability seen for other solar technologies.¹⁰ While flexible multi-layer barrier films can now often meet the oxygen and water vapor transmission rate requirements needed to extend device lifetimes to several years,²⁵ less progress has been made in preventing gas permeation in the adhesives used to seal devices between these films.²⁶ This allows for lateral gas permeation, also known as side ingress, to occur and degrade devices from the edges inward.

The goal of the work presented in this thesis is to better characterize and develop materials to limit the problem of lateral permeation into OPV devices, thus prolonging their device lifetimes. A new testing procedure is presented which aids in the characterization of permeation in OPV devices. This test, a modified form of the optical calcium test, allows for the comparison of multiple permeation pathways in encapsulation schemes, while also providing a tool for the comparison of different encapsulation materials. This modified optical calcium test, along with other established characterization techniques, is then used to develop and evaluate enhanced adhesives with decreased later permeation rates. These enhancements include modification of the adhesives' formulation and the addition of nanoparticles. Relatively impermeable passive nanoparticles are used to make adhesive nanocomposites as a method to lengthen the permeation pathway by creation of a tortuous pathway. A novel approach using active nanoparticles which bind permeating species is also investigated to create adhesive nanocomposites. The enhanced adhesives are then used to encapsulate OPV cells and subjected to accelerated aging to determine their relative impact on the device lifetimes of OPV devices. Finally, the photostability of the enhanced adhesives is analyzed to ensure the adhesives will continue to function as desired after exposure to light, which is of particular importance for OPV encapsulation materials which can spend years exposed to intense sunlight.

Chapter 1: Background

Introduction

In this chapter a bibliographic study of the literature is presented in order to establish a basis for further discussion and to provide an overview of the state of the art in the fields of encapsulation of organic photovoltaic devices, adhesive composites and permeation measurement. With these goals in mind, the principles of how organic photovoltaic devices work are presented along with their primary degradation mechanisms. Next, an overview of common encapsulation materials and how they are used to encapsulate devices is provided. Included in this overview is a discussion of the gas permeation mechanisms associated with each type of encapsulation material. Finally, testing techniques for measuring the low permeability rates found in encapsulation materials is discussed.

Organic Photovoltaic Technologies

Organic photovoltaic devices (OPV), as previously discussed, are a very promising technology to provide low cost electricity. Their use of organic semiconductors gives OPV devices unique characteristics in comparison to other solar technologies. This section aims to illuminate the principles of how these devices produce electricity from light along with how this process can become hindered by the various degradation mechanisms present in the devices. As one of the stated goals of this doctoral research is to improve the lifetime of OPV devices, a current understanding of what limits the device lifetime is crucial.

How OPV Devices Function

Just as with other photovoltaic technologies, OPV devices absorb light which produces an electron-hole pair that is then used to generate a current. Unlike other photovoltaic technologies however, the absorber material in OPV devices is an organic molecule instead of an inorganic semi-conductor. These molecules have a highly conjugated system of molecular orbitals which allows for the creation of a band gap that corresponds well to the energy of visible light.²⁷ The energy levels of the highest occupied molecular orbital (HOMO) and lowest

unoccupied molecular orbital (LUMO), and thus the band gap, are determined by the chemistry of the organic molecules. A large variety of absorber materials exist for OPV devices with different band gaps, absorption spectra, π - π stacking, solubility and intrinsic stability.^{10,27,28} These materials also range in molecular weight from smaller non-repeating molecules to longer chain polymers with examples shown in Figure 1.1. Since the ability of the absorber material to generate electron-hole pairs is of fundamental importance to a device's ability to generate a photocurrent, much research continues into the development of new absorbers.²⁷

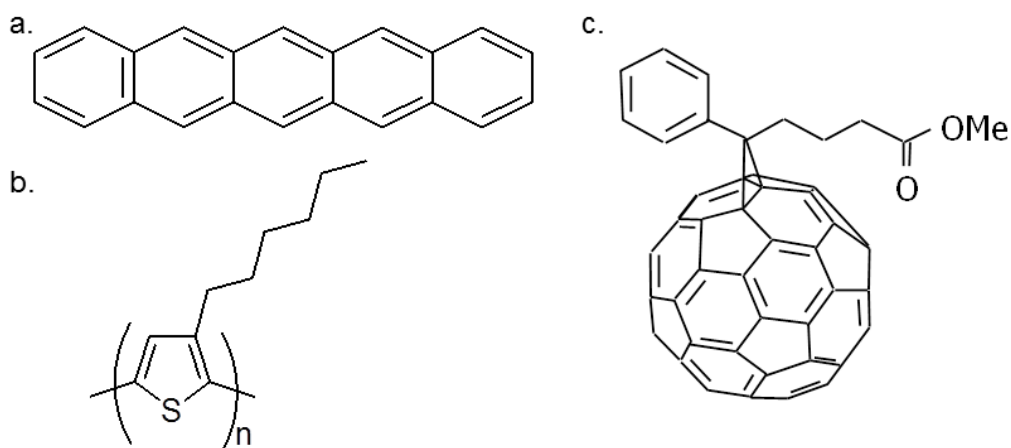


Figure 1.1 The chemical structures of (a) the small molecule absorber pentacene, (b) the polymeric absorber poly(3-hexylthiophene), and (c) the acceptor phenyl C₆₁ butyric acid methyl ester are shown as examples of commonly used OPV active layer materials.

Along with the absorber material, the rest of the so called active layer of the OPV is comprised of an electron acceptor material. This material aids in separating the charges of the electron hole pair as its LUMO energy level is carefully selected to create a favorable condition for the transfer of electrons from the absorber to the acceptor. While many different materials are possible for use as an acceptor, the most common materials are based on fullerenes such as the molecule seen in Figure 1.1c.¹⁰

Commonly, the absorber material is mixed with the acceptor material to form what is known as a bulk heterojunction structure. Because the two materials are generally immiscible, they phase separate to form micro-domains within the active layer. This greatly reduces the distance between the absorber and acceptor at any given point in the active layer, which is particularly advantageous for OPV as the length scales for geminate recombination are relatively short (~10nm). The morphology of this layer is therefore critical to the overall performance of the device as the domain sizes and distribution can greatly change the amount of recombination which occurs within the active layer.^{8,9}

With the planar nature of most OPV architectures, the active layer is sandwiched between a cathode and an anode to create a functioning photovoltaic cell. However, due to the HOMO and LUMO levels of the active layer materials and the work functions (energy barrier for transfer of electrons at a metallic surface) of the conductive electrode materials, it is often advantageous to include intermediate layers as electron or hole transporters. These layers facilitate the transport of charges from the active layer to the electrodes by providing an energy level which is between that of the active layer and the electrode. These materials can also improve the interfaces allowing for better transport of charges between layers.²⁷ Electron transport layers (ETL) usually consist of a metal oxide such as zinc oxide (ZnO) or titanium oxide (TiO_2 , TiO_x). Hole transport layers (HTL) are commonly made of poly{3,4-ethylenedioxythiophene} blended with poly{styrene sulfonate} (PEDOT:PSS), though inorganic materials such as molybdenum VI oxide (MoO_3), tungsten VI oxide (WO_3) and vanadium V oxide (V_2O_5) can also be used.^{10,29,30}

OPV electrodes consist of a transparent front electrode and a metallic back electrode. As there are very few known quality transparent conductors, the majority of OPV devices to date use indium tin oxide (ITO) for the transparent electrode. However, much research has been done to develop alternatives to ITO because of its cost and processing difficulties. Metallic grids and silver nanowires in conductive polymer matrices are two common ITO replacements for the transparent electrode. The transparent electrode is typically coated onto a transparent substrate such as glass or a polymer film.^{4,10,31,32} This electrode can be either the cathode or the anode depending on the desired architecture of the cell. In a classical structure, the HTL is coated on top of the transparent electrode followed by the active layer, ETL and back electrode. In this architecture, the electronic properties of the cell necessitate the use of a low work function electrode such as calcium or aluminum. In an inverted architecture the cathode and anode are switched (and thus also the ETL and HTL).^{9,10,25} This results in the ability to use a higher work function material with silver being by far the most common choice. A diagram showing the differences in these two architectures can be seen in Figure 1.2.

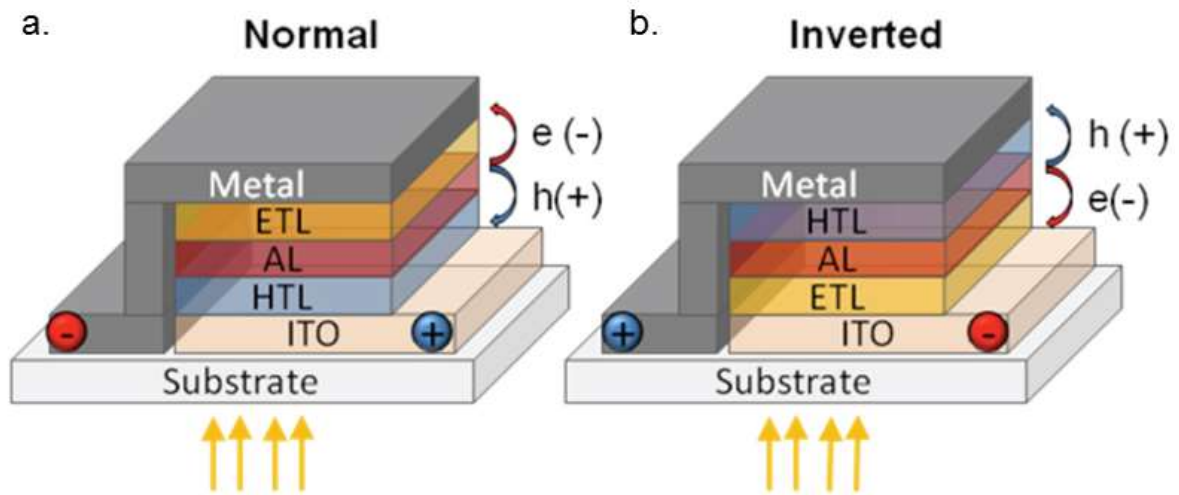


Figure 1.2 Diagrams of the structure of the (a) classical, or normal, and (b) inverted architectures for OPV are shown.⁹

One major drawback which has inhibited the widespread adoption of OPV technologies are their relatively low power conversion efficiencies in comparison to other solar technologies. In recent years the efficiencies of OPV devices have greatly improved however, as can be seen in Figure 1.3.³³ This increase in power conversion efficiencies to over 10% has greatly improved the prospects for the commercialization of OPV technologies as evidenced by a number of companies which are nearing industrial scale production of OPV devices.^{11,14–23}

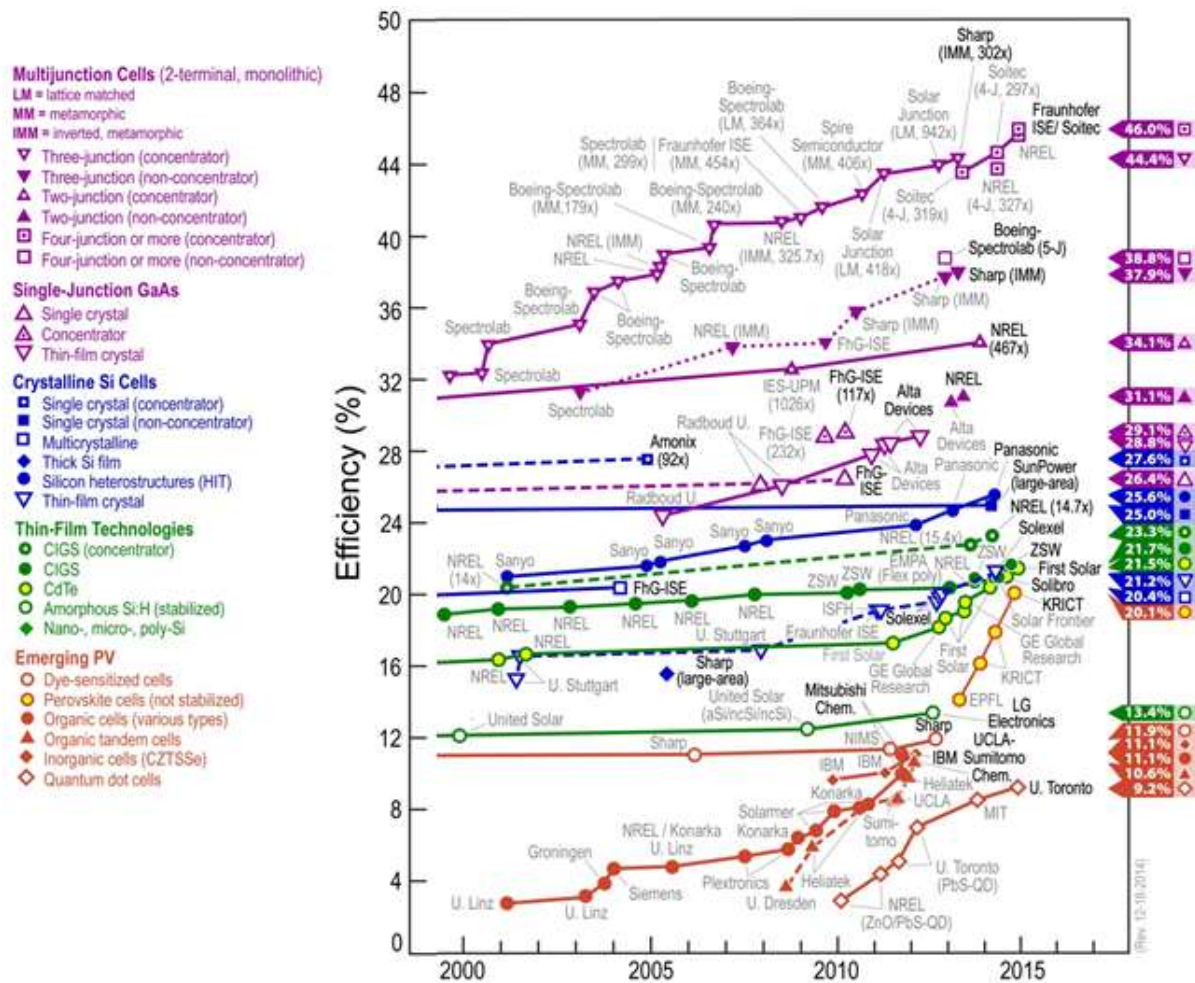


Figure 1.3 The record certified power conversion efficiencies for lab-scale solar cells is shown with OPV technologies represented by orange circles and triangles. This plot, reproduced here in modified form, is courtesy of the National Renewable Energy Laboratory, Golden, CO, USA.³³

Degradation Mechanisms

One of the major problems limiting the wide scale production and deployment of OPV is their instability. The performance of OPV tends to degrade over time and does so quite rapidly in comparison to most other solar technologies. This degradation comes from a combination of different mechanisms at different levels within the device. In fact, there are degradation mechanisms present at almost every material and interface within an OPV device, as can be seen in Figure 1.4.^{8-10,24,28} Limiting degradation and therefore extending device lifetimes is critical to the adoption of OPV on an industrial scale. In order to develop methods to prevent the loss of performance in OPV, it is necessary to understand its root causes.

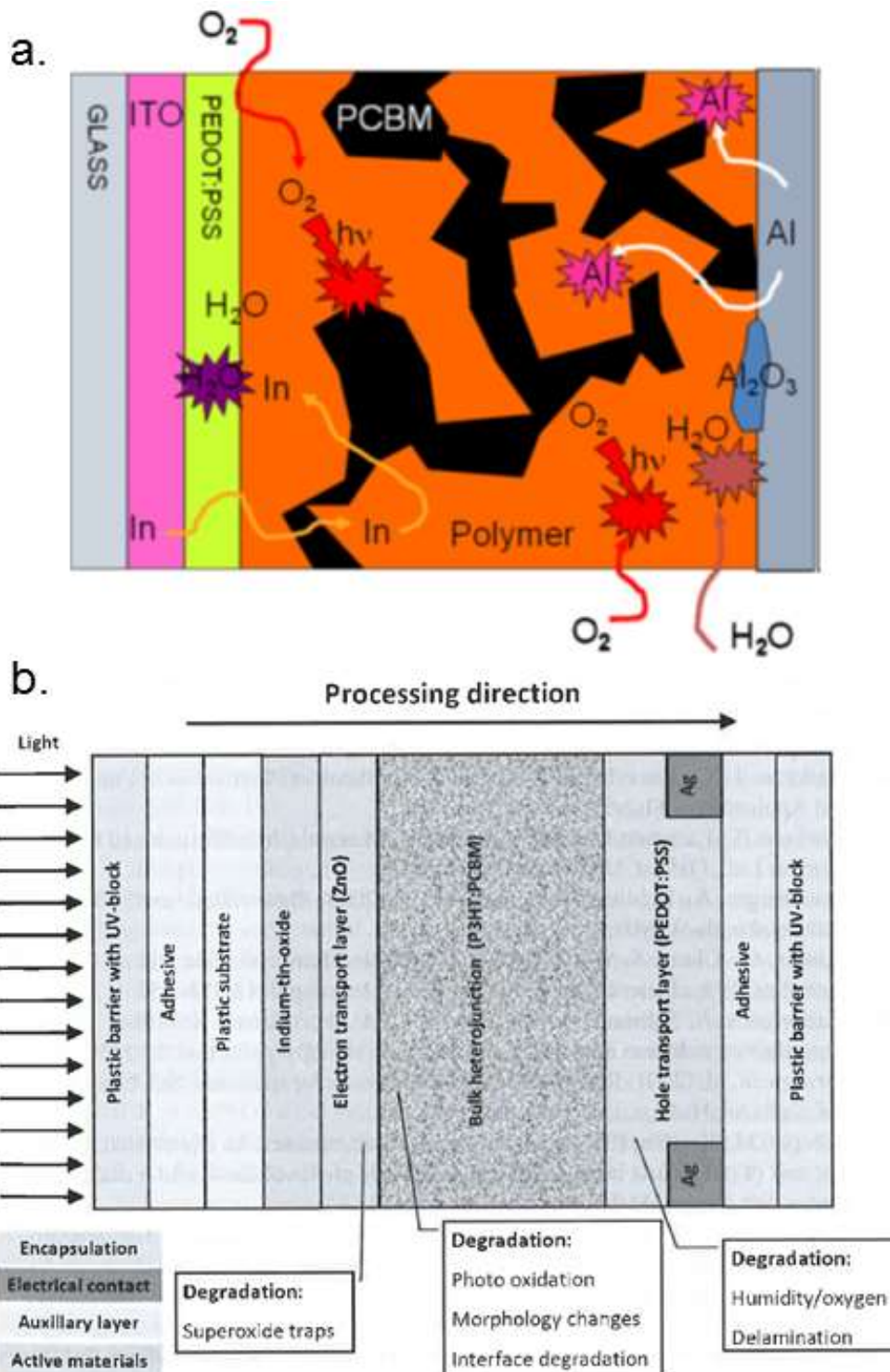


Figure 1.4 Several different possible degradation pathways for OPV are shown in these cross-sectional diagrams of a typical bulk-heterojunction OPV with (a) a classical structure and (b) an inverted structure. In these images “Polymer” refers to a polymeric active layer absorber material, “PCBM” is a fullerene based electron acceptor material and P3HT is the active layer absorber material poly(3-hexylthiophene).^{8,10}

Starting at the active layer, several different degradation pathways exist.^{8–10,28,34} The light absorbed by the electron donor material not only produces electron-hole pairs for electricity generation, but can also cause intrinsic degradation. The photostability of active layer

materials varies greatly as many different types of molecules with different chemistries can be used, however most will undergo some form of photo-degradation. This degradation can take the form of oxidation of the macromolecular chains, chain scission or cross-linking, but in any case the photo-degradation results in a modification of the electronic structure of the molecules thereby affecting the absorption, charge generation and charge transport of the active layer. While photolysis reactions will occur without the presence of oxygen, they tend to be at a relatively slow rate compared to the faster kinetics of the photo-oxidative reactions. An example of this is found in the common OPV absorber material poly(3-hexylthiophene) (P3HT) which shows very good photostability in photolysis conditions where no oxygen is present while showing pronounced degradation in photo-oxidative conditions in air.^{10,28,34,35} Therefore, limiting the presence of oxygen in the active layer can improve its stability. However, this result does not hold true for every active layer material with some materials, such as (MDMO-PPV), showing relatively poor photostability even when oxygen is not present.^{10,28,34} Also, the overall level of photo-degradation can be limited by the use of UV screening encapsulation as the higher energy UV light generally degrades the materials at a faster rate than visible light, though the materials will also degrade from visible wavelengths.^{10,26}

Non-photo-induced degradation can also occur in the active layer. Oxygen and water can react with the active layer via other reaction routes even under dark conditions, making their exclusion even more important.¹⁰ The active layer can also be responsible for changes in performance over time due to the nature of the bulk heterojunction structure. Since the active layer is a mix of two immiscible materials, phase domains form. These domains are critical to the proper functioning of the device in terms of charge separation and conduction of charges towards the electrodes. However, the morphology of these domains is not thermodynamically stable in most cases and can therefore change over time. Changes to the active layer morphology are generally thermally activated processes and can cause changes in device performance by increasing the distance charges must travel to reach the acceptor material. This leads to an increase in recombination as fewer electron hole pairs are effectively separated. Changes in the morphology can also lead to changes in the concentration of each phase at the interfaces with the adjacent layers which can affect the charge transfer to these layers.¹⁰ Additionally, fullerenes, which are commonly used as the acceptor material in the active layer of bulk heterojunction devices, tend to have very low surface energies making adhesion to adjacent layers difficult. This weak adhesion makes delamination more likely when mechanically stressed.^{10,36,37}

The intermediate charge transport layers can also contribute to the loss of performance in OPV.^{8-10,29} Many of the metal oxide materials used as electron transport layers can act as photo-catalysts by aiding in the formation of oxygen radicals when molecular oxygen is present. These radicals are then able to attack the adjacent organic active layer.^{8-10,34} These metal oxides can also react with oxygen to form superoxides which create electron trap states.¹⁰ Hole transport layers, in particular PEDOT:PSS, can contribute to the degradation of OPV. PEDOT:PSS is a very hygroscopic material and can speed the permeation of water throughout the device and act as source of water for other degradation processes in adjacent layers.¹⁰ PEDOT:PSS is also acidic in nature and can etch ITO over time in devices using the classical structure where the two materials are in contact, especially when water is also present.^{8,10} Additives and surfactants in commercial formulations of PEDOT:PSS can also diffuse to the surfaces of the layer and affect the interfaces with adjacent layers.^{8,10}

The transparent electrode can also cause a loss of device performance. Traditionally, the vast majority of OPV have used ITO for this layer. ITO is a brittle material however and is prone to cracking when flexed.¹⁰ Indium from the electrode can also diffuse throughout the rest of the device.^{8,10} As ITO also has several other processing concerns, replacements for ITO have been an active area of research. While other metal oxides have been considered for use in place of ITO, metal grids and silver nanowires are currently the most prevalent alternatives to TCOs, but both are usually embedded in a conductive polymer to form the electrode.^{4,10,31,32} The most common polymers for this task are high conductivity PEDOT:PSS formulations and therefore these electrodes tend to exacerbate the previously discussed degradation mechanisms associated with PEDOT:PSS.³⁸

The stability of the metal back electrode depends greatly on the architecture of the device.^{9,10,25,39} For classical structures, this can be one of the most sensitive materials in the device. For optimal electrical performance, metals such as aluminum and calcium are used. However, both of these materials are unstable in air. Aluminum can oxidize to form an electrically insulating layer at the interface where it is in contact with the device. Additionally, aluminum can react with and diffuse into fullerene layers when no intermediate layer is present.^{8,10} Calcium meanwhile is highly reactive with water to form the non-conductive calcium hydroxide.^{8,10} Using an inverted structure, these highly reactive metals can be replaced with the much more noble silver. This change in electrode material is credited as the reason why the inverted structure is several orders of magnitude less sensitive to water ingress as seen in Figure 1.5.^{9,10,25,40}

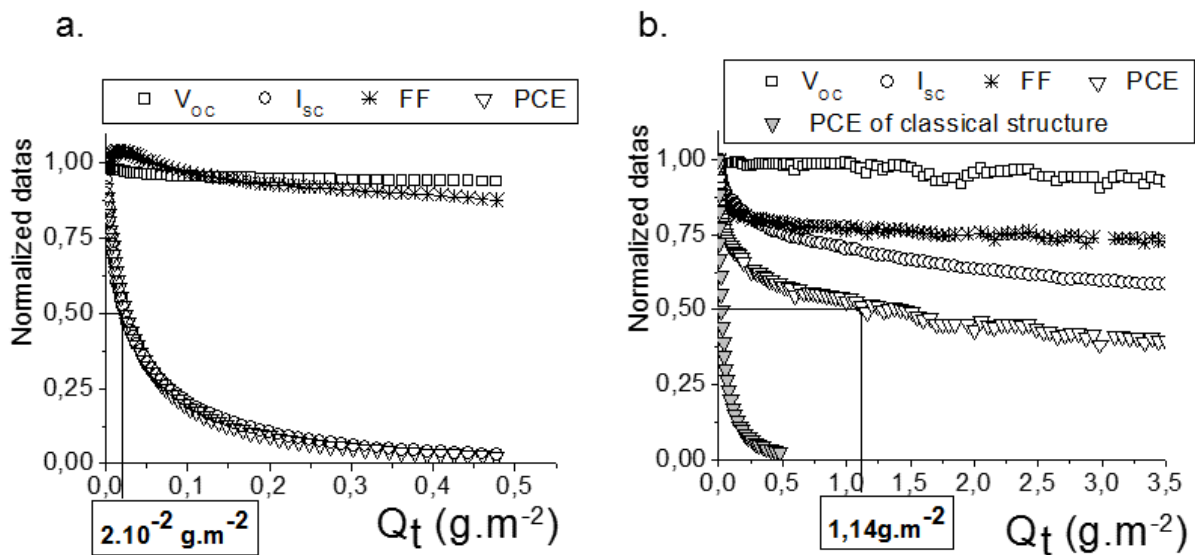


Figure 1.5 Plots of aging of OPV cells at 38°C and 100% relative humidity under illumination are shown as a function of the mass of water which had permeated across the encapsulation for both (a) classical and (b) inverted architectures. The inverted cells maintained 50% power conversion efficiency with 2 orders of magnitude more water present inside the encapsulation.²⁵

While many different materials are used throughout each layer of OPV devices, it can be seen that light, temperature, oxygen and water play significant roles in the loss of device performance. Photo and thermal degradation processes are more difficult to avoid and generally must be addressed by improvements to the materials and device architectures. Oxygen and water on the other hand, can be limited through the use of high gas barrier encapsulation. The elimination of these contaminants from the device can greatly improve the device lifetime without the need to modify the device itself.^{10,26}

Similar Technologies

While the main focus of this thesis is on the application of OPV, the same types of permeation testing, barrier materials and encapsulation techniques are also applicable to other technologies. The most similar analogous technologies are other organic electronic devices, but other types of inorganic solar technologies can also benefit from improved high-barrier encapsulation.

Organic electronics are a large class of devices, which include OPV, that use organic semiconductors to create electronic devices. All organic electronics are susceptible to the inherent instability of organic semiconductors compared to highly stable inorganic semiconductors. Some types of devices are more stable than others however. For example, organic thin film transistors are generally more stable due to their lack of illumination and an

architecture which usually incorporates an inorganic insulating material which provides some barrier protection.⁴¹⁻⁴³ On the other hand, some organic electronics are as, or more, vulnerable than OPV. Organic photodetectors are one such device which use the photovoltaic effect of organic semiconductors to sense the presence and/or intensity of light. These devices are constructed using device architectures very similar to those of OPV but are optimized differently in order to achieve more sensitive measures and clearer on/off signals. Although the operational conditions are different from OPV (indoor vs. outdoor, different spectra of illumination), they are nonetheless subject to the same degradation mechanisms as OPV.¹³ Another analogous organic electronic technology is the organic light emitting diode (OLED). Organic light emitting diodes operate in a manner similar to inorganic light emitting diodes in that they luminesce at certain wavelengths when subjected to an electric potential. While some of the materials used are slightly different than in OPV, they generally have device architectures which are nearly identical to those of OPV. This makes them vulnerable to all of the same degradation mechanisms as OPV. In addition, OLEDs usually have much poorer performance with inverted architectures, therefore most OLED devices use a classical architecture with easily degraded, low work function electrodes. This makes them even more sensitive than OPV and the generally recognized maximum water vapor transmission rate (WVTR) for OLED encapsulation is 10^{-6} g/m²/day compared to 10^{-3} g/m²/day for OPV.^{25,44-51} It should also be noted that OLEDs have different requirements for what constitutes a failed device as point defects such as dark spots are often considered unacceptable for OLED displays but are not a major concern for OPV which is concerned mainly with the total amount of energy harvested.

Other photovoltaic devices are also vulnerable to degradation from permeating gases and require barrier encapsulation. The prominent degradation mechanisms of several types of solar technologies are shown in Figure 1.6.¹⁰ Crystalline silicon modules are intrinsically very stable devices, however they still require encapsulation to avoid mechanical fracturing of the silicon and corrosion of the metal electrical connections. Preventing corrosion of the electrical connections requires only minimal barrier protection though and crystalline silicon modules are able to achieve very long device lifetimes using encapsulation materials with relatively high permeation rates such as poly(ethylene-co-vinyl acetate) (EVA).^{10,52,53} Thin film photovoltaics are much more susceptible to degradation than crystalline silicon modules, however they are still less sensitive than OPV. Amorphous silicon modules can suffer from photo-degradation of the active layer, however this has been mostly controlled through better control of the nano and micro crystallinity of the silicon.¹⁰ Cadmium telluride based modules can suffer from degradation due to the back electrode which can diffuse into the active layer or corrode in the

presence of humidity. This has largely been solved through the use of more stable electrode materials such as antimony-molybdenum alloys and encapsulation with relatively high permeation rate materials such as (EVA).¹⁰ The most sensitive inorganic photovoltaic modules are those which use a copper indium gallium diselenide (CIGS) active layer. This sensitivity comes primarily from the degradation of the Al:ZnO front electrode in the presence of humidity. While the traditional encapsulation techniques used for crystalline silicon modules can work for CIGS modules, they are not always sufficient water barriers for long device lifetimes. CIGS encapsulation is further complicated by their ability to produce flexible modules which cannot use impermeable glass sheets. This creates an encapsulation problem very similar to that of flexible OPV, though CIGS barrier requirements are less strict.⁵⁴⁻⁶⁰ Nonetheless, encapsulation technologies developed for flexible OPV are directly applicable to flexible CIGS modules as well. Recently, rapid advances have been made in organic-inorganic hybrid photovoltaic cells based on a perovskite structure with laboratory-scale cells showing power conversion efficiencies of up to 22%. While the materials and device physics are quite different for these materials as compared to OPV devices, they provide many of the same benefits as OPV devices including low-temperature processing, the use of printable inks, and the mechanical flexibility of the devices.⁶¹⁻⁶⁵ The stability and degradation mechanisms in these perovskite cells are still being investigated. It does appear that some type of flexible encapsulation will also be needed for this technology although it may still be too early to tell what level of gas barrier protection will be needed.

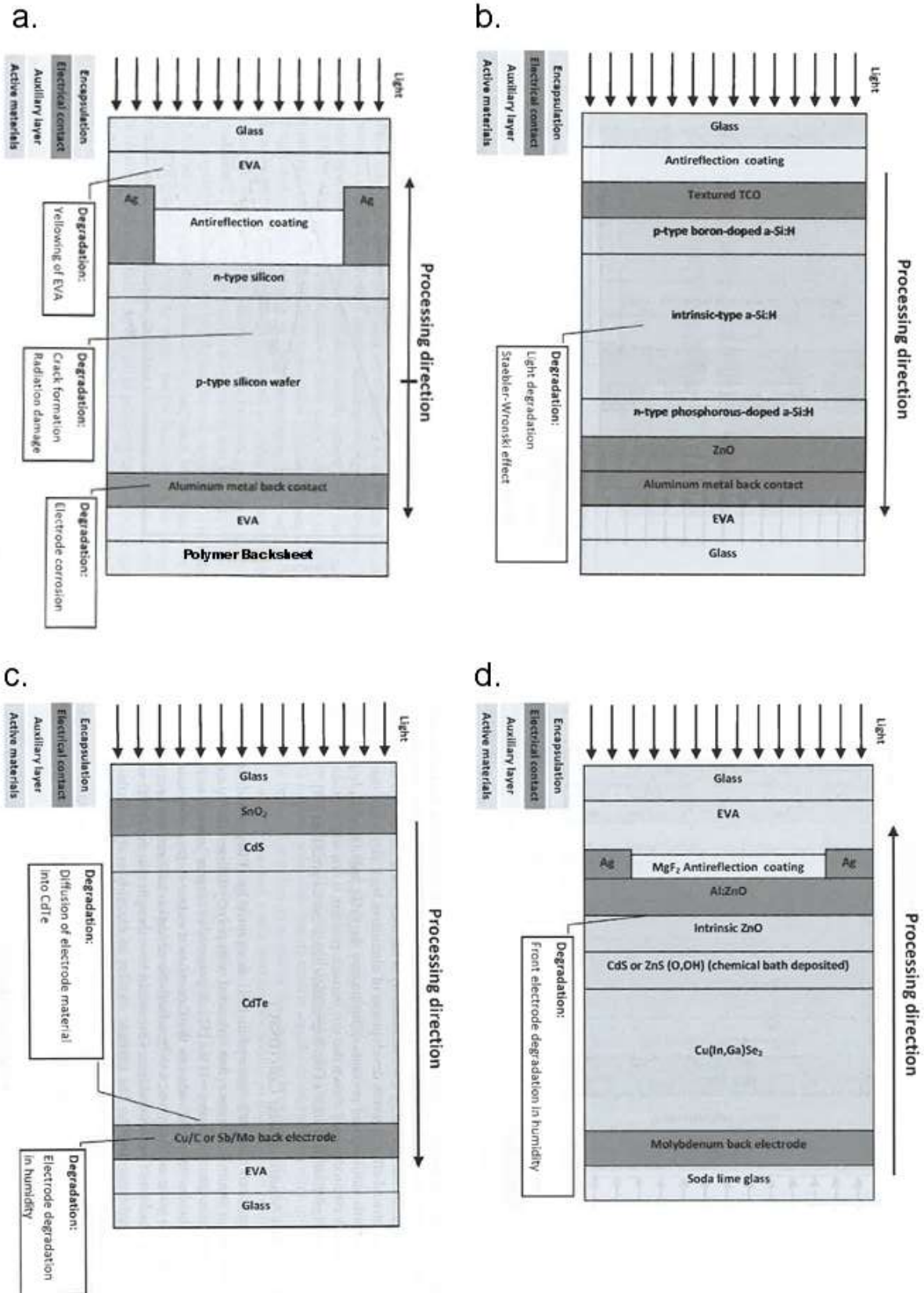


Figure 1.6 Cross-sectional diagrams along with the most prominent degradation mechanisms are shown for solar cells with active layers based on (a) crystalline silicon, (b) amorphous silicon, (c) cadmium telluride and (d) CIGS. Images modified from Krebs et al.¹⁰

Permeation Mechanisms and Encapsulation Materials

Permeation Mechanisms in Materials

Fickian Diffusion

Fick's Laws of diffusion were first published by Adolf Fick and provide a mathematical model of diffusion. Fick's First Law describes the flux of permeating species through a matrix as a function of the spatial concentration gradient as is seen in Equation 1.1 for the case of one dimensional diffusion.⁶⁶

$$\text{Equation 1.1} \quad J = -D \frac{\partial C}{\partial x}$$

In this equation J is the flux, D is a permeant and material dependent constant known as the diffusion coefficient, C is the concentration of the permeating species and x is the distance in the direction of diffusion. The diffusion coefficient, D , is a function of temperature with an Arrhenius type relation as seen in Equation 1.2.⁶⁶

$$\text{Equation 1.2} \quad D = D_0 e^{-E/RT}$$

In this equation E is an activation energy which is constant for a given material, R is the universal gas constant and T is the absolute temperature. Fick's First Law is particularly useful for modeling diffusion in the steady state. Steady state diffusion can be defined as a case where the spatial concentration gradient is constant resulting in a constant flux. Before achieving a steady state condition, the permeation is in the transient state. In this state, the concentration gradient within the material changes as a function of time.⁶⁶ This can be seen in Figure 1.7 which shows the stabilization time needed for the permeation of water vapor for a typical barrier material.²⁵

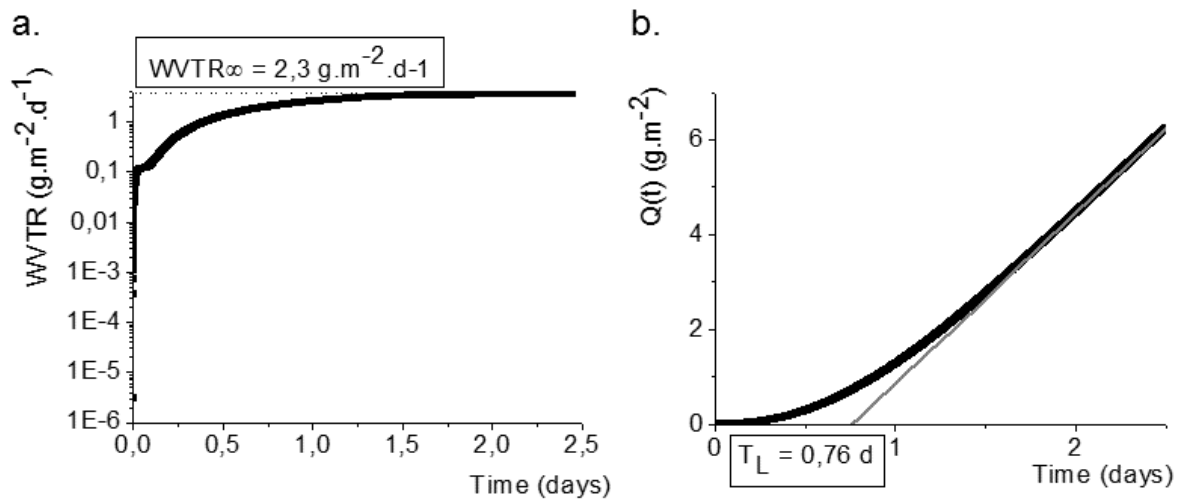


Figure 1.7 Plots for the water permeation of a flexible tri-layer laminate of polyethylene (46 μm) – ethylene : vinyl alcohol copolymer (6 μm) – polyethylene (46 μm) are shown as measured by a mass spectrometry based permeation cell using heavy water. (a) The WVTR of the material increases throughout the transient state until stabilizing to a constant value after approximately 1.5 days signifying that the steady state has been achieved. (b) When plotted as a cumulative mass of permeated water, Q , the time lag, T_L , can be calculated by extending a linear fit of the steady state region back to $Q=0$.²⁵

The amount of time needed for the significant amounts of gas to permeate across a barrier can be estimated as the time lag (T_L). The time lag is found by extending the linear, or steady state, portion of a plot of mass permeated versus time until it crosses the time axis. The value of time at the point along this linear curve where the mass permeated is 0 is defined as the time lag as illustrated in Figure 1.7b. This value, $h^2/6D$ where h is the thickness of the film, can be obtained from the linear part of the curve $Q=f(t)$, which is obtained by the resolution of the second Fick's law in the steady state regime. For barrier films, the barrier properties against a certain gas must therefore be reported with both a steady state permeation rate and the time lag in order to accurately predict the total permeation. Also, due to the temperature sensitivity of D , these two values are only valid for a given temperature.^{25,66–68} Figure 1.8 shows an example of how these two values can be used to predict whether a material can meet the barrier requirements for a certain application.²⁵

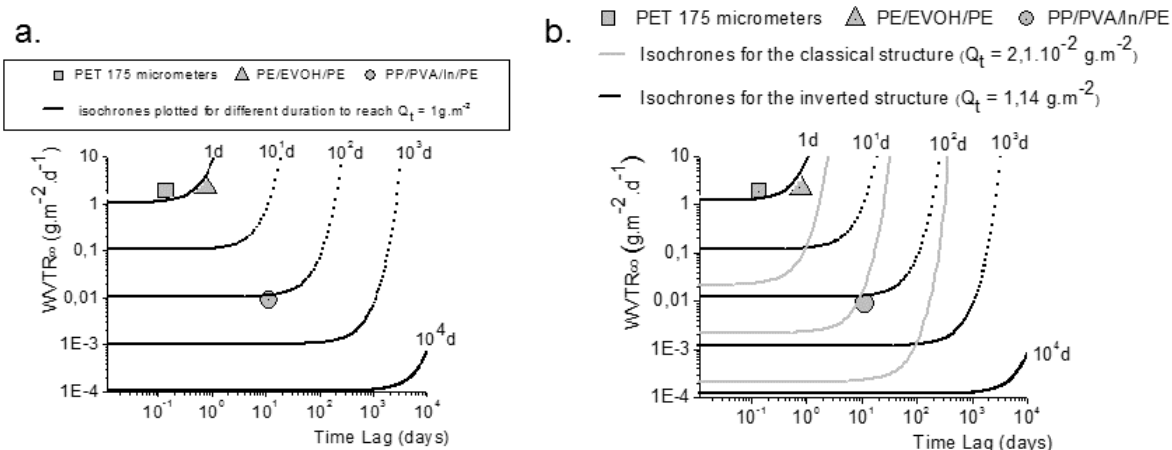


Figure 1.8 (a) Isochrones are plotted which correspond to the time required for a mass of 1 g/m² to permeate across a film. It should be noted that for short time lags, the permeation is dominated by the WVTR. However, as the time lag approaches the desired lifetime, the time lag becomes the dominant parameter. A homopolymer film, polymer laminate film and a polymer laminate with an inorganic barrier layer are also plotted as points. (b) If the quantity of permeant required to cause failure in a device is known, isochrones can be plotted for device lifetimes. Isochrones for classical and inverted OPV cells are shown in conjunction with the three example barrier films. If the point representing the barrier film is below/right of the isochrones, it will provide sufficient barrier protection to achieve the desired device lifetime.²⁵

For Fickian diffusion, the transient state can be modeled using Fick's Second Law which relates the change in the spatial concentration gradient with the temporal change in concentration as seen in Equation 1.3.⁶⁶

$$\text{Equation 1.3} \quad \frac{\partial C}{\partial t} = D \frac{\partial^2 C}{\partial x^2}$$

One important solution to this differential equation is for the case of one dimensional diffusion into a semi-infinite material. For this case, the steady state is never achieved as the leading edge of the diffusion front never reaches the opposite side of the material. Solving using these boundary conditions yields Equation 1.4 where *erf* is the error function, *C*₀ is the concentration at the exposed edge of the material and *A* is a constant.^{52,66,69}

$$\text{Equation 1.4} \quad C - C_0 = A \operatorname{erf} \left(\frac{x}{2(Dt)^{1/2}} \right)$$

By selecting a particular concentration, the difference *C* - *C*₀ becomes a constant meaning the operand of the *erf* must also be constant. This allows for the characterization of the advancement of the diffusion front, which is seen in Equation 1.5, where *K* is a material constant valid for a particular temperature and concentration.^{52,66,69}

$$\text{Equation 1.5} \quad x = K t^{1/2}$$

Polymeric Barrier Materials

Polymers are an excellent example of materials which follow Fick's Laws. The chain-like nature of polymers creates a large amount of free volume when compared to other dense solids. This free volume allows gases to permeate relatively easily through most polymers.⁷⁰ Reduction of the free volume through crystallinity and crosslinking can help to limit the permeability to an extent.⁷⁰ Polymers are commonly used as barrier materials for applications such as food packaging and a list of the oxygen transmission rate (OTR) and water vapor transmission rate (WVTR) for various polymers used for barrier applications can be found in Figure 1.9.^{26,71} As can be seen in this figure, even the best polymeric barriers remain several orders of magnitude higher than the OPV requirements of $10^{-3} \text{ cm}^3/\text{m}^2/\text{day}/\text{bar}$ and $10^{-3} \text{ g}/\text{m}^2/\text{day}$ for OTR and WVTR respectively.

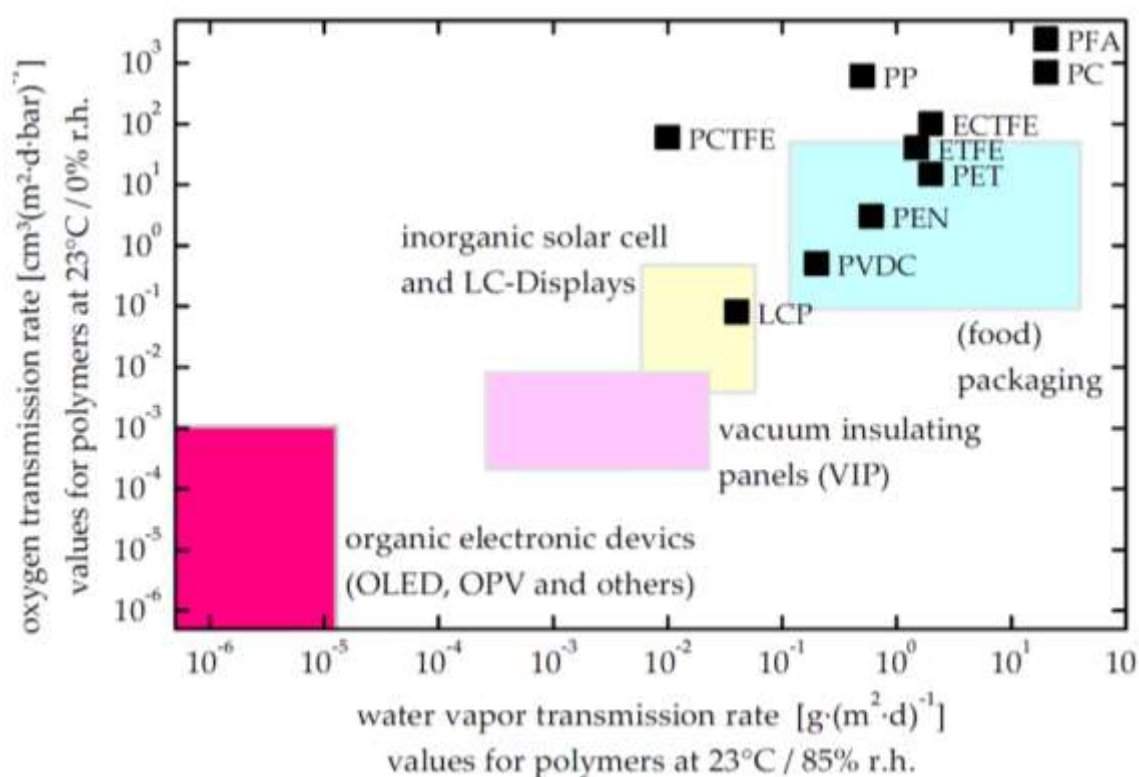


Figure 1.9 The permeation rates for oxygen and water vapor of various polymeric barrier materials are plotted. The colored regions of the plot correspond to the barrier requirements for various applications. It should be noted that this plot was published before the popularization of the inverted structure for OPV, therefore the OPV region on the plot could be extended to $10^{-3} \text{ g}/\text{m}^2/\text{day}$ on the water vapor transmission rate axis based on more current estimations.⁷¹

Inorganic Barrier Materials

Dense inorganic materials also display Fickian diffusion behavior in defect free regions. However, unlike polymers, the more tightly packed chemical structure of these materials greatly reduces their permeation rates. In fact, for many inorganic materials Fickian diffusion is so slow that they are effectively impermeable to oxygen and water at room temperature. This makes these materials prime candidates for barrier applications. Thin metallic coatings are

frequently used to improve the barrier properties of polymer films, however their opacity makes them ill-suited for use in the optical path where transparency is required. The best example of a transparent inorganic material displaying Fickian permeation is silica glass. The large thickness of glass sheets prevents the presence of defects which could traverse the sheet. This makes sheets of glass effectively impermeable to oxygen and water in the temperature range seen for outdoor applications.⁷² Glass has indeed been widely used to encapsulate OPV and other even more sensitive devices. However the thickness of glass required to provide effectively impermeable encapsulation generally results in rigid devices.^{10,26} While somewhat thin films of flexible glass can be used, they often remain relatively brittle and thus easily form large defects which gases can penetrate.^{73,74} For silica and other metal oxide materials to be highly pliable for use in flexible encapsulation, the thickness must be reduced to such a level that defects become unavoidable. This makes their permeation no longer Fickian and instead completely dependent on the density and size of the defects.^{75,76}

Defect-Dominated Permeation and Tortuous Paths

For the relatively thin layers of no more than several hundred nanometers required to make rigid inorganic materials flexible enough for use in flexible encapsulation, it becomes unavoidable to incorporate defects with almost all current technologies.⁷⁵ These defects traverse the thickness of the material and provide a much easier permeation pathway for gases. These defects can include cracks from mechanical stresses, deposition inhomogeneities, grain boundaries and nanoporosity. The presence of these defects across the thickness of an otherwise impermeable layer greatly changes its effectiveness as a gas barrier. This means that the overall permeation can no longer be described by Fick's Laws but is instead dominated by the relatively rapid permeation across the inorganic layer via defects. It has been shown that the permeation rates for thin layers are strongly dependent on the size and density of defects.^{68,76}

Commonly used inorganic materials for these thin, flexible barrier layers include SiO₂, Al₂O₃, TiO₂, Zr₂O₃, Zn₂SnO₄ and SiN as they are generally able to produce the best quality films in terms of defects. Many different deposition techniques can be used to create these films but there is always a balance of film quality, processing time and cost which has thus far prevented any one technology from gaining a large advantage over the others. Current deposition techniques include reactive sputtering, plasma enhanced chemical vapor deposition, atomic layer deposition and photo-conversion of liquid ceramic precursors.^{43,71,75,77-85} In order to minimize the probability that a defect will traverse the thickness of the material, thicker layers

are preferred. However, the brittle nature of these materials causes thicker films to be prone to cracking from mechanical and thermal stresses. Therefore a minimum permeation rate is usually obtained with a thickness in the range of 50-150nm as can be seen in Figure 1.10.^{75,77} However the permeation rates achieved at these thicknesses are still too high to achieve the requirements of OPV. Only atomic layer deposition has been shown to be capable of creating acceptable gas barrier protection for OPV devices with thicknesses below this range.^{45-47,71,81,86-89} However, there are currently other drawbacks to this process which will be discussed later in this chapter in the “Encapsulation Techniques” section.

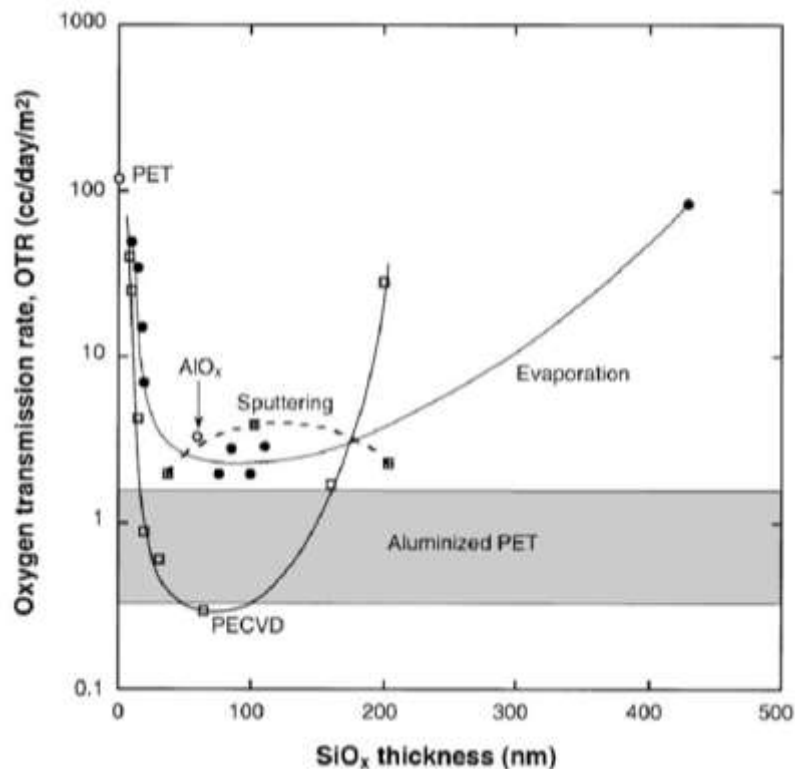


Figure 1.10 The OTR of SiO_x layers of various thicknesses deposited on PET are shown for various deposition techniques. Thicker layers limit the number of defects which completely traverse the SiO_x layer, however very thick layers become less mechanically stable and prone to cracking. This results in a minimum OTR at an SiO_x thickness in the range of 50-150nm.⁷⁵

In order to further improve the barrier properties of inorganic materials with defect-dominated permeation, multilayer systems have been employed. The goal of a multilayer system is to create stacks of inorganic barrier layers and therefore improve the barrier performance without cracking from stresses. This has been achieved by using softer intermediate layers in between the inorganic layers. Beyond providing more mechanical stability to the inorganic layers, this structure also creates discontinuities between the defects in each inorganic layer. The result is a so called tortuous path for the permeation of gases. After traversing a defect in an inorganic layer, the gas must then permeate along the next inorganic

layer until another defect allows for the gas to traverse the layer as shown in Figure 1.11. The increased path length for permeation caused by this tortuous path greatly enhances the barrier properties of the stack. A combination of one barrier layer and one intermediate layer is known as a dyad and reductions of the OTR and WVTR by multiple orders of magnitude have been reported for stacks with as few as two dyads.^{10,26,50,68,71,85,90–94}



Figure 1.11 The black arrows represent possible permeation pathways through a three dyad multi-layer barrier film. These pathways are tortuous as the permeating molecules cannot traverse the laminate in a straight line. Instead, the gas must permeate through each intermediate polymer layer along the impermeable inorganic barrier layers until it reaches another defect. This greatly increases the path length for permeation and therefore results in a low permeation rate.⁹²

Passive Composite Barrier Materials

The intermediate layers in a dyad structure are designed primarily to provide a planar layer for the next inorganic barrier deposition while breaking the transfer of defects from one barrier layer to the next. This is most commonly achieved through the use of an organic polymer which can be coated to a thickness on the order of microns.^{26,68} The relatively soft nature of polymers provide some stress relief to the brittle barrier layers, especially from the thermal stresses as many deposition techniques require elevated temperatures. They are generally not intended to serve as barrier layers themselves. However, an intermediate layer with some inherent barrier properties could slow the permeation rate of the multilayer stack even further as any permeating gas must pass through this material. With this goal in mind, several alternative intermediate layers have been proposed in the literature including heavily cross-linked organic polymers, composites of organic polymers and inorganic particles, and inorganic polymers.^{71,85,90,91,95–97} In addition to intermediate layers, it is often necessary to use an adhesive of some kind to secure a barrier stack or other encapsulation material to the device being encapsulated. Improving the barrier properties of these adhesives is also critically important as they are often present in much thicker layers than the intermediate dyad layer and can be a weak link in some encapsulation processes, which will be discussed in detail later in this chapter. These adhesives therefore have quite similar requirements to the intermediate layers of a multi-layer barrier and often use the same strategies to reduce their permeation rates.^{94–102}

The concept of the tortuous path can also be applied to polymeric systems through the incorporation of inorganic particles. By dispersing particles made of a relatively impermeable material throughout the polymer, any permeating gas must go around the particle. The resulting increase in the permeation path length is a tortuous path just as in the case of the previously discussed stacks of thin inorganic layers. Since the particles simply block the path of permeating gases and do not strongly interact with them either through sorption or chemical processes, this type of composite material is said to be passive in nature. The barrier effect caused by the introduction of passive particles is well known and has been heavily exploited for many years using a wide variety of particles. Commonly used particles include but are not limited to SiO_2 , Al_2O_3 and TiO_2 . These particles are often on a length scale of several microns or greater and are incorporated at high concentrations to achieve low permeation rates. However, high concentrations of these materials limit or eliminate the transparency of the composite and can often cause the composite to be quite rigid which causes any encapsulated device to lose its flexibility. Decreasing the concentration of particles shortens the tortuous path however and thus leads to high permeation rates. The large size of these particles also limits the minimum thickness of a layer of the material and can lead to a less planar surface.^{70,90,97,103–106}

To solve the problem of reducing the mass or volume fraction of particles while maintaining a tortuous permeation path, it quickly becomes apparent that a high aspect ratio particle is needed. A plate-like structure with a large diameter and small thickness should be able to provide a tortuous path even at low loadings. This has led to the widespread use of phyllosilicate particles in passive composite barrier materials. Phyllosilicates are silicate materials which also incorporate other cations into their tetrahedral bonding structure. The tetrahedrons are organized in manner that forms strong covalent bonds in two dimensions but relatively weak bonds in the third dimension resulting in a plate-like structure. A diagram of the structure of the phyllosilicate material montmorillonite is shown in Figure 1.12 as an example of this type of structure.¹⁰⁷ When properly dispersed in a solution or polymer, the plates become exfoliated and the thickness of each individual particle becomes the thickness of a single plate. This results in a particle with a diameter on the order of several microns and a thickness of only a few nanometers. To more effectively exfoliate phyllosilicates dispersed in polymers, they are often organically modified using salts with short organic chains covalently attached. These very high aspect ratio nanoparticles are able to provide a tortuous permeation path at loadings of just a few weight percent thus preserving the transparency of the composite.^{90,91,103–106,108–114}

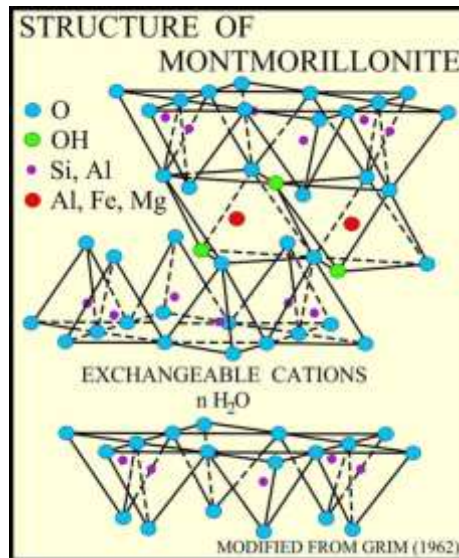


Figure 1.12 A diagram of the structure of montmorillonite is shown. Like other phyllosilicates, montmorillonite consists of sheets of tetrahedrally and octahedrally coordinated silicates. Between each sheet are cations and absorbed water. If the particles have been organically modified the organic salts would also occupy this space between sheets. When exfoliated, the sheets separate creating particles with a very high aspect ratio.¹⁰⁷

Getters

An alternative approach to the passive composite and tortuous path is the use of an active material which strongly interacts with a permeating gas. These active materials are commonly known as getters and can be broken into two major classes: those who consume a permeating gas through a chemical reaction; and those who trap permeating gas via sorption processes. Depending on the exact type of getter used, they can either be incorporated into polymer as a composite or placed inside a cavity with the device to be protected. By definition, a getter must interact with the permeating gas, therefore many getters are developed to interact with one particular gas. Getters which are designed specifically for water are often referred to as desiccants.

Reactive

Reactive getters consume permeating gas via a chemical reaction, thus eliminating the gas. These getters have traditionally been used in vacuum tubes in order to eliminate any contaminants which might degas over time in the tube. Though many different materials have been used as reactive getters, they are usually based on highly reactive metals such as barium, zirconium alloys and calcium or sometimes their intermediate reaction products (i.e. CaO which is an intermediate product in the reaction of Ca and water to ultimately form Ca(OH)₂). Some types of reactive getters, such as CaO, can also be prepared as particles and incorporated into composite materials.^{26,47,48,115}

Sorption

Rather than consume any permeating gas, some getters instead adsorb the gas molecules on their surface. As these materials need a high surface area to adsorb large quantities of gas, they are usually highly porous often with pore diameters on the order of only a few nanometers. Several common types of getters which use adsorption are silica gels, activated carbon, templated mesoporous materials and molecular sieves such as zeolites and aluminophosphates. Silica gels (aerogels, xerogels) have the highest water sorption of these materials due to the high porosity produced by their sol-gel processes. These materials take advantage of the ample silanol groups on their surfaces to bind polar water molecules. Templated mesoporous materials are also usually silicates or aluminosilicates which have been assembled into a mesoporous structure with the aid of organic surfactants which phase separate on nanometer length scales. Despite their high water sorption capabilities, these materials are often relatively expensive to fabricate and can have problems with long term stability. Zeolites are aluminosilicates which have an ordered highly porous structure that allows for a high water sorption capacity, though slightly lower than silica gels. Aluminophosphates are very similar to zeolites except that they are based on phosphate chemistry instead of silicates. These materials can have higher water sorption than zeolites but are generally less stable and more expensive. A comparison of some of the properties of these materials can be found in Table 1.1. Most of these materials are typically fabricated into particles on the micro-scale or larger, which severely limits their ability to maintain transparency when dispersed into a composite, especially activated carbon which strongly absorbs visible light.^{105,106,116-118}

Table 1.1 Comparison of different materials for water sorption

Material	Water sorption capacity (g/g)	Water sorption rate	Price	Long term stability
Silica Gels	0.40 – 1.45	Medium	Medium	High
Templated Mesoporous Materials	0.45 – 0.84	Medium	High	Low
Zeolites	0.20 – 0.45	High	Medium	High
Aluminophosphates	0.15 – 0.54	Medium	High	Low

Of particular interest are zeolites as they have the ability to be manufactured as nanoparticles. There are a wide variety of zeolite structures, but they are generally based on cage-like structures created by silicate and aluminosilicate tetrahedra. These cages form a series

of ordered pores with the smallest pore diameters in the range of 6-14nm. Water can adsorb on the structure via several different processes. Cations, such as aluminum, can create both Brønsted and Lewis acid sites which are capable of binding multiple water molecules. In addition, clusters of silanol groups within the pores create nests which can bind water molecules and other silanol groups present on the outer surface of the particles also provide sites to bind water. A diagram of these different binding sites can be seen in Figure 1.13.¹¹⁶⁻¹¹⁸ Nanoparticles of zeolites have been well researched, however their use in barrier composites has received only very limited attention.^{49,118}

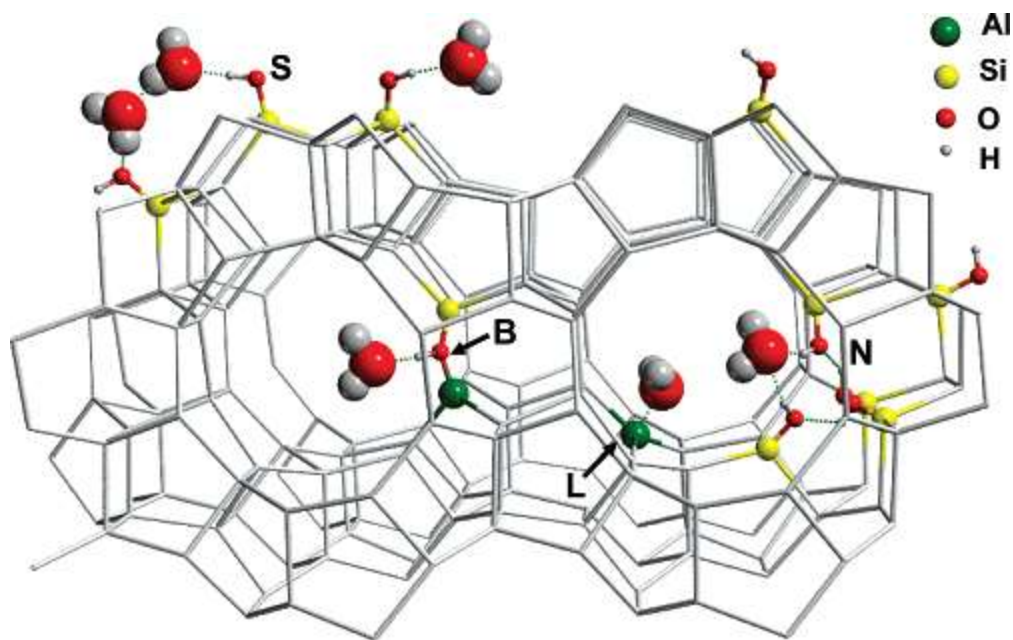


Figure 1.13 The different types of water binding sites are shown in the pore structure of a zeolite with an H-MFI structure. B refers to a Brønsted acid site. L refers to a Lewis acid site. N refers to a nest of SiOH groups. And S refers to a surface SiOH group. In this image, the B, L, and N sites are located within the pores of the zeolite.¹¹⁶

Interfaces

When two different materials meet to form an interface, a new permeation pathway can be created which does not follow Fick's Laws.¹¹⁹⁻¹²² Permeation along interfaces is often controlled by the surface energies of the materials and can occur both along the interface itself and/or in within one or both of the materials in the region immediately adjacent to the interface known as the interlayer.

Delamination

When permeation occurs along the interface itself, the result is often a delamination of the interface. Depending on the types of materials meeting at the interface and the type of permeant, this process can occur in different ways. In some cases, the sum of surface energies

of material A-to-permeant and material B-to-permeant is lower than the surface energy of material A-to-material B. When this occurs, the system's preferred state is delaminated and the change in surface energies becomes a driving force for delamination.^{103,104,123-125} When at least one surface is metal and the permeant is water, galvanic corrosion can occur using the water as an electrolyte which greatly changes the surface chemistry at the interface leading to delamination.^{103,104} Another mechanism which can cause delamination when water is the permeant is osmotic pressure. As water molecules fill the region between the two materials, the osmotic pressure created pushes the two materials apart and promotes the spread of the delamination along the interface. As the interface delaminates, more water enters the crevice and continues to apply osmotic pressure thus further propagating the delamination. This type of delamination can often be modelled as a mechanical crack growth in a solid material.¹²⁶⁻¹²⁹ Regardless of the type of delamination, access to the interface due to a lamination defect or mechanical stresses can greatly accelerate the start of delamination.

Interlayer Permeation

Even without complete delamination an interface can still provide a rapid permeation pathway. This can occur due to the effects of the interlayers. The region within each material which is immediately adjacent to the interface often has a structure which is different than the bulk material due to the presence of the interface. This modification of the structure can sometimes lead to a faster permeation rate in this region compared to the bulk material and thus increase the overall permeation rate.^{119,122,124,130} A different but common scenario which occurs in interlayer permeation is a surface energy effect. It is common for a saturated material to have a different surface energy than the same material with no concentration of permeant. If the surface energies favor an interface with the saturated material, this can create a driving force for more permeation in the interlayer.^{121,123} Conversely, if the interlayer is already saturated due to permeation in the bulk material, the interface can often times become much weaker due to the change in surface energy between the saturated and unsaturated material. This can increase the risk of delamination which would in turn cause more permeation along the interface.¹²⁷⁻¹²⁹

Encapsulation Processes

As previously discussed, the sensitivity of OPV devices to light, oxygen, water and combinations thereof requires that the devices be encapsulated in order to achieve economically viable device lifetimes. Many different encapsulation processes and schemes have been

proposed for this purpose and this section aims to provide an overview of the most prominent among these. Regardless of the encapsulation scheme, there are two main permeation pathways which will heretofore be referred to as orthogonal and lateral permeation respectively. Orthogonal permeation is defined as permeation which occurs orthogonally to the plane of the device. Lateral permeation on the other hand, refers to permeation in the plane of the device. Lateral permeation is also commonly referred to as side ingress. A diagram showing these two main permeation pathways can be seen in Figure 1.14. Due to the inherent aspect ratio of OPV devices (large area, small thickness), most encapsulation schemes employ some form of a stack with the device in the center.^{10,26} This creates interfaces which can provide permeation pathways in the lateral direction. Therefore, the lateral permeation can often be further broken down into bulk permeation through a material and permeation along the interface.

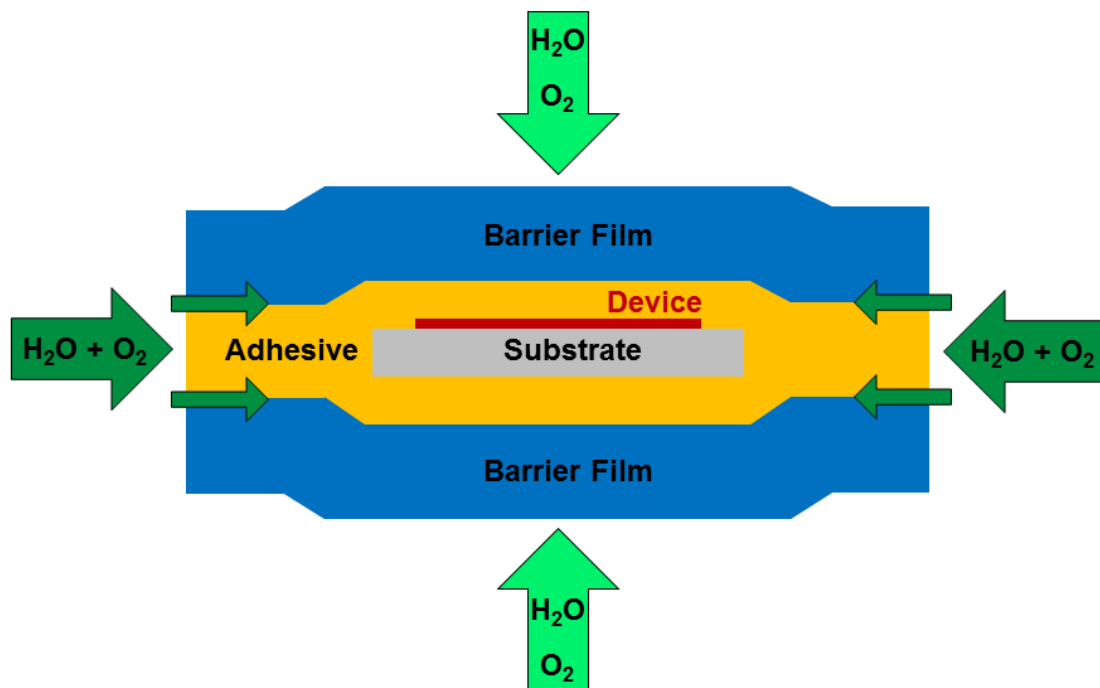


Figure 1.14 The different permeation pathways for water and oxygen are shown on a cross-sectional diagram of a typical encapsulation scheme for OPV. The lighter green arrows show orthogonal permeation while the darker green arrows indicate lateral permeation which can occur in either the bulk adhesive or along the interfaces.

Rigid Encapsulation

As previously discussed, silica glass is an ideal encapsulation material for solar applications as it is both highly transparent and impermeable to oxygen and water under outdoor conditions. As such, this material has been widely used to encapsulate OPV. Glass-to-glass encapsulation is a process which has been carried over from the industrial scale encapsulation of crystalline silicon solar modules. This technique seals the device between two plates of glass using an encapsulant adhesive. The device may be fabricated on its own substrate or directly

onto one of the glass plates.^{10,26} The weak-link in the barrier using this type of encapsulation is the encapsulant adhesive, which is much more permeable than the glass. This creates a scenario where the orthogonal permeation is negligible and the lateral permeation is the only major pathway. This lateral permeation includes both bulk permeation in the encapsulant adhesive and permeation along the adhesive-to-glass interfaces.^{10,26,53,57,131} To limit this permeation, edge seals around the perimeter of the glass are often employed. These are high-barrier adhesives, usually with high loadings of inorganic particles and often, though not always, quite rigid. Their high particle loading makes them almost universally opaque, hence why they are present only along the perimeter outside of the optical path.^{10,26,55,56,60,105,106,132} This encapsulation scheme is capable of providing an excellent encapsulation and long device lifetimes. However, glass-to-glass encapsulation is extremely rigid, thus negating many of the benefits of flexible OPV devices. Also, this rigidity eliminates the possibility of roll-to-roll processing.^{10,26}

Flexible Films

To make the scheme used in glass-to-glass encapsulation flexible, the glass must be replaced with a flexible material. This is achieved by the use of flexible barrier films. Though alternatives such as flexible glass films exist, most flexible films used for OPV encapsulation use a transparent multilayer dyad structure as previously described. These films have a relatively thick polymer substrate upon which inorganic barrier layers and intermediate layers are stacked. The exact design of these films varies greatly, but generally all are used in the same manner for encapsulation.^{10,26}

In this scheme, the device is laminated between two films using an adhesive in the manner shown in Figure 1.14: barrier film – adhesive – device – adhesive – barrier film. Recently, it has also become possible to build devices directly on flexible barrier films thus eliminating the need for one of the adhesive layers. Encapsulation using flexible films results in a slow orthogonal permeation rate since even though the films are not impermeable, they are often capable of meeting the requirements needed for OPV devices with device lifetimes on the order of several years.^{10,26}

Lateral permeation remains a major concern though as the adhesive presents the same weak-link in the barrier as seen in glass-to-glass encapsulation. However, the flexible nature of these films does provide much more versatility in the selection of the adhesive as bubble-free lamination without the use of vacuum is much simpler with flexible films. This is conducive to the use of liquid adhesives as well as allowing for the use of pressure sensitive adhesives.^{10,26,99}

This is of particular importance as it eases the development of flexible barrier adhesives. The flexibility of these films also allows for the use of roll-to-roll processing for encapsulation, which is particularly advantageous for OPV as the modules themselves are often fabricated using this process.^{3,5,10,12} However, processing via roll-to-roll makes the use of edge seals much more difficult as only two edges are exposed while on the web. Additionally, the flexibility of the films makes many edge seal materials less practical as many are quite rigid. Flexible edge seal materials can still be incorporated into this encapsulation scheme if sheet-to-sheet processing is used instead.¹³²

Direct Encapsulation

Rather than relying upon lamination, it is also possible to build barriers directly on top of devices. This method provides orthogonal protection similar to the flexible film method but can further limit lateral permeation depending on the exact scheme used.

Multilayer Systems

Multilayer dyad structures can also be fabricated directly on a device. This direct encapsulation method can be used for either rigid or flexible encapsulation. In this method, a planarizing layer is applied on top of the device in order to create a smooth, flat surface for the deposition of an inorganic barrier layer. Alternating intermediate and barrier layers are then deposited to form a stack of dyads. The first planarizing layer is often thicker than the subsequent intermediate layers in order to completely encapsulate and smooth the surface of the device. The first planarizing layer is still often times thinner than the adhesive layer in flexible film encapsulation, which can help to limit lateral permeation by reducing the exposed surface area of non-barrier material. The most well-known example of this scheme is the Barix[®] developed by Vitex Systems (now known as Vitriflex), an example of which can be seen in Figure 1.15. Other systems using this scheme are also being developed such as the YIELDjet[™] system from Kateeva.^{10,26,47,85,133,134}

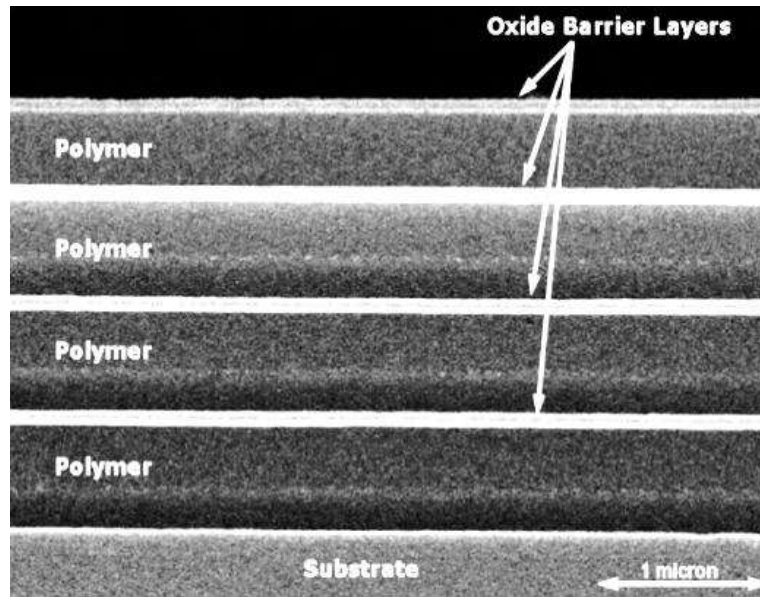


Figure 1.15 A scanning electron microscope image of the cross-section of a Barix® encapsulation comprising four dyads is shown. (Source: Vitex Systems/Vitriflex)

Atomic Layer Deposition (ALD)

ALD is a technique which can be used to create thin inorganic barrier layers as previously discussed. However ALD also provides the unique ability to create these layers conformally. This allows ALD to create barrier layers directly on devices without first applying a planarizing layer or adhesive, thus eliminating lateral permeation in the bulk material as the barrier layers are thick enough in the lateral direction to be effectively impermeable. This ability comes from the mechanism by which ALD deposits oxide materials. Two different chemical species are deposited sequentially and then react to form a conformal monolayer on all of the exposed surfaces. The deposition chamber is purged between each deposition and the process is repeated to grow the oxide layer one monolayer at a time. A diagram of this cyclic deposition and the resulting conformal coating are shown in Figure 1.16.⁸⁶ Perhaps most importantly, the monolayer by monolayer deposition creates an inorganic layer with remarkably few defects, and thus a very low permeability.^{45-47,71,81,86-89}

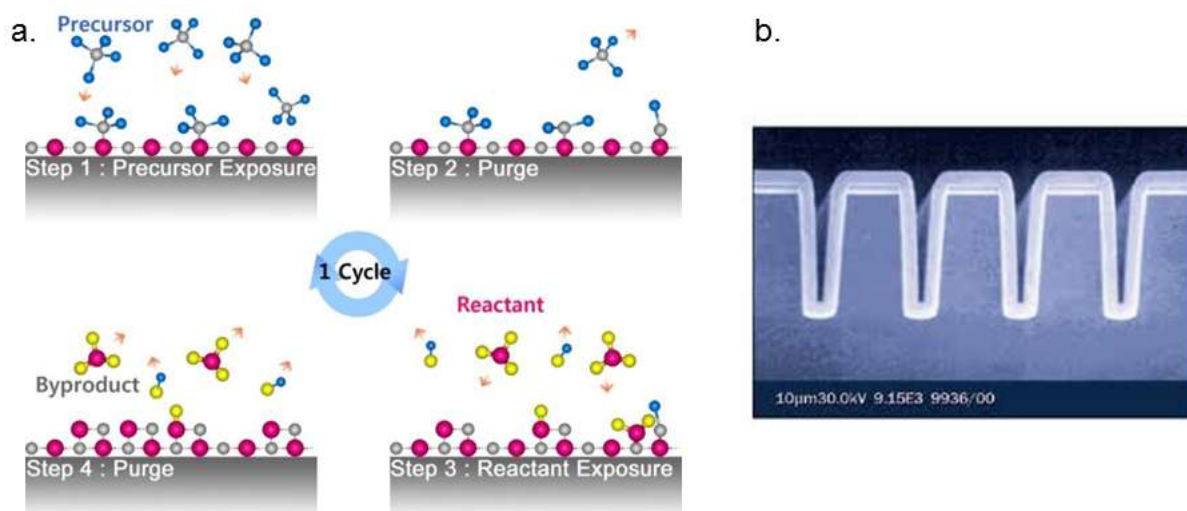


Figure 1.16 (a) The cyclic deposition process to create a single monolayer by ALD is shown step by step. (b) A conformal coating of Al₂O₃ was deposited by ALD onto silicon. The coating is able to conform to the unique geometry of the silicon substrate.⁸⁶

However, this same monolayer by monolayer process is also the greatest drawback to ALD. Needing to cycle through depositions and purges to create only a single monolayer means that it can be a very time consuming process which is not well suited to industrial scale encapsulation of OPV.^{10,26,87} Recent advances in ALD have reduced this time and the need for high vacuum in the deposition chamber, but it currently remains a difficult technique to scale up to an industrial production level.^{71,86}

Other Encapsulation Schemes

A wide variety of other encapsulation schemes have been reported in the literature, though they have not been adapted into widespread usage for various reasons.²⁶ Two examples are the use of inert gas spacers and embedding in a curable polymer. Inert gas spacers use stacks of edge-sealed barrier films or glass with a gap between films filled with an inert gas. The inert gas layer disperses and dilutes permeating gases and is capable of achieving low permeation rates. Getters can also be incorporated into the gas spacers to further limit permeation. Several different schemes using gas spacers can be seen in Figure 1.17a.¹¹⁵ However, the complicated nature of this scheme and the need for inert atmosphere processing makes it a less favorable method for industrial scale processing.

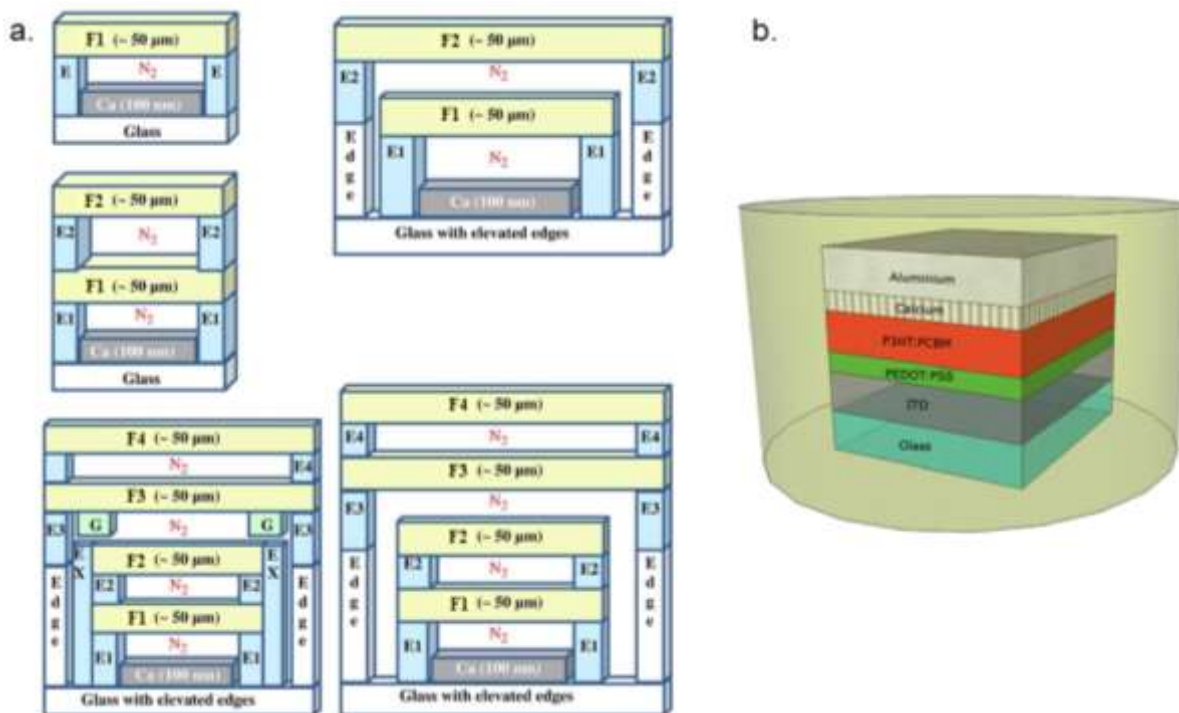


Figure 1.17 (a) Cross-sections of several different encapsulation schemes which incorporate inert gas spacers are shown. Though pictured for permeation testing via the optical calcium test, for an OPV the device would take the place of the “Ca” in the diagram. In the diagram, the yellow objects labelled “F_” are barrier films, the blue objects labelled “E_” are edge seals and the green objects labelled “G” are getters. (b) A diagram of an OPV embedded in an epoxy (tan cylinder) is shown.^{115,135}

Embedding the device in a curable polymer such as epoxy or polyurethane is a very simple method to protect devices and is similar to the techniques used for encapsulating inorganic light emitting diodes. This scheme, as seen in Figure 1.17b, uses a liquid adhesive to completely cover the device. The adhesive then polymerizes to form a solid, transparent, networked polymer which protects the device. The exothermic nature of most reactions can help the device by acting as an anneal, though large quantities of the embedding material can often produce too much heat and damage the device.¹³⁵ Also, the relatively high permeability of the polymers used as embedding materials often means that even thick layers on the order of centimeters cannot provide sufficient long term protection.

Adhesives

As can be seen in the discussion of encapsulation processes, adhesives are used in almost all of the encapsulation schemes currently used for OPV. Whether they are laminating glass plates or flexible films, acting as an edge seal, or forming the intermediate layer of a dyad structure, adhesives are needed. However, as polymers, adhesives often have much higher permeation rates than other barrier materials and are often the weak point in the encapsulation,

allowing for lateral permeation. This section discusses the different types of adhesives used to encapsulate OPV and their processes.

Theories of Adhesion

There are several different factors which can create adhesion between two surfaces, and different types of adhesives can exploit different factors in order to form a strong bond. One requirement for adhesion is good wetting of the surface by the adhesive. This is often considered in terms of surface energies. For wetting to occur, the surface energy of the adhesive-to-substrate interface (γ_{adh-s}) must be more favorable than the sum of the substrate-to-air (γ_{s-air}) and adhesive-to-air ($\gamma_{adh-air}$) surface energies as can be seen in the inequality shown in Equation 1.6.^{103,104,125}

$$\text{Equation 1.6} \quad \gamma_{adh-s} \leq \gamma_{s-air} + \gamma_{adh-air}$$

These surface energies can also be used to determine the theoretical amount of energy needed to rupture the interface. This value is defined as the work of adhesion, $W_{adhesion}$, and is the difference of the surface energies in the bonded and unbonded states as seen in Equation 1.7.^{103,104,125}

$$\text{Equation 1.7} \quad W_{adhesion} = \gamma_{adh-s} - \gamma_{s-air} - \gamma_{adh-air}$$

For negative values of the work of adhesion, there is no adhesion and the two surfaces will remain unbonded. Surface energies can be broken into different types of interactions such as dispersive and polar. When present, hydrogen bonding can also increase the work of adhesion. The work of adhesion often grossly underestimates the measured adhesion strength of an interface however. This is due to several other factors which can contribute to the strength of a bonded interface.^{103,104,125}

For rough surfaces and porous materials, mechanical interlocking can increase the adhesion. Some types of adhesives will form covalent bonds with the surface of the substrate which can also increase the adhesion strength. One of the strongest ways to increase the adhesion is through diffusion and entanglement. In this case the interface begins to blur as the two materials blend together at the interface. In polymers, this leads to chain entanglement while metals can form alloys, both of which create very strong bonding as the materials begin to act as one continuous material. However, this is often rare for polymer adhesives as polymers tend to be immiscible with other solids. One of the largest causes for the discrepancy between the theoretical work of adhesion and the measured adhesion comes from the dissipation of stresses within the materials. When a stress is applied to a bonded interface, some of the energy

is often dissipated by deformations in the adhesive and/or substrate, especially for softer materials which deform easily. This is partially why soft adhesives can still maintain very strong bonds. In some cases, these deformations can be large enough that the bonded assembly can rupture within the adhesive or substrate. This type of rupture is referred to as a cohesive failure. If not enough energy is dissipated by the materials, the assembly can instead rupture at the interface which is referred to as an adhesive failure.^{103,104,125}

Thermoplastic Encapsulants

Thermoplastic encapsulants encompass a wide variety of chemistries such as poly(ethylene-co-vinyl acetate), polyolefins, poly(vinyl alcohol), poly(vinyl butyral), and others, but all work in a similar manner. These materials are often applied as solid films and then heated, often under pressure or vacuum to avoid bubbles. The hot polymer becomes very soft and/or melts, thus allowing for wetting of the surface. Upon cooling, the polymer re-hardens and locks in the surface morphology to provide adhesion. Though called thermoplastic in this section due to the softening/melting process, many of these materials include thermal activators which crosslink the polymer once heated in order to create stronger adhesion and a more robust polymer. These materials are very commonly used for the encapsulation of crystalline silicon photovoltaic modules and are especially well suited for glass-to-glass encapsulation. However, these materials are generally poor barriers against oxygen and/or water vapor and often require high thicknesses on the order of hundreds of microns. While the process for using these materials is well known from other industries, it usually requires several minutes of heating and batch processing making them more difficult for use with the in-line roll-to-roll processing commonly used for OPV.^{26,52,53,55,57,90,95,99,102–104,131,136,137}

When this type of adhesive is heated and liquefied before application, they are often referred to as hot-melt adhesives. It is possible to incorporate hot-melt adhesives into a roll-to-roll system by heating the adhesive; applying it as a liquid; and immediately laminating the assembly. However, this requires the use of highly specialized and expensive coating equipment.^{26,103,104}

Thermal Epoxies

Epoxies are a class of polymers based on the polymerization of epoxide groups. They are generally liquid resins comprised of a blend of oligomers and monomers containing active epoxide groups. The resin is then mixed with a curing agent, typically an amine or peroxide,

which reacts with the epoxide groups causing a ring opening polymerization. Since molecules in the resin have multiple epoxide groups, the polymerization results in a networked polymer. This reaction sometimes requires thermal activation and the time needed for curing can be drastically reduced by heating. However, rapid polymerization at high temperatures often causes the material to contract as it cures which can create residual thermal stresses in the bonded assembly. These materials often have quite low permeation rates compared with other adhesives, though the wide variety of formulations of epoxies can produce a wide range of properties. The lowest permeation rate epoxies tend to be highly cross-linked, have high concentrations of inorganic fillers, and be quite rigid. This makes them ideal for edge seals but less practical for encapsulating in the optical path. Also the curing times often require minutes to hours for transparent thermally activated epoxies.^{103–106,135,138}

Thermal Polyurethanes

Thermal polyurethanes are quite similar to thermal epoxies and can produce adhesives with a wide range of properties. Though the final properties of the adhesive are often similar to epoxies, epoxies tend to be able to achieve lower gas permeation rates than polyurethanes but polyurethanes tend to be lower cost. Polyurethanes have been used to encapsulate less sensitive devices and devices which do not require a long lifetime. The main difference between epoxies and polyurethanes is their chemistry. Polyurethanes are generally liquid resins consisting of polyols which are then mixed with an isocyanate. The isocyanate reacts with the alcohol groups of the polyol to form a solid, networked polymer. As with epoxies, heat is often needed to start the reaction or accelerate its rate.^{98,103,104,139–146}

UV Curing Adhesives

As an alternative to heating liquid adhesives to cure them, many systems can instead use ultraviolet (UV) light to initiate curing. These systems do not use a traditional curing agent but instead have photo-initiators which form reactive species when they absorb light. Therefore, the adhesive will not polymerize until exposed to wavelengths of light which correspond to the absorption spectra of the photo-initiators. Most photo-initiators are designed to absorb in the UVA or UVB range so that they do not require dangerous high energy radiation nor do they polymerize rapidly under ambient light. Some photo-initiators also absorb in the violet and blue regions of the spectrum in order to facilitate curing through substrates which may block some

UV light. There are two main classes of UV curing adhesives which differ in the type of polymerization reaction used for curing.^{103,104}

Cationic

Cationic photo-initiators produce ions when they absorb specific wavelengths of light. These ions then start a living cationic polymerization of the adhesive. This type of curing system is commonly used with epoxy resins and produces cured epoxies with properties very similar to those of thermally cured epoxies. Thus all of the benefits provided by epoxies can be realized without the need for long curing times or high temperatures. Cationic curing epoxies typically need 1-5min of UV exposure at the correct wavelength and will continue to cure for up to 24 hours after exposure as the polymerization will continue even after removed from the light source. Gentle heating or post-cure annealing can often speed up the polymerization and lead to a higher total degree of polymerization.^{97,99,103,104,113}

Radical

The other major class of UV photo-initiators are those which produce radicals when they absorb light. These radicals then produce a radical polymerization within the adhesive. This type of photo-initiator is most commonly used with liquid resins containing acrylate groups. Because acrylate groups can be grafted onto other functional groups relatively easily, this class of adhesive is extremely versatile. It is common for the resin to contain oligomers of acrylics, epoxies and urethanes with one or more acrylate groups grafted onto the oligomer for functionality. The fast kinetics of radical curing requires much shorter UV exposures than cationic epoxies and often need only a few seconds of illumination to reach the maximum level of polymerization. Because of the short lifetimes of the radical species involved in the curing, recombination of the radicals occurs once removed from illumination and the polymerization stops almost immediately. The radicals produced also readily react with molecular oxygen in the atmosphere to form peroxy radicals which are more stable and have much slower reaction kinetics. This creates an effect known as oxygen inhibition which prevents the adhesive from polymerizing when large amounts of oxygen are present. This can be avoided by laminating the adhesive between two substrates before curing or by curing in an inert atmosphere. It is also possible, but often difficult, to minimize this problem using careful formulation and additives. It should also be noted that in general, radical curing acrylates tend to have lower adhesion than cationic epoxies, though this strongly depends on the formulation and the substrates being bonded.^{103,104,110,111,147-154}

Pressure Sensitive Adhesives

Pressure sensitive adhesives (PSA) are viscoelastic solids which are above their glass transition temperature, making them soft and capable of a limited amount of flow. Wetting the surface is of critical importance for PSAs, therefore applying pressure to create better contact between the adhesive and substrate creates better adhesion and is the source of their name. The viscoelastic nature of these adhesives means that the adhesive will continue to further wet the surface for some time after application as viscous flow occurs to relieve internal stresses. For this reason most PSAs require a period of 24-72 hours after application to achieve their maximum adhesion strength, though this can often be greatly shortened by annealing at an elevated temperature. Whether or not a material could possibly be used as a PSA can be approximated by the Dahlquist Criterion which states that the elastic portion of the shear modulus, G' , should be less than about 10^{-5} Pa. For viscoelastic materials, it is important to apply this criterion to the mechanical frequencies that will be seen not only when applying the adhesive, but also during the lifetime of the bonded assembly. PSAs can be made from a variety of different chemistries and can be either thermoplastic or cross-linked. Some common materials for PSAs are acrylates such as poly(n-butyl acrylate), rubbers and rubber co-polymers such as styrene-*block*-butadiene-*block*-styrene, silicones such as poly(dimethyl siloxane), and many other soft polymers. As they are not liquids, the application methods for PSAs are usually limited to lamination using rollers or presses. However these methods, combined with their immediate adhesion known as tack, make PSAs extremely compatible with roll-to-roll processing which is commonly used for the production of OPV.^{99,103,104,125,155-158}

Composites

It is very common for adhesives to be combined with particles of other materials to form adhesive composites. The creation of composites is a relatively simple method to modify the properties of an adhesive and has been widely exploited for many years. While many different types of particles have been used in adhesive composites, passive inorganic particles are the most common choice for improvement of barrier properties. Low WVTR adhesives are very commonly made by adding high concentrations of micro-scale particles of relatively impermeable materials such as silica, alumina, titania and unmodified clays. The high concentration of impermeable particles creates a more tortuous permeation pathway and also greatly reduces the cross-sectional area of adhesive through which permeation can occur as the

particles take up a large volume fraction of the composite. While these composites can greatly reduce the permeation rates of adhesives, the high concentrations of particles often also cause them to become significantly more rigid and opaque. This makes them unsuited for use both in the optical path and with flexible substrates. These composites are therefore popular edge seal materials, especially in conjunction with rigid encapsulation schemes.^{70,90,97,103–106}

Nanoparticles have also been used to improve the barrier properties of adhesives. Silica, alumina and titania nanoparticles are common nano-fillers used in adhesive composites although they can also suffer from the same opacity and rigidity problems as seen with micro-scale fillers, but usually to a lesser extent.^{100,105,106,138,148,157} Carbon nanotubes can also provide decreased permeation rates when used as fillers but very strongly absorb visible light leading to a loss of transparency at relatively low loadings. The electrical conductivity of carbon nanotubes can also sometimes cause problems when used in electronic devices if the concentration is high enough.³⁹ The most popular and well-studied nano-filler used in adhesive composites are organically modified phyllosilicates. The organic modification of these particles causes them to disperse much more easily in a polymer matrix leading to an exfoliation of the platelet structure. This exfoliation creates a large number of very high aspect ratio particles at relatively low loadings. This combination of factors creates a highly tortuous permeation pathway, and thus a lower permeation rate, without much change in transparency or rigidity. Organically modified phyllosilicates are now widely used with many types of adhesive chemistries but the achievable permeation rates are still much higher than those of adhesives highly loaded with micro-scale particles.^{90,91,103,104,109–111,113,139,145,146}

A different approach to composite adhesives is to use active getter particles. In this scenario, the permeating gas becomes trapped in the particle, thus limiting permeation further into the adhesive until the particle is saturated. This is most often applied to the case of water vapor as the permeating gas and a variety of desiccants have been used for this purpose including nanoporous carbon, calcium oxide, zeolites and others.^{105,106} Because the method of limiting permeation is different, active particles are more able to be loaded into highly flexible adhesives therefore alleviating any increased rigidity. However, these micro-scale particles still require high loadings and therefore greatly reduce the transparency of the composite. For this reason, desiccant loaded adhesive composites are used as edge seals but rarely in the optical path. Nanoparticles of active getters, especially zeolites, have been well studied at the lab scale for various applications but there are very few examples in the literature of their use in adhesive composites.^{49,118} These nanoparticles could potentially allow for lower loadings of particles to

achieve the low permeation rates with a more limited effect on the transparency of the composite. This possibility is explored in depth in later chapters of this thesis.

Photostability of Adhesives

Since by definition a photovoltaic device is exposed to light, it is important that any material used to encapsulate the device must possess enough photostability to properly function throughout the lifetime of the device. Any adhesive used to encapsulate OPV must therefore maintain its transparency, barrier properties, flexibility and adhesion for several years in outdoor conditions where they will be exposed to sunlight, oxygen and water. Photo-degradation can occur without the presence of air or other oxidative species through a process known as photolysis, but often times the dominant reaction route changes when oxygen is present. When ambient oxygen plays a role in the photo-degradation, the process is known as photo-oxidation and often has faster reaction kinetics than photolysis reactions. Since adhesives used for encapsulating OPV are designed to be barrier materials, the inner portions of the adhesive are frequently in a low oxygen environment where photolysis is more likely while the regions closer to the edges of the encapsulation may be exposed to higher levels of oxygen and thus can experience photo-oxidation. Also, the quantity of oxygen will gradually increase throughout the device over time as the barrier materials are not perfect. For these reasons, both photolysis and photo-oxidation must be considered when discussing the photostability of materials for OPV encapsulation. As many materials with different chemistries are used as adhesives, their photostability can vary widely.¹⁵⁹ This section will discuss the prominent photo-degradation mechanisms for several adhesive chemistries with special attention paid to those studied in this thesis.

Acrylic Pressure Sensitive Adhesives

Acrylic and methacrylic chemistries are well known for their good photostability. For adhesive applications, acrylic polymers with low glass transition temperatures are commonly used as pressure sensitive adhesives. To achieve low glass transition temperatures longer side chains are often employed. However, acrylate and methacrylate polymers tend to be more photo-stable with shorter side chains. One common material for pressure sensitive adhesives is poly(n-butyl acrylate). The photostability of this material has been studied at various atmospheric conditions and temperatures and is a relatively photo-stable polymer under outdoor conditions. Both photolytic and photo-oxidative reactions have been shown to occur in this

polymer however. While poly(n-butyl acrylate) is quite stable when compared to some other adhesive chemistries (see section on UV Curing Acrylates), it is not as photo-stable as shorter side chain acrylic/methacrylic polymers such as the highly stable poly(methyl methacrylate). Shorter side chains also cause the polymer to have a higher T_g often causing these polymers to be too rigid for use as PSAs.^{155,160-163}

UV Curing Adhesives

As previously discussed, UV curing acrylates can contain several different types of oligomers each with their own unique chemistry. Because of the variety of chemistries used, it is necessary to consider the photostability of all the different constituent chemistries present in a formulation when discussing the overall photostability of the adhesive. This means that not only acrylics, but also epoxies and polyurethanes must be evaluated as they can make up the backbones of oligomers used in UV curing acrylate adhesives. In addition, photo-initiators can act as impurities that can accelerate the rate of photo-degradation.¹⁵⁹

Oligomers with an acrylic backbone and acrylic monomers are both generally quite photo-stable in the UVA, UVB and visible ranges as previously discussed for pressure sensitive adhesives. This photo-stability holds true for cross-linked acrylates as well. However, it is common for a UV cured acrylate adhesive to not achieve 100% conversion of the acrylate groups during curing. This leads to an initial reaction of the remaining double bonds of the uncured acrylate groups during irradiation. The photo-initiators in the formulation can also cause photo-degradation to occur as they can act as chromophoric impurities in the polymer network. For this reason, the selection of the photo-initiators must take into account their potential for accelerating the photo-degradation of the adhesive. Careful formulation of the adhesive can often limit this degradation pathway.^{159,164,165}

While many different variations exist, including aliphatic chemistries, epoxies commonly have an aromatic backbone. These aromatic epoxy resins, for example those based on the diglycidyl ether of bisphenol-A, are generally susceptible to yellowing under exposure to UV radiation regardless of the presence of oxygen. An example of this yellowing phenomenon can be seen in Table 1.2.¹⁴⁵ It has been proposed that the major cause of this discoloration comes from quinone methide groups which are formed via a photolytic reaction of the aromatic rings. Photo-oxidation introduces other degradation pathways which can speed the overall degradation of the epoxy.¹⁴¹⁻¹⁴⁶

Table 1.2 The yellowing of an aromatic epoxy based on the diglycidyl ether of bisphenol-A is shown after exposure to UV centered at 340nm at 42°C and 30% relative humidity.¹⁴⁵

Exposure time, t (h)	Luminance, L	Photograph
0	181.6	
133	166.1	
333	153.7	
533	142.1	
733	133.6	
933	128.6	
1500	123.0	
2000	120.7	

Polyurethanes are also commonly used as oligomer backbones in UV curing acrylate formulations. While the polyurethane portion of these materials is more susceptible to photo-oxidation than the acrylic crosslinks, they are generally more photo-stable than epoxies. The main photo-oxidation pathway for polyurethanes involves a chain scission at the α -carbon to the nitrogen atom which leads to the formation of crosslinks and acids among other volatile photo-products. These materials are also very effectively stabilized through the inclusion of additives such as a hindered amine light stabilizer (HALS).¹⁵¹⁻¹⁵³

Composites

The addition of particles to adhesives can often affect the photo-stability of the adhesive. While inorganic particles rarely experience significant photo-degradation under outdoor conditions, they can change the mechanisms of photo-degradation within the polymer matrix and must therefore always be accounted for when determining the stability of the composite. Many metal oxides can have a photo-catalytic effect. This comes from their ability to sensitize molecular oxygen leading to the formation of radicals which can then attack the polymer. The inclusion of transitional metal ions can also produce a photo-catalytic effect in the presence of oxygen. An example of this can be seen in Figure 1.19 where the valence state of the metal ion can reversibly change to produce radicals from hydroperoxy groups.¹⁴⁵ These types of ions are common in minerals and particles which contain ions as part of their structure such as

phyllosilicate clays. These same materials can also often retard photo-oxidation by increasing the barrier properties of the adhesive. By limiting the rate of oxygen permeation, these particles can decrease the amount of oxygen available for photo-oxidative reactions. This often results in a balance between the two competing processes which is highly dependent on the chemistry and purity of both the particles and the polymer.^{90,91,145,146}

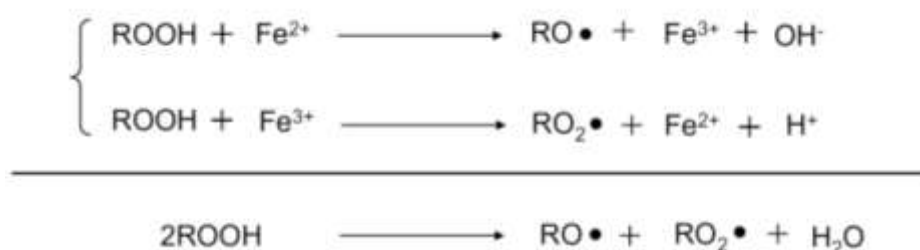


Figure 1.19 An example of accelerated hydroperoxy degradation in the presence of iron ions is shown where R is an organic molecule. The formation of hydroperoxy groups is common during photo-oxidation of polymers, thus the degradation rate is increased by the presence of ions.¹⁴⁵

Permeation Measurement

The strict requirements of encapsulation materials for OPV necessitate the use of materials with very low permeation rates. However, it can often be quite difficult to measure these rates. A variety of techniques exist for measuring low permeation rates each with its own advantages and disadvantages. A list of some of the techniques which can be used is presented in Table 1.3 along with a general range of the permeation rates they are capable of measuring. There are two major classes of permeameters: those based on permeation cells and those based on scavengers.

Table 1.3 Techniques for measuring the permeation rates of high-barrier materials

Technique	Permeating Gas	Minimum WVTR Measurement
Coulometric Permeation Cell ¹⁶⁶	Water	10 ⁻⁵ g/m ² /day
Tunable Laser Diode Spectroscopy Permeation Cell ¹⁶⁷	Water	10 ⁻⁶ g/m ² /day
Mass Spectroscopy Permeation Cell ⁹²	Helium, Oxygen, Water	10 ⁻⁶ g/m ² /day
Electrical Calcium Test ^{168,169}	Water	10 ⁻⁷ g/m ² /day
Optical Calcium Test ¹⁶⁸⁻¹⁷⁰	Water	4 X 10 ⁻⁷ g/m ² /day

Permeation Cells

One class of permeameter is the permeation cell. In a permeation cell, the sample to be measured acts as a membrane between an upstream side and a downstream side. The atmosphere on the upstream is carefully controlled and contains the gas to be measured. The downstream side contains a sensor which measures the gas of interest as it permeates across the membrane. A variety of different methods can be used to control both the upstream and downstream atmospheres depending on the exact experimental set-up. The upstream side may be static or dynamic and contain a pure gas or a mixture of gases. The downstream side can also be static or dynamic and is often either an inert gas or vacuum. In permeation cells, the detection limit is determined by the sensitivity of the sensor, the level of contamination in the downstream side, and the quality of the seal made at the sample between the upstream and downstream sides of the cell. For very sensitive sensors, the detection limit is often determined by the amount of background permeant present in the downstream side. This can come from contamination in the downstream atmosphere or permeation around the edge of the sample and through the seals between upstream and downstream side.^{92,166–168}

Several different types of sensors have been proposed for this type of permeameter. One common detector is based on coulometric sensing. This sensor uses phosphorous pentoxide to absorb water. A voltage is then applied to split the water into H₂ and O₂ via electrolysis. Using Faraday's Law of electrolysis, the voltage can then be converted to a mass of permeated water.¹⁶⁶

Another type of sensor capable of measuring very low permeation rates are those based on tunable laser diode spectroscopy. This technology shines a laser through the downstream atmosphere at a sensor on the other side. Trace gases in the downstream atmosphere which interact with the wavelength produced by the laser lead to a variation in the intensity measured at the sensor. This signal can then be used to calculate the concentration of permeated gas.¹⁶⁷

A third type of sensor is based on mass spectrometry. In this technology, the downstream side is kept under high vacuum which enables the use of a mass spectrometer as the gas sensor. This technology enables the testing of multiple different gases and the use of isotopic labelling of the challenge gas. The use of isotope labelling reduces background noise and thus allows for precise measures of very low permeation rates.⁹²

Scavenger Sensing

Another method for measuring permeation is scavenger sensing. In this method a scavenger which interacts with the permeant is encapsulated using the material to be tested and placed into a controlled atmosphere. As the permeant traverses the material, it interacts with the scavenger and causes a change to the scavenger which can be measured. The type of change being measured is dependent on the type of scavenger being used. The geometry of the encapsulation can also change greatly for different types of testing.

Gravimetry

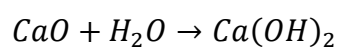
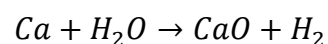
The most well established type of scavenger sensing is gravimetric sensing. This test uses a material which strongly absorbs/adsorbs the permeant gas which is sealed inside a relatively impermeable container using the material to be tested. As gas permeates into the container, it becomes trapped by the absorbent material. By measuring the change in mass of the absorbent material over time, the permeation rate can be determined. This method is used mainly for higher permeation rate materials as it can be difficult to accurately measure the very small mass changes over the long time scales associated with very low permeation rates.^{171,172}

Indicator Paper

Indicator paper is a simple method to visualize optically the rate of permeation. In this test a paper or other film treated with a sensitizer is encapsulated inside the material to be tested. When exposed to the permeant gas, the sensitizer causes the film to change color thus providing a visual representation of the permeation front as it moves through the material. Unfortunately, it is often quite difficult to precisely link the color change to an exact concentration of permeant, thus limiting its effectiveness as a quantitative test.⁶⁰

Calcium Test

Calcium is an excellent material for the scavenger sensing of water as it does not readily react with oxygen at room temperature, but does with water according to the following^{173,174}:



The high sensitivity of calcium to water allows it to very accurately measure the small quantities of water associated with very low permeation rates. Though the exact thickness varies

depending on the test method, thin layers of calcium are generally used as they make the measurable changes to the calcium more evident.¹⁶⁸ Detailed studies of calcium degradation using atomic force microscopy have shown that the degradation of the calcium layer is not completely homogenous over very short length scales. However, the macro-sized area of the deposits used in testing creates average measures which are effectively homogenous given that the concentration of water across the area being measured is also homogenous. It should be noted though that this inhomogenous degradation does cause some error in the measured permeation rate with the exact amount of error varying depending on the exact analysis method used.¹⁷⁵ The degradation of calcium is usually measured either electrically or optically.

Electrical Calcium Test

The electrical calcium test places two electrodes at the ends of a thin deposit of calcium. The calcium is then encapsulated using the material to be measured, often leaving a gas spacer of inert atmosphere between the calcium and the barrier material. This spacer helps to more evenly disperse any permeating water leading to a more homogenous macro-scale degradation of the calcium. The electrodes are then connected as part of a circuit and the resistance of the calcium deposit is measured over time. A diagram showing an example of an electrical calcium test can be seen in Figure 1.20.^{168,169} Since metallic calcium is a conductor while calcium hydroxide is an insulator, the resistance of the deposit grows as the calcium reacts with water and allows for a precise calculation of the amount of metallic calcium remaining. The amount of remaining calcium is then easily converted to a mass of permeated water using the stoichiometry of the reaction. Because of the geometry needed to incorporate electrodes, electrical calcium tests are usually limited to measuring the orthogonal permeation through films. Additionally, the electrical calcium test can often times slightly underestimate the time lag and WVTR. However, the test does still provide an excellent approximation of water vapor barrier properties and is usually simpler to automate than the optical calcium test.^{169,176-178}

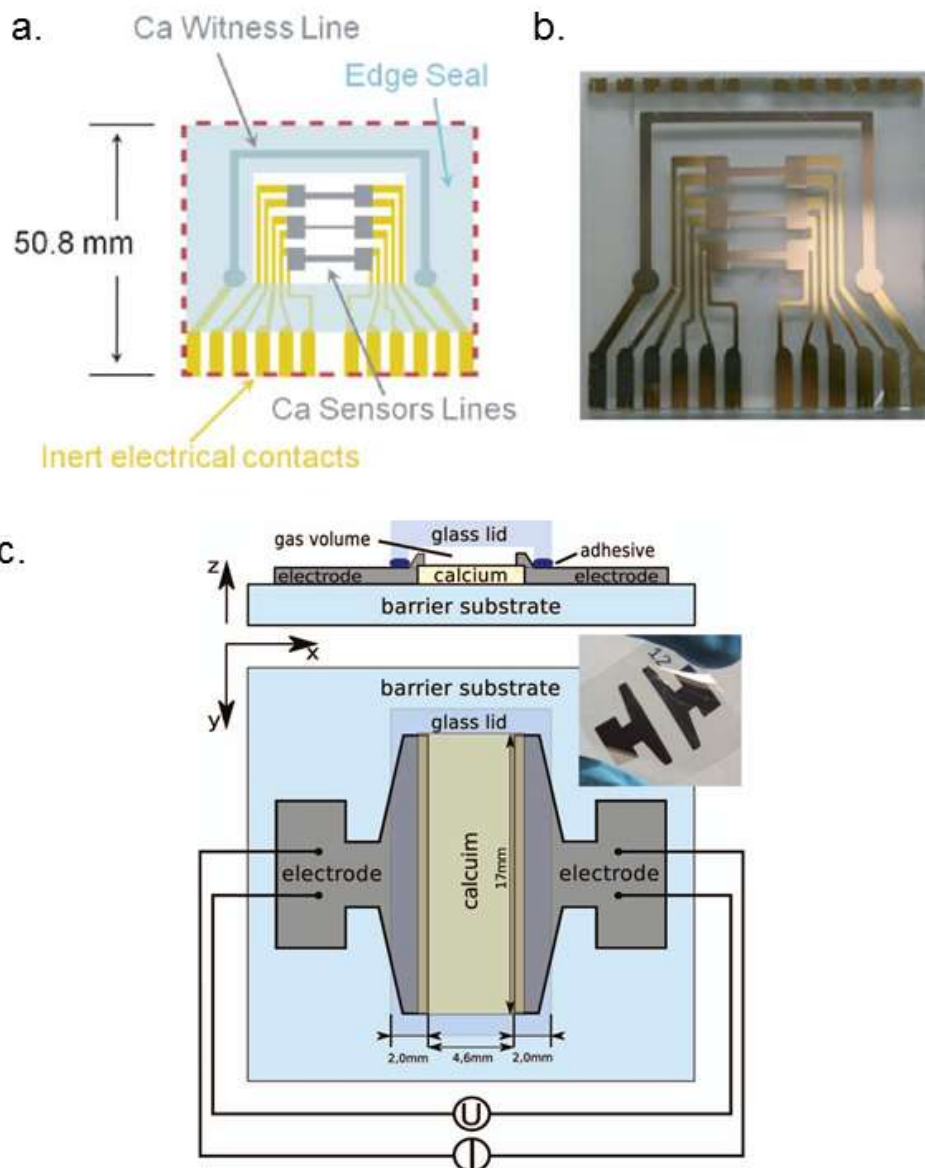


Figure 1.20 (a) A diagram of an example test geometry for an electrical calcium test is shown next to (b) an image of a sample. (c) An alternative sample geometry for an electrical calcium test is also shown as there is no international standard for this type of test. The electrical contacts would then be connected into a circuit and the resistance of each calcium sensor would be measured over time in order to measure the amount of water which has permeated across the barrier.^{168,169}

Optical Calcium Test

The other option for measuring the degradation of calcium is to do so optically. This method takes advantage of the change in color from mirror-like metallic calcium to transparent calcium hydroxide. Therefore, by using a CCD camera to take a series of images over time, it is possible to track the degradation of a thin layer of calcium. This test is particularly useful for visualizing the permeation of water, but is much more precise than indicator paper. While this test is ostensibly qualitative in nature, it is possible to extract quantitative values through the use of calibration curves.¹⁶⁸ Several different variants of the optical calcium test have been

reported which are capable of measuring different aspects of water permeation. The three major types of optical calcium tests are intrinsic, extrinsic and lateral.

Intrinsic tests are used mainly to evaluate deposited barrier layers such as those used in dyad structures and also for materials to encapsulate OLEDs where the formation of dark spots is of high importance. For this type of test, the calcium is deposited directly onto a barrier layer. The calcium is then sealed inside a glass cap and edge sealed with a high barrier sealant. This geometry minimizes the presence of lateral permeation effectively limiting permeation to that which traverses the barrier layer being tested. Since permeation in these barrier layers is defect-dominated, the calcium will degrade first at the defects and then continue degrading outward from the defect. Visually, this creates transparent spots in the calcium which grow larger with time. When the defects in the barrier layer are separated by a sufficiently large distance, it is possible to see the density and relative size of the defects by the density and size of the transparent spots in the calcium. An example image from this type of calcium test can be seen in Figure 1.21.^{71,168,170}

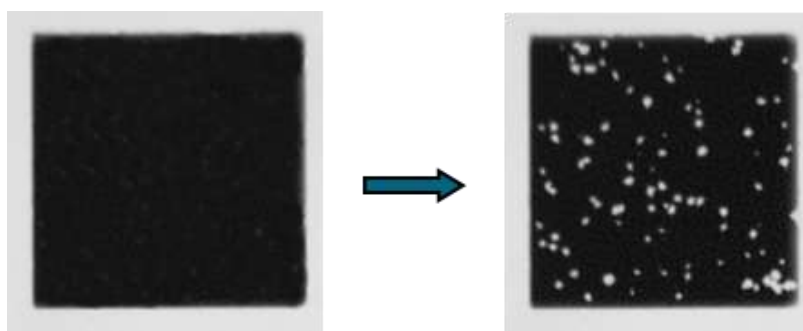


Figure 1.21 An encapsulated calcium deposit is shown before and after aging in a humid environment during an intrinsic optical calcium test. The white points in the second image are regions where the calcium has degraded into transparent calcium hydroxide. Each point is centered on a defect in the barrier layer of the encapsulation.¹⁶⁸

Extrinsic tests are quite similar but instead show an average permeation instead of the specific points seen in intrinsic tests. This is achieved by depositing the calcium on the glass cap instead of directly on the barrier being measured. This geometry creates a spacer of inert gas between the barrier material and the calcium, thus allowing the permeated water vapor to disperse and degrade the calcium more homogeneously on the macro-scale. As previously mentioned, the degradation of calcium is not perfectly homogeneous at small length scales, however the assumption of homogeneity does allow for an excellent approximation of the water vapor permeation. An example image from this type of calcium test can be seen in Figure 1.22.¹⁶⁸ To extract quantitative values from the optical images, a calibration curve is established by determining the transparency/grayscale of known thicknesses of calcium. This curve is then used to relate the transparency/grayscale of each image to a remaining thickness of calcium.

Alternatively, the change in the calcium thickness can also be calculated using the Beer-Lambert Law shown in Equation 1.8 where I is the intensity of light measured in transmission, ε is the absorptivity (material constant), l is the path length through the absorber (calcium thickness) and c is the concentration of the absorber (calcium).

$$\text{Equation 1.8} \quad I/I_0 = e^{-\varepsilon lc}$$

Regardless of the calculation method for the calcium thickness, a change in the amount of calcium can be converted to a mass of permeated water via the stoichiometry of the reaction.^{88,168,170,175}

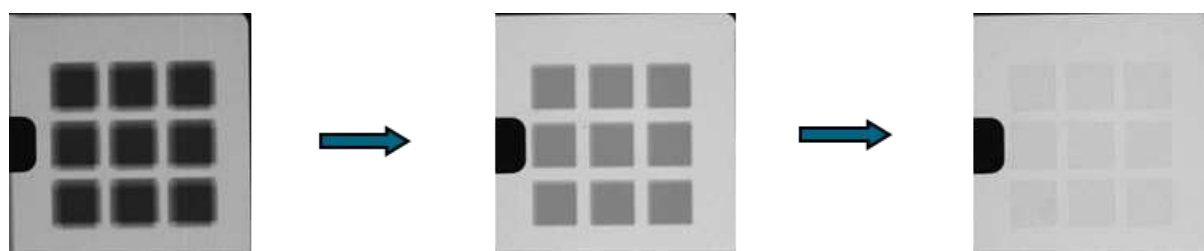


Figure 1.22 A series of calcium deposits which have been encapsulated as a single sample are shown at different stages of degradation after aging in a humid environment during an extrinsic optical calcium test. Rather than white spots of completely degraded calcium as seen in intrinsic tests, the calcium in these deposits degrades over the entire area of the calcium. As the metallic calcium layer becomes thinner as it degrades, it becomes more transparent leading to the progressively lighter shades of gray in the images.¹⁶⁸

Lateral permeation can also be measured using the optical calcium test. In this variant, the calcium is encapsulated between two plates of glass. This prevents any orthogonal permeation and allows for only lateral degradation, thus making possible the measurement of the adhesive or edge seal material. Figure 1.23 shows an example of images from this type of test where the calcium deposit appears to shrink inward from the edges.⁶⁹ The rate at which the opaque calcium deposit shrinks shows the rate at which water is permeating laterally. This permeation is well modeled using a moving boundary approach as the calcium consumes the water thus altering the permeation rate once the permeation front has reached the calcium. This technique provides an excellent tool to not only compare adhesives and encapsulants, but also to aid in encapsulation design by estimating the distance between the edge of the encapsulation and the edge of the device needed to achieve the desired device lifetime. One major limitation of this test however is the influence of the interface on the lateral permeation. The interface would only be valid for a device using glass-to-glass encapsulation. There can be drastic differences in the interface of an adhesive on a glass substrate versus the plastic surface of a flexible multi-layer barrier film. This makes it very difficult to predict the interfacial permeation of a flexible device using this method of calcium test. Replacing the glass with the desired barrier film in the calcium test would require a new analysis method since the barrier film is

not impermeable and would therefore cause changes to the thickness of calcium, invalidating the modelling which assumes a constant thickness of calcium.^{52,69,168}

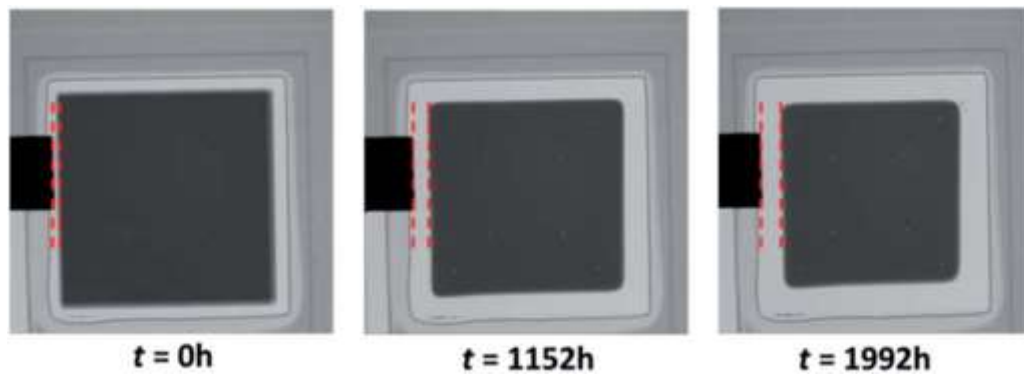


Figure 1.23 An example of an optical calcium measuring lateral permeation is shown. The red lines are added to aid in the visualization of shrinking size of the calcium deposit as it is degraded by water permeating inward from the edges of the sample.⁶⁹

Chapter 2: Experimental Procedures and Testing

Raw Materials

Barrier Films

Three different commercially available multi-layer barrier films along with one grade of poly(ethylene terephthalate) (PET) were used throughout the project. The barrier film VX 25T-2PO from Oike & Co., Ltd. was designated as the “reference” barrier film and was used for the majority of the investigations where flexible barrier films were needed. This barrier film uses a dual dyad structure consisting of 25 μ m PET – inorganic barrier layer – 25 μ m optically clear adhesive – inorganic barrier layer – 25 μ m PET as can be seen in Figure 2.1 a. This film was supplied with protective polymer films on both exposed surfaces which were removed by hand immediately prior to utilization of the films. This barrier film has a water vapor transmission rate (WVTR) of 3×10^{-4} g/m²/day at 40°C and 90% relative humidity as reported by the manufacturer.

Another multi-layer barrier film which was also supplied by Oike & Co., Ltd. was VX-50TH. This film uses a structure consisting of an inorganic barrier layer – 50 μ m PET – hard coat as can be seen in Figure 2.1 b. The barrier film was supplied with a protective polymer film on the inorganic barrier layer which was removed immediately prior to utilization of the films. An alternative version of this film called VX-50TH-OCA was also used. This barrier film is identical to VX-50TH but also includes a 25 μ m layer of an optically clear adhesive on top of the inorganic barrier layer. The protective polymer film is therefore placed on to the adhesive layer. This barrier film, both with and without adhesive, has a water vapor transmission rate (WVTR) of $1-4 \times 10^{-3}$ g/m²/day at 40°C and 90% relative humidity as reported by the manufacturer.

The third multi-layer barrier film used was FTB3-50a supplied by 3M. This barrier film uses a structure of 50 μ m PET – polymer – barrier oxide – polymer – 25 μ m barrier adhesive (FTBA-25) as can be seen in Figure 2.1 c. The barrier film was supplied with protective polymer films on both exposed surfaces which were removed immediately prior to utilization of the

films. This barrier film, both with and without adhesive, has a water vapor transmission rate (WVTR) of 10^{-4} - 10^{-5} g/m²/day at 60°C and 90% relative humidity as reported by the manufacturer.

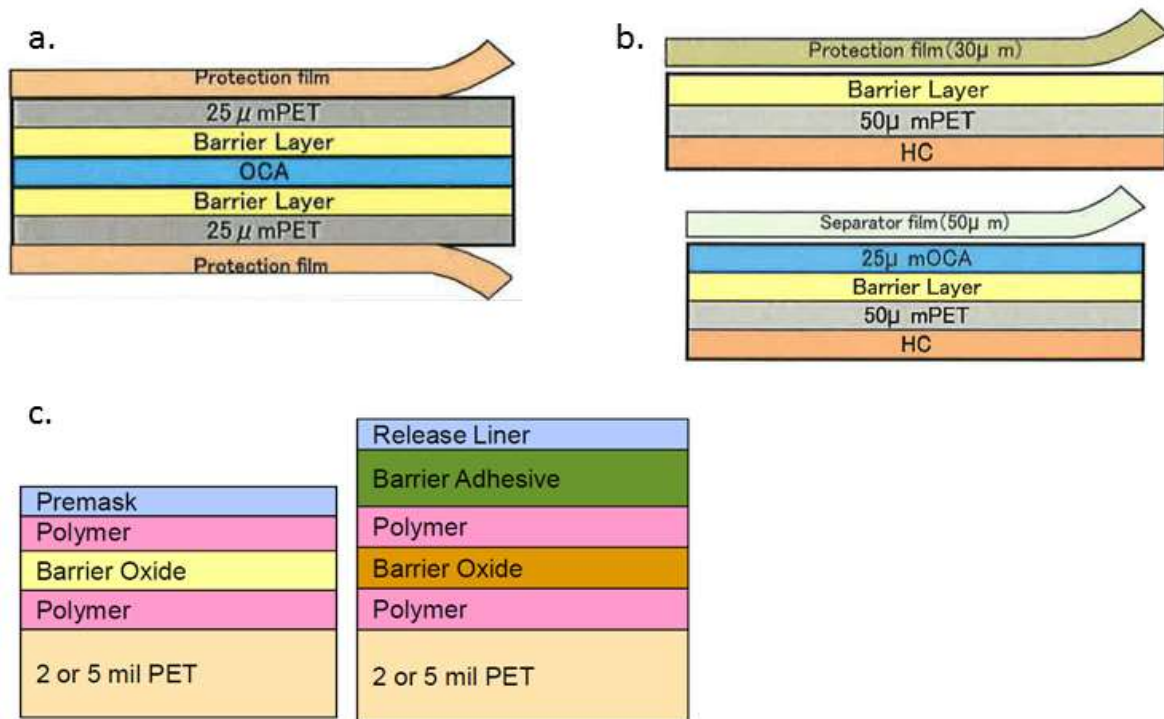


Figure 2.1. The structure of the barrier films are shown as provided by the manufacturers: a) Oike VX 25T-2PO where OCA refers to an optically clear adhesive and Barrier Layer refers to a thin inorganic layer; b) Oike VX-50TH with and without an optically clear adhesive where HC refers to a hard coat; and c) 3M FTB3-50 without and with (FTB3-50a) adhesive. For the 3M barriers, only the 2mil (50μm) versions were used.

In addition to the barrier films, PET was used as an inexpensive barrier film replacement for some types of testing and also as a substrate for the evaporation of calcium in the optical calcium test. The PET film used was Dupont-Teijin Melinex 401 with a film thickness of 50μm.

Adhesives

Commercially Available Adhesives

Several commercially available adhesives were used as benchmark materials during the project. All of these adhesives were pressure sensitive and supplied in the form of films with a homogenous thickness.

The adhesives 467MP and 468MP from 3M (United States) are chemically identical and have thicknesses of 50μm and 125μm respectively. While the exact chemical structure of these

materials is unknown, they are based on an acrylic chemistry and are crosslinked. The adhesives were supplied as rolls coated onto a release liner.

Another pressure sensitive adhesive provided by 3M (United States) is FTBA-25 which is a state-of-the-art barrier adhesive. No information is currently available in regards to the formulation of this adhesive. It was supplied both as a 25µm film between two release liners and pre-coated to 25µm on a multilayer barrier film (FTB3-50a).

The final commercially available adhesive tested was and optically clear adhesive from Oike & Co., Ltd. (Japan). This is also a pressure sensitive adhesive, though no information is currently available in regards to its formulation. The adhesive was supplied pre-coated to 25µm on Oike VX-50TH multilayer barrier films.

MAM Nanostrength® Block Co-Polymers

MAM Nanostrength® adhesives are a class of materials currently under development at Arkema (France). They are pressure sensitive adhesives based upon an A-B-A block copolymer structure where the A-block is poly(methyl methacrylate) (PMMA) and the B-block is poly(butyl acrylate) (PBA). Four different grades with varying ratios of the blocks were used as is described in Table 2.1. The block ratios are as follows: M65 contains 65% PBA and 45% PMMA, M75 contains 75% PBA and 25% PMMA, and M85 contains 85% PBA and 15% PMMA. M85M has identical block ratios to M85 except that the PMMA block is instead a copolymer of PMMA and poly(methacrylic acid). All four formulations are produced by Arkema via a patented “BlocBuilder®” controlled radical polymerization technique. M65 and M75 were supplied as pellets while M85 and M85M were supplied as slabs of bulk polymer.

Table 2.1 The block ratios for the MAM Nanostrength® adhesives are listed. *M85M contains an unknown amount of poly(methacrylic acid) in the PMMA block.

Adhesive	PMMA	PBA
M65	35%	65%
M75	25%	75%
M85	15%	85%
M85M	15%*	85%

Acrylate Oligomers, Monomers and Solutions

UV curing acrylate adhesives consist of a mix of monomers, oligomers and photo-initiators. For these adhesive formulations, a monomer is defined as a small molecule with one or more functional acrylate groups. Oligomers are defined as molecules which are much larger than monomers and are often very short chain polymers. The chemistry of the oligomer backbones can vary greatly (acrylic, epoxy, polyurethane, etc.) however there is always at least one functional acrylate group. The number of functional acrylate groups per molecule is listed as the “functionality”. A functionality of one will create a straight chain polymer when cured whereas higher functionalities will create a networked structure when cured. Details of the monomers and oligomers can be found in Table 2.2 and Table 2.3 respectively. All monomers and oligomers were provided by Sartomer (Arkema Group).

Table 2.2 Information on the Sartomer monomers is shown as provided by the manufacturer.

Product Name	Description	Homopolymer T_G	Acrylate Functionality
SR238	1,6-hexanediol diacrylate	43°C	2
SR285	Tetrahydrofurfuryl acrylate	-11°C	1
SR484	Mix of octyl and decyl acrylates	NA	1
SR504	Ethoxylated 4-nonyl phenol acrylate	-28°C	1
SR506D	Isobornyl acrylate	94°C	1
SR9003	Propoxylated 2-neopentyl glycol diacrylate	32°C	2
SR9050	Monofunctional acid ester	NA	1

Table 2.3 Information on the Sartomer oligomers is shown as provided by the manufacturer.

Product Name	Description	Molecular Weight	Homopolymer T_G	Acrylate Functionality
CN131B	Aromatic epoxy acrylate	300g/mol	14°C	1
CN966H90	Aliphatic urethane diacrylate + 10% 2-(2-ethoxyethoxy) ethylacrylate	7000g/mol	-35°C	2 1
CN9001	Aliphatic urethane diacrylate	3250g/mol	54°C	2
CN9002	Aliphatic urethane diacrylate	7650g/mol	-55°C	2

Two different photo-initiators were used to start the radical curing reaction of the UV curing acrylate adhesives. Irgacure 184 from Ciba Specialty Chemicals is a powder of 1-hydroxy-cyclohexyl-phenyl-ketone and is a radical photo-initiator which is activated mainly in the UVA spectrum. Lucirin TPO-L from BASF is a liquid photo-initiator which is activated by longer wavelengths of light than Irgacure 184 and consists of ethyl-2,4,6-trimethylbenzoylphenylphosphinate. The chemical structure and absorption spectra of these materials at different concentrations in a solvent can be seen in Figure 2.2.

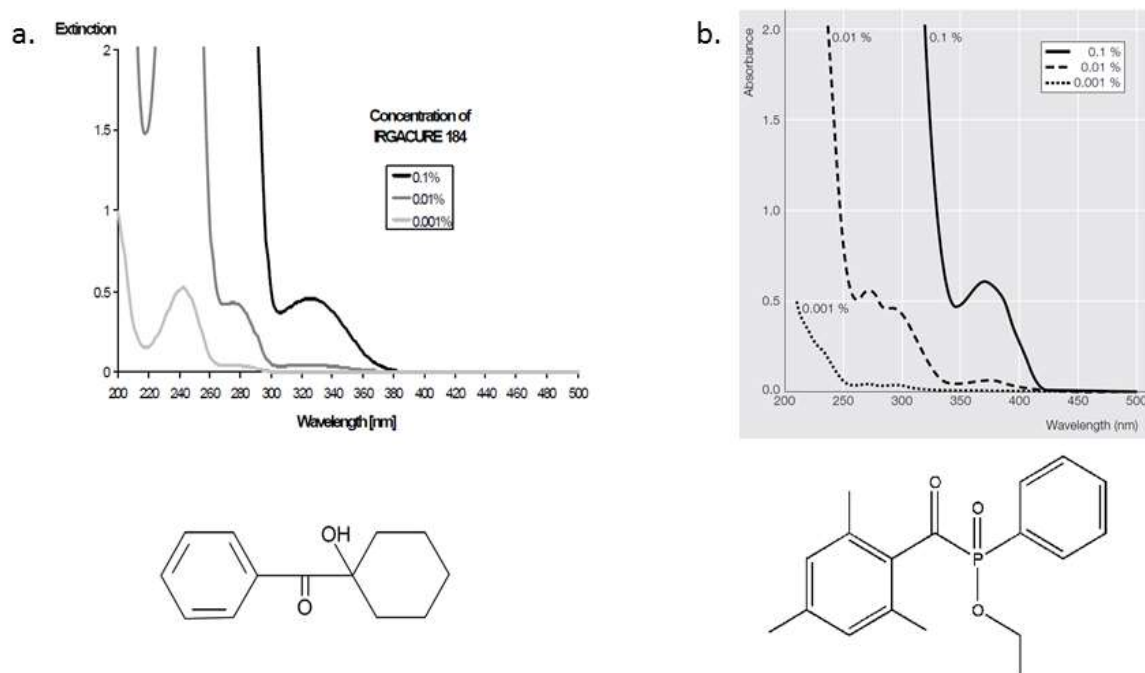


Figure 2.2 The chemical structure and absorption spectra as provided by the manufacturer for (a) Irgacure 184 in acetonitrile and (b) Lucirin TPO-L in ethanol.

Nanoparticles

Phyllosilicates

Two different grades of phyllosilicates from Southern Clay Products (United States) were used. Cloisite 10A consists of bentonite modified with benzyl(hydrogenated tallow) dimethyl quaternary ammonium salt. As can be seen in Table 2.4, the typical particle diameter is $<10\mu\text{m}$ (d_{50}) while the d_{001} spacing is 1.9nm. Cloisite 15A consists of a natural montmorillonite modified with dimethyl di(hydrogenated tallow) quaternary ammonium chloride. The typical particle diameter is $<6\mu\text{m}$ (d_{50}) while the d_{001} spacing is 3.15nm.

Table 2.4 Information on the phyllosilicate particles is shown as provided by the manufacturer.

Product Name	Organic Modification	Diameter (d ₅₀)	d ₀₀₁ Spacing
Cloisite 10A	Benzyl (hydrogenated tallow) dimethyl quaternary ammonium salt	<10µm	1.9nm
Cloisite 15A	Dimethyl di(hydrogenated tallow) quaternary ammonium chloride	<6µm	3.15nm

Zeolites

The zeolite nanoparticles NZL-40 were supplied from Clariant International Ltd. (Germany). These particles have a Linde Type L (LTL) zeolite structure and the exact ratios of cations in the oxide structure can be seen in the elemental analysis shown in Table 2.5. The typical particle size is 30-60nm which, combined with porosity of the zeolite structure, produces a specific surface area of 150-170m²/g.

Table 2.5 The elemental analysis of NZL-40 was provided courtesy of Ievgeniia Topolniak of the Institute de Chimie de Clermont-Ferrand.

Chemical Elements										
	H (%)	Si (%)	Al (%)	K (%)	Fe (ppm)	Zn (ppm)	Cu (ppm)	Co (ppm)	Mn (ppm)	Na (ppm)
NZL-40	1.20	24.75	9.07	13.31	63	<20	<20	<20	<20	≤20

Two batches of these zeolites were used. The first batch was produced in Clariant's research lab and produced highly homogenous particles within the specifications of the datasheet. The second batch however was purported by Clariant to be far less homogenous with some contamination of larger particles as it was manufactured not in the research lab but instead on an industrial production line. Despite this warning from the manufacturer, dynamic light scattering and transmission electron microscopy were unable to confirm the presence of these larger particles. Therefore the batch manufactured on an industrial production line was deemed acceptable for the work performed in this project.

Materials Preparation

MAM Pressure Sensitive Adhesives

The MAM Nanostrength[®] adhesives were not available in the form of homogenous films but were instead supplied as pellets or slabs of bulk polymer. This necessitated the use of solution processing in order to create homogenous films which was possible thanks to the thermoplastic nature of these adhesives. Solution processing was also advantageous as it allowed for facile mixing with nanoparticles. The following section describes the processes used to create solutions, composites and films of the MAM Nanostrength[®] adhesives.

Solutions

Solutions of the neat adhesives were created by magnetic stirring of the adhesive with either acetone or toluene in a closed glass bottle or vial. The exact ratio of adhesive-to-solvent was dependent on the adhesive and concentration of nanoparticles due to the variations in viscosity. In general, 30-45 weight% of adhesive was sufficient to fully dissolve the adhesive and maintain a viscosity easily workable with a wide mouthed disposable pipette. Acetone was used in early experiments as it is generally considered to be less toxic than toluene. However the rapid evaporation rate of acetone led to problems under certain conditions which in turn led to the use of toluene as the preferred solvent. The fast evaporation rate of acetone under ambient conditions caused the substrate to cool. This cooling effect was often enough to cause water vapor in the atmosphere to condense onto the adhesive / substrate in the summer or on especially humid days. Heating the substrate to avoid this cooling caused the evaporation to become too rapid and often introduced bubbles and/or inhomogeneities in the coatings. The slower evaporation rate of toluene does not have these problems and was therefore selected as the preferred solvent for the MAM Nanostrength[®] adhesives.

Cloisite 10A was found to be slightly more soluble in toluene than Cloisite 15A and was therefore used for all MAM-phyllsilicate composites. Solutions containing zeolites used Clariant NZL-40 nanoparticles. The particles were measured as a powder using a balance and were then added to a previously prepared solution of adhesive in toluene. The composite was then allowed to stir on a magnetic stir plate until only large clumps of particles or precipitates remained undispersed. The solution was then sonicated at 45 kHz for 15-30min and returned to

magnetic stirring. If necessary, this cycle was repeated until the particles were completely dispersed. These solutions were generally milky in appearance in comparison to the transparent solution before the addition of the particles, especially for the phyllosilicates. All solutions of composites were sonicated again just prior to use.

Solvent Evaporation

Once coated it is necessary to evaporate all of the solvent before using the adhesive. Residual solvent in the adhesive can greatly affect the properties of the adhesive and cause the formation of bubbles if it evaporates during subsequent processing. Therefore all samples were dried immediately after coating. To limit surface roughness, thickness inhomogeneity and formation of bubbles caused by rapid evaporation of the solvent, the toluene was allowed to evaporate at room temperature in a fume hood or ventilated bench until no liquid remained. This was generally achieved in 5-10min. The coated substrates were then dried on a hot plate at 90°C in a fume hood for 10-15min to remove any toluene which remained absorbed in the polymer.

UV Curing Acrylates

All UV curing acrylate adhesives used in this project were supplied in the form of monomers, oligomers or blends of monomers, oligomers and additives. It was therefore necessary to complete the formulations before use by mixing these materials in the appropriate ratios with photo-initiators. This class of adhesive also requires the additional step of curing with ultraviolet light. The process involved for the fabrication and curing of these adhesives is discussed in this section.

Fabrication

All solutions were mixed in glass bottles or vials via magnetic stirring. Components were all measured by mass and added directly to the main solution. This was done due to the tendency of many of the monomers and oligomers to leave a significant amount of residue on all containers and measuring devices which they come into contact with. Very high viscosity oligomers were always added first via spatula followed by the remaining liquid monomers and oligomers whose precision was achieved through dropwise addition. The solution was then allowed to mix, though not always completely, before the addition of the photo-initiators. After

the addition of the photo-initiators the solutions were allowed to thoroughly mix via magnetic stirring. For several formulations their high viscosity made stirring ineffective. For these solutions, the magnetic stir plate was warmed to 60°C in order to reduce the viscosity of the solution and allow for thorough mixing. This warming technique was also used when these solutions need to be deposited via pipette as they otherwise would not be able to be easily manipulated by a pipette. Thorough mixing was identified visually by a lack of changes in refractive index and particulates.

For certain samples, it was necessary to use the adhesives inside an inert atmosphere glove box. Since the raw materials and the solutions were all prepared in air, oxygen and water were removed by bubbling dry nitrogen through them overnight. The solutions were then immediately sealed in their glass bottle under dry nitrogen and placed in the glove box. This procedure was used as the solutions contain some volatile components which may have been lost using a vacuum de-gassing process.

For phyllosilicate composites, Cloisite 15A was found to be more soluble in the adhesives than Cloisite 10A and was therefore used for all UV curing acrylate-phyllosilicate composites. Cloisite 15A was measured as a powder using a balance and then added to the adhesive solution. For some earlier composites, the phyllosilicate was added to the solution and allowed to fully mix before the addition of the photo-initiators. However, this was later changed to the phyllosilicate being added after the photo-initiators were already well mixed into the solution. This is because the composites had a milky appearance which made it difficult to visually confirm if the photo-initiators had fully mixed into the solution.

Zeolite composites used a slightly different method than the phyllosilicates. Because the zeolites could not be dried under vacuum after addition to the adhesive, they were instead dried using a Mettler Toledo HX-204 moisture analyzer at 130°C. The particles were then immediately sealed in a vial under dry nitrogen and placed into an inert atmosphere glove box. The fully mixed adhesive, including photo-initiators, was also entered into the glove box as previously described. The dry zeolite particles were then measured as a powder using a balance and added to the adhesive solution in the glove box. The solution was then mixed via magnetic stirring in the glove box. The glass bottle of the adhesive solution was then sealed and removed from the glove box for sonication. Immediately following sonication, the solution was returned to the glove box for continued stirring. This process of sonication and stirring was repeated as needed until the solution was well mixed. Care was taken to never expose the solution itself to air after the addition of the zeolites.

Curing

The curing of UV curing acrylate adhesives was carried out using two different lamps. Curing parameters were confirmed for each lamp separately, however once validated the two lamps were used interchangeably and considered to provide an equivalent cure. Curing parameters were confirmed by FTIR-ATR. Parameters for curing include illumination time, distance from the lamp, intensity of the lamp and type of atmosphere.

A medium pressure mercury lamp, Hönle UVASPOT 400/T-F, with a quartz filter was used for curing in air and was located in a fume hood or ventilated bench. This lamp produces a broad spectrum of wavelengths from approximately 200-600nm which can be seen in Figure 2.3. While the intensity of this lamp could not be adjusted, decreasing the distance from the lamp to the sample does increase the intensity seen by the sample.

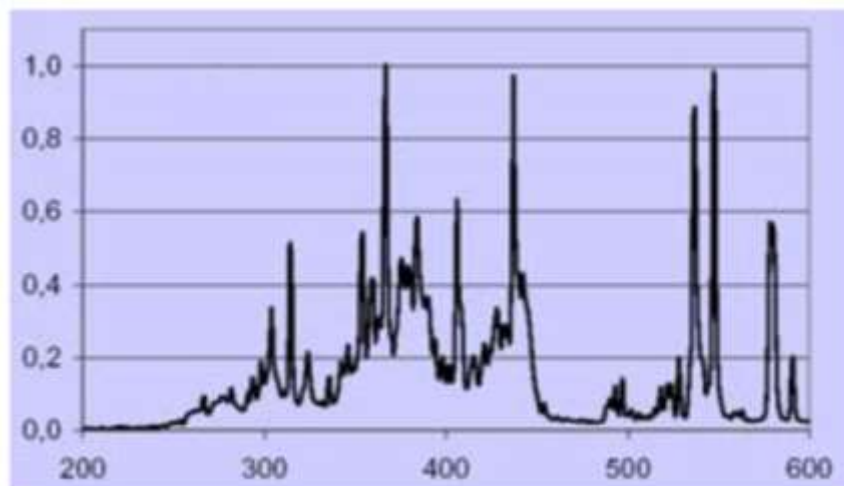


Figure 2.3 The spectrum of a Hönle UVASPOT 400/T-F lamp, as published by the manufacturer, is shown with the vertical axis being Relative Intensity and the horizontal axis being Wavelength in units of nm.

The second UV lamp was located inside an inert atmosphere glove box and used light emitting diodes (LED) as its source. This lamp, a DELOLUX 20/400, produced a narrow spectrum of wavelengths with a peak at ~400nm. The structure supporting this lamp did not allow for the distance between the lamp and the sample to change, however the control unit did allow for the adjustment of the power supplied to the lamp (and therefore its intensity).

Corona Treatment

Surface treatments by a corona-type discharge were used to modify the surface energy of substrates prior to bonding with an adhesive. The treatments were performed using a unit which was incorporated into a roll-to-roll manufacturing line. Samples were affixed to the web

just in front of the corona unit using an adhesive tape and were removed immediately after treatment, thus ensuring the treated surface of the substrate did not come into contact with any rollers before or after treatment. From contact angle studies on PET surfaces previously performed internally by the CEA Laboratoire des Modules Photovoltaïques Organiques, a power of 250W with a web speed of 0.2m/min was selected for the operating parameters.

Other corona treats were also performed using a Vetaphone VE1A-A 620 unit which was incorporated into a Grafisk Maskinfabrik roll-to-roll manufacturing line. Due to this unit's higher power, treatments were performed at 500W with a web speed of 0.4m/min. However, the increased power of this unit was found to compromise the structural integrity of Oike VX 25T-2PO barriers as discovered in adhesion tests. Therefore this unit was deemed to be unsuited for use on this project.

Coating

The coating of the adhesive solutions was performed via blade coating using an Erichsen Coatmaster 509-MC located in a fume hood or ventilated bench or a Zehntner Testing Instruments ZAA-2300 located inside an inert atmosphere glove box. These machines push the liquid to be coated with a blade over a flat plate upon which the substrate is fixed. The thickness of the resulting coating is controlled by the height of the blade over the surface, the speed at which the blade moves, the temperature and the viscosity of the liquid. To simplify the coating process and the optimization of the coating thickness, a speed of 25mm/s was used for all coatings. In addition, all coatings were performed with the blade coater at 23-24°C with the exception of MAM Nanostrength[®] composites containing zeolites, which were coated at 40°C. The coating process was performed by fixing a clean substrate onto the flat plate using an adhesive tape. The blade was then adjusted to the desired height and positioned over the substrate. The arm of the blade coater which pushes the blade was then moved into contact with the blade. The adhesive solution was then deposited along the leading edge of the blade via pipette. To minimize variations in viscosity (and therefore final coating thickness) due to solvent evaporation and/or temperature variations between the solution and blade coater, the coating was performed as quickly as possible after deposition of the adhesive solution.

Lamination and Encapsulation Methods

Pressure Sensitive Adhesives

Both the commercially available pressure sensitive adhesives supplied in this form and laboratory prepared coatings of pressure sensitive adhesives were laminated using one of two procedures: dual roller lamination or weighted hand rolling. For both techniques, the adhesive and substrate are prepared in the same manner. Firstly, both the substrate and adhesive were cut to the approximate size of the final sample. Since it can be difficult to have a perfect alignment during lamination, it was found to generally be simpler and more accurate to cut the sample to its correct dimensions after lamination. The surface of the substrates was then prepared in the desired manner (solvent rinse, sonication in solvent, corona treatment). The next step is to remove the protective liner (if present) from one side of the adhesive, thus leaving the adhesive exposed on one side and protected by either a substrate or a second protective liner on the other side.

At this stage, the two lamination processes differ slightly. Dual roller laminations were performed using a Dynachem ML-3024 laminator on a Teflon coated glass carrier with a total thickness of 3.35mm, a roller air pressure of 4bar and a speed of 0.5m/min. This machine, pictured in Figure 2.4, uses two rubber coated rollers which turn in opposite directions (one clockwise and one counter-clockwise). The sample is then placed between the two rollers which provide the pressure needed for lamination. The gap between the rollers can be controlled using compressed air. Despite the fact that the amount of air pressure directly influences the pressure the rollers apply to the sample, it should be noted that the actual pressure applied to the sample is unknown. To perform a lamination with this machine, the substrate is first fixed to the carrier. The adhesive is then aligned by sight and allowed to contact the leading edge of the substrate. The carrier is then inserted between the rollers while attempting to minimize contact between the adhesive and the substrate before entering the rollers. This machine is particularly useful for larger samples, though the large size of the machine itself prevents its use inside a glove box.

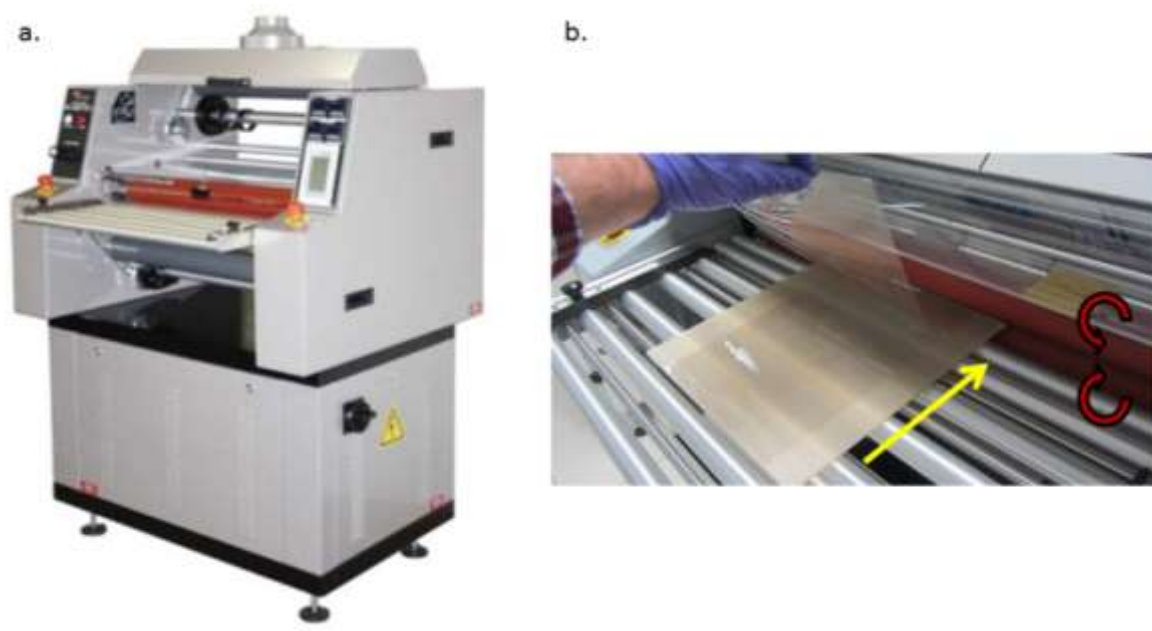


Figure 2.4 (a) A Dynachem ML-3024 laminator such as the one used in this thesis is shown. (b) A close up of a lamination of two flexible films using the Dynachem ML-3024 is shown. The tan Teflon coated glass plate is advanced through the red rollers which push the two flexible films into contact.

For those samples using the weighted hand roller technique, the substrate is placed onto a flat surface with the surface to be laminated facing upward. The adhesive was then aligned by hand and laminated carefully to the substrate. The weighted hand roller provides the pressure to ensure good contact between the surfaces and to limit the number of bubbles. The roller, which can be seen in Figure 2.5, conforms to the PSTC-101 standard and is made of a 45mm wide steel roll (ϕ 83mm) with a 6.25mm outer coating of a rubber with a Shore A hardness of 80. The mass of the roller portion is 2.045kg. The weighted hand roller is particularly useful for smaller samples and was used for all laminations inside the glove box.



Figure 2.5 The weighted hand roller used for laminating samples is shown. The gray, soft rubber coating on the metallic, heavy, steel roller is clearly visible in the image.

For both methods, the type of sample being made determined the next step. For samples which were not for encapsulation of calcium coupons or OPV cells, any remaining protective liners were removed and any remaining laminations subsequently performed in the same manner. For samples involving encapsulation, moisture was then removed from the adhesive

coated substrates by drying in a vacuum oven at 80°C / 1-5mbar for a least two days followed by a cool down to 30°C while still under vacuum. Samples containing zeolites had an additional first temperature step at 130°C for 30-60min before cooling to 80°C for the standard drying procedure. For ease of handling and to prevent movement of the samples as atmosphere was re-introduced, two glass microscope slides were placed on opposite edges of each sample before the drying step. Once the vacuum oven had returned to 30°C, samples were removed and rapidly placed inside an inert atmosphere glove box. Once in the glove box, the glass microscope slides were removed and the object to be encapsulated was positioned onto the adhesive by hand. A second adhesive coated substrate was then laminated on top using a weighted hand roller.

UV Curing Acrylates

The liquid nature of UV curing acrylates required the use of a different encapsulation method as compared to the pressure sensitive adhesives. The substrates were first cut to the approximate size of the final sample. Just as with PSA laminations, it can be difficult to have a perfect alignment during lamination, thus it was generally found to be simpler and more accurate to cut the sample to its correct dimensions after lamination. Substrates were surface treated as desired (solvent rinse, sonication in solvent, corona treatment) and then dried in vacuum oven at 80°C / 1-5mbar for a least two days followed by a cool down to 30°C while still under vacuum. The substrates were then rapidly moved to the glove box. The substrates were then coated with adhesive inside the glove box as previously described. The object to be encapsulated was immediately laminated onto an adhesive coated substrate by hand. A second adhesive coated substrate was then laminated on top also by hand. The laminated sample was then immediately cured as required by the adhesive. The sample was then flipped over and cured for a second full cycle in order to ensure that areas underneath the encapsulated object were well cured.

Aging Conditions

For experiments requiring aging, artificial accelerated conditions were used in order to minimize testing time and ensure that conditions remained consistent for all samples. Two different aging conditions were used depending on the specific study: accelerated moisture and accelerated photo-stability testing.

Accelerated Moisture

Accelerated moisture aging was performed at 65°C and 85% relative humidity for all testing regardless of sample type. These conditions were chosen as they correspond to the ISOS-D-3 standard, which uses the same conditions as described above for the damp heat aging of organic photovoltaic devices without illumination. These conditions were produced in a humidity chamber using either a Dycometal CM-25/48 or a Clima Temperatur Systeme C-40/100. For both chambers, samples were placed on shelves consisting of metal grids. An image of samples inside a humidity chamber can be seen in Figure 2.6.



Figure 2.6 A sample for an optical calcium test (left) and an encapsulated OPV cell (right) are shown inside a humidity chamber.

Accelerated Photo-Aging

Accelerated photo-aging was performed using an Atlas Material Testing SEPAP 12/24. In this apparatus, seen pictured in Figure 2.7a, samples are placed in metal sample holders which are attached to a carousel that rotates in the center of four 400W medium pressure mercury lamps. The lamps produce a spectrum as seen in Figure 2.7b thus providing a large dose of ultraviolet irradiation. The chamber ventilated to maintain a temperature of 60°C.

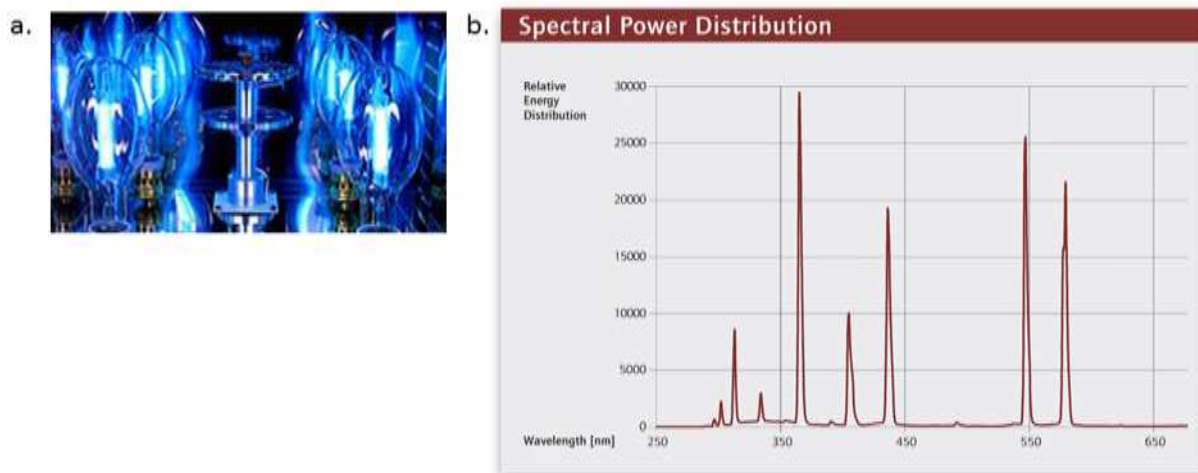


Figure 2.7 (a) The interior of a SEPAP 12/24 is shown with an empty carousel and the four UV lamps. (b) The spectrum of the UV lamps used in a SEPAP 12/24 is shown as provided by the manufacturer.

Experimental Techniques

Spectroscopic Techniques

Transmission Fourier Transform Infrared Spectroscopy (FTIR)

All testing was performed using a Thermo Electron Corporation Nicolet 5700 and analyzed using Omnic 8.3 software. Measures were made in absorbance mode with 32 scans per measure. Measures were made on both free standing films and thin coatings on potassium bromide substrates.

Attenuated Total Reflection Fourier Transform Infrared Spectroscopy (FTIR-ATR)

Attenuated total reflection (ATR) is a variant of infrared spectroscopy used to probe the chemical structure of thin surface layers. The difference between ATR and transmission FTIR lies in the test configuration, as the basic principles are the same for both techniques. In ATR, the laser is passed through a crystal at an angle which produces total internal reflection. The sample to be measured is placed on top of this crystal with care taken to ensure good contact between the sample and the crystal. As the light reflects off the interface between the crystal and sample, it penetrates slightly into the sample thus allowing for the absorption of the

frequencies corresponding to specific resonant vibrations of the covalent bonds in the sample. The exact penetration depth, described in Equation 2.1, is dependent on the exact refractive indexes of the crystal and sample at the wavelengths being tested but is generally on the order of a few microns for polymeric samples on a diamond crystal.

Testing was performed using a Thermo Electron Corporation Nicolet 5700 with a SmartOrbit single reflection diamond ATR crystal attachment. This crystal provides a penetration depth generally in the range of 0.7-2 μm depending on the refractive index of the material being measured. Measures were made in absorbance mode with 32 scans per measure. All samples used Omnic 8.3 software for analysis. For solid samples, the surface to be measured was pressed onto the crystal by hand and held in place by a metal point on the ATR attachment. Liquid samples were made by depositing a drop of the sample onto the crystal via pipette. The crystal was always wiped with ethanol, isopropanol, and/or acetone before and after each measure regardless of the type of material being tested.

Ultraviolet-Visible Spectroscopy (UV-Vis)

All UV-Vis testing was performed using a Shimadzu UV-2600 spectrometer controlled using UVProbe 2.42 software. Scans were performed over a range of wavelengths from 200-800nm. Both direct and integrating sphere detectors were used depending on the measure.

Thermo-mechanical Testing

Dynamic Mechanical Thermal Analysis (DMTA)

DMTA is a technique for measuring the viscoelastic properties of a material over a range of frequencies and/or temperatures. This machine applies a cyclic load to a sample and has the ability to control the force, frequency, strain and temperature. The cyclic nature of the loading causes a time or frequency shift between the stress and the applied load in the case of viscoelastic materials. The mathematical treatment of the shifted signals allows for the separation of their in-phase and out-of-phase components, thus leading to the calculation of an elastic (energy storage) component of the mechanical modulus of the sample (E'), and a viscous (energy loss) component (E'') of that same modulus.

All testing was performed with a TA DMA Q800 with a liquid nitrogen cooling unit. Tests were performed in tension mode using a strain of 0.1%, a constant frequency of 1Hz and a temperature sweep from -70°C to 120°C or until failure of the sample. Samples were analyzed using TA Universal Analysis 2000 4.2E software.

Differential Scanning Calorimetry (DSC)

DSC measures the difference in heat flow between a sample and a reference in order to illuminate various thermal changes in a sample. These changes include melting, glass transition, evaporation and chemical reactions and can be either exothermic or endothermic in nature.

Measures were made using a Mettler Toledo DSC 822 controlled with STARe 11.00 software or a TA DSC Q20 using TA Universal Analysis 2000 V4.2 software. All tests were performed using a temperature sweep at a constant heating rate, with most samples tested from -70°C to 140°C, though some samples used slightly different ranges depending on the material being tested. Regardless of the sweep range, the same heating/cooling profiles were used. Tests began with a 5min isothermal hold at the minimum temperature then ramped at 10°C/min to the maximum temperature. This was followed by a cooling cycle back to the minimum temperature with an isothermal hold for 5min once the minimum temperature was reached. Finally the sample was heated for a second time at 10°C/min. When possible, values from the second heating run were used for analysis.

T-Peel Adhesion

T-peeling is a technique to measure adhesion when using two flexible substrates. In this technique, the two substrates are pulled apart at 180° to each other and the force is measured as a function of the distance peeled. The value is reported as peel strength and is the average force per unit of width (i.e. N/cm). It should be noted that this value can change as a function of adhesive thickness and substrate thickness even for the same bonding conditions.

In order to accurately compare samples, an adhesive thickness of 50µm was used whenever possible. Samples with different adhesive thicknesses are noted as such. All testing was performed to PSTC 101 standards with a sample width of 24mm and a peeling rate of 300mm/min. The testing was performed using an Instron 3365 electromechanical load frame equipped with a 50N load cell. The testing configuration can be seen in Figure 2.8. The reported average peel strength for each individual sample does not include the first and last 10% of the peeling distance in order to avoid edge effects. Whenever possible, at least 4 individual samples

were tested for each condition and the reported peel strength is an average of all individual samples.

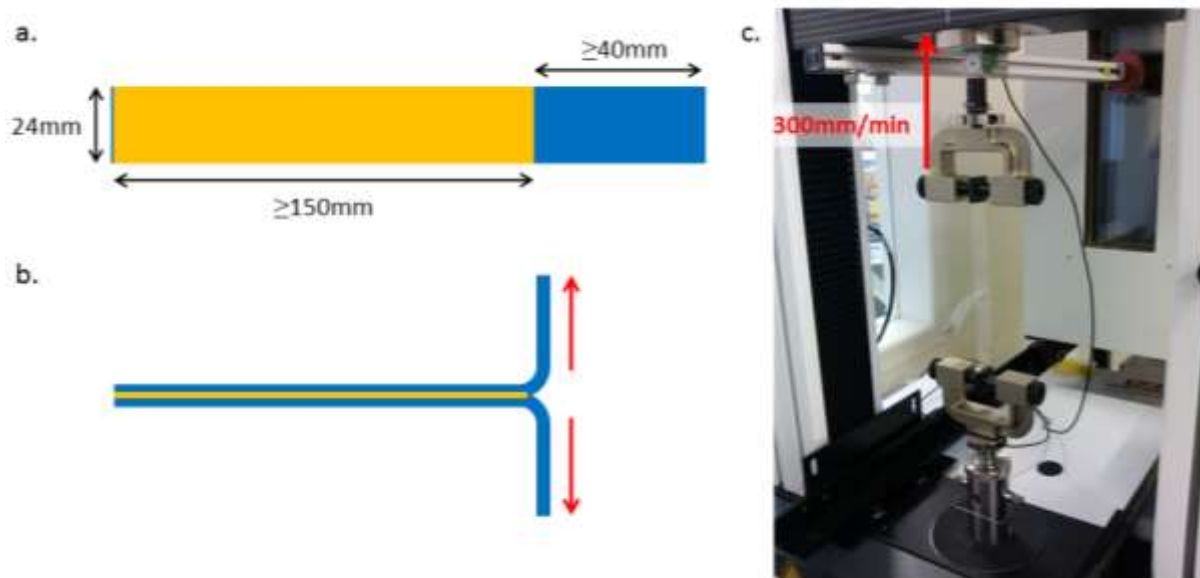


Figure 2.8 A diagram of a T-peel adhesion sample with blue representing the substrates, yellow representing the adhesive, and red arrows showing the directions of the applied forces is shown in (a) an un-bent top view and (b) a bent side view. (c) An image of a T-peel adhesion sample in the load frame during a test is shown. The upper clamp moves away from the fixed bottom clamp at a constant speed of 300 mm/min.

Microscopy

Atomic Force Microscopy (AFM)

AFM uses an extremely fine tipped cantilever to probe the surface of a material. The displacement of the tip as it interacts with forces from the surface being observed is able to provide information on the surface roughness and phase domains of the material. In tapping mode, as was used for all images in this thesis, the tip is oscillated up and down by a piezoelectric element at the base of the cantilever. The deviations in the oscillation of the tip are measured using a laser and allow for the imaging of the surface based on the forces acting on the tip as it approaches the surface. In this manner the topography, or height, of the surface can be measured. In addition, phase shifts in the oscillation can be caused by viscoelastic and adhesion properties of the material being imaged as they dissipate the energy of the tip. This allows for phase images which can show different domains and morphology even for flat samples.

All AFM images used in this thesis were taken using a Veeco Nanoscope IIIA mounted on an air pressure table to minimize vibrations. A digital camera was used to precisely position

the tip. Images were taken in tapping mode using a phosphorous doped silicon tip with a radius of <15nm and a depth of 20 μ m.

Transmission Electron Microscopy (TEM)

TEM is a versatile imaging technique in which measures the transmission of an electron beam across a sample. In the bright field technique used in this thesis, the resulting image is created by differences in electron density within the sample which scatter the electron beam. The transmitted beam then interacts with a detector which fluoresces to produce an image. The image is then in turn captured by the CDD camera. In this manner, more electron dense regions appear darker than those with lower electron density.

All images were taken using a Hitachi H7650 120kV operating with an electron beam at 80kV and equipped with a Hanamatsu AMT HK 1K x 1K CDD camera. Samples were prepared by evaporating a dilute solution on a carbon grid. All images were taken with the aid of the staff of the Centre Hospitalier Universitaire de Clermont-Ferrand where the microscope was located.

Other Testing

Optical Calcium Test

For a detailed description of the optical calcium test please refer to Chapter 3, which provides an in-depth explanation of this test.

Optical calcium test measures for this project used an Olympus Optical Co. DP70 Microscope Digital Camera controlled using Olympus DPController 1.2.1.108 software. Images were analyzed using ImageJ software (Wayne Rasband, National Institutes of Health) using the plugins TurboReg and StackReg (P. Thévenaz, U.E. Ruttimann, M. Unser, Ecole Polytechnique Federal de Lausanne). The light source, though replaced occasionally throughout the project, was always a Coherent ML-0405 cold cathode backlight panel. A foam tape was placed around the perimeter of the light source in order to elevate the samples above the surface of the light source. This was done to protect the surface from scratches caused by the sample holders. The camera was fixed vertically over the light source and placed inside a wooden light blocking enclosure in order to avoid background light from affecting the images. The experimental set up used for imaging can be seen in Figure 2.9.

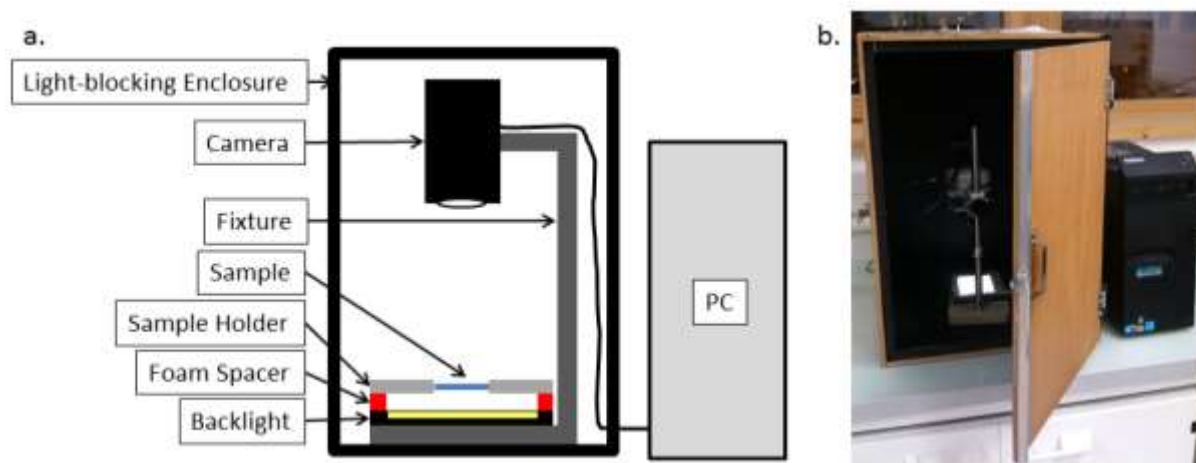


Figure 2.9 (a) A diagram of the configuration used for imaging in the optical calcium test is shown next to (b) an image of the actual apparatus.

Calcium deposits were made onto Melinex 401 PET substrates with dimensions of 5cm x 5cm x 50 μ m which were cleaned by sonication in isopropyl alcohol and then dried for at least 2 days at 80°C under vacuum (1-5mbar) followed by cooling to 30°C while still under vacuum. The deposits of calcium were made via physical vapor deposition under vacuum (10^{-5} - 10^{-6} mbar) using a shadow mask. The deposition rate was always <2nm/s as measured by a quartz microbalance incorporated into the evaporation chamber. The evaporation chamber was located inside an inert atmosphere glove box and all subsequent storage and handling of the calcium deposits before testing was performed in an inert atmosphere so as to minimize the oxidation of the deposit.

Dynamic Light Scattering (DLS)

DLS is a technique which can be used upon true solutions of polymer molecules or upon dispersions of particles in an inert liquid. In this thesis, the latter case was used exclusively. It allows for the determination of the particle size distribution for nanoparticles dispersed in the liquid medium. A laser is passed through a dilute dispersion of the particles which scatter the light. The constructive and destructive interference patterns of the scattered light vary as a function of time due to the Brownian motion of the particles. These variations, along with knowledge of the solvent and composition of the particle, allow for the calculation of the relative amounts of particles of different sizes through mathematical models which exploit a spatial-temporal second order correlation function. This function is valid for a given type of particle dispersed in a given liquid medium.

All tests used a Malvern Instruments Zetasizer ZEN3600 with a 633nm, 4mW He-Ne laser. Analysis was performed using Malvern Instruments Zetasizer 7.02 software.

Moisture Content Analysis

The analysis of the moisture content is performed by heating the material to be measured and recording the mass change as a function of time. Once the rate of mass loss falls below a specified value, the material is considered to be dry. The loss of mass due to the evaporation of volatile components is reported as a percentage of the initial mass.

Moisture content analysis was performed using a Mettler Toledo HX204 Moisture Analyzer. Drying was performed isothermally at 130°C until the rate of mass loss fell below 1mg / 140s. The typical sample size was 1-2g in initial mass.

Current Density – Electric Potential Characterization (J-V)

J-V characterization is a method to measure the performance of photovoltaic devices. In this test, a device is cycled through a range of electric potentials while measuring the electric current. This testing can be done with or without illumination of the photovoltaic device depending on the desired properties to be measured. From this measurement many different properties of the device can be measured including the power conversion efficiency, short circuit current density, open circuit voltage, fill factor, series resistance, shunt resistance, leak current and others.

Two sets of equipment were used: one in air and one integrated with a nitrogen atmosphere glove box which allowed for the device to be measured to remain in an inert atmosphere. The apparatus in air used a Keithley 2602A Sourcemeter and illumination from a Newport Oriel 92190 solar simulator with an Oriel 62771 1600W xenon arc lamp which provided an AM 1.5 spectrum and an intensity of 100mW/cm². This experimental set up can be seen in Figure 2.10a. The apparatus integrated with a glove box used a Keithley 2400 Sourcemeter and illumination from a Newport Oriel 9403A-SR1 solar simulator with an Oriel 6280NS 450W xenon arc lamp which provided an AM 1.5 spectrum and an intensity of 100mW/cm². The experimental set up for this lamp is shown in Figure 2.10b. For both sets of equipment, analysis was performed using software developed in-house by the CEA.

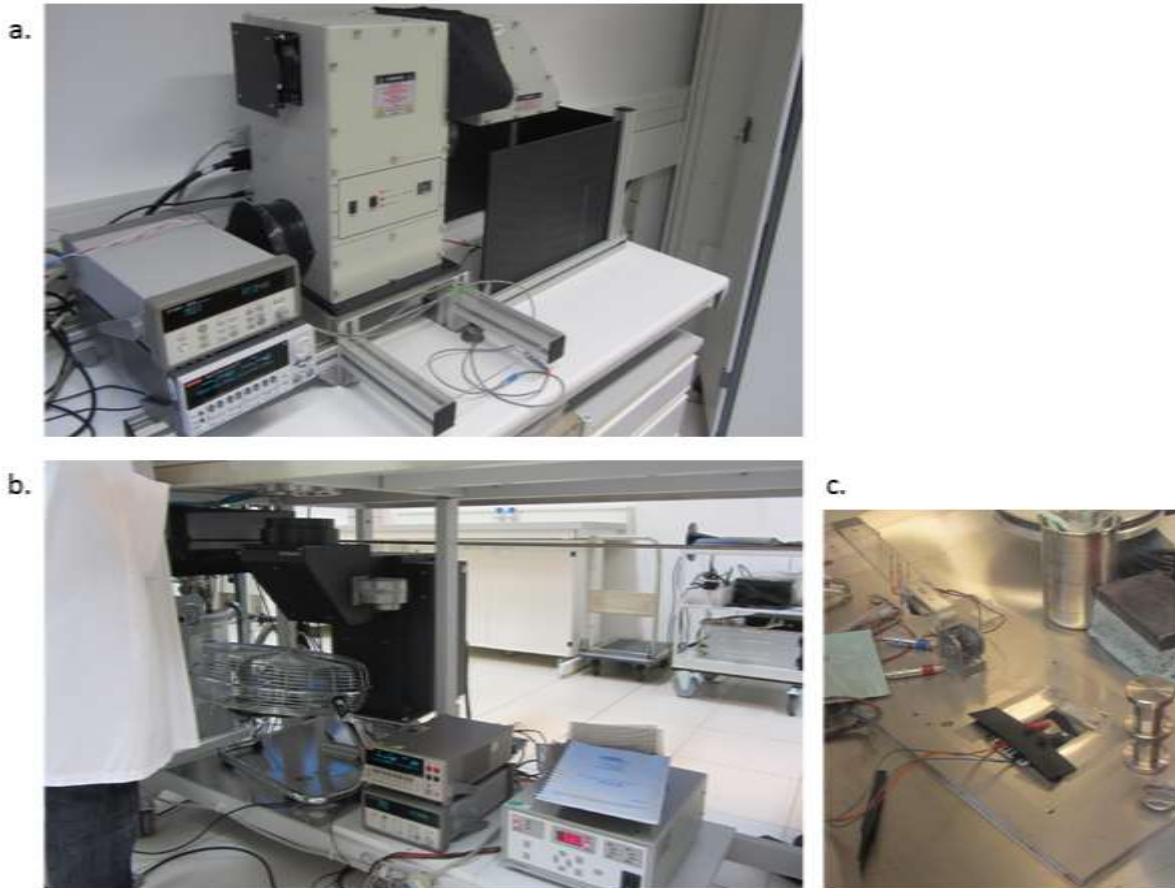


Figure 2.10 The configurations of the equipment for J-V characterization are shown. (a) The solar simulator in air is positioned to shine light downward onto the sample to be measured and is surrounded by a light blocking enclosure (pictured partially open to show the sample) for safety reasons. (b) The simulator which is integrated into the inert atmosphere glove box is situated underneath the glove box in air. The light is shone upward through a window into the glove box where (c) the sample is positioned. Several different types of electrical connections are available to ease the measuring of samples with various different geometries.

Chapter 3: Development and Optimization of the Optical Calcium Test

Introduction

As previously discussed in Chapter 1, the OPV barrier requirements necessitate the use of materials with very low gas permeation rates which can often be difficult to measure. However, most of the techniques available for the measurement of permeation are designed for the measurement of films. Due to their soft and often sticky nature, these techniques are generally impractical for the measurement of flexible adhesives. However, there are several techniques which have been designed to measure adhesives, namely indicator paper and the lateral version of the optical calcium test. Indicator paper is significantly less sensitive than a calcium probe and can require longer measurement times to achieve a qualitative assessment of water permeation. For this reason the lateral version of the optical calcium test is generally the preferred method despite its requirement for sample preparation in inert atmosphere.

This version of the optical test is based upon the assumption of impermeable substrates which block any orthogonal permeation. Therefore all calcium degradation can be attributed to lateral permeation. While this is a powerful technique for the evaluation of the water vapor barrier properties of an adhesive, it does contain a major flaw for flexible encapsulation: the interfaces. In order to achieve the level of impermeability required to fit the model, thick silica glass substrates are used. A rigid silica glass plate can present a surface which is vastly different from a flexible multi-layer barrier film, even if the surface of the film is a thin SiO_x barrier layer. More commonly, the surface of a flexible multi-layer barrier film in contact with the adhesive is a polymer. The lower surface energies of many polymers can make adhesion to their surfaces more challenging than silica glass. This different, and usually weaker, interface makes it difficult to truly evaluate the lateral permeation into a device since the lateral permeation depends not only on the bulk permeation rate of the adhesive, but also the interfacial permeation rate. Therefore, for a more accurate evaluation of an adhesive for encapsulating OPV devices, a lateral optical calcium test should use the same flexible barrier film that is used for

encapsulating the device. However the use of flexible substrates would invalidate the basic assumption of impermeable substrates needed to analyze this type of test since flexible films will allow for some degree of orthogonal permeation.

This chapter describes an alternative sample geometry and data analysis which makes possible the use of flexible substrates with the lateral version of the optical calcium test. The analysis method described allows for evaluation of not only the lateral permeation, but also of flexible barrier films and the relative impacts of the bulk adhesive and interface on the lateral permeation. The sample geometry of this test also allows for the simulation of actual devices which can provide insight into the design of encapsulation schemes for OPV.

Sample Geometry

The most important change to the lateral testing procedure originally described by Kempe et al. is the geometry of the sample.⁵² The sample geometry should maintain the large area of the calcium deposit in order to accurately measure the lateral permeation. The sample geometry should also be designed in a way to mimic an actual device as much as possible. Since many flexible OPVs are manufactured on a polymer substrate before being laminated between two barrier films, the same scheme was selected for the modified calcium test geometry. This combination of factors led to the calcium test sample geometry shown in Figure 3.1.

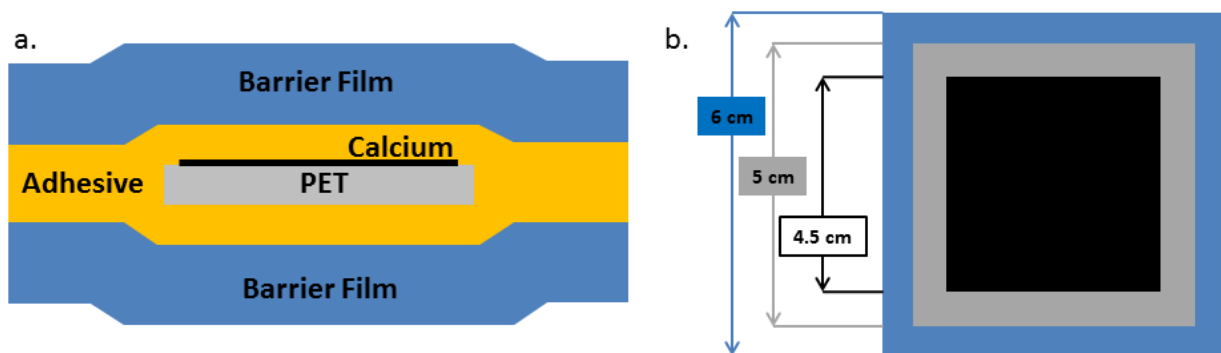


Figure 3.1 A diagram of the sample geometry for the modified lateral optical calcium test is shown in (a) cross-sectional view and (b) top view. In the top view, the sample is a square and the marked dimensions are also the same for the horizontal dimensions. Please note that the diagram is not drawn to scale.

Advantages of Modified Sample Geometry

This geometry closely mimics one of the most popular schemes for OPV encapsulation. This allows any results from the calcium test to be directly applicable to an actual device. The geometry also allows this version of the calcium test to provide an evaluation of complete

encapsulation schemes or encapsulation process changes which would otherwise require testing with functional devices. Compared with a functional device, a calcium probe is more sensitive to water (i.e. shorter testing time), simpler to prepare, and degrades much more predictably as the stability of individual devices can vary greatly. Though testing with actual devices is still necessary to evaluate the effects of the encapsulation materials and processing on the device itself, this version of the calcium test as a screening process provides a faster, simpler and more accurate measure of permeation.

The size of the calcium deposit also provides advantages to this sample geometry. Just as with the geometry proposed by Kempe et al., the larger area of the calcium deposit compared to other optical calcium tests allows for a longer period of observation of the lateral permeation, and therefore a more accurate measure of this permeation. The area of the deposit also has another important characteristic in that it allows for the measure of both the lateral and orthogonal permeation at the same time. Since calcium rapidly consumes water, the concentration of water at the surface of the calcium is very low. For the case of lateral permeation this leads to a visualization of the permeation front where the edge of the calcium deposit is the leading edge of the front. On the degraded side of the calcium, permeated water is present while on the metallic side of the calcium the concentration of laterally permeated water is negligible. This means that regions with metallic calcium have not been affected by lateral permeation. As a result, any measured changes in the calcium in the interior of the deposit cannot come from lateral permeation and must be due to orthogonal permeation. This makes possible the measurement of both the lateral and orthogonal permeation on a single sample as long as a measureable area of metallic calcium is present. The larger area of the calcium deposit is therefore extremely helpful as it creates a larger region of calcium in which to measure the orthogonal permeation.

The impetus for designing this sample geometry comes from the interfaces of glass substrates which are quite different than those seen in flexible encapsulation. As such, this geometry also recreates the same types of interfaces present in an actual device. This allows for an evaluation of the interfacial permeation as well. The exact method of how this is achieved is detailed in the section on “Modeling and Analysis”.

Limitations of Modified Sample Geometry

Though this sample geometry remedies several of the problems with other published geometries, it also creates several problems. If either the barrier film or the adhesive is a poor

barrier, it may only be possible to measure just the poor barrier material. If too much calcium is degraded too quickly from either lateral or orthogonal permeation, there may not be sufficient data to accurately characterize the other permeation pathway. For example a poor adhesive may cause most of the calcium to degrade rapidly leaving a very small region to measure orthogonal permeation over a very few time points, thus preventing accurate characterization of the barrier film. Conversely, a poor barrier film could lead to the degradation of too much calcium before the lateral permeation front has reached the edge of the calcium deposit and thus prevent the measurement of the lateral permeation. However, this type of problem is not common as poor barrier materials are rarely considered for use in encapsulating sensitive devices.

One reason why other lateral optical calcium tests use thick glass substrates is to prevent orthogonal permeation. This allows for the lateral permeation to be modeled using the assumptions that the calcium thickness is constant and that all water is due to lateral permeation. The change in calcium thickness due to orthogonal permeation can be accounted for relatively easily as described in the section on “Modeling and Analysis”. However, the change of the lateral concentration gradient due to moisture from orthogonal permeation would greatly complicate any quantitative model of lateral permeation. The concentration of water in the adhesive over regions of metallic calcium would remain quite low as it is consumed rapidly by the calcium, thus having only a small impact on the assumption that the water concentration at an infinite permeation distance, C_{∞} , is zero. The problem arises in the regions behind the permeation front. In this region the concentration of water will become elevated due to water vapor which has permeated across the barrier films. This causes a change in the lateral concentration gradient which can lead to error when calculating quantitative values for lateral permeation. While this can have a detrimental effect on quantitative values, the qualitative assessment of lateral permeation in the system actually becomes more applicable as a similar effect occurs in actual devices.

Modeling and Analysis

The previously described changes to the sample geometry necessitate modifications to how the data acquired from this test is analyzed. This section details the modeling and analysis used to treat the images acquired via this version of the lateral optical calcium test.

Image Analysis

The optical calcium test provides a series of images taken over time. Using this sample geometry, images such as the ones in Figure 3.2, are acquired which clearly show both the orthogonal and lateral permeation. The lighter color of the calcium deposit after humidity aging comes from a decrease in the thickness of the metallic calcium as it reacts with water vapor which has traversed the barrier films, i.e. orthogonally, to form transparent calcium hydroxide. On the other hand, the shrinking size of the metallic calcium is due to water vapor which has permeated laterally and fully degraded the edges of the calcium deposit.

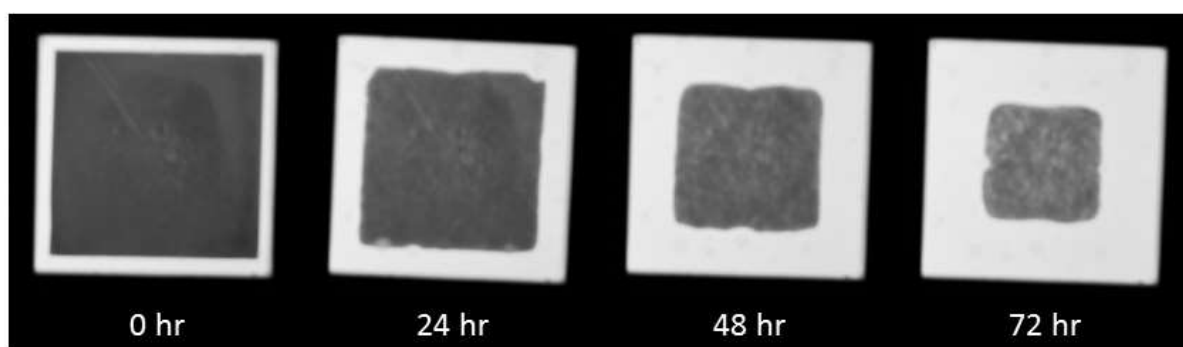


Figure 3.2 A selection of images from a modified optical calcium test is shown at various times of storage at 65°C and 85% relative humidity. The lightening shade of gray with time is due to a decrease in metallic calcium thickness from orthogonal permeation of water vapor. The decreasing size of the calcium deposit is due to degradation of the metallic calcium from laterally permeating water vapor.

The change in calcium thickness can be determined using a calibration curve. This curve, such as the one shown in Figure 3.3, is created by measuring the grayscale of calcium deposits of known thickness. These samples are created by evaporating calcium onto a clean, dry glass substrate inside an inert atmosphere glove box. The thickness of the calcium is determined using a quartz microbalance which is integrated into the evaporation chamber. A bead of a previously degassed, high-viscosity UV curing adhesive is then applied around the edge of the glass substrate. A second glass substrate with no calcium deposit is then applied on top and the adhesive is cured under a UV lamp to seal the calcium deposit in an inert atmosphere. The sample is then removed from the glove box and an image is captured using the optical calcium test apparatus described in Chapter 2. Care is taken to minimize the time between the evaporation of the calcium and imaging so as to limit any degradation of the calcium layer. A series of these images is then used to create a calibration curve of calcium thickness vs. grayscale which can be used to convert experimental grayscale values to a thickness of calcium. The range of calcium thicknesses which can be measured is determined by the brightness of the lamp and the sensitivity of the camera settings. Calcium deposits which

are too thick will register as completely black/opaque while deposits which are too thin appear as white/transparent. The validity of the calibration curve is verified before every test using a reference sample of tinted PET which is stored in the dark at room temperature. The thickness of calcium was then converted to a mass of permeated water via the stoichiometry of the reaction of calcium and water to form calcium hydroxide.

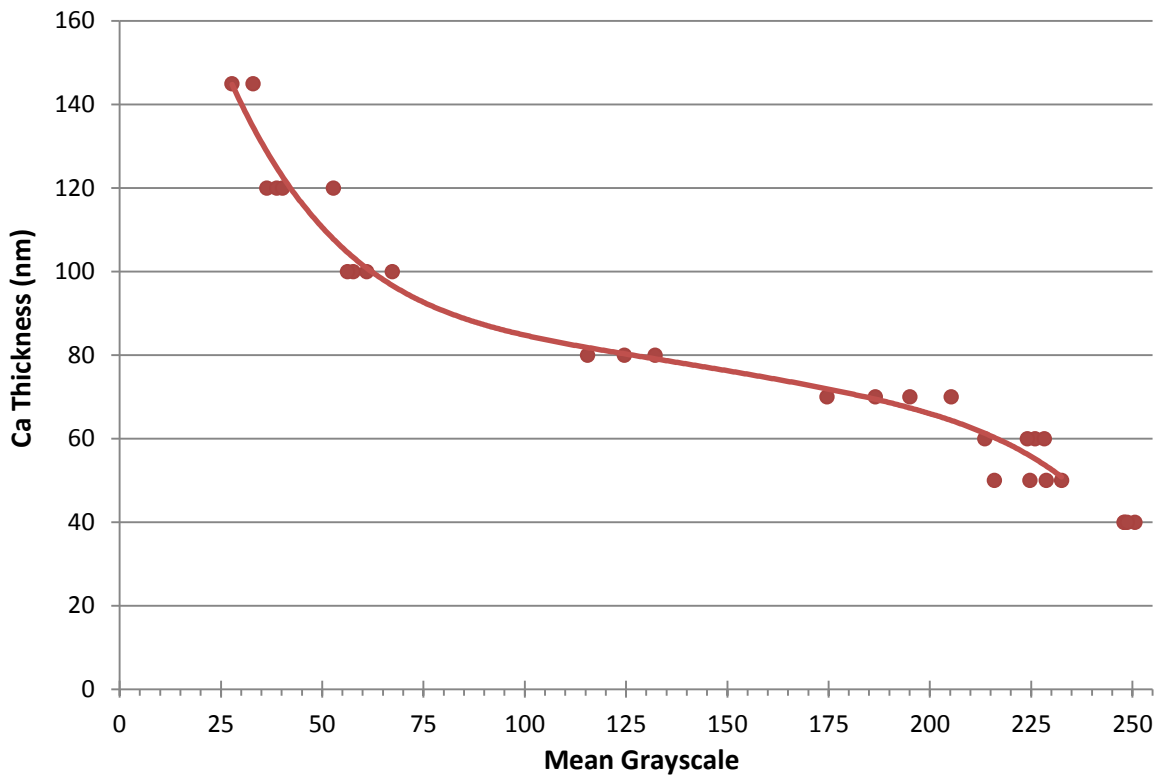


Figure 3.3 A calibration curve for the modified optical calcium test shown where 0 grayscale is completely black and 250 grayscale is completely white. Each point represents a calibration sample. The curve is a polynomial fit of the data. To avoid the increased potential for error as the curve steepens at the ends, samples were prepared to have calcium thicknesses which correspond to the central part of the curve.

Orthogonal Permeation

To measure the orthogonal permeation, the change in the grayscale values over time was used. To avoid the inclusion of degradation due to lateral permeation, a Central Zone was defined in the center of the calcium deposit. The boundaries of the Central Zone, such as the one seen in Figure 3.4, were defined so that no point within the zone was ever subjected to lateral permeation throughout the test. Using only the data from within the Central Zone, the orthogonal permeation can be found. A mean grayscale value for the Central Zone is calculated for each image and these values are used for all subsequent calculations.

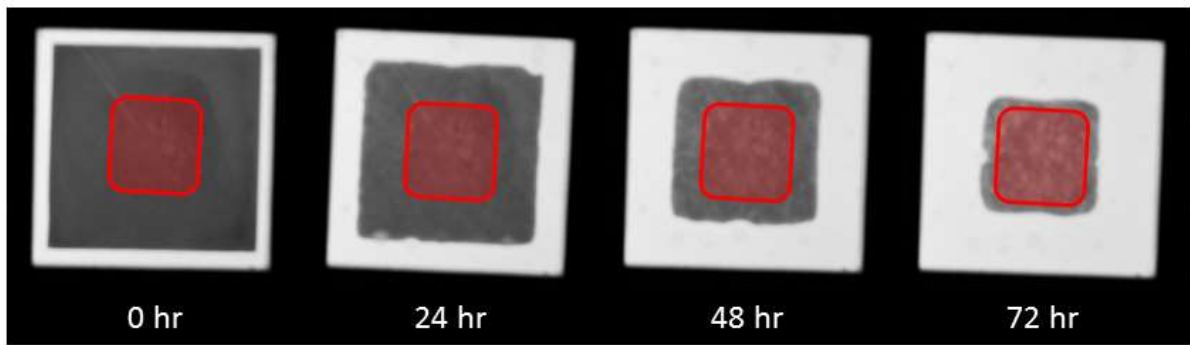


Figure 3.4 A selection of images from a modified optical calcium test is shown at various times of storage at 65°C and 85% relative humidity. The red region represents the Central Zone which remains unaffected by lateral permeation for the duration of the test.

By plotting the mass of permeated water in the Central Zone against time, such as in Figure 3.5, a curve typical for the permeation of a gas across a membrane is obtained. The elevated temperature and humidity used for testing generally led to a very short time lag and the rapid achievement of steady state permeation, which prohibited the presence of a clear transient region on the curve. The slope of the linear portion of the curve provides a mass transfer rate which is easily converted to a WVTR by dividing by the area of the Central Zone. It should be noted that the WVTR of the barrier film itself is one half the total orthogonal WVTR as there is one film on each side of the calcium probe.

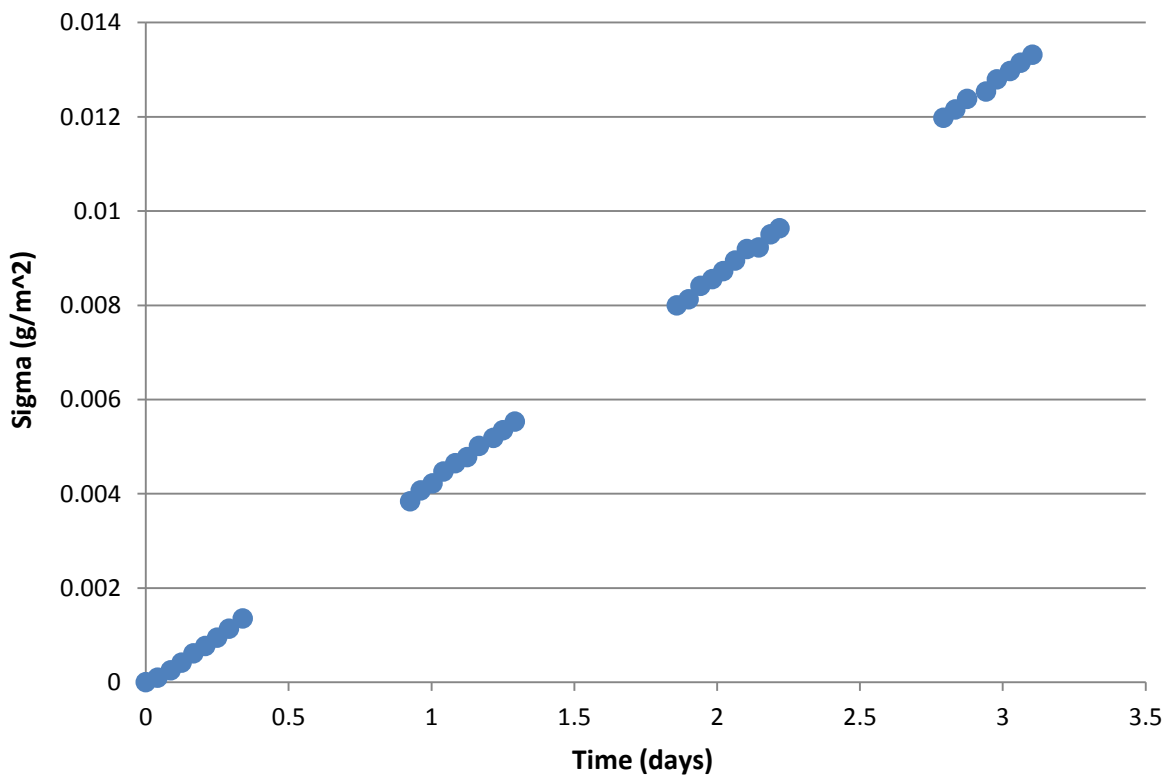


Figure 3.5 A plot of the permeated water vapor per unit area is shown as measured in the Central Zone of a modified optical calcium test sample. The barrier film used for this sample was 3M FTB3-50 and the storage conditions were

65°C and 85% relative humidity. The linear nature of the curve with no clear transient region indicates a very short time lag and the rapid establishment of steady state permeation.

The previously discussed modified sample geometry presents neither a completely extrinsic nor a completely intrinsic measurement. Extrinsic measures use gas spacers to disperse orthogonally permeated water vapor more evenly across the sample. However a gas spacer would also disperse lateral permeation thus making it impossible to distinguish between the two. However, the calcium in the modified sample geometry also is not evaporated directly onto an inorganic barrier as is done with intrinsic measures. Instead, a combination of both behaviors is seen with the character of each sample being highly dependent on the materials being tested and their exact architecture. While polymers are not nearly as effective at dispersing water vapor as a gas spacer, they will disperse the water vapor to some extent. While a detailed study is needed to confirm the exact mechanisms, the available evidence has led to the following hypothesis for the mechanisms.

As water vapor exits a defect in the final inorganic barrier layer of a barrier film and enters an adjoining polymer layer which contains no permeant, (i.e. an adhesive in contact with a calcium deposit), it has an equal probability to diffuse in all directions except those blocked by the inorganic barrier layer. If there is another such defect in close proximity, the diffusion fronts from each defect will merge. If there are many defects in close proximity a limiting case of a single 1-D diffusion front is achieved as shown in Figure 3.6a. This limiting case would lead to an extrinsic calcium test. On the other hand, if the defects are spaced far enough apart that they do not interact, an intrinsic calcium test would result. The distance between defects needed for mixing of the diffusion fronts is controlled by the distance between the final inorganic barrier layer and the calcium deposit which corresponds to the thickness of the polymer layers between the two. This effect is seen in Figure 3.6b. For smaller polymer thicknesses, the permeating water can reach the calcium before it reaches the permeation front of the closest defect. The limiting case of this would be direct contact between the calcium and inorganic barrier layer – the geometry used for intrinsic calcium tests. Conversely, larger polymer thicknesses make it more likely that permeating water will reach a neighboring defect's permeation front before reaching the calcium thus increasing the extrinsic behavior of the test. If the polymer thickness becomes very large in comparison to the spacing of the defects, a limiting case of fully extrinsic behavior is achieved. Therefore the degree of intrinsic and extrinsic behavior is expected to be a function of the defects in the final inorganic barrier layer, the thickness of any subsequent polymer layers in the barrier film, and the thickness of the adhesive.

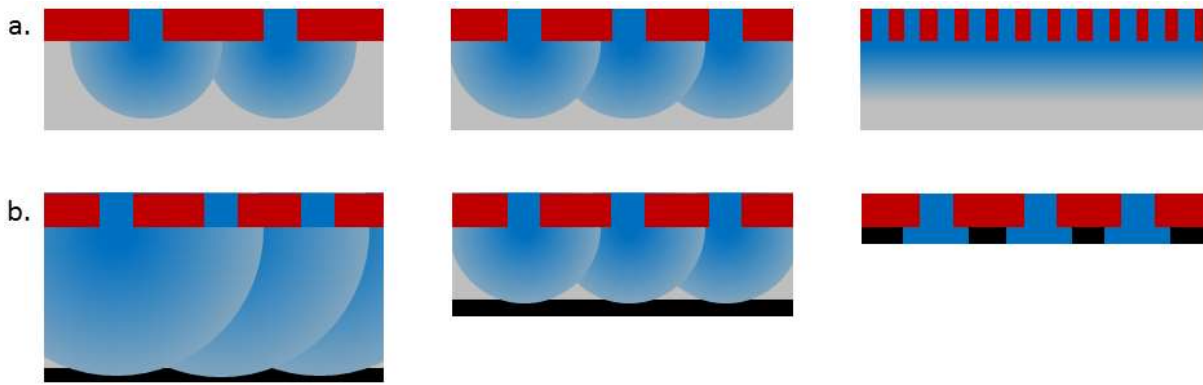


Figure 3.6 These cross-sectional diagrams show water vapor (blue) permeating through defects in an inorganic barrier layer (red) and into a polymer layer (gray). (a) As the spacing between defects becomes smaller, the permeation fronts become more convoluted until the limiting case of a single continuous permeation front is achieved. This means that low defect densities will have more intrinsic behavior in calcium tests while higher defect densities will lead to a more extrinsic calcium test. (b) At large polymer thicknesses the contact area of the water vapor with the calcium (black) is very large and thus more extrinsic in nature. As the polymer thickness decreases, the behavior becomes more intrinsic until the limiting case of a fully intrinsic calcium test is achieved.

The evidence for this hypothesis is not particularly strong at this time as no tests have been performed using barriers with known defect sizes and densities. Additionally, it is difficult to establish accurate ratios of extrinsic-to-intrinsic behavior. This determination is currently a judgment of the researcher based on naked eye observation. This has led to only three categories of behavior: highly extrinsic, mixed, and highly intrinsic. It should be noted that all three categories are a mix of the two behaviors. Many tests with widely varying adhesive thicknesses have been performed using the same barrier film (Oike VX 25T-2PO), however it has proven difficult to draw any conclusions from this data. This is mainly due to the large variation in the measured WVTR of the barrier film which indicates a large variance in the defects of the inorganic barrier layers in the production of the film. The best evidence for this hypothesis currently comes from the comparison of the Oike VX 25T-2PO barrier film to the 3M FTB3-50a barrier film. The 3M film's final barrier layer has a polymer coating of less than 2 microns and uses an adhesive layer of only 25 μ m thickness. This is quite small compared to the Oike film which has 25 μ m of PET over the final barrier layer and can be coated to high adhesive thicknesses if desired. A comparison of typical samples for each film is shown in Figure 3.7 which clearly shows the increased intrinsic behavior of the 3M film in agreement with the proposed hypothesis.

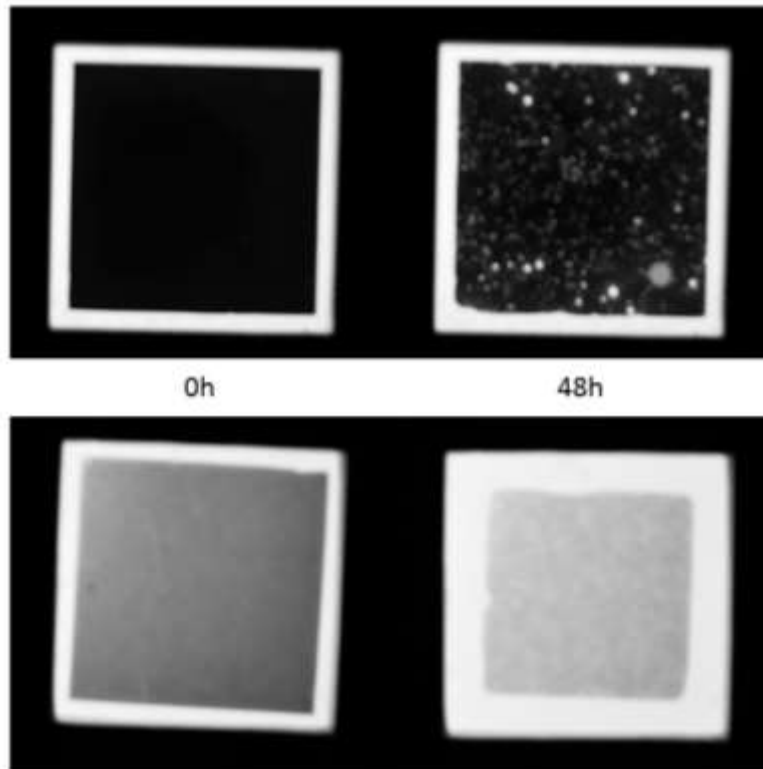


Figure 3.7 Calcium test images showing (top) 3M FTB3-50a with heavily intrinsic behavior and (bottom) Oike VX 25T-2PO with a homemade UV curing adhesive, F#18, with heavily extrinsic behavior. The two barrier films have similar WVTR values but the 3M sample has only a $2\mu\text{m}$ polymer coating and a $25\mu\text{m}$ thick adhesive between the final inorganic barrier and the calcium probe. On the other hand the Oike sample has $25\mu\text{m}$ of PET and $165\mu\text{m}$ of adhesive between the final barrier and the calcium probe.

There is one final factor which can affect the ratio of extrinsic-to-intrinsic behavior: time. The permeation fronts emanating from each defect expand as more water vapor traverses the defect. Therefore as time increases, the permeation fronts mix more and more producing a more extrinsic behavior as time increases as seen in Figure 3.8. This is particularly hard to visualize in practice though, as the relative differences in calcium thickness become easier to see as the total thickness decreases.

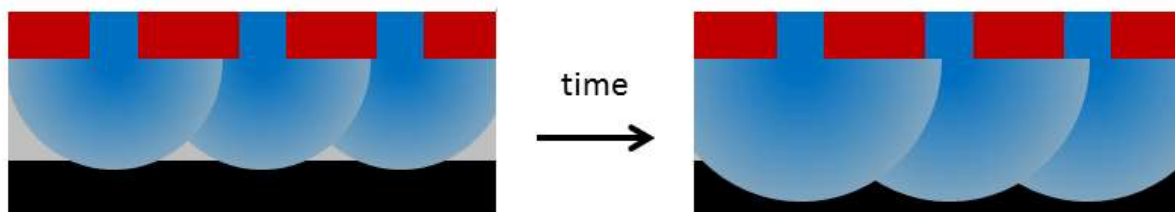


Figure 3.8 These cross-sectional diagrams show water vapor (blue) permeating through defects in an inorganic barrier layer (red) and into a polymer layer (gray). Early in a calcium test, the contact of water vapor with the calcium (black) is limited to small spots, therefore producing intrinsic behavior. As time goes on and the permeation fronts grow and mix with those of neighboring defects, nearly all of the calcium is in contact with water vapor resulting in a more extrinsic behavior later in the test.

Lateral Permeation Measurement

The first step to analyze the lateral permeation is to isolate it from the orthogonal permeation. This can be achieved through the use of a background subtraction of the orthogonal permeation as measured in the Central Zone. To perform this calculation, a Global Zone is defined which corresponds to the size of the calcium deposit at the start of the test. An average grayscale of the Global Zone is calculated for each image and then converted to a mass of water. Using the orthogonal permeation rate previously calculated for the Central Zone, the amount of water which would permeate orthogonally in the Global Zone is calculated and subtracted from the total measured amount of permeated water in the Global Zone for each image. The difference can be attributed to lateral permeation. Because the mass of water calculated for each image is based on the amount of calcium degraded, the changing thickness of the calcium deposit does not affect the calculation of the lateral permeation.

However, the calculated value of the mass of permeated water grossly underestimates the actual amount of water which has permeated into the sample laterally. This is due to the presence of water vapor in the regions behind the edge of the permeation front. This region has a concentration gradient with higher water vapor concentrations closer to the edge of the sample. Using simulations, Michels et al. have proposed that the exact shape of this concentration gradient is dependent on several factors and can vary from sample to sample.⁶⁹ For this reason it is impossible to estimate the amount of water in the region behind the edge of the permeation front unless the calcium test data is combined with other permeation testing and computer simulations. Although the value of laterally permeated water calculated from the calcium test does not provide an accurate quantitative value, it is still quite useful for relative comparisons of different adhesives, edge seals and adhesive-to-barrier film interfaces.

When the mass of laterally permeated water is plotted against time, three unique regions are visible as seen in Figure 3.8. At the beginning in Region I, little to no degradation is observed as the leading edge of the permeation front has not reached the edge of the calcium. In Region II, the curve then becomes fairly linear, though not perfectly so. The curve of both the Global Zone and lateral permeation then begin to flatten and obtain a constant value in Region III. It is not uncommon for individual samples to actually display an increase in the amount of calcium at the end of the test even though this should not be possible. As the calcium degrades, often small bubbles can form which eventually fill with water and expand as the concentration of water vapor in the sample increases. These regions of water are not completely

transparent and refract light, often giving them a grayscale value in transmission measurements if they become large enough. At the end of the test, little metallic calcium remains and these water filled regions can be quite large, thus creating a non-negligible effect on the average grayscale of the Global Zone. This is seen as the apparent darkening of the sample and thus the flattening of the water permeation curves. Therefore, all calculations for lateral permeation are limited to the region after the permeation front has reached the edge of the calcium but before 60% of the calcium deposit has been degraded, i.e. Region II.

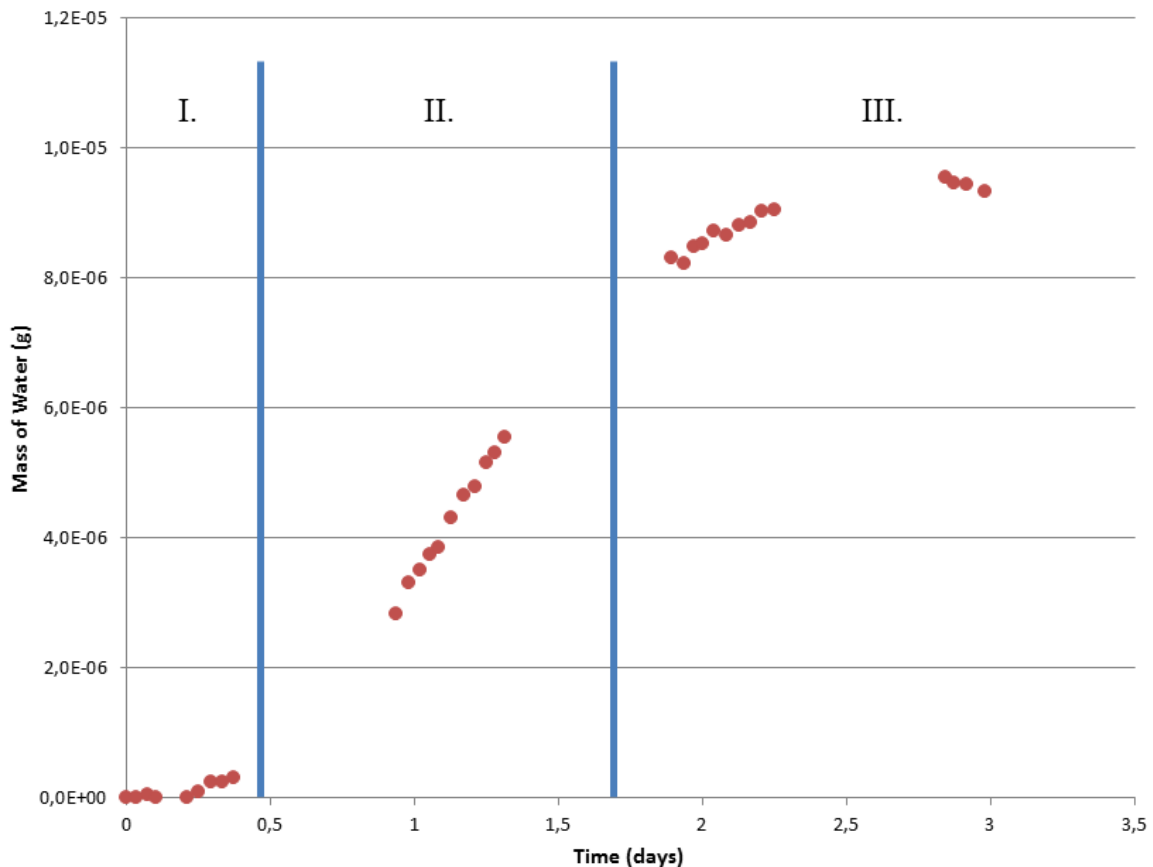


Figure 3.8 The cumulative lateral permeation as measured by the modified optical calcium test is shown for a typical sample (Oike VX 25T-2PO barrier films; 145 μ m of Sartomer S3 adhesive; 65°C; 85%RH). Three distinct regions are visible. Region I shows little permeation as the permeation front has yet to reach the edge of the calcium deposit and Region III is invalid due to testing artifacts. Therefore only Region II is used for calculations.

Within Region II of the lateral permeation curve, the experimental data is well modeled using a linear function. While a square root of time dependence is expected for this transient state permeation, it is not observed.^{52,66} The reason for this is not known but could come from the change in calcium thickness due to orthogonal permeation, the effect of non-Fickian interfacial permeation or other unknown causes. Regardless of the cause, a linear function is used to model the lateral permeation observed during the test as it provides a relatively good fit. This also allows for the calculation of an apparent permeation rate using the slope of the

curve. In addition to the potential non-linearity of the permeation, this value does not include the water vapor which is in the regions with no metallic calcium. Therefore it should not be confused with a steady state permeation rate. However, this apparent permeation rate does allow for an estimation of the water which has entered the sample laterally.

Interfacial Permeation

Using the calculated values for lateral permeation it is possible to separate the relative effects of the two major pathways for later permeation: permeation in the bulk adhesive and permeation along the interface and/or interlayer. For clarity, the term “interface” will heretofore be used to refer to both the interface (the surface where two materials meet) and the interlayer (the region in each material immediately adjacent to the interface where the structure is modified due to the presence of the interface). Though their mechanisms of permeation are different, as discussed in Chapter 1, it is often difficult to differentiate between the two, even with an intensive failure analysis after testing. Therefore the two will be treated as a single permeation pathway for the purposes of analysis.

To separate the relative permeation in the bulk adhesive and the interface using the calculated values of lateral permeation, the following three assumptions have been made:

1. Permeation in the bulk adhesive is not affected by changes in the interface.
2. Permeation along the interface is not affected by changes in the adhesive thickness.
3. Permeation in the bulk adhesive and along the interface are independent of each other.

By assuming that the two pathways are independent of each other, the total lateral permeation becomes a summation of the two pathways as seen in Equation 3.1.

$$\text{Equation 3.1} \quad \textit{lateral permeation} = \textit{bulk permeation} + \textit{interfacial permeation}$$

The amount of water which permeates through the bulk adhesive is dependent on the cross-sectional area of the adhesive, which for this sample geometry is the product of the perimeter and the adhesive thickness. Alternatively the interface is effectively 2-D in nature as its thickness is negligibly small. Therefore it is dependent only on the exposed perimeter. This leads to the modification of Equation 3.1 to create Equation 3.2 where Q_{lat} is the mass of laterally permeated water, p is the perimeter, h_{adh} is the thickness of the adhesive, $WVTR_{ap-bulk}$ is the apparent water vapor transmission rate of the bulk adhesive in units of mass per time per area, and \dot{P}_{inf} is the interfacial permeation rate in units of mass per time per length. It should be

noted that the apparent $WVTR_{ap-bulk}$ is not a steady state WVTR but is still a material property which is constant for the material at the same temperature and humidity.

$$\text{Equation 3.2} \quad \frac{\partial Q_{lat}}{\partial t} = p h_{adh} WVTR_{ap-bulk} + 2 p \dot{P}_{intf}$$

Experimentally, all values other than $WVTR_{ap-bulk}$ and \dot{P}_{intf} can be measured for a single sample. Using the assumption that changing the adhesive thickness will not impact the interfacial permeation, two samples with the same adhesive and interfaces but different adhesive thicknesses would provide a system of two equations with two unknowns, thus allowing for the calculation of $WVTR_{ap-bulk}$ and \dot{P}_{intf} . This means that the relative contributions of the bulk adhesive and the interface to the lateral permeation can be calculated. As previously discussed for the apparent lateral permeation rate, $WVTR_{ap-bulk}$ and \dot{P}_{intf} are not accurate values and underestimate the amount of permeation. They do, however, provide the ability to elucidate information about the relative contributions of the bulk adhesive and the interface to the lateral permeation. This ability allows for a better understanding of where the weak points in the encapsulation lie and whether changing the adhesive thickness or surface would be useful for a particular combination of barrier film and adhesive.

Identification of Permeation Pathways Using Reference Materials

Design of Experiment

The previously described modified version of the optical calcium test was used to elucidate the relative importance of the different permeation pathways present in encapsulated OPVs. This study was performed using reference materials which are commercially available. The barrier film used for all tests was Oike VX 25T-2PO. The adhesive was the pressure sensitive film 3M 467MP or 468MP, which are the same adhesive with thicknesses of 50 μ m and 125 μ m respectively. All samples were encapsulated between two adhesive coated barrier films with the lamination carried out inside an inert atmosphere glove box using a weighted hand roller. This created a total adhesive thickness of 100 μ m and 250 μ m for the respective adhesives. Please note that all data shown in this study has been adjusted so that the time is zero for the first measurement after the lateral permeation front had arrived at the edge of the calcium.

Modified optical calcium tests were performed on both adhesives with the same type of barrier film and the same surface treatment in order to see the effect of adhesive thickness on the permeation of water vapor. This also allowed for the use of the previously described analysis to estimate the relative contributions of orthogonal, bulk adhesive and interfacial permeation. Tests were also performed using different surface treatments of the barrier film in order to vary the interface and limit the permeation through this pathway. The two surface treatments used were a solvent cleaning in isopropyl alcohol (IPA) and a corona treatment.

Orthogonal vs. Lateral Permeation

The orthogonal permeation per unit area for all samples is shown in Figure 3.9. The average WVTR of the barrier film for 467MP IPA cleaned samples was determined to be 3.89×10^{-3} g/m²/day; 2.76×10^{-3} g/m²/day for 468MP IPA cleaned samples; and 3.98×10^{-3} g/m²/day for the 467MP corona treated samples. This discrepancy in measured WVTR is likely due to variations in the fabrication and handling of the barrier films as this level of variance was seen quite often when using this barrier film.

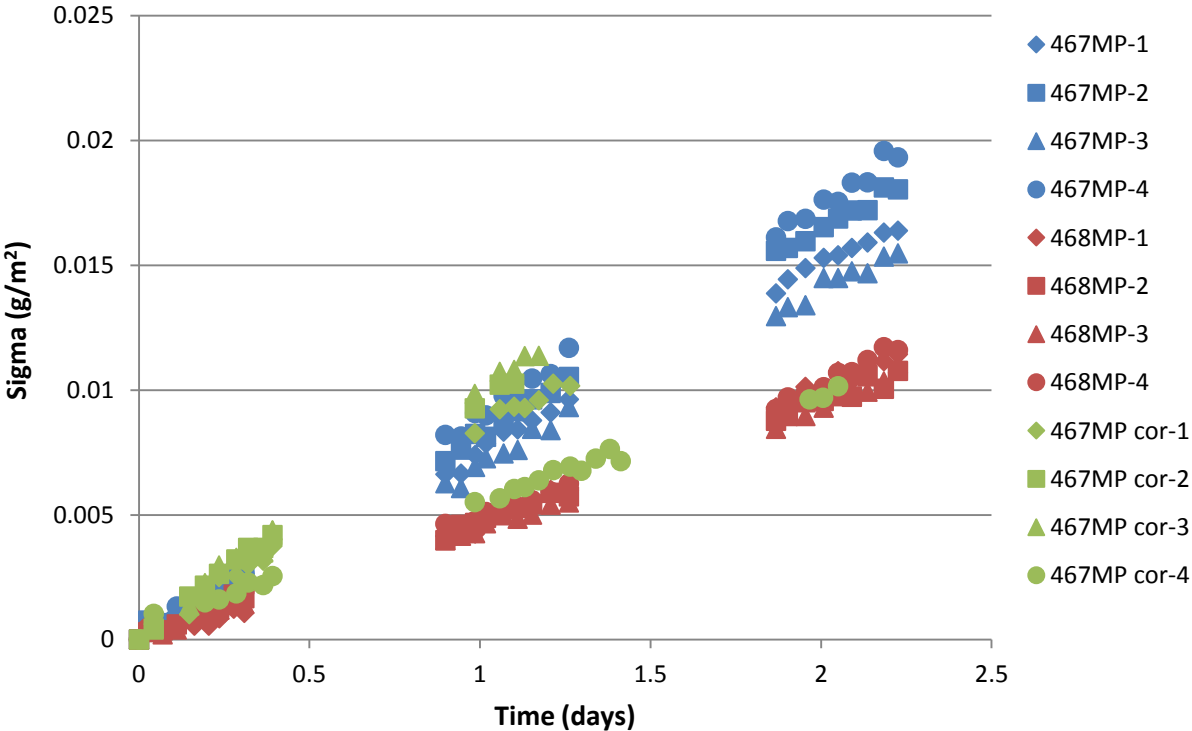


Figure 3.9 The cumulative water vapor permeation as measured by the modified optical calcium test is shown in units of mass of permeated water per unit area. All measures were in the Central Zone of the respective samples. The time axis has been adjusted so that 0 corresponds to the first point after residual water in the sample had been consumed. All curves are linear indicating steady state permeation.

A comparison of the percentages of the calcium deposit degraded by each permeation pathway for the IPA cleaned samples is shown in Table 3.1. For a 45mm X 45mm sample, the lateral permeation has a very strong impact on the overall permeation accounting for 46% and 62% of the calcium degradation for 467MP and 468MP respectively. This exemplifies the importance of the lateral permeation when designing the encapsulation of devices. With a poor choice of adhesive or poor encapsulation design, the lateral permeation can easily become the more dominant permeation pathway for water vapor. Large area OPV would be less susceptible to this problem as a larger proportion of the device is further from the edges. Smaller devices would be highly susceptible though as the distance to the edge of the device is never large. This is particularly applicable to modules designed for niche applications such as backpacks, clothing and decorative pieces along with OLED applications for handheld devices and wearable technologies.

Table 3.1 The average percentages of the total calcium degradation measured during modified optical calcium tests of samples using IPA cleaned barrier films are shown for each permeation pathway.

Adhesive	Percentage of total calcium degradation			
	Orthogonal	Total Lateral	Bulk Adhesive	Interface
468MP	38%	62%	27%	35%
467MP	54%	46%	11%	35%

Influence of Adhesive Thickness

The lateral permeation for each adhesive thickness on IPA cleaned barrier films is shown in Figure 3.10. It can be seen that the thicker 468MP samples had more lateral permeation than the thinner 467MP samples with $p=0.0012$ as calculated from an independent samples t-test. A reduction in the exposed surface area of the adhesive is expected to limit permeation in the bulk adhesive as can be seen in Equation 3.2 (linear dependence on h_{adh}). This is an important conclusion as it directly influences the design of OPV encapsulation. The experimental data from this study indicates that a thinner adhesive layer is indeed preferred for minimizing permeation. This information must be taken into account when weighing the benefits of a thinner adhesive layer (less permeation, thinner final product, less material used) against the benefits of a thicker adhesive layer (better adhesion strength, easier to avoid voids around the edges of the device).

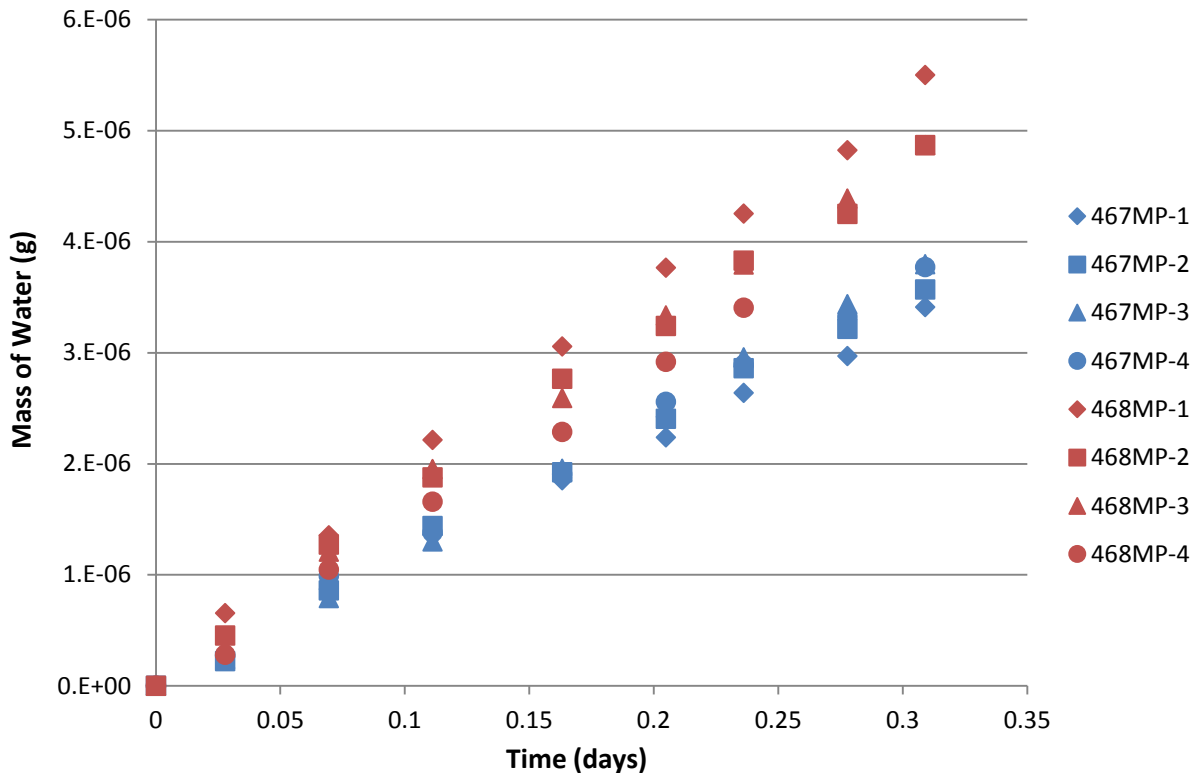


Figure 3.10 The cumulative lateral permeation as measured by the modified optical calcium test is shown for samples with IPA washed barrier films. The time axis has been adjusted so that 0 corresponds to the first point after the permeation front had reached the edge of the calcium deposit. The slopes of these curves show thinner adhesive layer of 467MP had less lateral permeation than the thicker 468MP adhesive with $p=0.0012$ as calculated from an independent samples t-test.

Influence of Surface Treatment

Referring back to Table 3.1, it is important to note the respective percentages of the calcium degradation due to the bulk adhesive and the interface. The model shown in Equation 3.2 suggests that the interfacial permeation is higher than the permeation in the bulk adhesive for both IPA cleaned samples. The plot in Figure 3.11, which shows the lateral permeation as a function of adhesive thickness, also suggests a large amount of interfacial permeation. If all of the permeation were in the bulk adhesive, one would expect a linear dependence on adhesive thickness with a fit passing through the origin (zero thickness, zero permeation). However, this is not the case as a linear fit of the IPA cleaned samples predicts significant permeation at an adhesive thickness of zero.

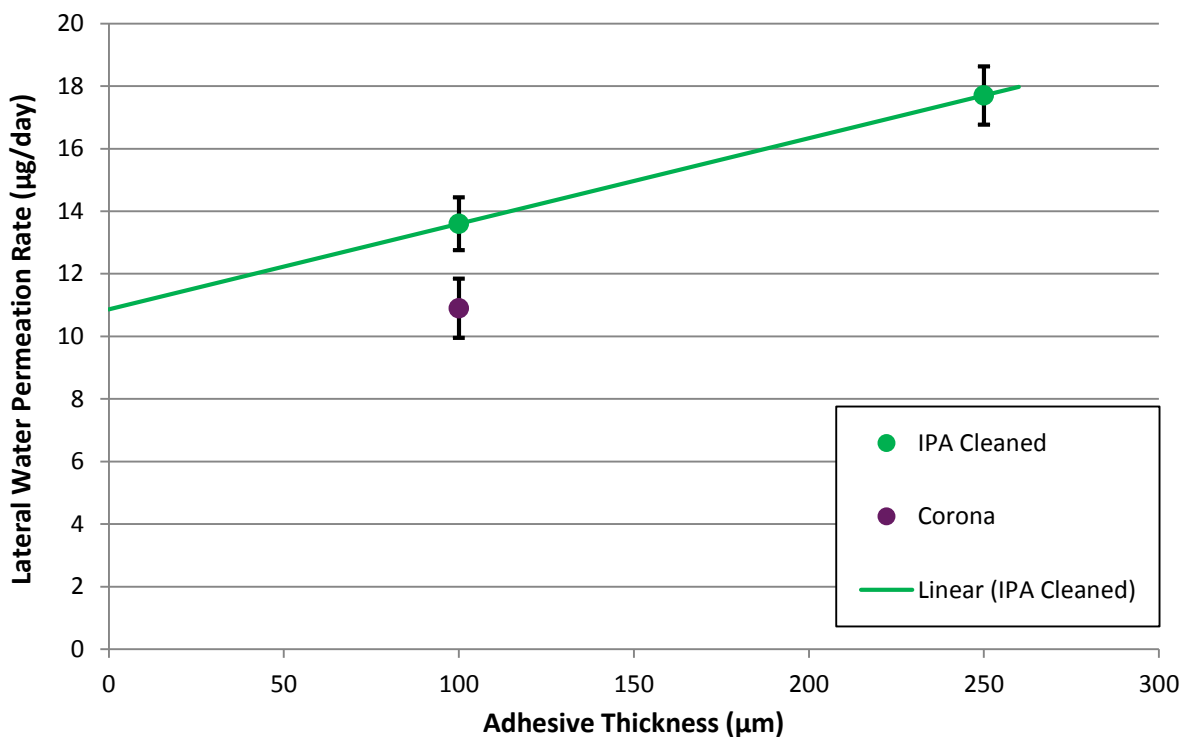


Figure 3.11 A plot of the lateral permeation rate as measured by the modified optical calcium test is shown for 467MP/468MP. All values have been normalized to 45mm X 45mm calcium deposits to adjust for slight differences between samples. Error bars represent ± 1 standard deviation.

The large amount of interfacial permeation was surprising for this adhesive as it is not specifically designed for good bulk barrier properties but has good adhesion to the barrier film. To address the problem of interfacial permeation, a corona treatment of the surface was tested as a method to improve the interface. Corona treatments use a plasma of ambient air at room pressure to modify the chemistry of a surface and increase its surface energy. Corona treatments of barrier films were performed just prior to the application of the adhesive and showed a stronger interface with the adhesive as evidenced by the adhesion tests shown in Figure 3.12.

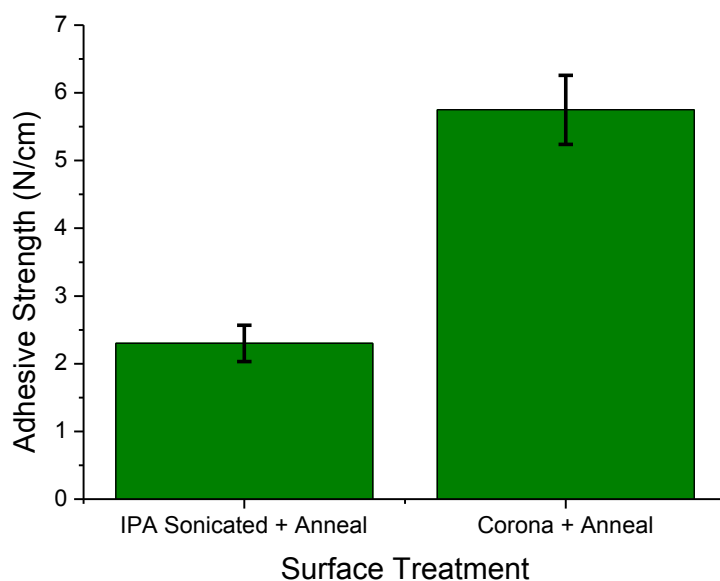


Figure 3.12 The T-peel adhesion strength for 467MP on Oike VX 25T-2PO barrier films is shown for two different surface treatments. The anneal used for all samples was identical to the vacuum degassing process used for calcium test samples in order to simulate as closely as possible the conditions of the calcium test. Error bars represent ± 1 standard deviation.

Calcium test samples were prepared using 467MP as the adhesive on corona treated barrier films and the results of the lateral permeation are shown in Figure 3.13. This figure shows that samples which were corona treated presented lower levels of overall lateral permeation with $p=0.016$ as calculated from an independent samples t-test. Using the previously calculated values of apparent bulk adhesive WVTR and interfacial permeation rate, a value for the interfacial permeation rate of the corona treated samples was calculated and found to be $1.84 \times 10^{-5} \text{g/m/day}$ compared to $2.86 \times 10^{-5} \text{g/m/day}$ for IPA cleaned samples, a reduction of 38%. Table 3.1 is reproduced with the addition of the corona treated samples in Table 3.2. These results imply that the interface was indeed a source of water vapor permeation as modification of only the interface changed the lateral permeation. It also provides evidence that corona treatment is an effective technique for the reduction of water vapor permeation.

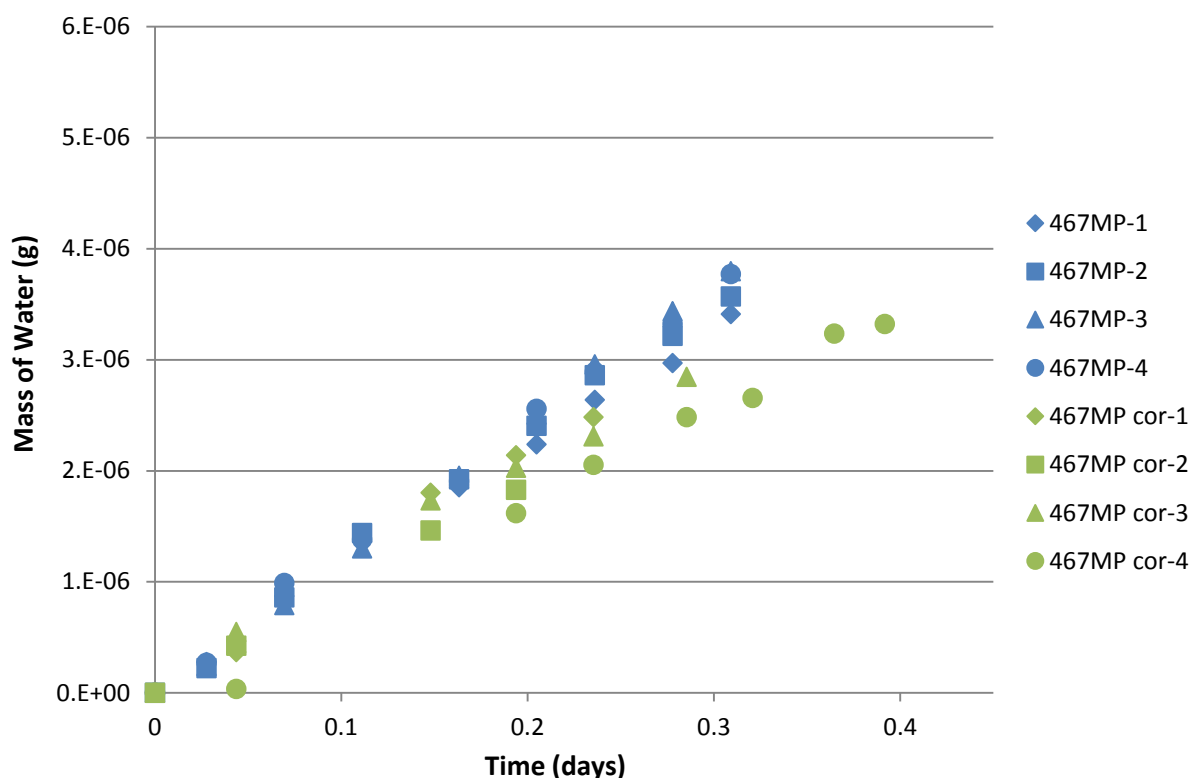


Figure 3.12 The cumulative lateral permeation as measured by the modified optical calcium test is shown for samples with 3M 467MP as the adhesive on both IPA cleaned (blue) and corona treated (green) barrier films. The time axis has been adjusted so that 0 corresponds to the first point after the permeation front had reached the edge of the calcium deposit. The slopes of these curves show corona treated samples had less lateral permeation with $p=0.016$ as calculated from an independent samples t-test.

Table 3.2 The average percentages of the total calcium degradation measured during modified optical calcium tests of samples using either IPA cleaned (IPA) or corona treated (Cor) barrier films are shown for each permeation pathway.

Sample	Percentage of total calcium degradation			
	Orthogonal	Total Lateral	Bulk Adhesive	Interface
468MP IPA	38%	62%	27%	35%
467MP IPA	54%	46%	11%	35%
467MP Cor	57%	43%	30%	13%

Conclusions

The modified optical calcium test for the measure of water vapor permeation presented in this chapter addresses several of the problems associated with other versions of the optical test including simulation of actual flexible devices, interfacial permeation and measurement of multiple permeation pathways. By using a sample geometry which closely mimics that of a flexible device, a more analogous measurement is achieved which will display the same types

of permeation and interactions seen in actual devices. The sample geometry, which uses a calcium deposit laminated between two flexible barrier films using an adhesive, alleviates the problem of other lateral calcium tests which do not have the same interfaces as a device. This provides information on the interfacial permeation for specific adhesive-barrier film pairs. The large calcium deposit also allows for the measurement of both the orthogonal and lateral permeation for the same sample. While this version of the optical test does not provide accurate quantitative values for lateral permeation, it does provide the novel ability to compare the relative amounts of permeation between barrier films, the bulk adhesive and the interfaces.

This ability to compare permeation pathways was exploited using commercially available reference materials in order to determine the relative impact of each permeation pathway. Tests showed that for small devices, similar in size to the calcium test samples, the lateral permeation can account for more than half of the total calcium degradation. This highlights the importance of limiting lateral permeation in encapsulation schemes. The data also showed a higher rate of lateral permeation for a high adhesive thickness, thus providing encapsulation design guidelines for the effect of changing the adhesive thickness. The tests also showed that interfacial permeation for this system was a significant permeation pathway for water vapor. This was confirmed by the decreased lateral permeation seen for samples whose surface had been modified by corona treatment. The use of a corona treatment, which greatly improves the adhesion, was shown to be effective in limiting the interfacial permeation for this system of materials.

Chapter 4: Adhesive Characterization

Introduction

There are many factors which must be considered when selecting an adhesive for use in the flexible encapsulation of OPVs. They must be flexible enough to maintain the advantages of flexible solar panels, including roll-to-roll processing. They must be transparent as any loss of light arriving at the active layer directly results in a loss of power conversion efficiency. They must not interact in a harmful manner with any component of the OPV as this could degrade the performance. They must have good adhesion to flexible barrier films in order to provide both mechanical stability and to create an interface which is less susceptible to permeation. And finally, they must be good barriers to oxygen and water as the main goal of encapsulation materials is to protect the device.

As can be seen, there are indeed many factors which need to be addressed when considering an adhesive for use in encapsulating OPV. There is one additional requirement too as they must also be stable enough to maintain these properties over the course of the device's lifetime. This last requirement will be discussed in detail later in Chapter 7. In this current chapter though, the characterization of several adhesives is presented to evaluate the suitability of each adhesive for use in OPV encapsulation. The adhesives evaluated fall into two main categories: pressure sensitive adhesives (PSA) based on block co-polymers and UV curing materials based on acrylate chemistries. The materials were first evaluated in terms of their formulation and structure, with the highest risk liquid materials also tested for compatibility. They were then subjected to various testing to elucidate their physical properties including rigidity, adhesion, optical transparency and water vapor permeation. Both PSAs and UV curing acrylates are presented here and compared to each other and reference materials to provide an overview of why these materials are good candidates for OPV encapsulation.

MAM PSAs

MAM PSAs are a newer class of adhesives which have several advantages compared to traditional PSAs. The MAM in their name refers to their triblock co-polymer structure of methyl methacrylate – *block* – n-butyl acrylate – *block* – methyl methacrylate while the PSA, as previously mentioned, stands for pressure sensitive adhesive. Their advantages compared to other PSAs come from their structure and several different ratios of the blocks were evaluated.

Structure of MAM Block Co-Polymers

Block co-polymers have polymer chains with at least two distinct regions of the backbone consisting of different chemistries. MAM co-polymers have an A-B-A structure which is represented visually in Figure 4.1. The covalent link between two otherwise different polymers gives these materials their unique properties. Since most polymers are immiscible with each other, the different blocks of the co-polymer attempt to phase separate. However, the covalent link between the blocks limits the length scale of this separation and leads to the formation of nanoscale morphologies consisting of domains of the different polymers. Longer chains, i.e. higher molecular weights, will lead to larger domain sizes. Adjusting the ratios of the blocks can also have an effect on the domain size but can additionally cause changes to the morphology as different configurations will be favored for different volume ratios of the blocks. For MAM co-polymers, the large difference in mechanical properties between the blocks is quite important. At room temperature, PBA is very soft and has a strong pressure sensitive adhesive character whereas PMMA is below its glass transition temperature (T_g) and relatively rigid. For MAM co-polymers with a majority of PBA, this leads to a pressure sensitive adhesive with rigid domains of PMMA that mechanically act in a manner similar to cross-links, thus changing the mechanical properties of the adhesive. Unlike thermosetting polymers with covalent cross-links, MAM co-polymers remain fully thermoplastic and capable of being fully dissolved in organic solvents, thus making their available processing techniques much more varied. Another important aspect of the rigid domains acting as cross-links is that it allows for changes in the block ratios to control the mechanical properties of the adhesive without making large changes to the chemical nature of the adhesive.

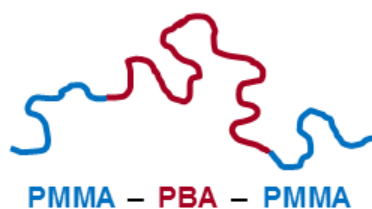


Figure 4.1 A diagram of a hypothetical MAM block co-polymer is shown with poly(methyl methacrylate) blocks in blue and poly(n-butyl acrylate) in red.

The MAM co-polymers used in this thesis were Nanostrength[®] adhesives provided by Arkema Group. These adhesives are all majority PBA and have the naming convention of MXX where XX represents the percentage of PBA in each polymer chain. AFM images of bulk deposits of the three grades of these adhesives used in this thesis can be seen in Figure 4.2. While further characterization is needed to definitively identify the morphologies, all of the adhesives except M65 show structures in AFM which are consistent with spherical micelles. M65 however appears to be consistent with a worm-like morphology. This is more difficult to identify using only AFM images as horizontally aligned hexagonal cylinders and lamellar sheets can also present a similar pattern. However, after several images in different regions, the lack of any edge-on cylinders or large domain spacings from viewing lamellar sheets at an angle makes worm-like the more likely cause of this pattern. The worm-like morphology, which show only short range order, could be representative of a thermodynamically unstable structure which was not allowed enough time to fully organize. Alternatively, it could also be thermodynamically stable with the morphology being due to the relatively large polydispersity of the polymer.

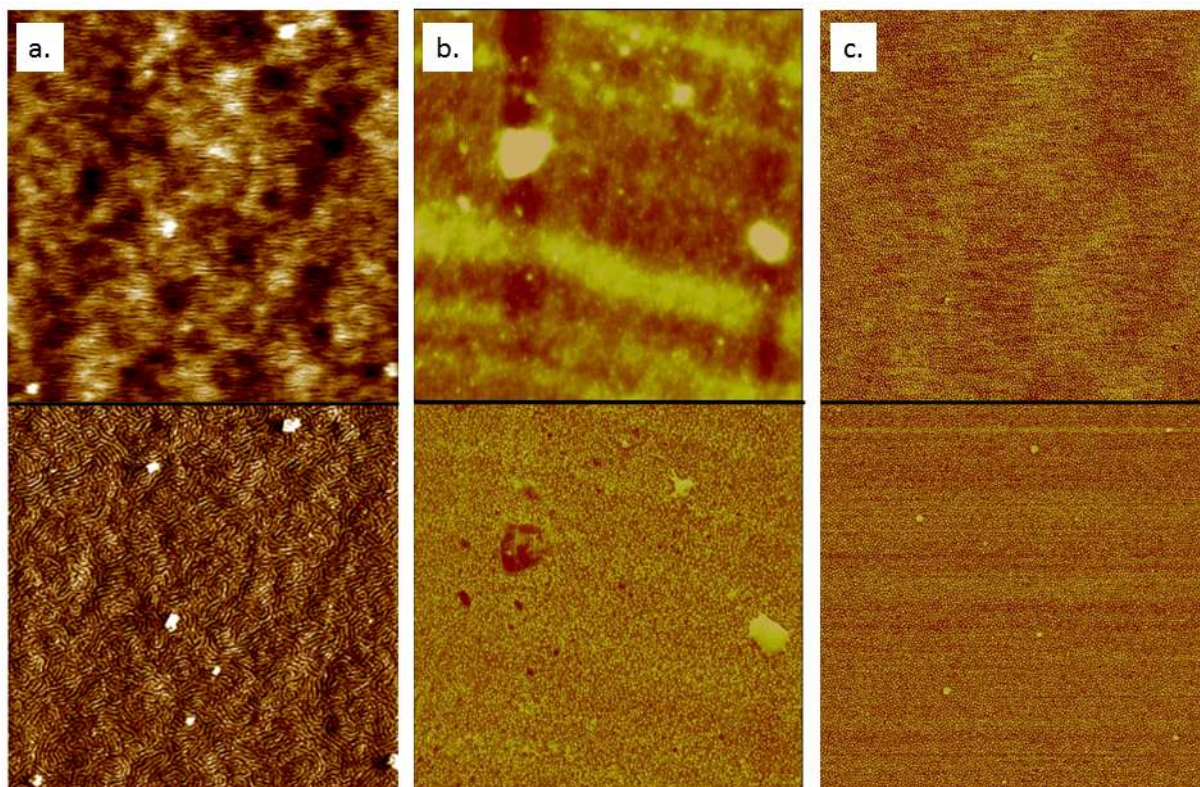


Figure 4.2 AFM images taken in tapping mode of (a) M65, (b) M75 and (c) M85 are shown in both (top) height and (bottom) phase. All images show an area of $5\mu\text{m} \times 5\mu\text{m}$. The images for M65 and M85 were taken with the aid of Isabel Fraga Dominguez at the Institut de Chimie de Clermont-Ferrand while the images of M75 were provided by Arkema. It can be seen that M75 and M85 have spheres of rigid PMMA in a soft matrix of PBA. The decreased PMMA content in M85 leads to smaller PMMA domains. M65 shows a much different morphology which is consistent with a worm-like structure.

Thermo-Mechanical and Optical Properties

The T_g of each adhesive was found via differential scanning calorimetry (DSC) and the results are shown in Table 4.1. As the materials have two distinct polymer domains, two glass transitions were observed. The low temperature T_g corresponds to the soft PBA block (bulk T_g of -42°C ¹⁷⁹) and was very similar for all three adhesives. M65 and M75 also displayed a second higher temperature T_g which corresponds to the rigid PMMA block (bulk T_g of 105°C ⁷⁰). This higher temperature T_g was not observed for M85 most likely due to the relatively small amount of PMMA not producing a strong enough endothermic signal to be measured. The measurement of M85 was repeated by Dr. Manuel Hidalgo on a different DSC instrument at Arkema and similar results were found. All samples also showed an endothermic transition in the range of $60\text{-}75^\circ\text{C}$ during the first heating run which was no longer present in the second heating run. This was attributed to the evaporation of residual solvent dissolved in the polymer.

Table 4.1 The glass transition temperatures for the MAM Nanostrength[®] adhesives are shown for both DSC and DMTA methods. DSC used a 10°C/min ramp rate while DMTA was performed at 3°C/min, 1Hz and 0.1% strain. M85 results in parentheses were performed at Arkema.

Adhesive	DSC Lower T _g (PBA)	DMTA Lower T _g (PBA)	DSC Upper T _g (PMMA)
M65	-48°C	-37°C	98°C
M75	-44°C	-36°C	92°C
M85	-44°C -47°C, Arkema)	-39°C	Not detected (Not detected, Arkema)

The T_g was also calculated from the peak of the loss modulus curve in tensile dynamic mechanical thermal analysis (DMTA). Only the low temperature T_g of the PBA block was visible in this method. These measures were slightly elevated in comparison to DSC measures due to the strain rate effects of cyclic mechanical testing compared to the extremely low frequency of DSC where no load is applied. DMTA also showed that all three polymers had similar T_g values just as was seen in DSC. DMTA was also used to evaluate the storage and loss moduli of the adhesives with results shown in Figure 4.3. M85 was clearly the softest of the materials which was in-line with the observations of handling the material at room temperature. In fact, the polymer was too soft and surpassed the limit of detection of the apparatus during testing before reaching the desired temperature of 150°C. As the polymer with the lowest PMMA content, this result is consistent with the hypothesis that changing the block ratios can create a large change in properties without large changes in the chemical composition of the material. However, the results of M65 and M75 do not agree with this hypothesis as both displayed remarkably similar behavior in DMTA. While further study outside the scope of this thesis is needed to confirm the exact reasons for this deviation, the most likely cause is the change in morphology.

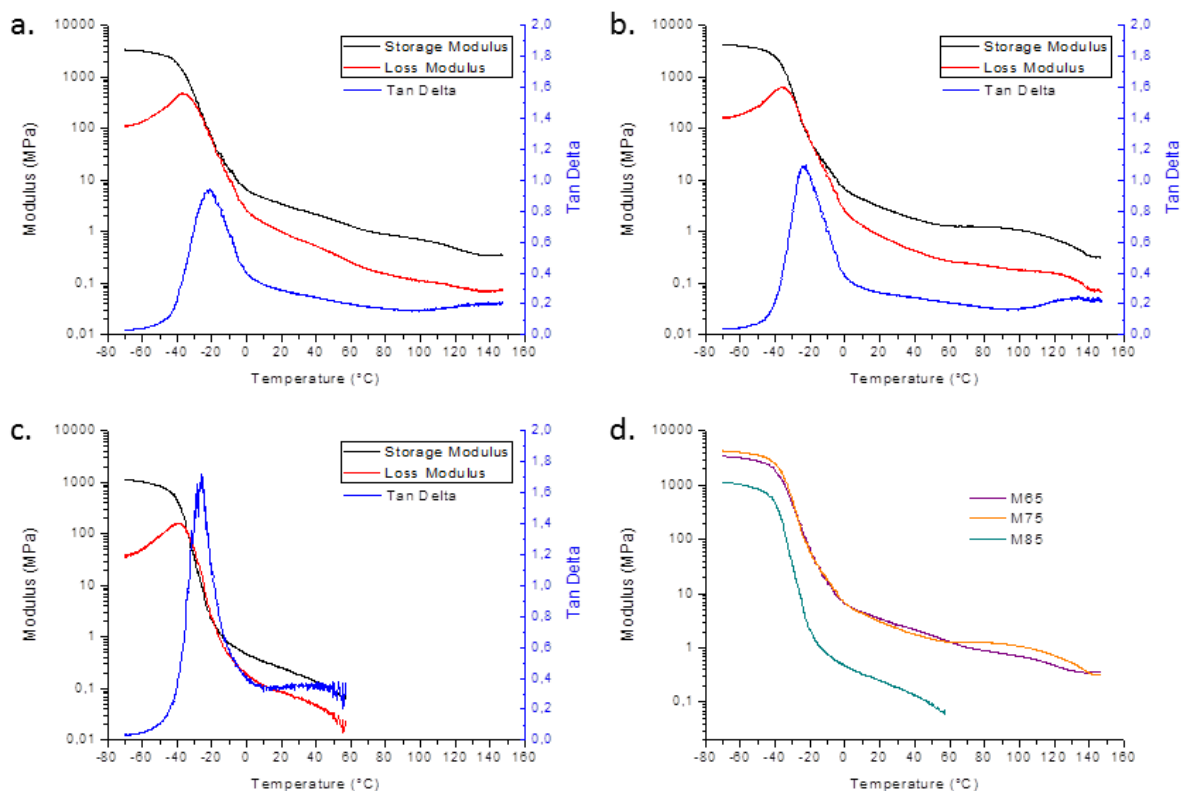


Figure 4.3 Tensile DMTA plots are shown for (a) M65, (b) M75 and (c) M85. (d) An overlay of the storage modulus curve of all three adhesives shows the comparison of the three adhesives. All tests were performed at 3°C/min, 1Hz and 0.1% strain.

Another important observation from the DMTA data is that of the value of the storage modulus at room temperature. At 23°C and 1Hz, conditions which correspond well with the lamination of an adhesive, only M85 meets the Dahlquist criterion for pressure sensitive adhesion with its measured E' of 2.3×10^5 Pa. M65 and M75, with E' values of 3.2×10^6 Pa and 2.8×10^6 Pa respectively, are an order of magnitude higher than the Dahlquist criterion. This was also observed as both of these adhesives, especially M65, had low tack when laminated at room temperature. However, this criterion can be met by heating the adhesives causing a drop in the storage modulus.

The T-peel adhesion of each adhesive was also tested to measure the adhesion to flexible substrates. The results of these tests on poly(ethylene terephthalate) (PET) substrates which had been rinsed with isopropyl alcohol (IPA) are shown in Table 4.2. PET was chosen as it is a common substrate for the fabrication of flexible barrier films. These samples used two adhesive coated substrates which were laminated together at room temperature. This led to the creation of a third interface where the two adhesive layers meet. This configuration was chosen as it closely resembles the encapsulation scheme for devices. M85 showed good tack and adhesion strength when laminated at room temperature. However, as predicted by the Dahlquist criterion,

the adhesion of M65 and M75 was very low when laminated at room temperature since they are too rigid to have a high degree of PSA character. This led to the use of post-lamination anneals in order to soften the adhesives and allow them to better adhere to the surface. An annealing study performed on M75 is shown in Figure 4.4. Since OPVs can be sensitive to high temperatures, anneals were limited to less than 150°C. When the relatively thicker Oike barrier films were used as substrates instead of PET, slightly longer annealing times were needed. To be sure that all samples were properly annealed, all subsequent testing with MAM Nanostrength® adhesives were annealed at 130°C for 10min.

Table 4.2 T-peel adhesion results are shown for samples using 50µm thick PET substrates. Lamination was performed using two adhesive coated substrates and testing was performed at least 3 days after lamination. Values in parentheses are the standard deviation. The failure type is color coded where yellow is adhesive failure at the adhesive-to-adhesive interface; green is adhesive failure at the adhesive-to-substrate interface; and blue is cohesive failure in the adhesive.

Post-Lamination Processing	M65	M75	M85
Room Temperature Storage	0.69 N/cm (0.55 N/cm)	1.63 N/cm (0.50 N/cm)	2.83 N/cm (0.29 N/cm)
Annealed	4.85 N/cm (0.70 N/cm)	4.77 N/cm (0.55 N/cm)	Not tested

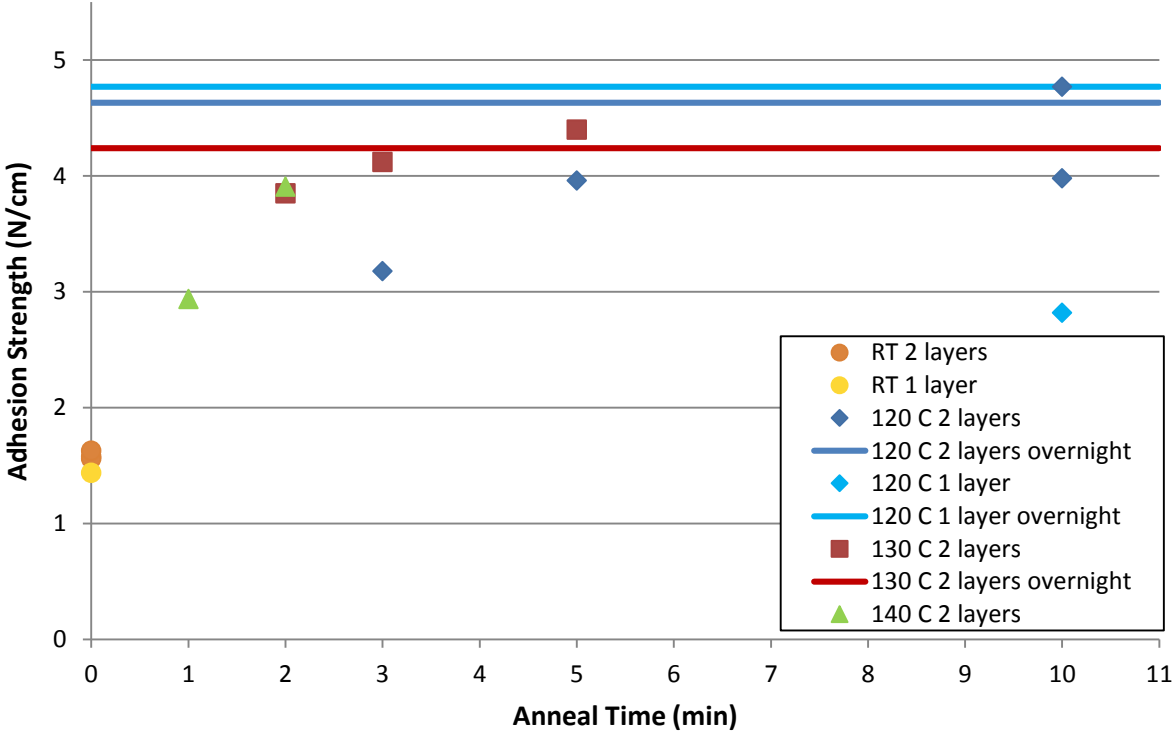


Figure 4.4 Average T-peel adhesion strengths are shown for M75 with various post-lamination anneals on IPA rinsed 50µm PET substrates. All anneals were performed on a hot plate except for overnight samples which used an oven. All samples had a total adhesive thickness of approximately 50µm, though some had a single layer of adhesive (adhesive coated substrate-to-uncoated substrate) while others had two thinner layers of adhesive (adhesive coated substrate-to-adhesive coated substrate).

To better match the processes used for the other types of adhesives used in this thesis, subsequent adhesive testing used a single adhesive coated substrate which was laminated to an un-coated substrate, thus eliminating the adhesive-to-adhesive interface. The results of this testing are shown in Table 4.3 and, due to the testing conditions used, these values are the most comparable to the other adhesives used in this thesis. Just as with DMTA, M65 and M75 showed similar performance in adhesion testing while M85 had different results. The better adhesion for M85 likely comes from the ability of softer materials to better dissipate strain energy, thus making the strain energy at the interfaces lower. Additionally, the higher PBA fraction and micellar morphology provides more PBA at the surface which allows for more PSA character. M65, which is the most rigid of the three adhesives and does not have a micellar morphology, was prone to stick-slip rupture during adhesion testing. This type of rupture occurs when the adhesive is unable to dissipate enough strain energy leading to a rapid adhesive failure over a large area (slip) once the strain energy at the interface passes a critical value (stick). Since strain energy dissipation is dependent on the volume of material, thinner adhesive thicknesses are more prone to exhibiting this type of behavior. This means that M65 was close to the limit of the minimum thickness which can be used for T-peel adhesion but does not necessarily indicate insufficient adhesion.

Table 4.3 T-peel adhesion results are shown for samples with a total adhesive thickness of 50 μ m and 50 μ m thick PET substrates. Lamination was performed using one adhesive coated substrate and one uncoated substrate and testing was performed at least 3 days after lamination. Values in parentheses are the standard deviation. The failure type is color coded where yellow is adhesive failure at the adhesive-to-adhesive interface; green is adhesive failure at the adhesive-to-substrate interface; and blue is cohesive failure in the adhesive. *Values with 2 layers of adhesive with a combined thickness of 50 μ m are shown for comparison for M65 which was too rigid to measure as a single layer.

Processing	M65	M75	M85
Single Adhesive Layer, 50 μ m PET, Annealed	NA: Stick-Slip	4.77 N/cm	7.41 N/cm
	4.85 N/cm* (0.70 N/cm)*	(0.68 N/cm)	(0.53 N/cm)

Transparency is also an important property for an adhesive which will be in the optical path of a device since any loss of light transmission directly results in a loss of power conversion efficiency of the solar cell. Therefore UV-Vis spectroscopy was also performed on the adhesives. The MAM adhesives were highly transparent and caused little to no loss of transmission compared to a PET film. An example is shown in Figure 4.5 where a 50 μ m layer of M85 coated on a PET substrate showed almost identical transmission to a PET film with no adhesive. This adhesive thickness was used as it corresponds well to the thickness of adhesive

present between the device and the barrier film in a flexible encapsulation scheme. This high transparency makes these adhesives ideal materials in terms of optical clarity.

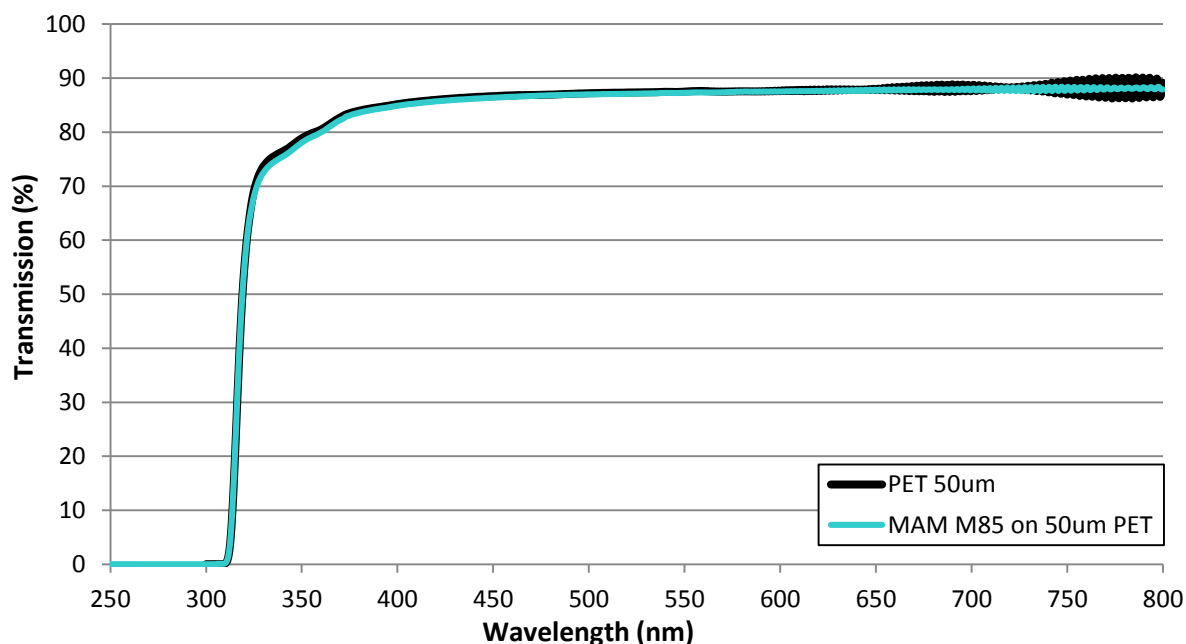


Figure 4.5 UV-Vis spectroscopy using a standard detector was performed on both a 50 μ m thick PET film and a PET film with a 50 μ m coating of M85. For the M85 sample, the PET surface was facing the laser source so that the same amount of reflection was present for both samples.

Permeation

The barrier properties of the MAM Nanostrength[®] adhesives were evaluated using the optical calcium test described in Chapter 3. The ability to limit the permeation of water vapor is of critical importance for OPV encapsulation materials. The results of these tests can be seen in Figure 4.6 in terms of the total apparent lateral permeation. All samples in this study used Oike VX 25T-2PO barrier films which had been sonicated in IPA prior to bonding. The adhesives were coated onto the barrier films from solution in toluene and were annealed at 130 $^{\circ}$ C prior to testing. The large variance for some test conditions comes from the formation of voids and bubbles in the adhesive which led to an increase in the lateral permeation rate. While great care was taken to avoid the presence of voids during sample preparation, even small voids and bubbles grew rapidly once exposed to water vapor for this class of adhesives. This was especially true for the low tack adhesives M75 and M65, where eliminating voids during fabrication was extremely difficult. For example, of 11 calcium test samples prepared using M65, only 3 were able to be analyzed as the rest had large voids and lamination defects.

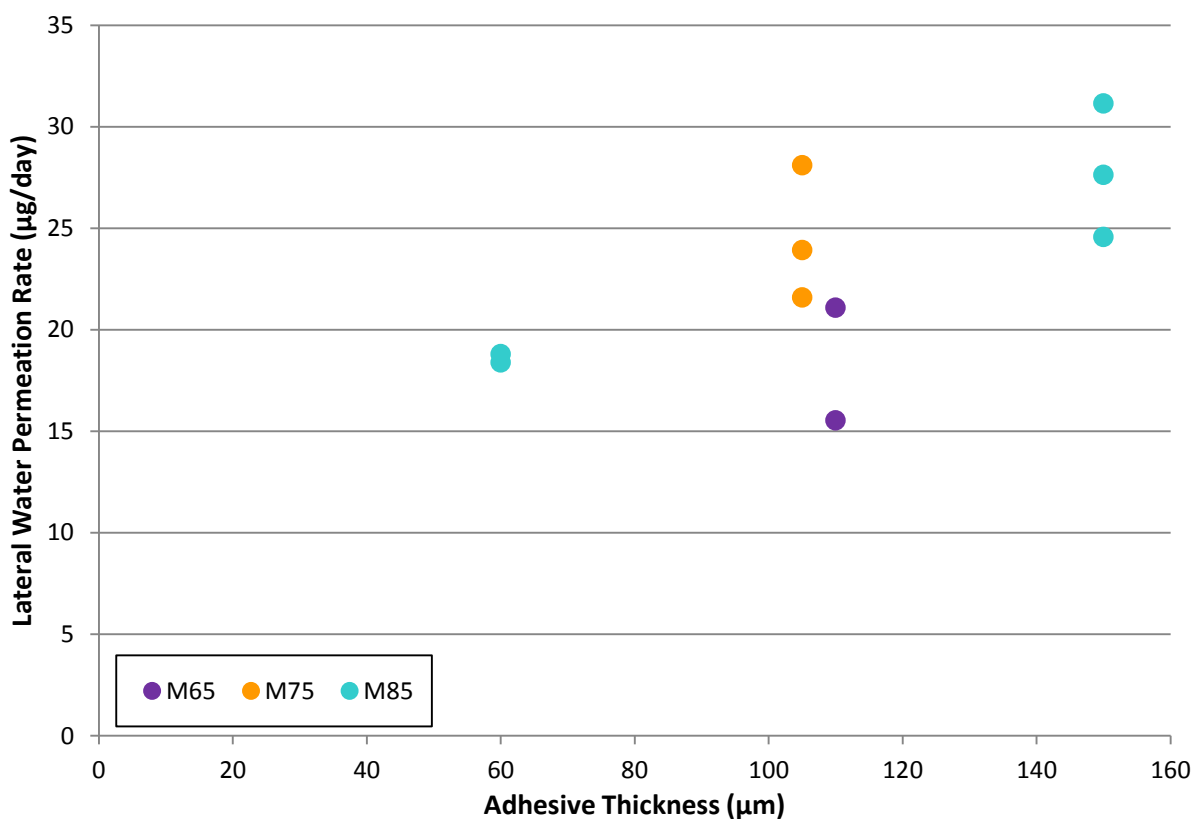


Figure 4.6 A plot of the apparent lateral permeation rate as measured by the modified optical calcium test is shown for the MAM Nanostrength[®] adhesives. All values have been normalized to 45mm X 45mm calcium deposits to adjust for slight differences between samples.

The variance in the measures makes it difficult to draw firm conclusions from this data, though there are noticeable trends especially when focusing on the best samples which had the fewest voids. It appears that M85 and M75 show very similar permeation rates while M65 appears to be slightly less permeable to water vapor. Two initial hypotheses were formulated for potential trends in permeation. One hypothesis was that the ratio of the blocks affects the permeation rate as higher percentages of PMMA, which is less permeable to water vapor than PBA, would result in decreased permeation. This hypothesis would predict that the adhesives would be consecutively less permeable, but the experimental data does not confirm this. Alternatively, a hypothesis based on the mechanical properties was also considered. This hypothesis considered the rigidity of the materials to be an indicator of chain mobility. Higher chain mobility within a materials with very similar chemical structures was predicted to lead to more permeation. As M65 and M75 show very similar results for both DMTA (at both room temperature and 65°C) and T-peel adhesion, this hypothesis predicted that these adhesives would have similar permeation rates. M85 on the other hand, being much softer indicating more

chain mobility, would be more permeable. However, this hypothesis also does not fit the experimental data.

Despite the lack of clear agreement for both of these hypotheses, the competing permeation pathways of the bulk adhesive and the interface could describe this phenomenon. The much higher adhesion of M85 compared to the other adhesives may have led to this adhesive showing a lower total lateral permeation. Optical calcium tests with different thickness of M65 and M75 are needed to confirm if this effect exists. However, this effect is unlikely to be very large as the adhesion of M65 and M75 was still quite strong, even though it was much lower than that of M85.

A third hypothesis which better explains the data observed was also developed. Upon reviewing the properties of the three adhesives, one difference does appear which could potentially explain the experimental results: morphology. M75 and M85 both have micellar morphologies while M65 does not. The worm-like morphology of M65 results in more permeating molecules being forced to either traverse the less permeable PMMA domains or take a much longer tortuous path through the PBA domains. However, it appears that this effect only slightly decreases the permeation rate and the statistical uncertainty of the experimental data makes it unclear if the effect exists at all.

UV Cure Acrylates

UV curing acrylate adhesives present a very different approach compared to PSAs. As reactive liquids that do not require a solvent evaporation, they are much easier to process into void/bubble free samples. The fast curing times also mean that no long waiting times are needed between lamination and testing, unlike with PSAs which often take days. However, they also require the extra processing step of curing and can be more difficult to completely degas at the lab scale, as vacuum can remove needed volatile species. Nonetheless, the advantages of UV curing acrylates make them a very interesting alternative to PSAs for OPV encapsulation.

Formulation of the Adhesives

UV curing acrylate adhesives consist of a mix of oligomers, monomers, photo-initiators and potentially other additives, and thus require a balanced formulation to achieve the desired properties. The formulation of UV curing acrylate adhesives must also take into account several

other factors in addition to the general requirements for OPV encapsulation. These include compatibility with OPV devices and the ability to properly cure using light sources which must transmit across the barrier film.

Monomers present the greatest risk for incompatibility with the various layers of OPV devices as they are relatively small organic molecules and contain reactive groups. This can cause monomers to act as solvents or react chemically with the various layers of an OPV device, and therefore affect the performance of the device. To ensure that any monomers used in the formulation did not have an adverse effect on the device, a screening process was used. Several different monomers were screened by spin coating them onto OPV cells in a dry nitrogen glove box and characterizing the cells using current density-voltage (J-V) curves after approximately 5min and 10min of exposure to the monomer. The cells used an inverted architecture and had a structure of PET – indium tin oxide (ITO) – zinc oxide nanoparticles (ZnO) – P3HT:PCBM – PEDOT:PSS – silver (deposited via evaporation). P3HT:PCBM is a bulk heterojunction active layer comprised of a blend of poly(3-hexylthiophene) and phenyl C₆₁ butyric acid methyl ester. PEDOT:PSS is a hole transport layer (HTL) which is a blend of poly(3,4-ethylenedioxythiophene) and poly(styrene sulfonate). The monomers were spin coated onto the backside of the cell and were thus directly in contact with both the silver and PEDOT:PSS layers, though side ingress through the other layers was still possible as well. The results of this testing can be seen in Table 4.4 and show that most of the tested monomers were compatible with this type of inverted OPV cell. Only the monomer SR285 (tetrahydrofurfuryl acrylate) showed strong degradation of the solar cell's performance after short exposure times. SR238 (1,6-hexyldiol diacrylate) and SR484 (blend of octyl and decyl acrylates) both have, except for their acrylate groups, completely aliphatic structures which likely limited their ability to interact with the highly hydrophilic PEDOT:PSS layer. SR9003 (propoxylated 2-neopentyl glycol diacrylate) is a fairly large molecule which may have limited its ability to diffuse into the layers of the solar cell.

Table 4.4 The results of J-V testing for OPV cells after exposure to acrylate monomers are shown. OPV cells used the structure PET – ITO – ZnO – P3HT:PCBM – PEDOT:PSS – Ag and had an active area of 0.28cm². Two cells were present per substrate and measurements were made without a light mask. The t=0 measurements were made immediately before application of the monomer.

Sample	Time (min)	V _{oc} (mV)	J _{sc} (mA/cm ²)	FF (%)	PCE (%)	Normalized ΔPCE (%)
SR238 Cell 1	0	540.5	9.61	47.53	2.47	---
	4	541.7	8.96	48.17	2.34	-5.26
	10	541.6	8.85	48.18	2.31	-6.48
SR238 Cell 2	0	553.0	9.70	51.62	2.77	---
	5	557.0	10.0	51.82	2.89	4.33
	10	561.7	9.72	51.26	2.80	1.08
SR285 Cell 1	0	540.6	6.98	53.95	2.04	---
	6	543.7	6.45	50.99	1.79	-12.1
SR285 Cell 2	0	549.4	9.23	52.51	2.66	---
	5	554.6	8.71	51.52	2.49	-6.39
	10	553.4	8.38	51.41	2.38	-10.5
SR484 Cell 1	0	581.2	9.23	48.39	2.42	---
	4	525.5	9.51	46.59	2.33	-3.72
	10	525.6	9.47	46.73	2.33	-3.72
SR484 Cell 2	0	562.3	10.0	52.00	2.93	---
	5	556.4	10.2	53.08	3.03	3.41
	10	552.8	10.2	53.94	3.04	3.75
SR9003 Cell 1	0	544.8	8.22	50.81	2.28	---
	6	547.3	8.41	50.64	2.33	2.19
	10	544.5	8.43	51.16	2.35	3.07
SR9003 Cell 2	0	550.8	9.87	52.76	2.87	---
	5	553.2	10.0	52.96	2.93	2.09
	10	553.0	10.0	53.23	2.96	3.14

Using the information from this monomer compatibility study, along with the advice of experts from Sartomer, Formulation #1 (F1) was devised consisting of 2 oligomers, 2 monomers and 2 photo-initiators. As this adhesive was unable to properly polymerize between PET substrates, the photo-initiator ratio was changed in favor of longer curing wavelengths to form F2. This adhesive was able to polymerize but had no adhesion to PET and thus the formulation was modified further. As can be seen in Table 4.5, Formulations 2-8 and 10 varied the ratios of the oligomers and monomers more and more in favor of those known to provide better adhesion to plastic substrates (CN9002 and SR506D). F5 was the first to show any adhesion, though it was not enough to be measurable in a T-peel test. F6 and F10 also showed some adhesion but were measured to be at the limit of detection in T-peel testing while displaying stick-slip behavior. F12 and F15 tried using additional oligomers and adhesion promoters, but due to the lack of good adhesion, this series of formulations was abandoned in favor of a new suggestion from Sartomer which became F9. This formulation also had very weak adhesion at the limit of detection in T-peel testing while displaying stick-slip behavior.

F9 was then modified using the oligomers and monomers from the previous iterations which were known to aid in adhesion to plastic substrates in other adhesives. The resulting modifications, seen in Table 4.6, showed no improvement until F13 which showed measurable adhesion in T-peel testing. Despite this adhesion, there was still a large degree of stick-slip behavior present in F13. The “slips” are seen in the peel test data in Figure 4.7 as sudden losses in strength. The ratios of the oligomers and monomers in F13 were further modified in the hopes of reducing this stick-slip, ultimately resulting in F18. This formulation had the best adhesion without having a large degree of stick-slip, and as a result, F18 was selected for further study.

Table 4.5 The formulations based on F1 are shown with red and green values representing decreases and increases from the previous iteration respectively.

	F1	F2	F3	F4	F5	F6	F7	F8	F10	F12	F15
CN131B Low Tg oligomer	--	--	--	--	--	--	--	--	--	10.7%	10.1%
CN9001 Mid Tg oligomer	20.9%	21.1%	10.5%	10.5%	10.5%	5.2%	8.9%	4.0%	--	--	--
CN9002 Very low Tg oligomer	20.9%	21.1%	31.4%	31.4%	31.4%	36.6%	62.4%	27.3%	42.5%	31.9%	30.2%
SR238 Di-acrylate monomer	31.4%	31.8%	31.2%	21.0%	10.4%	10.5%	4.7%	12.6%	--	--	--
SR506D Monoacrylate monomer	21.3%	21.2%	21.1%	31.4%	41.9%	41.9%	19.1%	50.0%	51.9%	52.1%	49.2%
SR9050 Adhesion Promoter	--	--	--	--	--	--	--	--	--	--	5.4%
Irgacure 184 UVA initiator	4.8%	2.4%	2.9%	2.9%	2.9%	2.9%	2.4%	3.1%	2.8%	2.6%	2.6%
TPO-L VIS initiator	0.6%	2.4%	2.9%	2.8%	2.9%	2.9%	2.4%	3.1%	2.8%	2.6%	2.6%
Adhesion	Not cured	None	None	None	Below testing limit	At testing limit: Stick-slip	None	None	At testing limit: Stick-slip	At testing limit: Stick-slip	At testing limit: Stick-slip

Table 4.6 The formulations based on F9 are shown with red and green values representing decreases and increases from the previous iteration respectively.

	F9	F11	F13	F14	F16	F17	F18
CN131B Low Tg oligomer	89.5%	89.3%	67.0%	44.8%	78.3%	55.9%	61.6%
CN9002 Very low Tg oligomer	--	--	22.3%	44.6%	11.2%	33.6%	28.0%
SR9050	5.6%	--	5.7%	5.7%	5.7%	5.7%	5.6%

Adhesion Promoter							
SR506D Monoacrylate monomer	--	5.8%	--	--	--	--	--
Irgacure 184 UVA initiator	3.8%	3.8%	3.8%	3.8%	3.7%	3.8%	3.8%
TPO-L VIS initiator	1.1%	1.1%	1.1%	1.1%	1.0%	1.0%	1.0%
Adhesion Strength	At testing limit: Stick-slip	At testing limit: Stick-slip	1.46 N/cm Stick-slip	0.74 N/cm	1.97 N/cm Stick-slip	1.28 N/cm	1.32 N/cm

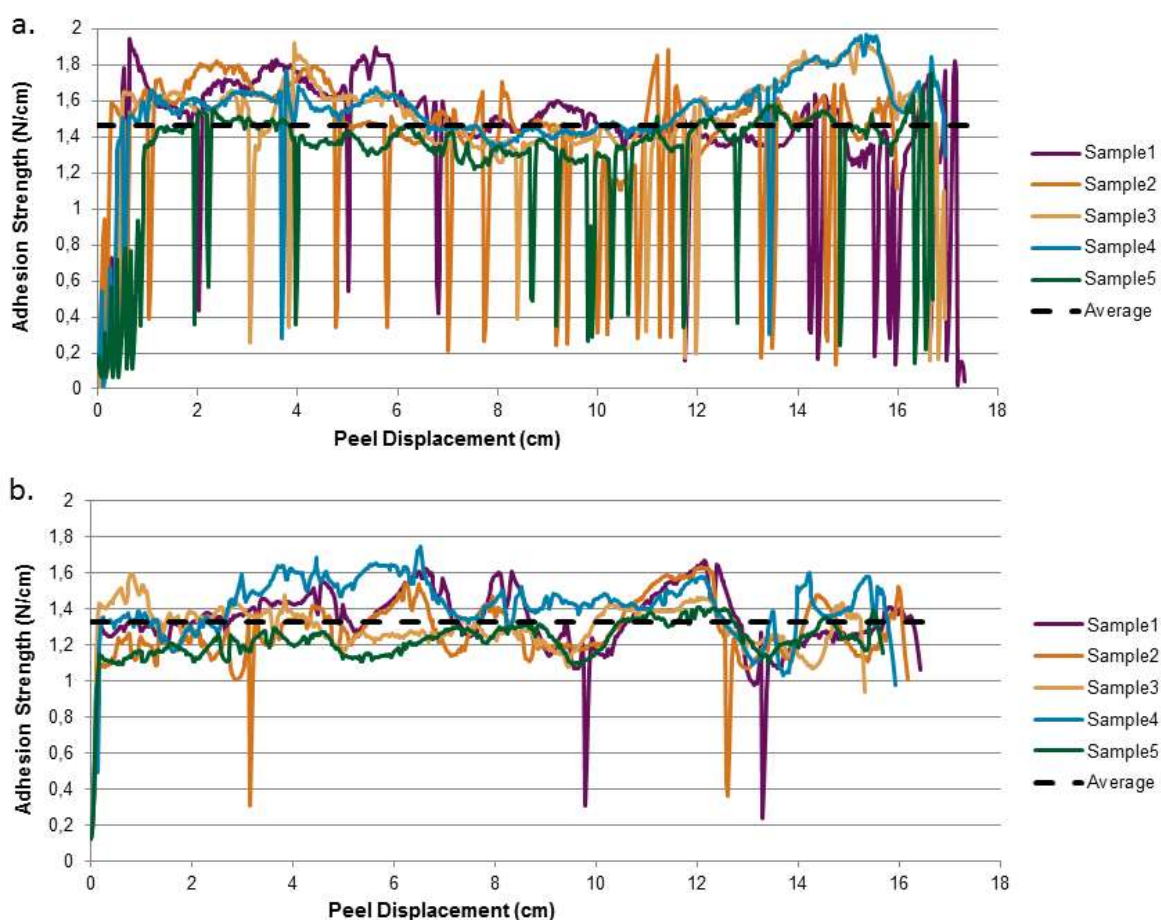


Figure 4.7 T-peel adhesion tests are shown for (a) F13 and (b) F18. F13 showed a large amount of stick-slip behavior which can be seen as sudden decreases in adhesion strength. F18 showed only rare instances of stick-slip.

The ability of the adhesive to correctly cure was analyzed using FTIR-ATR on samples after peeling. This calculation was performed as described in the literature by comparing the areas of the peak at approximately 830cm^{-1} (epoxy backbone) and the peak at approximately 810cm^{-1} (out of plane bending of C-H on $\text{RCH}=\text{CH}_2$).¹⁴⁹ F18 exhibited fairly strong oxygen inhibition of the curing reaction, necessitating that all samples be cured between two substrates when cured in air. This geometry is also preferred as it replicates the conditions seen for

encapsulating devices. Tests were performed using both 50 μ m PET and Oike VX 25T-2PO barrier films as they have different transmission spectra. Tests were also performed with both available UV lamps to confirm the effectiveness of each process. The results for F18 are shown in Figure 4.8 and show that very short curing times are sufficient regardless of the process used. To ensure that all samples were thoroughly cured, a curing time of 30s was selected for subsequent use with both lamps.

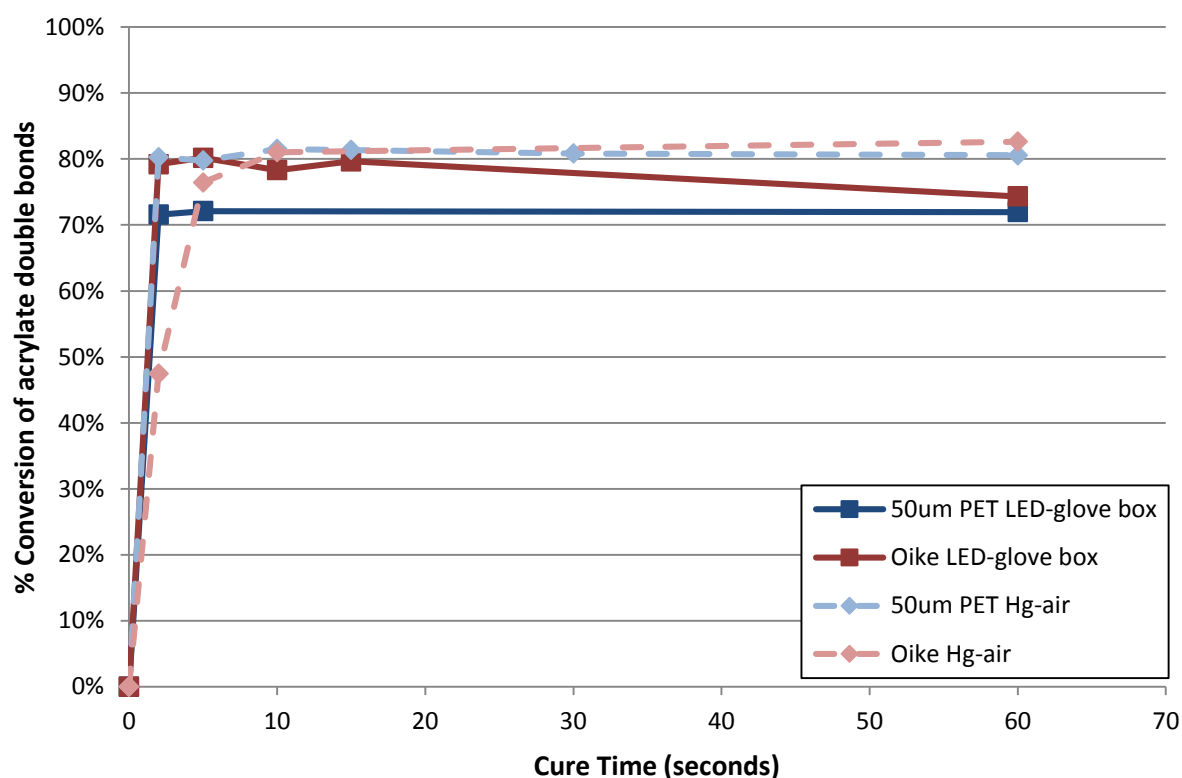


Figure 4.8 The curing of F18 is shown as calculated from FTIR-ATR measurements. Samples were cured between either 50 μ m PET substrates or Oike VX 25T-2PO substrates. The lamps used were a 400nm LED source located in a dry nitrogen glove box and a medium pressure mercury lamp located in air.

Another adhesive was also formulated using a similar iterative process at Sartomer with the goal of improving the adhesion in comparison to F18. This was achieved by replacing the two oligomer blend of F18 with a blend of a different oligomer and a monomer. Simultaneously, a non-reactive aliphatic tackifying resin, Norsolene S95, was also added to the formulation as an adhesion promoter. The resulting adhesive, named S3 and described in Table 4.7, had an adhesive strength of 3.01N/cm on PET compared to 1.32N/cm for F18. This improved adhesion made S3 an interesting alternative to F18 and it was therefore selected for further study. Due to a large amount of peak convolution, it was not possible to use FTIR-ATR to determine a quantitative value of the conversion of double bonds, though qualitative comparisons were still possible to confirm the adhesive had reached its maximum conversion.

Table 4.7 The formulation of S3 is listed with a brief description of each component.

Component	Description	wt%
CN966H90	Aliphatic urethane di-acrylate oligomer	29.5%
SR504	Mono-acrylate monomer	30.6%
SR9050	Adhesion promoter	5.6%
Norsolene S95	Aliphatic tackifying resin	29.5%
Irgacure 184	UVA photo-initiator	3.8%
Lucirin TPO-L	VIS photo-initiator	1.0%

Comparison of Thermo-Mechanical and Optical Properties

Just as with the PSAs, the T_g of the UV curing acrylates was also tested by DSC. Because the conversion of the monomers is not complete during the UV curing of F18, an exothermic behavior at higher temperatures ($>100^\circ\text{C}$) was seen in DSC which likely corresponds to the curing of residual monomers. As a result, the T_g observed during the second heating run was elevated in comparison to the first heating run. The first T_g corresponds to the polymer as it is after curing while the second T_g is more applicable to samples which have seen an anneal after curing. However, S3 was tested only to 100°C and did not display this behavior. Both T_g values are reported in Table 4.8 along with the T_g as measured by the peak of the loss modulus (E'') curve in DMTA. The value from DMTA is more comparable to the first heating run of DSC as the sample had not been previously exposed to high temperatures.

Table 4.8 T_g values for UV curing acrylates are shown as calculated from the midpoint of DSC transitions and the peak of the loss modulus (E'') curve in DMTA. The DSC heating ramp rate was $10^\circ\text{C}/\text{min}$ for all samples.

Adhesive	1 st DSC Heating	2 nd DSC Heating	DMTA peak E''
F18	-17°C	-11°C	-20°C
S3	-27°C	-28°C	NA

Tensile DMTA was performed on both adhesives, however all attempts at measuring S3 were unsuccessful. The relatively strong adhesion of S3, along with its soft nature, made it difficult to separate DMTA samples from the substrate after curing. The few samples which

were obtained were then very soft and consistently failed during testing. Testing in shear with a rheometer was also attempted, but samples of sufficient size could not be separated from the substrates after curing. However, F18 was much easier to process as it is both more rigid and has lower adhesion. The DMTA curve for F18 tested at 3°C/min, 1Hz and 0.1% strain is shown in Figure 4.9. The adhesive displayed behavior typical of a crosslinked polymer with a clear glass transition and a rubbery plateau showing a slight and gradual increase in the storage modulus above T_g . The loss modulus fell below the detection limit of the equipment at higher temperatures resulting in its apparent rapid descent to 0 in Figure 4.9. For the purposes of this thesis F18 is sufficiently flexible, however, there should be some concern about the increased rigidity at colder temperatures for its use in actual OPV encapsulation where devices can be exposed to cold winter temperatures outdoors. A slightly softer version of this adhesive may be needed if the end product is expected to be used in colder climates.

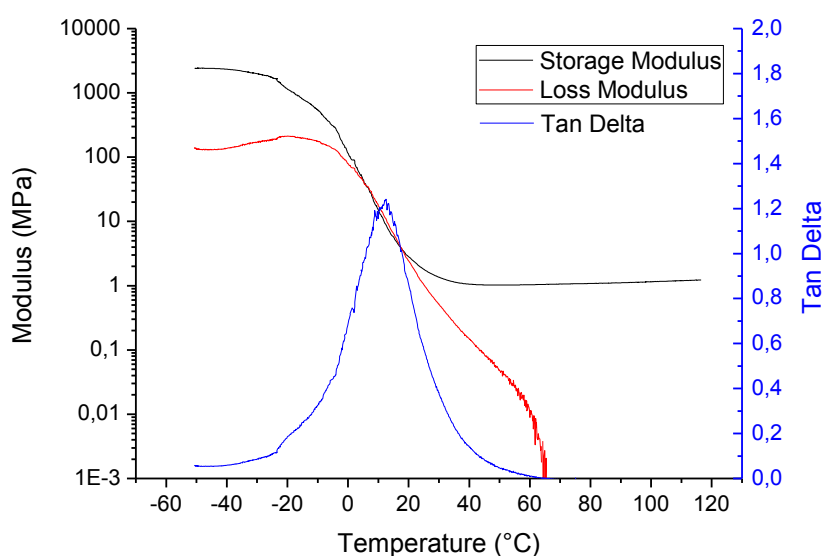


Figure 4.9 The tensile DMTA curve for F18 is shown as tested at 3°C/min, 1Hz and 0.1% strain.

The adhesion of both adhesives was briefly discussed in the formulation section since it was used as a screening tool for their development. Additional adhesion testing was also performed on these adhesives using barrier films as substrates. While F18 showed identical adhesion to both PET and Oike VX 25T-2PO barrier films, S3 showed a large drop in the measured adhesion compared to PET substrates. Though quantitative measures were not possible due to peak convolution, a relative comparison of FTIR-ATR peaks, seen in Figure 4.10, showed that the samples using Oike substrates were not fully cured. This was remedied by increasing the exposure time and intensity of the UV lamp which allowed the adhesive to recover some of its adhesion. It should also be noted that after adhesion testing, S3 displayed

high tack and PSA character. This is likely due to its low modulus and T_g . F18 meanwhile, showed almost no tack and remained as an intact film after adhesion testing. As the adhesion values shown in Table 4.9 indicate, the adhesion was not particularly strong for the UV curing adhesives, especially F18. Therefore adhesion tests on corona treated substrates were also performed as a method to increase the adhesion. While corona treatments did improve the adhesion of both adhesives, it was to a lower extent than the increases seen in the PSAs, especially for F18.

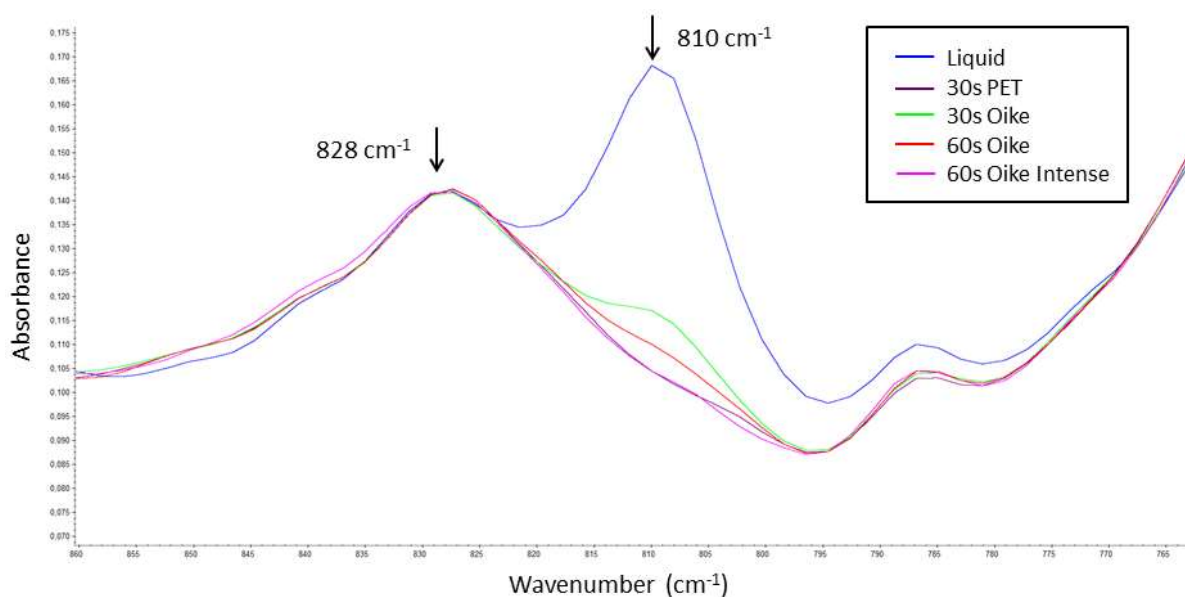


Figure 4.10 FTIR-ATR spectra of S3 are shown for various curing times and substrates. All samples, except for the liquid, were cured using a medium pressure mercury lamp in air. The conversion of the adhesive can be seen by the peak at 810cm^{-1} which corresponds to the out of plane bending of C-H on $\text{RCH}=\text{CH}_2$.

Table 4.9 The T-peel adhesion strength of the UV acrylate adhesives are shown with the standard deviation in parentheses. All samples had an adhesive thickness of approximately $50\mu\text{m}$. The failure type is color coded where green is adhesive failure at the adhesive-to-substrate interface and blue is cohesive failure in the adhesive.
*Longer/more intense cure

Adhesive	PET (IPA rinsed)	Oike (IPA rinsed)	Oike (Corona)
F18	1.32 N/cm (0.15 N/cm)	1.32 N/cm (0.15 N/cm)	1.82 N/cm (0.08 N/cm)
S3	3.01N/cm (0.10 N/cm)	1.00 N/cm (0.07 N/cm)	2.84 N/cm* (0.16 N/cm)*
		1.76 N/cm* (0.20 N/cm)*	

To evaluate the transparency of the adhesives, UV-Vis spectroscopy was performed and the results are shown in Figure 4.11. All samples were cured between two PET substrates. Since both adhesives are known to fail adhesively at the PET interface, they were then peeled apart

to produce a coating of adhesive on a single PET film. The PET film was positioned facing the laser source so that the reflection would be the same for all samples. Both samples have more absorption at lower wavelengths than the uncoated PET, with S3 being particularly less transparent at these shorter wavelengths. This is unsurprising as S3 has a yellow-orange color in very thick layers, though it remains quite clear to the eye in layers of tens of microns. This color comes mainly from the tackifying resin, thereby creating a trade-off between adhesion and optical clarity. The lower transparency of S3 could potentially affect the performance of certain OPV active layers which absorb strongly in the blue part of the spectrum.

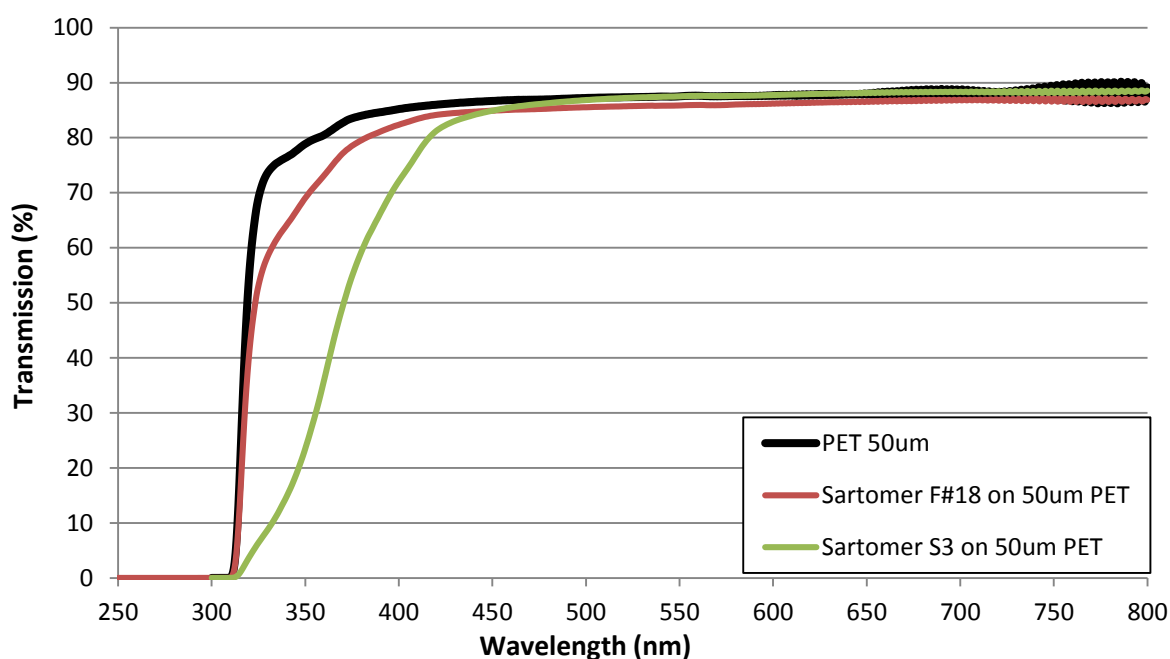


Figure 4.11 UV-Vis spectroscopy using a standard detector was performed on both a 50 μ m thick PET film and PET films with 50 μ m coatings of adhesive. For the adhesive samples, the PET surface was facing the laser source so that the same amount of reflection was present for all samples.

Permeation

The water vapor permeation of both UV curing acrylate adhesives was studied using the optical calcium test described in Chapter 3. The apparent lateral permeation measured for each sample is shown in Figure 4.12. It is immediately evident in this plot that the interfacial permeation plays a very large role as the adhesive thickness has no significant effect on the lateral permeation for either adhesive. Since bulk permeation is dependent on the adhesive thickness while interfacial permeation is not, the experimental data implies that the water vapor permeation in the bulk adhesive is much slower than the interfacial permeation. The relatively weak adhesion of the UV curing acrylates indicates a weaker interfacial bond which could make interfacial permeation easier to occur. Also, polymer adhesives are known to have a general

trend that higher cross-link densities lead to lower permeation rates as the chain mobility and free volume of polymer become smaller. The cross-linked network structure of the UV curing acrylates may help to limit bulk permeation. The combination of a weaker interface and a cross-linked bulk structure may have caused the interfacial permeation to become dominant for these adhesives.

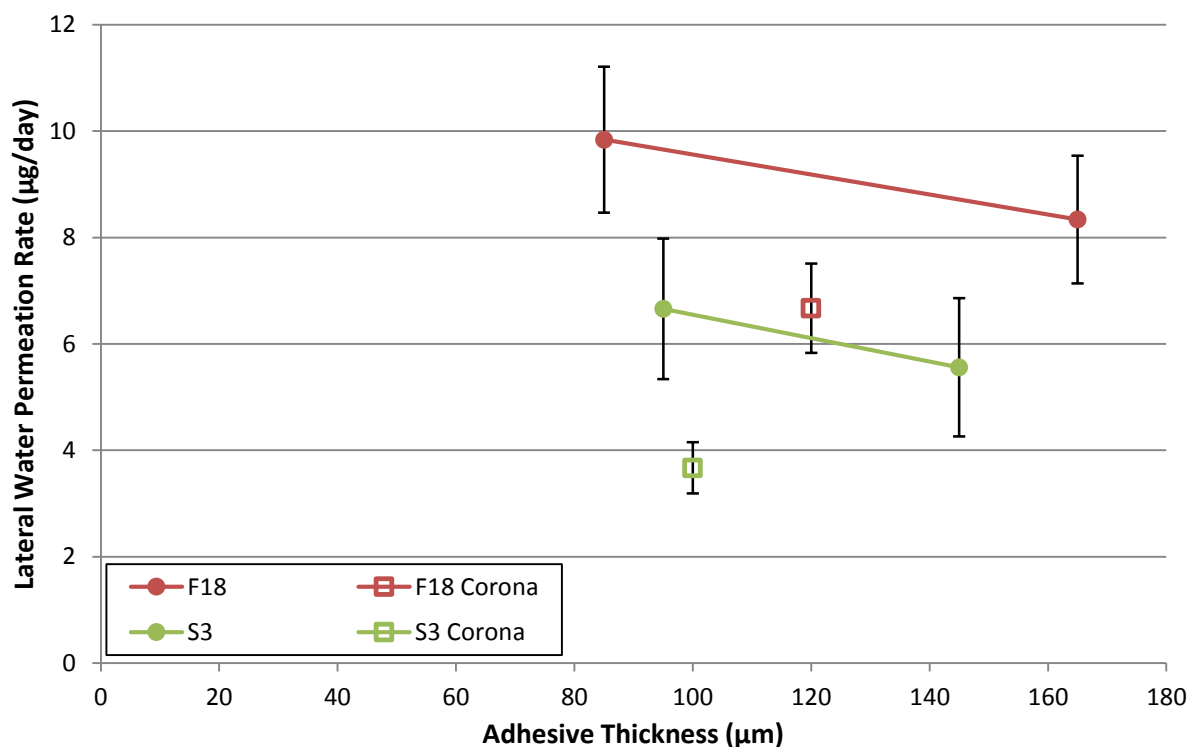


Figure 4.13 A plot of the apparent lateral permeation rate as measured by the modified optical calcium test is shown for the UV curing acrylate adhesives. All values have been normalized to 45mm X 45mm calcium deposits to adjust for slight differences between samples. Error bars represent ± 1 standard deviation.

A second trend that can be noted from Figure 4.13 is the lower interfacial permeation for S3 in comparison to F18 for which $p=0.0025$ using an independent samples t-test. As the two adhesives are chemically different, there may be a variety of causes for this difference in permeation, but one major difference which likely played a large role is the presence of a tackifying resin in S3. The tackifying resin is known to act as an adhesion promoter and S3 did indeed show more adhesion than F18. This increased adhesion is likely a major cause of the lower permeation of S3 compared to F18. Additionally, the mostly aliphatic nature of the tackifying resin makes it hydrophobic in nature, which could potentially further limit the permeation of highly polar water vapor in the adhesive.

Samples were also prepared using corona treated barrier films for both adhesives. Improving the interface is of extra importance for F18 and S3 as they are dominated by interfacial permeation. Corona treatments were shown to improve the adhesion of both

adhesives and also limited the lateral permeation in optical calcium tests with $p=0.069$ and $p=0.0059$ for F18 and S3 respectively using independent samples t-tests. The relation between the adhesion strength and the lateral water permeation rate for the corona treated sample closely matched the trend seen for the non-corona treated samples as can be seen in Figure 4.14. This trend provides further evidence that the interface is the dominant permeation pathway for these adhesives. Despite the different chemistries of F18 and S3, the points for corona treated F18 samples and non-corona treated samples of S3 have very similar results for both adhesion and water permeation, which indicates that the interface is the dominant factor controlling the lateral water permeation for these adhesives.

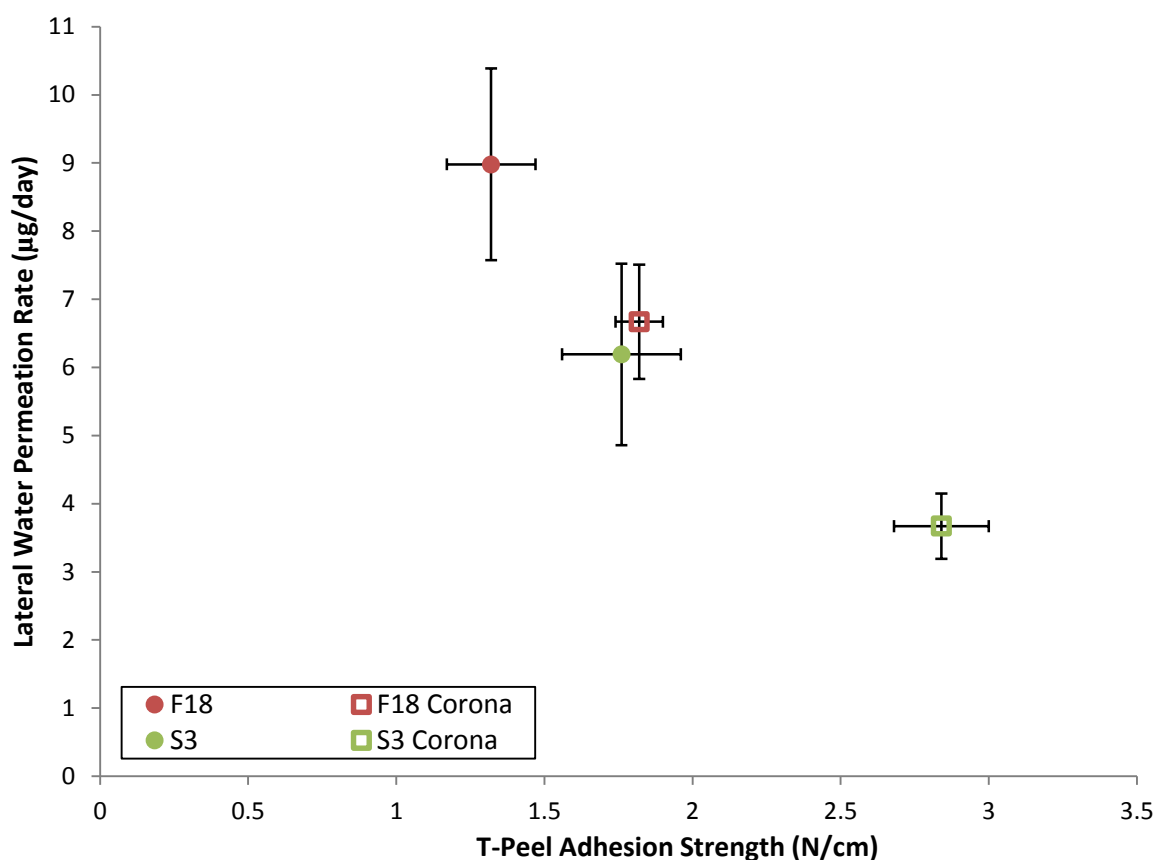


Figure 4.14 The apparent lateral permeation rate as measured by the modified optical calcium test is plotted against the T-peel adhesion strength for the UV curing acrylate adhesives on Oike VX 25T-2PO barrier films. The permeation values are averages from all previously presented samples regardless of adhesive thickness. All permeation values have been normalized to 45mm X 45mm calcium deposits to adjust for slight differences between samples. All adhesion samples had an adhesive thickness of approximately 50µm. Error bars represent ± 1 standard deviation.

Comparison of Adhesive Chemistries

Both MAM PSAs and UV curing acrylates have their own advantages and disadvantages when it comes to OPV encapsulation. Their very different processing techniques

are but one of the many differences between the two types of adhesives which must be considered for their application to OPV encapsulation. To better compare these materials and provide context for their measured properties, reference adhesives were also tested alongside the MAM PSAs and UV curing acrylates. 3M 467MP and 468MP, which differ only in thickness, are cross-linked acrylic PSA films which were used as the reference material for most testing. These materials, while not specifically designed as gas barrier adhesives, have been used for OPV encapsulation in studies by other laboratories and thus provide a good reference point for evaluating the materials used in this thesis. This section aims to provide a general overview of how the two types of adhesives used in this thesis compare to each other and their suitability for OPV encapsulation.

In general, all of the adhesives were fairly flexible, though F18, M65 and M75 remained more rigid throughout the entire operating range of temperatures as can be seen in Figure 4.15. F18 in particular raises some concerns over its rigidity at low temperatures since its T_g falls within the operating temperature range of outdoor solar modules. It may be possible to reformulate this adhesive to have a lower T_g , though this would likely come at the cost of the adhesion strength as seen from the evaluation of F14 and F17. Overall however, all of the materials tested are flexible enough to be used in OPV encapsulation for many applications. If extremely high flexibility or very cold temperature operation is needed, M85 and S3 would be the best candidates.

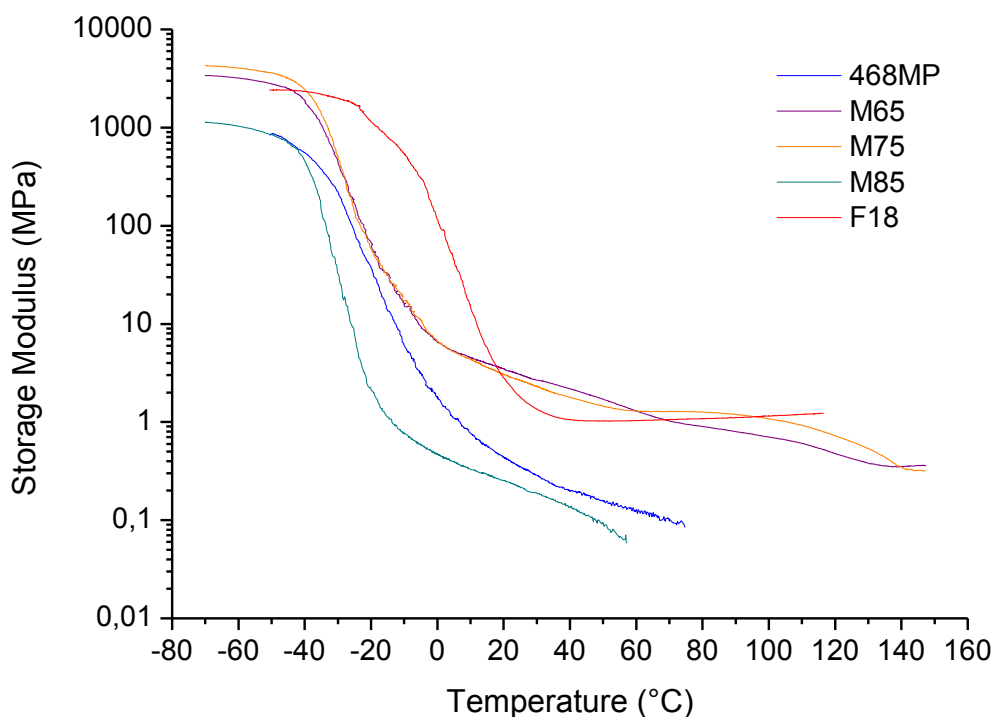


Figure 4.15 Plots of the storage modulus, E' , as measured by tensile DMTA at 3°C/min, 1Hz and 0.1% strain are shown for several adhesives.

The adhesion of the PSAs was generally found to be much stronger than that of the UV curing acrylates. Just as with the MAM adhesives, the reference adhesive was also found to have greatly varying adhesion depending on the processing conditions as can be seen in Figure 4.16. To properly compare values from T-peel adhesion tests, it is important that the samples use the same substrates and have the same adhesive thickness as both of these factors can greatly affect the results. A comparison of the adhesion strength of several adhesives using the same substrates and adhesive thickness can be seen in Table 4.10. The MAM PSAs, once annealed, showed stronger adhesion than the reference material on PET. M85 in particular showed excellent adhesion to both PET and barrier films. Despite their good adhesion after annealing, the low tack of M65 and M75 made them quite difficult to process using standard PSA lamination techniques. This led to many problems when testing these materials in the optical calcium test and greatly reduces their suitability for OPV encapsulation. Laminating these adhesives at an elevated temperature may help to alleviate these issues, though this complicates the lamination process. While S3 showed adhesion similar to that of the reference material, F18 was much weaker. This could be a potential problem for application of this adhesive for OPV encapsulation due mainly to permeation along the interface. Mechanically, although its adhesion was lower than that of the reference PSA, F18 did provide enough adhesion to avoid

facile delamination of the encapsulation and cannot be ruled out for OPV encapsulation on the basis of its adhesion.

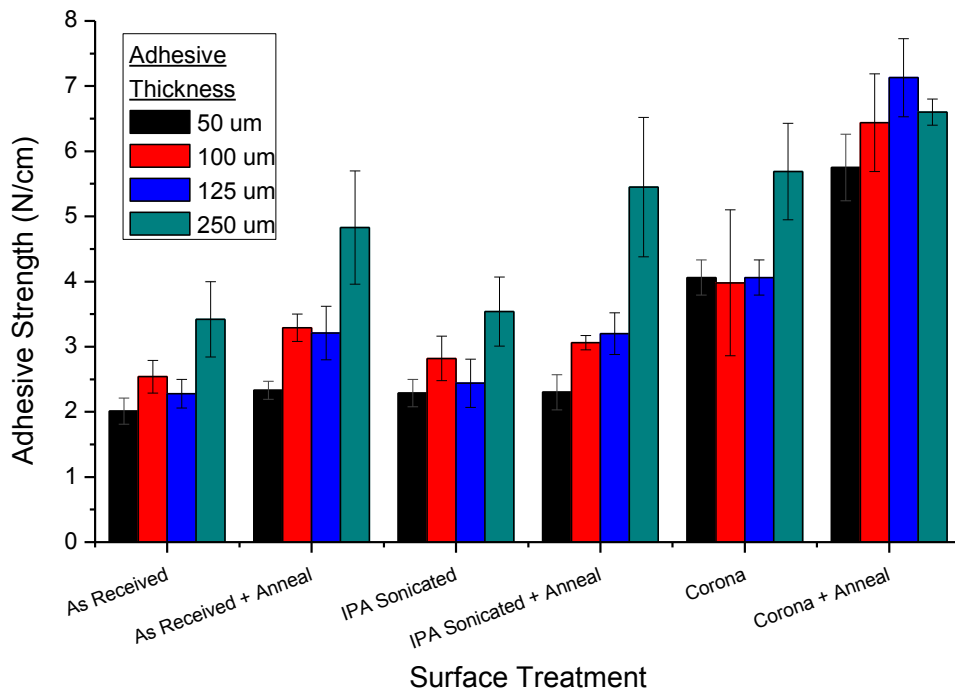


Figure 4.16 T-peel adhesion results are shown for the reference adhesives 3M 467MP and 468MP on Oike VX 25T-2PO substrates with various processing. The anneal used in this study was the same as the drying procedure for optical calcium test samples: 80°C for 2-3 days in a vacuum oven at 1-5mbar. “As Received” samples were laminated to the barrier film immediately after removal of the barrier film’s protective layer with no subsequent surface preparation. Error bars represent one standard deviation.

Table 4.10 The T-peel adhesion strength of several adhesives are shown with the standard deviation in parentheses. All samples had a single adhesive layer with a thickness of approximately 50µm. The failure type is color coded where yellow is adhesive failure at the adhesive-to-adhesive interface; green is adhesive failure at the adhesive-to-substrate interface; and blue is cohesive failure in the adhesive. *Values with 2 layers of adhesive with a combined thickness of 50µm are shown for comparison for M65 which was too rigid to measure as a single layer.

Substrate	467MP	M65	M75	M85	F18	S3
PET (50µm)	2.35 N/cm	4.85 N/cm* (0.70N/cm)	4.77 N/cm (0.68N/cm)	7.41 N/cm (0.53N/cm)	1.32 N/cm (0.15N/cm)	3.01 N/cm (0.10N/cm)
Oike VX 25T-2PO	2.30 N/cm (0.27N/cm)	Stick-Slip	Not Tested	7.54 N/cm (1.55N/cm)	1.32 N/cm (0.15N/cm)	1.76 N/cm (0.20N/cm)

For optical properties, UV-Vis transmission spectra can be seen in Figure 4.17. The MAM PSAs have excellent transparency in the UVA and visible range and have no major concerns in this regard. F18 shows similar performance to the reference PSA with some absorption of UVA wavelengths. However, most flexible barrier films, such as Oike VX 25T-2PO, are designed to be UV blocking in order to protect the OPV from photo-degradation. This makes any UVA absorption by the adhesive moot as this light is mostly blocked before it would

arrive at the adhesive layer in an encapsulated device. One adhesive which does have some cause for concern from transparency is S3, which does have some absorption of wavelengths which are transmitted by the barrier film. This region is quite small however and should not cause a large loss of power conversion efficiency in the device unless the active layer has very strong quantum efficiencies in the blue region. It should also be noted that all of the adhesives outperformed the reference material at longer wavelengths.

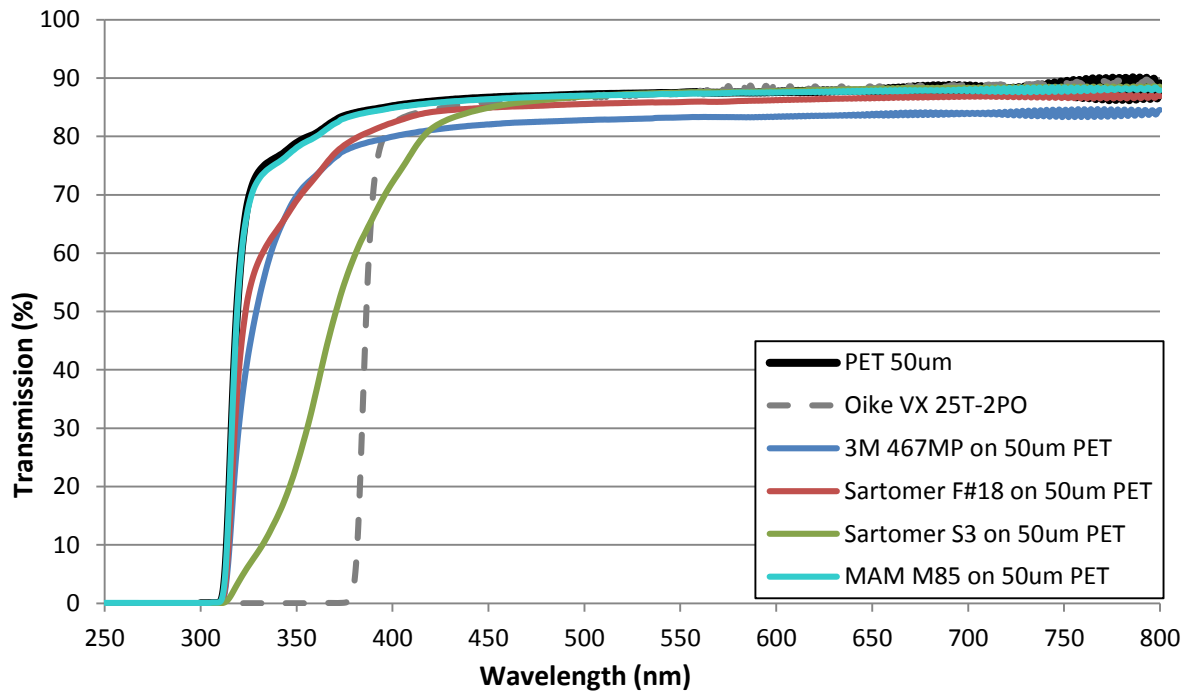


Figure 4.17 UV-Vis spectroscopy using a standard detector was performed on both a 50 μ m thick PET film and PET films with 50 μ m coatings of adhesive. For the adhesive samples, the PET surface was facing the laser source so that the same amount of reflection was present for all samples. The transmission spectrum for the barrier film Oike VX 25T-2PO with no adhesive coating is also shown to illustrate its UV blocking.

The permeation of the adhesives was evaluated using the optical calcium test and the results for lateral permeation are shown in Figure 4.18. It is immediately noticeable that the PSAs had much higher lateral permeation rates than the UV curing acrylates. As previously mentioned, the UV curing acrylates do not show a dependence on the adhesive thickness which indicates that the bulk barrier properties are quite good and that the interface is the dominant permeation pathway for water vapor. By comparison, M85 shows a strong dependence on adhesive thickness which indicates relatively high bulk water vapor permeation compared to the interface. When using the analytical model described in Chapter 3, M85 has an apparent interfacial permeation rate of 6.59×10^{-5} g/m/day compared to 2.86×10^{-5} g/m/day for the reference material. This shows that despite its strong adhesion, the interface remains an important permeation pathway for the MAM PSAs. The contrasting trends of M85 to the UV curing acrylates appear to indicate that good adhesion is necessary but not sufficient for limiting

interfacial permeation. The already strong adhesion and high bulk permeation rate of M85 make improvement of its bulk barrier properties the simplest method to improve its overall barrier performance. On the other hand, improvements to the bulk barrier properties of the UV curing acrylates can be predicted to have only minimal effects on the overall lateral permeation rate of these adhesives. These hypotheses are investigated in detail in Chapter 5.

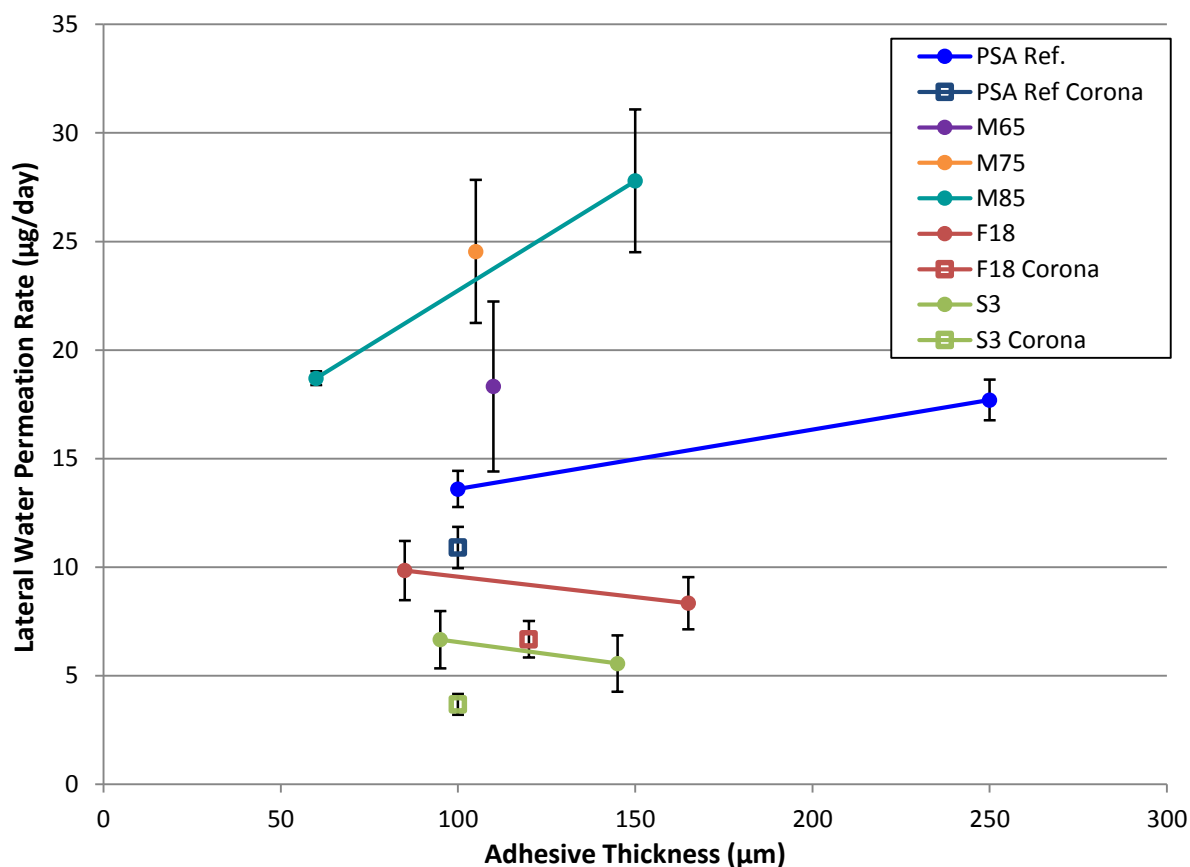


Figure 4.18 A plot of the average apparent lateral permeation rate as measured by the modified optical calcium test is shown for several adhesives. All values have been normalized to 45mm X 45mm calcium deposits to adjust for slight differences between samples. Error bars represent one standard deviation. “PSA Ref” refers to 3M 367MP and 468MP.

Conclusions

The thermo-mechanical, optical and permeation properties of MAM PSAs and UV curing acrylate adhesives were studied in order to determine their applicability to OPV encapsulation. MAM PSAs, which are based on solution processed block co-polymers, showed very strong adhesion to flexible plastic surfaces after annealing and also provided extremely good optical clarity in the UVA and visible wavelengths. However, before annealing the most rigid materials were difficult to properly laminate due to their low tack at room temperature. While their mechanical properties generally follow the trend of more PMMA leading to more

rigidity, there is a discontinuity in this behavior due to a change in morphology from micellar to worm-like for the highest PMMA content adhesive. This discontinuity was also seen in optical calcium tests where the two micellar adhesives had similar water vapor permeation while the worm-like adhesive is possibly slightly less permeable. However, even the lowest water vapor permeation rates were still quite high compared to the reference PSA and UV curing acrylates. Not only the bulk permeation but also the interfacial permeation was found to be high for these materials despite their strong adhesion.

Unlike the MAM PSAs, UV curing acrylates had adhesion problems on flexible plastics which required adjusting the formulations. The addition of a tackifying resin was found to increase the adhesion and flexibility of these adhesives, though it also caused the adhesive to become less transparent in the UVA and blue wavelengths. The UV curing acrylates outperformed both the MAM PSAs and the reference PSA in optical calcium tests. The results show no dependence on the adhesive thickness, indicating that the interface was the dominant permeation pathway for water vapor. The use of a hydrophobic tackifying resin and corona treatments did lower the permeation rate even further as the lateral water permeation was strongly linked to the adhesion. The lower water vapor permeation rates and acceptable levels of adhesion make these adhesives good candidates for OPV encapsulation.

Both types of adhesive showed promise in meeting different requirements for OPV encapsulation and merit further investigation. The high bulk permeation rate of the MAM adhesives could potentially be improved through the addition of inorganic particles which limit permeation. UV curing acrylates on the other hand could benefit from a stronger interface. Additionally, both types could potentially benefit from the use of active getter materials to limit permeation. The investigation of these hypotheses for improving the performance of these adhesives will be discussed in Chapter 5.

Chapter 5: Nanocomposites

Introduction

In order to alter various properties of adhesives, the addition of nanoparticles of inorganic materials to form a nanocomposite is a common method. This idea has been applied to the adhesives studied in this thesis in order to improve their barrier properties. Two different approaches to improving the water vapor barrier properties were employed through the use of either passive or active nanoparticles. Passive phyllosilicate particles were used to lengthen the diffusion pathway by creating a tortuous path. On the other hand, active zeolite nanoparticles were used to bind permeating water molecules via adsorption.

Overview of Particles

Phyllosilicates

Phyllosilicates are particles which are commonly used for passive barrier composites. Although they can often have high water sorption and thus an active nature, this is reliant upon their structure remaining in the form of stacked layers. Between these layers, ions can be added which aid in the sorption of water. However, in place of metal ions, organic ions can also be added. The organic ions then often have other organic structures attached which cause the particles to become exfoliated into individual plates once introduced into an excess of an appropriate organic solvent. The exfoliated plate-like particles have very high aspect ratios with diameters of several microns and thicknesses of only a few nanometers. This creates a large number of nanoparticles which create a tortuous path for permeating species, thus making a passive nanocomposite.

Three different grades of phyllosilicates were evaluated consisting of either montmorillonite or bentonite (a mix of mostly montmorillonite with other phyllosilicates). Cloisite Na⁺ used sodium ions between the layers and remained as a precipitate in both acetone and toluene even after sonication and overnight magnetic stirring. Its lack of organic modification made this material a poor choice for use in adhesive nanocomposites. Cloisite 10A and 15A both used ammonium salts to organically modify the particles. Both had two organic

tails on each ammonium ion. Cloisite 10A used one benzyl group and one hydrogenated tallow while 15A used two hydrogenated tallow groups. Both types of particles were able to be dispersed in toluene, with Cloisite 10A being faster and easier to disperse than 15A. When tested in dynamic light scattering (DLS) after dispersion in toluene, mono-disperse signals were seen for both types of particles. Due to their very high aspect ratio and the fact that DLS calculations assume spherical particles, the sizes of the particles calculated from DLS do not correspond to accurate particles sizes. Nevertheless, the calculated particle spherical diameters were 84nm and 237nm for 10A and 15A respectively. Due to its relative ease of use in toluene, Cloisite 10A was chosen for use with MAM PSAs which are deposited from solution in toluene.

When the particles were added to uncured F18 and S3 however, it was found that Cloisite 15A was easier to disperse than 10A, and thus Cloisite 15A was chosen for use with UV curing acrylates. However, it should be noted that the dispersion into these adhesives was more difficult than into toluene and required long periods of magnetic stirring and several cycles of sonication. 5wt% of Cloisite 15A did cause the liquid adhesives to become cloudy and produced a slight increase in viscosity. Concentrations of 10wt% phyllosilicate did not fully disperse and thus testing was limited to 5wt% phyllosilicate composites.

Zeolites

Nanoparticles of zeolites were tested as active materials which can adsorb water molecules to prevent them from permeating further into the adhesive. The zeolites tested were NZL-40 which are nanoparticles of approximately 30-60nm in size with a Linde Type L (LTL) structure. This structure has pore diameters in the range of 8-11Å and smaller channels of <4Å in diameter.¹⁸⁰ Though aluminosilicates by nature, these particles have had some ions exchanged with sodium ions. When dispersed in toluene, DLS showed that the particles could indeed be well dispersed, though they quickly aggregate. However, the aggregations were relatively weak and could be easily re-dispersed by shaking the cuvette by hand for a few seconds. This can be seen in Figure 5.1 which shows consecutive runs of DLS measurements with each measure starting when the previous measure was complete. When cast from toluene, the particles showed some aggregation as can be seen in the transmission electron microscopy images in Figure 5.2. It can be seen that despite the aggregation, the total size remains quite small and the particles were deemed acceptable for use with MAM PSAs. To limit any aggregation, MAM PSA nanocomposites using NZL-40 particles were sonicated immediately prior to deposition.

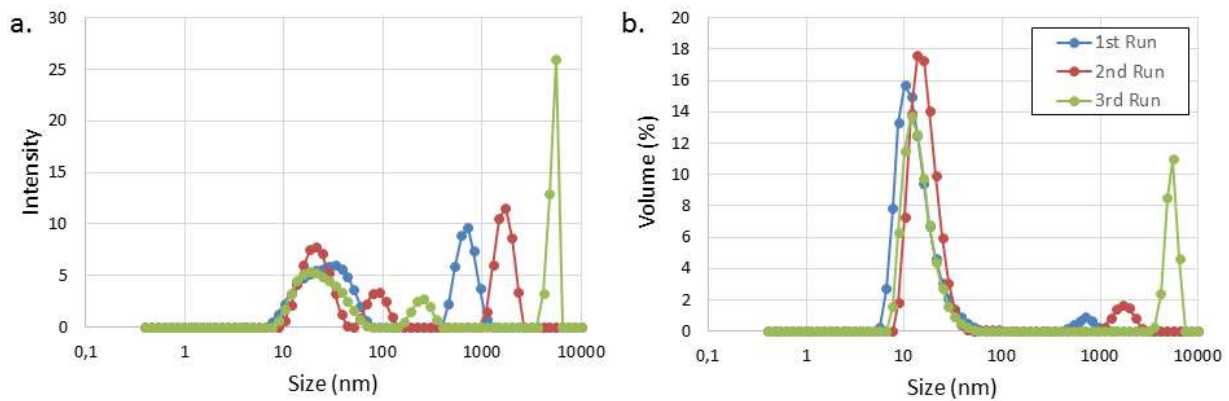


Figure 5.1 DLS curves in both (a) measured intensity and (b) volume average are shown for 0.03wt% NZL-40 in toluene. The three measures, taking about 30s-60s each to complete, were made consecutively without removing the sample. The growth of aggregates can be seen as a shift to the right of the peaks and the the growth of the amplitude of the right most peaks.

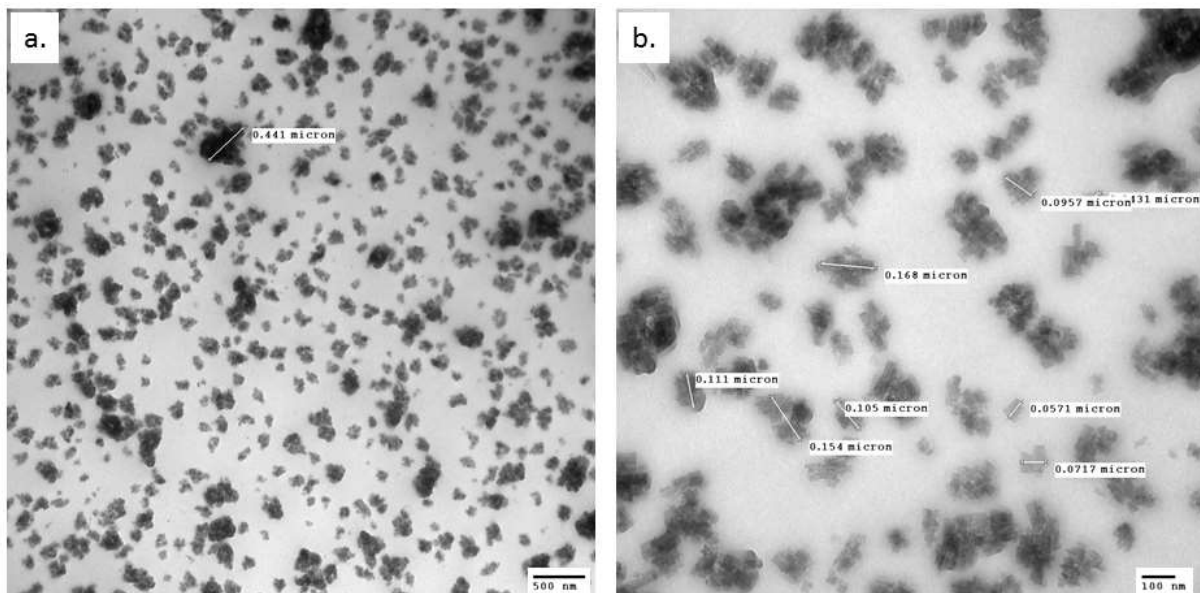


Figure 5.2 TEM images of NZL-40 nanoparticles as deposited from a 20wt% dispersion in toluene are shown at two different magnifications in order to show the size of typical aggregates. Images were taken with the aid of the staff of the Centre Hospitalier Universitaire de Clermont-Ferrand where the microscope was located.

It was also seen that when the standard solvent evaporation procedure for MAM PSAs in toluene was used, the zeolite particles often migrated to the lower interface. This can be seen in the spectra from attenuated total reflection mode of Fourier transform infrared spectroscopy (FTIR-ATR) in Figure 5.3. It was found that this could be avoided by drying the samples immediately at an elevated temperature instead of room temperature, which is seen in Figure 5.3 as nearly equivalent spectra for the top and bottom surfaces of a cast film. The increased temperature caused a faster evaporation of toluene, therefore giving the particles less time to migrate. The migration of the zeolite particles during deposition of the adhesive nanocomposite was studied and characterized by Diane Delbégue as part of her internship at the Institut de

Chimie de Clermont-Ferrand. Additionally, it can be seen in Figure 5.4 that the addition of the zeolite nanoparticles did not change the morphology of the MAM PSAs.

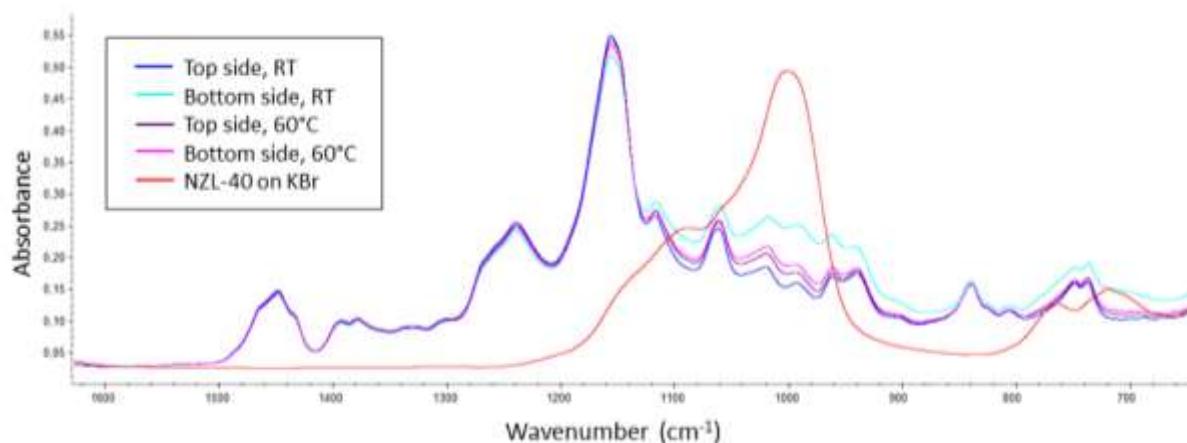
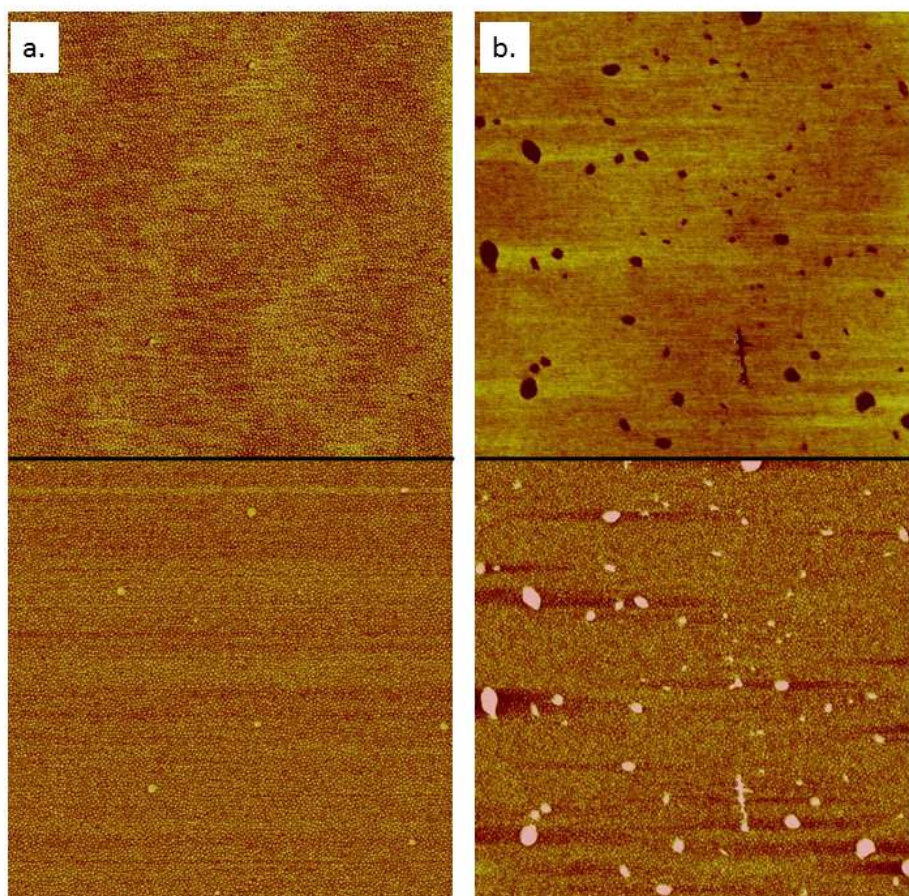


Figure 5.3 FTIR-ATR spectra of M85 with 5wt% NZL-40 are shown for both the top and bottom surfaces for films cast with initial drying at room temperature (RT) and at 60°C. After initial drying, all samples were fully dried at 90°C for 10min. All films were cast to an uncontrolled thickness on fluoropolymer sheets from a solution of 25wt% adhesive nanocomposite in toluene. The NZL-40 spectrum was recorded in transmission FTIR using a potassium bromide substrate. All testing was performed by Diane Delbeuge.



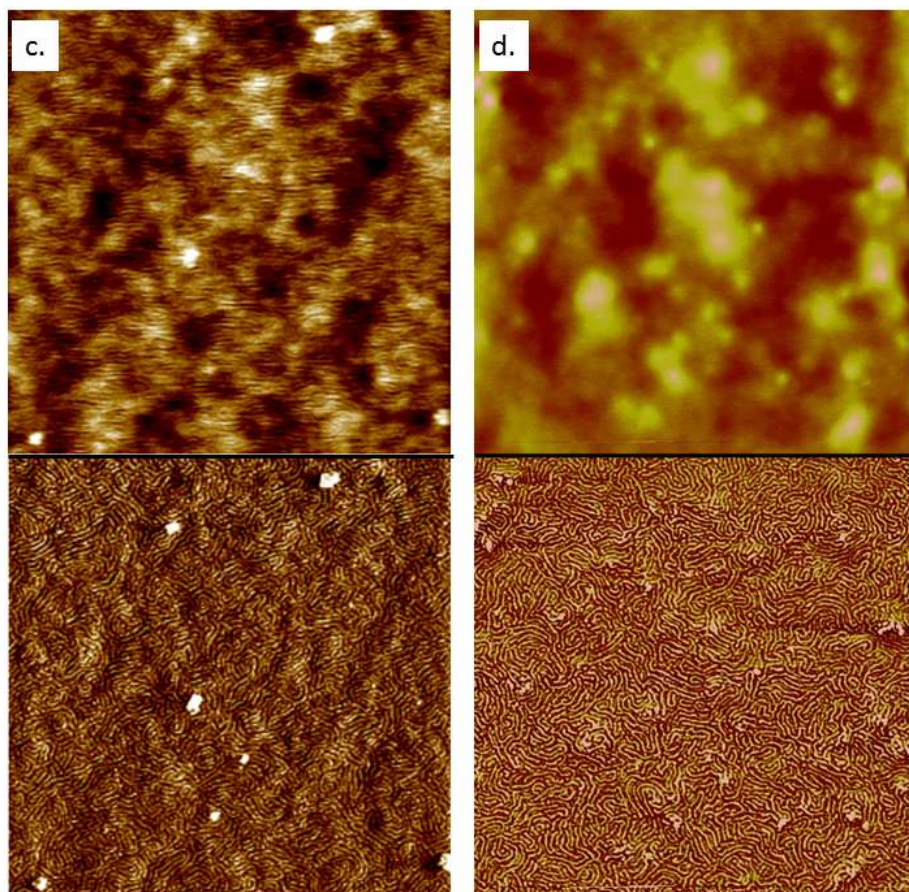


Figure 5.4 AFM images taken in tapping mode of (a) M85, (b) M85 with 5wt% NZL-40, (c) M65 and (d) M65 with 10wt% NZL-40 are shown in both (top) height and (bottom) phase. All images show an area of $5\mu\text{m} \times 5\mu\text{m}$. The images for M65 and M85 were taken with the aid of Isabel Fraga Dominguez at the Institut de Chimie de Clermont-Ferrand. It can be seen that the addition of NZL-40 nanoparticles did not change the morphology of the MAM PSAs.

As active water getters, the sorption of water by NZL-40 particles was also characterized using moisture content analysis. This testing measures the change in mass of a sample when it is heated. The loss of mass during heating can then be attributed to desorbed gases, which in the case of zeolites is mainly due to water vapor. In the testing shown in Figure 5.5, particles were dried using the moisture analyzer at 130°C and then exposed to ambient air for various periods of time before being dried and measured at 130°C . The results show a rapid sorption of 2-3wt% almost immediately upon exposure to ambient air. The sorption then continues to increase rapidly after only a few minutes of exposure, ultimately achieving a total water sorption capacity of 14% after overnight exposure to ambient air. This is a similar capacity to the 10-13wt% reported by the manufacturer. The results of this testing show the importance of thoroughly drying the zeolites immediately before use, and that an inert atmosphere should be used whenever possible when handling the zeolites.

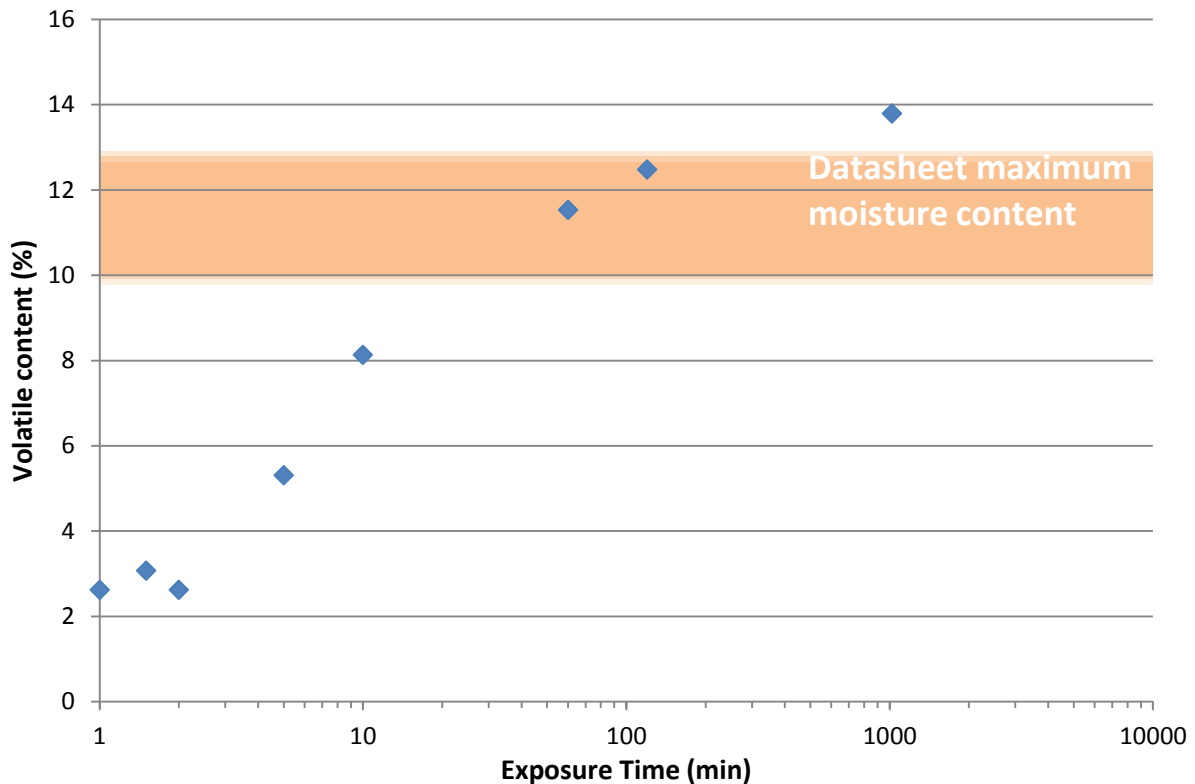


Figure 5.5 The measured volatile content of NZL-40 nanoparticles from drying at 130°C is shown after various exposure times to ambient air at 24°C and 57% relative humidity.

Comparison of Properties: Neat vs. Phyllosilicate vs. Zeolite

The addition of nanoparticles to the adhesives studied in this thesis was designed to impact the gas barrier properties of the adhesives. However, as is almost always the case when changing a material's formulation, other properties can change as well. It therefore becomes important to look at all of the changes to the adhesive regardless of whether the goal is to modify or maintain that property. In this section the effects on the properties of the adhesives as a result of modification with nanoparticles are discussed. For the MAM PSAs, the similar performance by all three adhesives in optical calcium tests made M85 the most logical choice for further testing as it provides the best adhesion and is the easiest of MAM PSAs to laminate. For this reason, most nanocomposite testing for the MAM PSAs used this polymer adhesive.

Thermo-mechanical and Optical Properties

In general, the addition of inorganic particles into a polymeric adhesive causes the composite to become more rigid than the neat adhesive with increases in both elastic modulus and the glass transition temperature (T_g). Tensile dynamic mechanical thermal analysis (DMTA) was used to compare the nanocomposites to the neat adhesives in this regard. Figure 5.6 shows curves for M85 and F18 for the neat adhesives, phyllosilicate nanocomposites and zeolite nanocomposites.

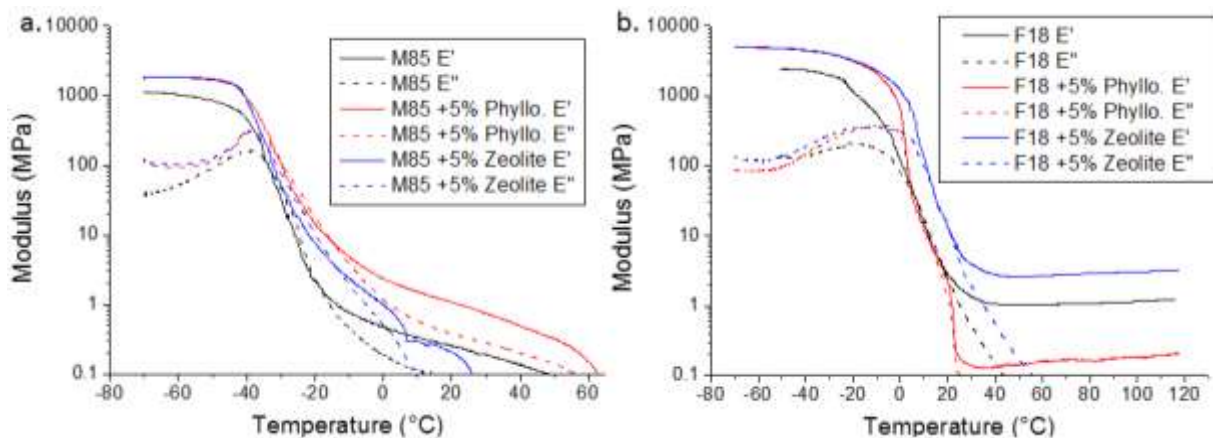


Figure 5.6 The storage (E' , solid lines) and loss moduli curves (E'' , dotted lines) from tensile DMTA tests for materials based on (a) M85 and (b) F18 are shown. All tests were performed at 3°C/min, 1Hz and 0.1% strain.

The T_g of M85, as measured by the peak of the loss modulus curve, remained relatively stable with the addition of nanoparticles for both organically modified phyllosilicates and zeolites. However, a slight increase in the rigidity of the composites below T_g was seen for both nanocomposites, especially for organically modified phyllosilicates. Despite this increase in rigidity, the nanocomposites are still very soft and flexible, thus posing no issue for use in flexible OPV modules. Unfortunately, this soft nature also caused all samples to fall below the limit of detection for the machine before reaching the 65°C temperatures used for optical calcium tests.

For F18, the addition of organically modified phyllosilicates did little to change the rigidity of the adhesive. This nanocomposite did show an elevated storage modulus at temperatures well below T_g , but then exhibited a sharper transition which gave it a nearly identical storage modulus as neat F18 throughout most of the glass transition region. The peak of the loss modulus curve was also slightly modified, moving from -20°C for the neat adhesive to -9°C for the nanocomposite and thus showing an increase in the T_g . For the purpose of encapsulating OPV modules, the mechanical properties can be considered to be very similar for

this nanocomposite. On the other hand, zeolite nanoparticles did cause the adhesive to become more rigid and showed an increase in the storage modulus throughout the entire temperature ranged tested. The peak of the loss modulus curve was also shifted from -20°C for the neat adhesive to -10°C for the nanocomposite, thus indicating an increase in the T_g . This increase in rigidity furthers the need for a more flexible version of F18 if the encapsulated flexible OPV modules are to be used in colder climates, as discussed in Chapter 4.

As can be seen in Table 5.1, the addition of nanoparticles to M85 had only a minimal effect on the adhesive strength. Both organically modified phyllosilicates and zeolite nanoparticles led to slight increases in the adhesion compared to the neat polymer, though the increases were not large. On the other hand, the addition of nanoparticles caused losses of adhesion for F18, especially with organically modified phyllosilicates. Given the dominance of interfacial permeation seen in neat F18 during the optical calcium test, losses in adhesion are particularly worrying for F18 based nanocomposites. In an effort to increase this adhesion, tests on corona treated substrates were also performed. The results plotted in Figure 5.7 show that much of the adhesion loss for F18 with organically modified phyllosilicates could be recovered through the use of a corona treatment with an average adhesion strength of 1.65N/cm for 50 μ m of adhesive on Oike VX 25T-2PO substrates. As this nanocomposite was the weakest in adhesion testing, it was also tested using the procedures employed for the preparation of optical calcium test samples. This process requires an extended degassing procedure at 80°C under vacuum (1-5mbar) between the corona treatment and the deposition of the adhesive onto the barrier film. This reduces the surface energy gain from the corona treatment and thus raised concerns for the relatively weak adhesion of the nanocomposite of F18 with organically modified phyllosilicates. An average adhesion strength of 1.18N/cm was achieved with this method, which, though lower than when the adhesive is deposited immediately after corona treatment, is still much larger than the non-corona treated samples which had an average adhesion strength of only 0.68N/cm.

Table 5.1 The T-peel adhesion strength for several adhesives are shown with the standard deviation in parentheses. All samples had a single adhesive layer with a thickness of 50-70 μ m. The failure type is color coded where green is adhesive failure at the adhesive-to-substrate interface and blue is cohesive failure in the adhesive.

Polymer	Neat	+5wt% Phyllo.	% Change	+5wt% zeolite	% Change
M85	7.54 N/cm (1.55N/cm)	7.95 N/cm (0.60N/cm)	+5.4%	8.10N/cm (0.48N/cm)	+11.5%
	1.32 N/cm (0.15N/cm)	0.68 N/cm (0.03N/cm)	-48.5%	1.14N/cm (0.06N/cm)	-13.6%

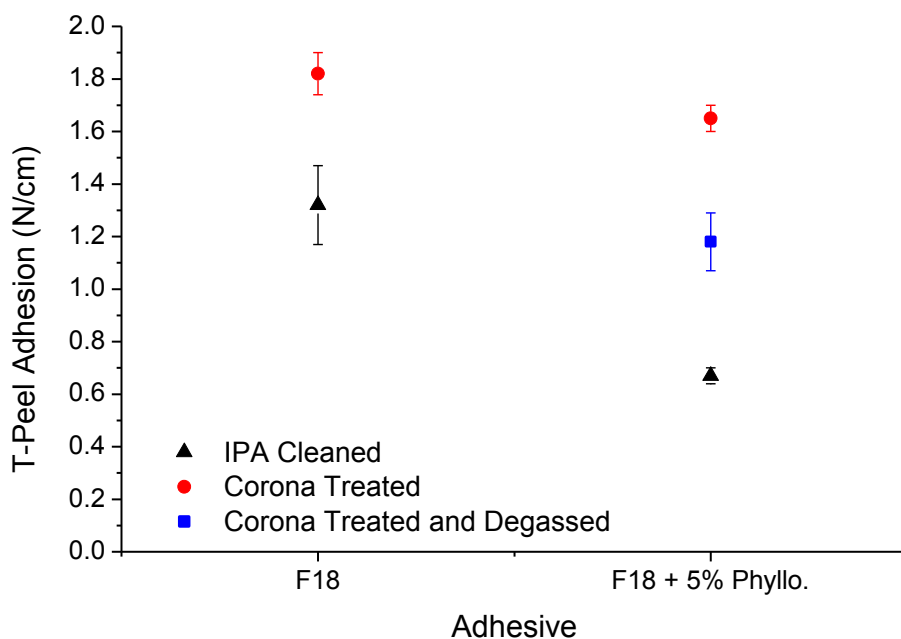


Figure 5.7 The T-peel adhesion on Oike VX 25T-2PO barrier films for F18 and a nanocomposite of F18 with 5wt% organically modified phyllosilicates is shown for various surface treatments of the barrier film. The degassing procedure is the same used for the optical calcium test of 80°C and 1-5mbar for 2 days before cooling to 30°C still under vacuum.

The addition of nanoparticles also had an influence on the optical properties of the nanocomposites as can be seen in Figure 5.8. All samples were coated onto a single 50µm thick PET substrate and tested with the PET facing the incoming laser in order to avoid changes from reflection. M85, which showed almost no difference compared to uncoated PET when neat, was unaffected optically by the addition of zeolite nanoparticles. However, organically modified phyllosilicate particles caused a reduction in transparency across the visual spectrum, especially at shorter wavelengths. F18 showed the opposite behavior in nanocomposites with organically modified phyllosilicates causing only a minimal loss of transparency at short wavelengths while zeolite nanoparticles caused a large loss across the whole visual spectrum. Both M85 with organically modified phyllosilicates and F18 with zeolite nanoparticles would likely have an impact on the overall performance of OPV modules as they block light which would normally traverse the barrier film. While further investigation is needed to determine the exact cause of this contrasting behavior between M85 and F18, the most likely cause is a difference in ability of the particles to disperse within the polymer matrix. It should also be noted that all measures were made using a standard detector and not with an integration sphere. This means that the actual transmission of the composites could be higher as the particles may have caused enough light scattering that some light that was transmitted across the sample exited the material at a sufficiently large angle to miss the detector. While a larger amount of

diffuse light being transmitted across the material would aid in the performance of an OPV module, diffuse light is converted to an electrical current less efficiently than more direct angles of incidence thus limiting its effect.

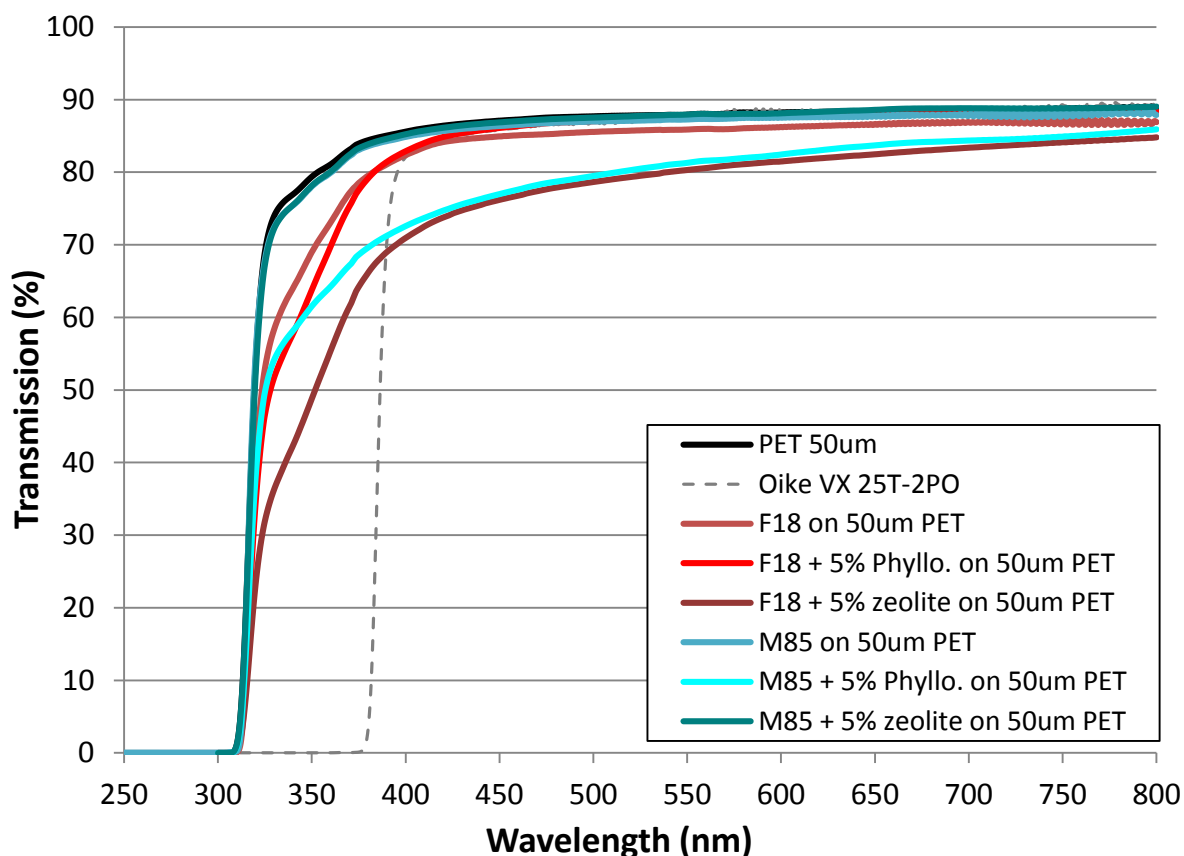


Figure 5.8 UV-Vis spectroscopy using a standard detector was performed on both a 50 μ m thick PET film and PET films with 50-60 μ m coatings of adhesive. For the adhesive samples, the PET surface was facing the laser source so that the same amount of reflection was present for all samples. The transmission spectrum for the barrier film Oike VX 25T-2PO with no adhesive coating is also shown to illustrate the UV blocking of barrier films.

Permeation

The original goal of the modification of the adhesives with nanoparticles in this thesis was to limit the gas permeation of the materials. Therefore, optical calcium tests using the method described in Chapter 3 were performed using the nanocomposite adhesives. Given the relatively large contribution to the lateral permeation by the bulk adhesive, M85 was the most likely to be improved by the addition of nanoparticles. The results of optical calcium tests of neat M85, M85 nanocomposites and reference materials are shown in Figure 5.9. The addition of nanoparticles did indeed limit the lateral permeation of M85. When the results are normalized to 45mm x 45mm calcium deposits for comparison, the organically modified phyllosilicates provided a decrease in lateral water vapor permeation of 23% with the addition of only 5wt%

of Cloisite 10A compared to the neat adhesive at the same thickness. This value becomes a 53% decrease when the nanoparticle loading is increased to 10wt%. Though the ability of passive nanocomposites based on organically modified phyllosilicates to limit gas permeation has been well demonstrated, these results confirm that this type of nanocomposite is indeed an effective method to limit the water vapor permeation in thermoplastic block copolymer PSAs. However, to the knowledge of the author, no gas permeation data has been published for nanocomposites of zeolite nanoparticles in PSAs. For the active nanocomposite of M85 with NZL-40 nanoparticles, a decrease in lateral water vapor permeation of 57% was seen for a loading of only 5wt% of nanoparticles compared to neat M85 at the same thickness and calcium deposit size. This large decrease in the apparent lateral water vapor permeation rate demonstrates the effectiveness of this type of active nanocomposite for improving gas barrier properties of flexible adhesives.

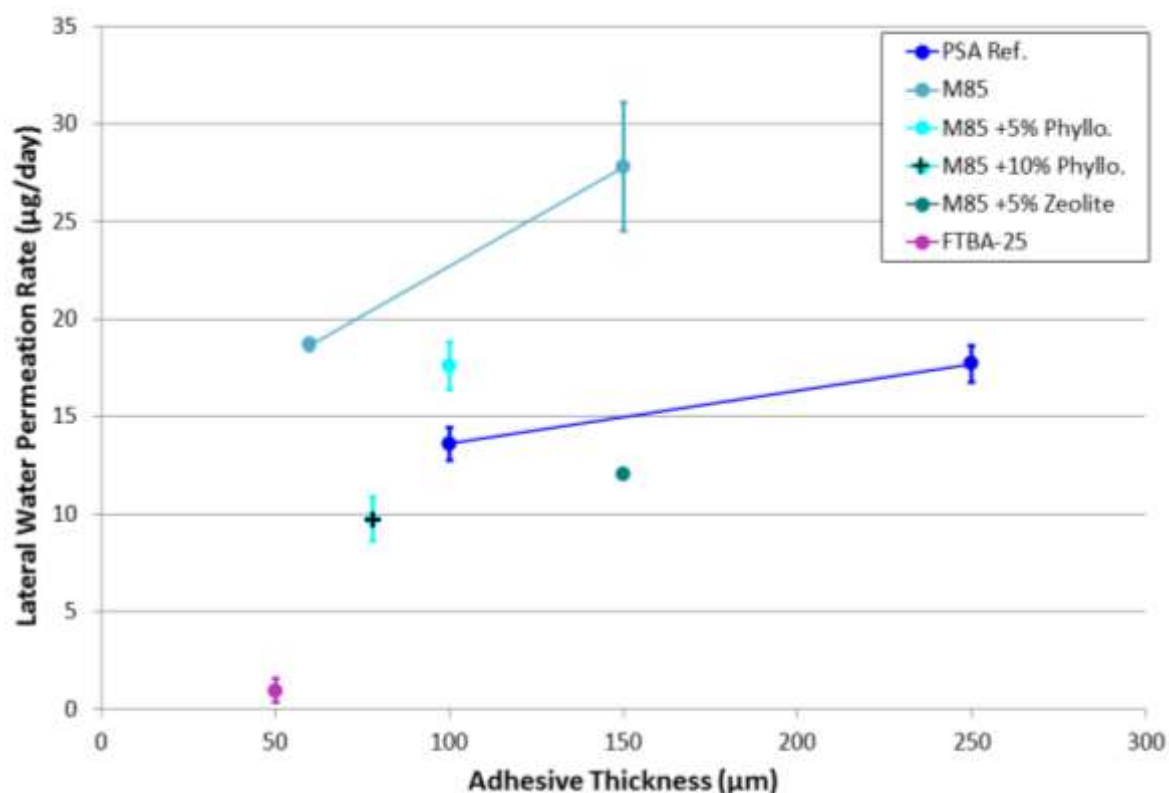


Figure 5.9 A plot of the average apparent lateral permeation rate as measured by the modified optical calcium test is shown for M85 based adhesives and reference materials. All values have been normalized to 45mm X 45mm calcium deposits to adjust for slight differences between samples. Error bars represent one standard deviation. “PSA Ref” refers to 3M 367MP and 468MP while FTBA-25 is a state-of-the-art commercial barrier PSA.

Nanocomposites of both 10wt% organically modified phyllosilicate and 5wt% of zeolite nanoparticles in M85 were able to outperform the reference material of 3M 467MP and 468MP in optical calcium tests. Despite the large decrease in apparent lateral water vapor permeation, the relatively high lateral water vapor permeation in neat M85 prevented the nanocomposites

from outperforming the state-of-the-art barrier PSA FTBA-25 from 3M. Further development and formulation of adhesives based on M85 will be required to reach this level, though the use of active nanoparticles such as NZL-40 provides a powerful tool to improve the water vapor barrier properties of this class of adhesive without harming the flexibility, adhesion or transparency.

Nanocomposites of F18 were also tested in optical calcium tests. The dominance of the interfacial permeation compared to that in the bulk adhesive for F18 made addition of nanoparticles less likely to limit the overall lateral water vapor permeation than for the MAM PSAs. Nevertheless, Figure 5.10 shows that there was some improvement, especially for nanocomposites with organically modified phyllosilicates. This result is particularly surprising since these nanocomposites showed decreased adhesion, which would imply a weaker interface for an adhesive which is already susceptible to interfacial permeation. The combination of weaker adhesion and decreased permeation could indicate an increased concentration of organically modified phyllosilicate particles near the interface due to sedimentation. This could lower the permeation rate of the interlayer while simultaneously affecting the adhesion, though further study is required to test this hypothesis. Regardless of its lower adhesion compared to neat F18, this nanocomposite did exhibit lower lateral water permeation for corona treated samples. This continues the trend seen for other materials where increased adhesion leads to lower lateral water permeation, as long as the adhesives are of the same chemistry.

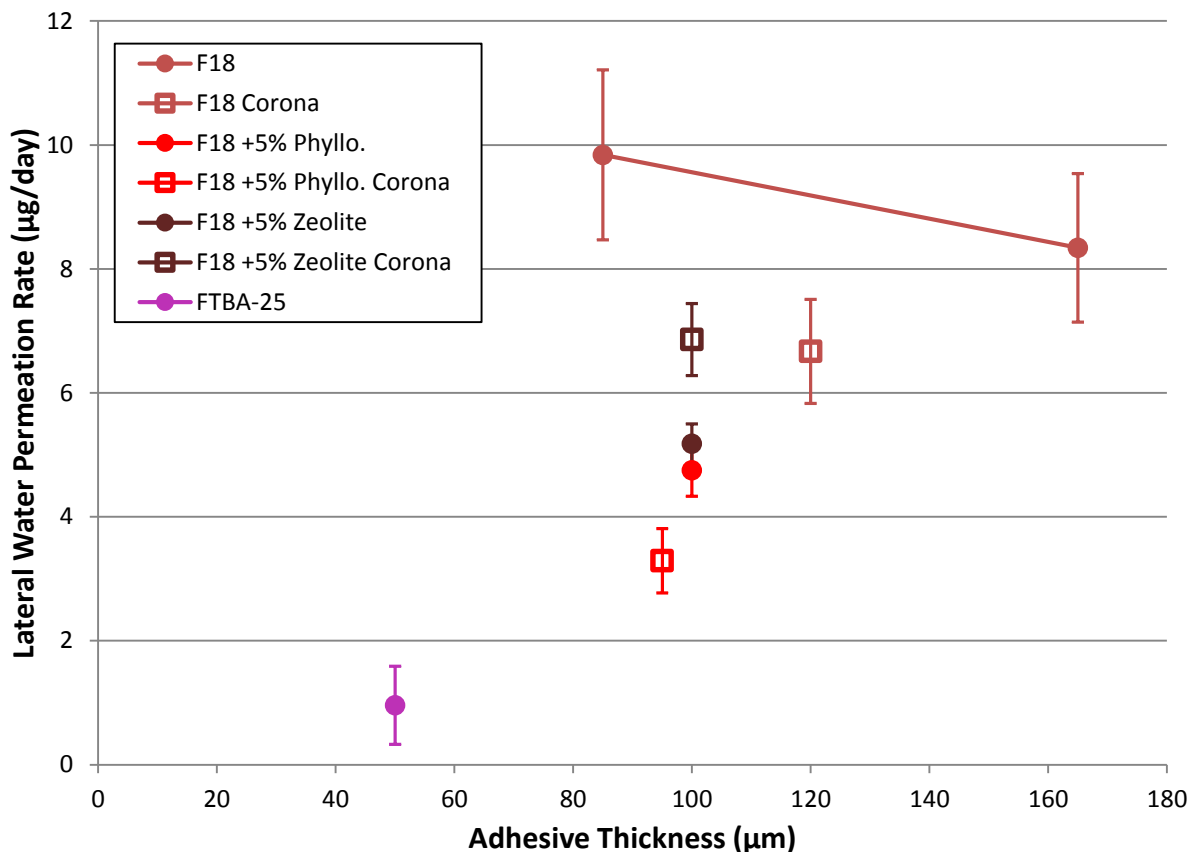


Figure 5.10 A plot of the average apparent lateral permeation rate as measured by the modified optical calcium test is shown for several F18 based adhesives and a reference material. All values have been normalized to 45mm X 45mm calcium deposits to adjust for slight differences between samples. Error bars represent one standard deviation.

Samples with zeolite nanoparticles also showed an improvement compared to neat F18, with the apparent lateral water permeation being very similar to that of the nanocomposites using organically modified phyllosilicates. The relatively small loss of adhesion compared to neat F18 for nanocomposites using zeolite nanoparticles indicates a smaller presence of particles in the interlayer compared to that seen for the organically modified phyllosilicates. However, the particles continued to act as a sink for moisture in the adhesive allowing for the decreased water permeation. The lack of a larger impact on the water vapor permeation by the zeolite nanoparticles in F18 nanocomposites is also somewhat surprising considering the large effect of these particles on M85's water vapor permeation. However this result does agree with the initial hypothesis that improvements to the bulk barrier properties of F18 would not greatly affect the apparent lateral water vapor permeation as the dominant permeation pathway is along the interface. Another surprising result for this composite was the increase in water permeation caused by the use of a corona treatment as this was the only material to display such behavior. The adhesion for this nanocomposite was not measured on corona treated substrates so it is still possible that this nanocomposite did not exhibit the same increase in adhesion seen for other

materials on corona treated substrates. Although further study is needed to determine the exact cause of the increased lateral water permeation using corona treated substrates, it is possible that the increased polarity caused a larger migration of zeolite particles to the interface leading to a weaker interface.

It should also be noted though, that even the best performing F18 based nanocomposites did not achieve the same level of water vapor barrier protection as the state-of-the-art barrier adhesive 3M FTBA-25. In order to reach this level of performance in the optical calcium test, improvements to the interface rather than the bulk adhesive will likely be needed due to this pathway's relatively high water vapor permeation for F18.

Nanocomposites based on S3 were also tested in the optical calcium test, though they were not studied in-depth for changes to thermo-mechanical and optical properties. As the neat adhesive with the lowest apparent lateral water vapor permeation rate in optical calcium tests, attempts were made to further improve S3 with the hope of outperforming FTBA-25 in optical calcium tests. However, changes to the bulk adhesive through the introduction of nanoparticles showed little effect on the water vapor permeation as can be seen in Figure 5.11. As with F18, the dominance of the interface as a permeation pathway must first be overcome in order for S3 based materials to reach state-of-the-art water vapor barrier performance.

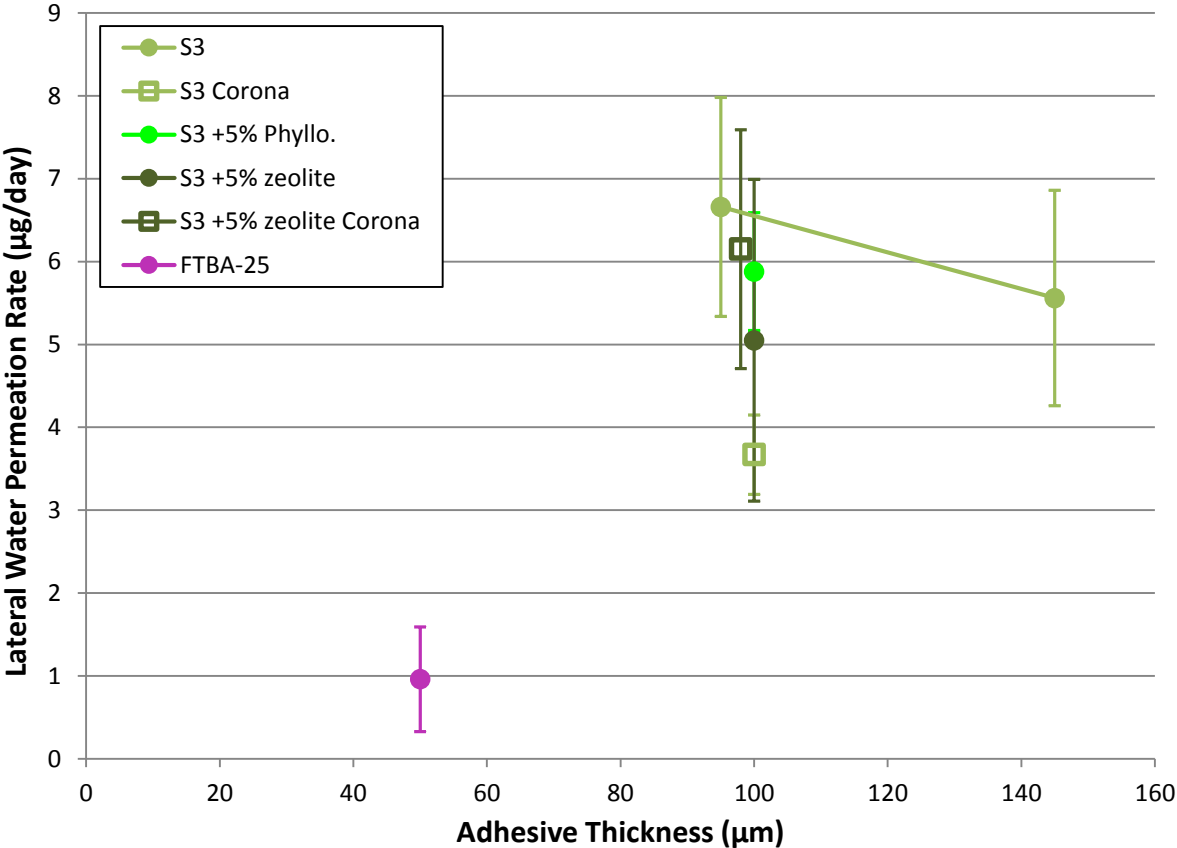


Figure 5.11 A plot of the average apparent lateral permeation rate as measured by the modified optical calcium test is shown for several F18 based adhesives and a reference material. All values have been normalized to 45mm X 45mm calcium deposits to adjust for slight differences between samples. Error bars represent one standard deviation.

Conclusions

The inclusion of inorganic nanoparticles into both MAM PSAs and UV curing acrylates was achieved using both phyllosilicate and zeolite particles. To properly disperse the phyllosilicates, an appropriate organic modification was necessary, especially for UV curing acrylates where dispersion took longer to achieve. Zeolite nanoparticles were able to be dispersed without the use of organic modifiers, though some aggregation did occur over a period of a few minutes. However, these aggregates were easily re-dispersed leading to the sonication of all nanocomposites immediately prior to deposition. The observed sedimentation of zeolite nanoparticles in MAM PSAs during deposition was easily remedied by increasing the evaporation rate of the solvent. The addition of nanoparticles also caused slight increases in the viscosity of the adhesives, especially for the UV curing acrylates which already have higher viscosities. AFM images also confirmed that the morphology of the MAM PSAs was unchanged by the addition of zeolite nanoparticles.

For the MAM PSAs, the presence of organically modified phyllosilicates caused the adhesive to become more rigid and less transparent, though neither property was altered to the point of making the material unsuitable for OPV encapsulation. Zeolite particles had a much smaller effect on these properties showing only a very slight increase in rigidity and almost no change in transparency. Both types of nanoparticles had little effect on the adhesion of the adhesive showing very minor increases in t-peel adhesion strength. For the UV curing acrylate adhesive F18 however, different trends were seen. Unlike the MAM PSAs, it was zeolite nanoparticles that had stronger increases in rigidity and larger losses of transparency. The organically modified phyllosilicates did show an elevated T_g , but did not greatly affect the rigidity or transparency. The changes in adhesion were more notable for F18 based nanocomposites with both types of particles showing decreased adhesion compared to the neat adhesive. This was especially true for organically modified phyllosilicates, though most of the loss of adhesion could be recouped through the use of a corona treat on the substrate prior to bonding. This is of particular importance for F18 which was shown in Chapter 4 to water vapor permeation dominated by the interfacial pathways.

When subjected to optical calcium tests, M85 and F18 both had decreases in apparent lateral water vapor permeation for all nanocomposites in comparison to the neat respective

adhesives. This change was greatest for M85 where nanocomposites of 5wt% and 10wt% organically modified phyllosilicates decreased the lateral permeation rate by 23% and 53% respectively compared to the neat adhesive. A nanocomposite of 5wt% zeolite nanoparticles was even more effective, resulting in a 57% decrease in lateral permeation in optical calcium tests as compared to the neat adhesive. The relatively large amount of permeation through the bulk of M85 made the use of nanoparticles to limit permeation very effective. For F18, the decreases in permeation were smaller, but still present. Nanocomposites of 5wt% organically modified phyllosilicates and nanocomposites of 5wt% zeolite nanoparticles showed similar performance to each other in optical calcium tests. It was expected that nanocomposites would have only minimal effects on the lateral permeation of F18 due to the interfacial permeation pathway being dominant, however both types of particles were able to decrease the water vapor permeation as they were also present near the interface. This is especially true for the organically modified phyllosilicates which showed a large loss in adhesion indicating the presence of particles in the interlayer and at the interface. In this location the nanoparticles were able to have a large enough effect on the water vapor permeation to overcome the decrease in adhesion, which, according to the trends seen in Chapter 4, would be expected to cause an increase in permeation.

The results seen in the characterization of nanocomposites of both MAM PSAs and UV curing acrylates with both organically modified phyllosilicates and zeolite nanoparticles indicate that these materials have great potential for use in encapsulating flexible OPV devices, which will be discussed in Chapter 6. In particular, the use of zeolite nanoparticles in MAM PSAs is very promising given their large reduction in permeation while having little effect on rigidity, adhesion or transparency. Nanocomposites using UV curing acrylates are also very intriguing options as they showed the lowest water vapor permeation rates of any of the materials developed in this thesis.

Chapter 6: Encapsulation of Organic Photovoltaic Cells

Introduction

In addition to the characterization of the adhesives and nanocomposites described in Chapters 4 and 5, these materials were also tested by encapsulating functional organic photovoltaic (OPV) devices and subjecting them to accelerated aging conditions. As the end goal for the development of the materials in this thesis is the encapsulation of flexible OPV devices, this testing allows the materials to demonstrate their ability, or lack thereof, to be implemented for their designed purpose. This testing also allows for a comparison of the water permeation results from optical calcium tests with the aging of actual OPV devices in humid environments. In this thesis, three different studies were performed using various encapsulation schemes to test various adhesives.

All tests used OPV cells with an inverted structure and were all fabricated in the same manner. The exact architecture of the cells can be seen in Figure 6.1 along with an image of a complete device before encapsulation. All OPV devices for the various studies were prepared by Lukas Wagner, Florence Ardiaca and Nathalie Nguyen, all of whom worked at the CEA's Laboratoire des Modules Photovoltaïques Organiques. The cells used 17mm x 25mm x 175 μ m substrates consisting of PET with a transparent conducting oxide (TCO) on one surface. Pads of chromium coated in gold were then deposited sequentially via evaporative physical vapor deposition at the ends of the substrates to aid in contacting the electrodes when measuring the completed cell. The electron transport layer (ETL) was made of zinc oxide nanoparticles spin coated in ambient atmosphere from a suspension in ethanol. The active layer had a bulk heterojunction structure of poly(3-hexylthiophene) (P3HT) for an absorber and phenyl C₆₁ butyric acid methyl ester (PCBM) as an electron acceptor. This active layer was spin coated onto the ETL from solution in dichlorobenzene inside an inert atmosphere glove box. The hole transport layer (HTL) consisted of poly(3,4-ethylenedioxythiophene) blended with poly(styrene sulfonate) (PEDOT:PSS) and was spin coated onto the active layer in air from an aqueous solution. Finally, a silver back electrode was deposited by evaporative physical vapor deposition in a manner that created two cells per substrate. All cells were then both measured

via J-V characterization and stored inside an inert atmosphere glove box. Only cells showing good performance in J-V characterization were used in the encapsulation studies. All accelerated aging was performed according to the ISOS-D-3 standard which uses 65°C and 85% relative humidity without illumination.

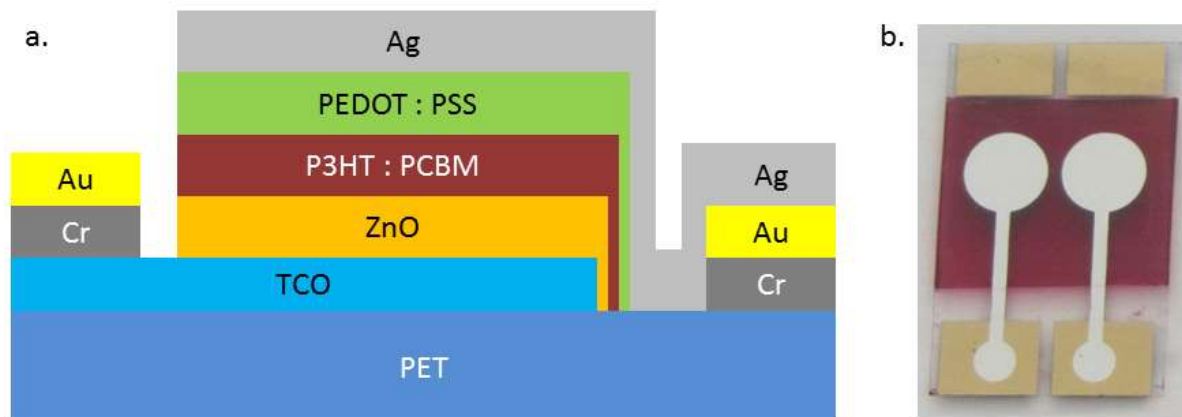


Figure 6.1 (a) A cross-sectional diagram of an OPV cell used in this thesis is shown with the different layers labeled. Please note that the diagram is not to scale. (b) An image of the backside of a completed cell is shown. The red color comes from the active layer while the light gray regions are the silver electrodes and the tan regions are the gold pads. The configuration of the silver electrodes and gold pads demonstrates how two separate cells were fabricated on a single substrate. (Photo taken by Matthieu Manceau of the Laboratoire des Modules Photovoltaïques Organiques)

Encapsulation Processes

As different encapsulation schemes present different advantages and problems, several were considered for the testing used in this thesis. Exiting wires for electrical connections can often create alternative pathways for permeation and were thus avoided when possible. This is especially an issue for pressure sensitive adhesives (PSA) which, due to their limited ability to flow, can often leave a gap at large, sharp changes in a surface such as a wire or bussing on a substrate. One solution to this problem was to fully encapsulate the cells with no exiting wires or electrical connections. To measure the cells, the barrier film can be cut open over the electrodes. To protect the device from the scalpel used to cut the barrier film and from the scraping needed to remove residual adhesive, a ribbon of 3M Charge-Collecting Solar Tape 3307 bussing was placed over the electrodes prior to encapsulation. This destructive process means that each device can only be measured once after encapsulation, eliminating the ability to measure the cells immediately after encapsulation and to track the aging of a single cell over multiple time points. This scheme will henceforth be referred to as “one-shot” encapsulation and can be seen in Figure 6.2a. Another solution which avoids exiting wires is to leave the electrodes un-encapsulated. This scheme allows for repeated and facile measure of the cells,

however it also allows for much less control over the distances from the edge of the encapsulation to the cell. It can also potentially cause the hygroscopic PEDOT:PSS layer to be exposed to air in some regions outside the encapsulation, which provides a potential pathway for water vapor permeation. This scheme can be seen in Figure 6.2b and will be henceforth referred to as “open-electrode” encapsulation. A final encapsulation scheme which was used in this thesis consists of using 3M Charge-Collecting Solar Tape 3307 bussing to connect the two cells in parallel and then exit the encapsulation. This scheme provides good control over the distance from the edge of the encapsulation to the cell and allows for repeated and facile measure of the cells, however, it also creates the previously discussed problem of electrical connections which exit the encapsulation. This scheme can be seen in Figure 6.2c and will henceforth be referred to as “ribbon” encapsulation.

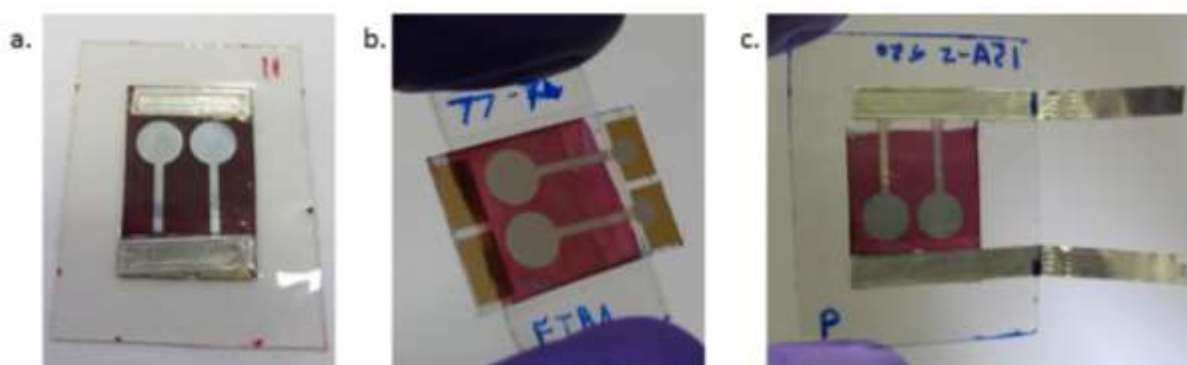


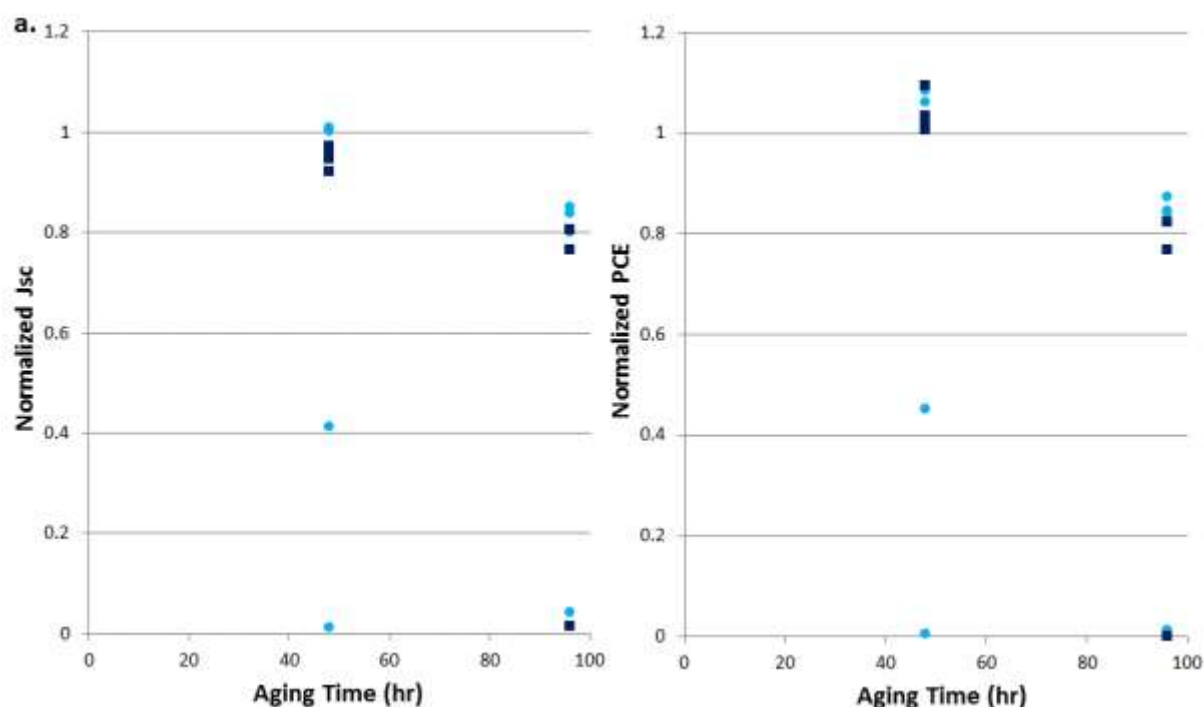
Figure 6.2 Images of encapsulated OPV cells after ISOS-D-3 aging are shown for (a) one-shot, (b) open electrode and (c) ribbon encapsulation schemes.

Accelerated Humidity Testing

Reference PSA

In order to verify the findings presented in Chapter 3 that adhesive thickness plays a role in the total amount of lateral permeation, OPV cells were encapsulated using both 3M 467MP and 468MP. As PSAs are more susceptible to leaving voids along the edge of electrical connections which exit the encapsulation, the one-shot encapsulation scheme was chosen for this study. This scheme also provides a geometry which is the most similar to the one used for the optical calcium test. In order to measure each cell independently despite being connected in parallel, a light blocking mask was used which caused only one cell to be illuminated during J-V characterization. Four OPV devices (8 cells) were encapsulated using each adhesive and Oike VX 25T-2PO barrier films. Two devices per adhesive were tested after 48 hours of exposure to

65°C and 85% relative humidity in dark storage while the remaining two devices per adhesive were tested after 96 hours of exposure under the same conditions. The results of this testing, which can be seen in Figure 6.3, were quite varied with some cells showing little degradation of performance while others showed large amounts of degradation despite having identical experimental conditions. Both the open circuit voltage (V_{oc}) and fill factor (FF), which are not shown in Figure 6.3, remained quite stable for most cells with the majority of the loss of performance coming from a loss in short circuit current density (J_{sc}). For the cells which did not show major degradation, the normalized power conversion efficiency (PCE) was quite similar for both adhesives with the thinner 467MP being generally slightly less degraded for measures after 96 hours. However, the very small difference in performance, combined with the catastrophic failure of several cells, makes it difficult to draw conclusions as to whether one adhesive outperformed the other. As OPV cells are much more complicated devices to fabricate than a calcium deposit and contain multiple degradation mechanisms, they will often show more variance in aging tests. This appears to have been the case in this study resulting in the inability to confirm the effect of adhesive thickness on permeation presented in Chapter 3.



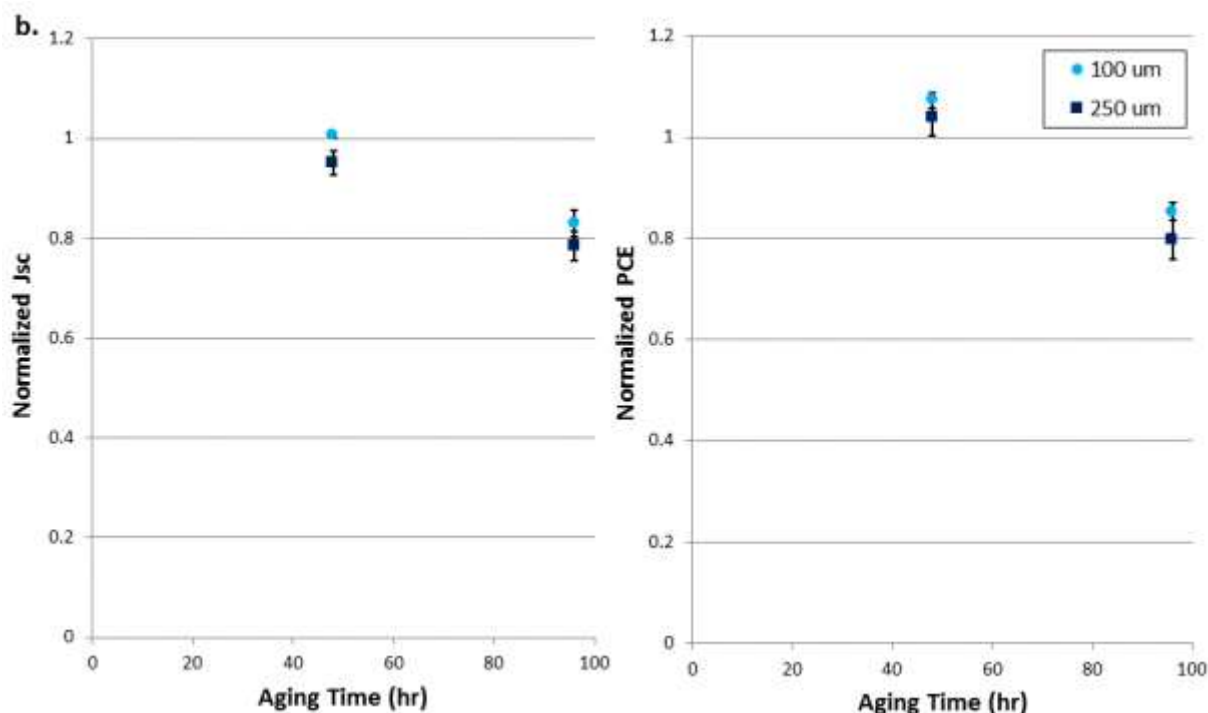


Figure 6.3 Plots of the short circuit current density (J_{sc}) and power conversion efficiency (PCE) of one-shot encapsulated OPV cells using Oike VX 25T-2PO barrier films are shown after storage for various times at 65°C and 85% relative humidity without illumination. Plots are shown for (a) each individual cell and also as (b) average values which exclude highly degraded cells. Error bars represent ± 1 standard deviation.

Comparison of Different Adhesives

A second more wide ranging study of OPV cell aging was also performed in order to compare the relative effectiveness of several different adhesives for OPV encapsulation. Because of the larger number of cells needed for one-shot testing and the desire for repeated measures to construct aging curves for each cell, the open-electrode encapsulation scheme was used for this study. F18 at different thicknesses and surface treatments was compared to the reference material 3M 467MP and the state-of-the-art barrier adhesive 3M FTBA-25 with all samples using Oike VX 25T-2PO barrier films. The power conversion efficiencies for cells encapsulated with 150 μm of F18 and corona treated barrier films as measured from J-V characterizations as a function of aging time can be seen in Figure 6.4. These results show a very large dispersion with some cells greatly outperforming others despite using identical encapsulation materials and design. Although the encapsulation is designed to extend 7.5mm outward from the edge of the substrate (the same distance as the optical calcium test) on the ends sides with no electrodes, thinner materials formed voids along the edge of the device as can be seen in Figure 6.5a. Since these voids have the potential to shorten the permeation path-

length from this edge, samples with these voids are denoted in Figure 6.4 with open markers while samples with no voids in this location have solid markers.

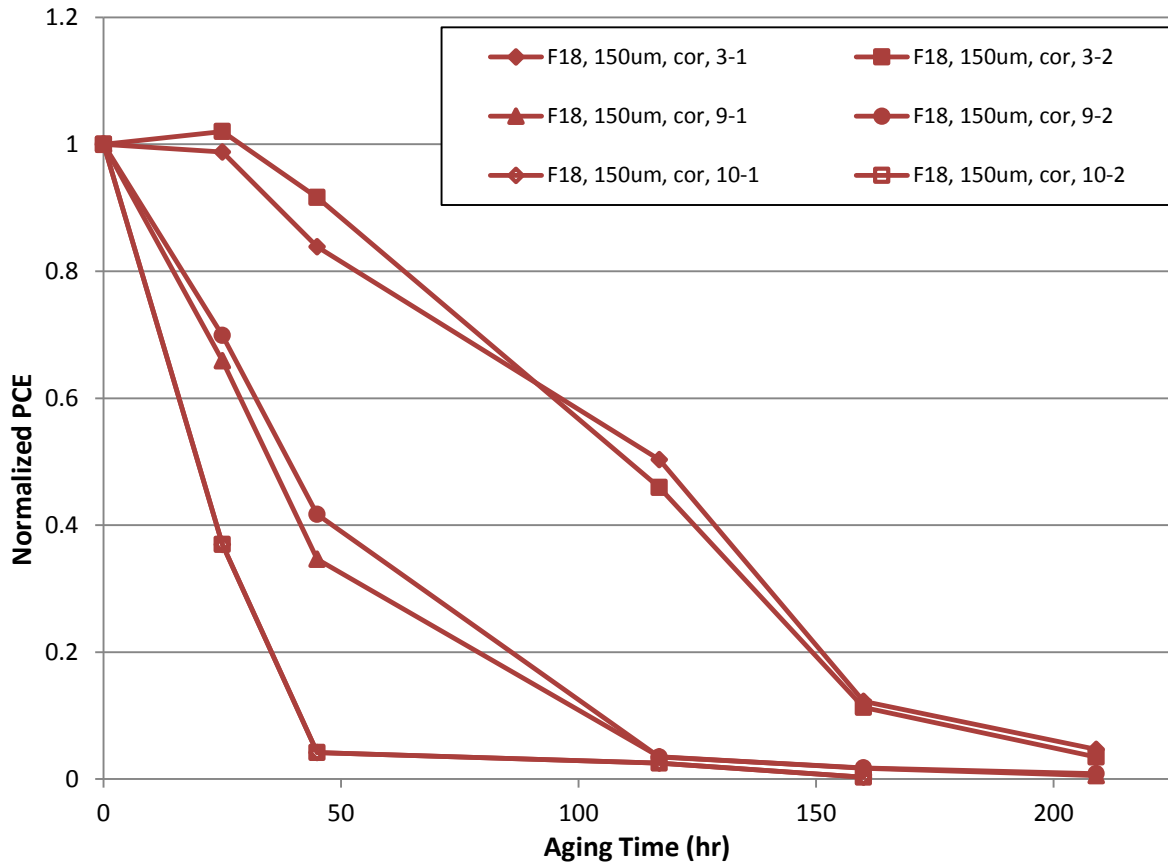


Figure 6.4 Plots of the power conversion efficiency of open-electrode encapsulated OPV cells using 150 μ m of F18 and corona treated Oike VX 25T-2PO barrier films are shown after storage for various times at 65°C and 85% relative humidity without illumination. Open markers indicate voids in the encapsulation along the edge of the devices as seen in Figure 6.5.

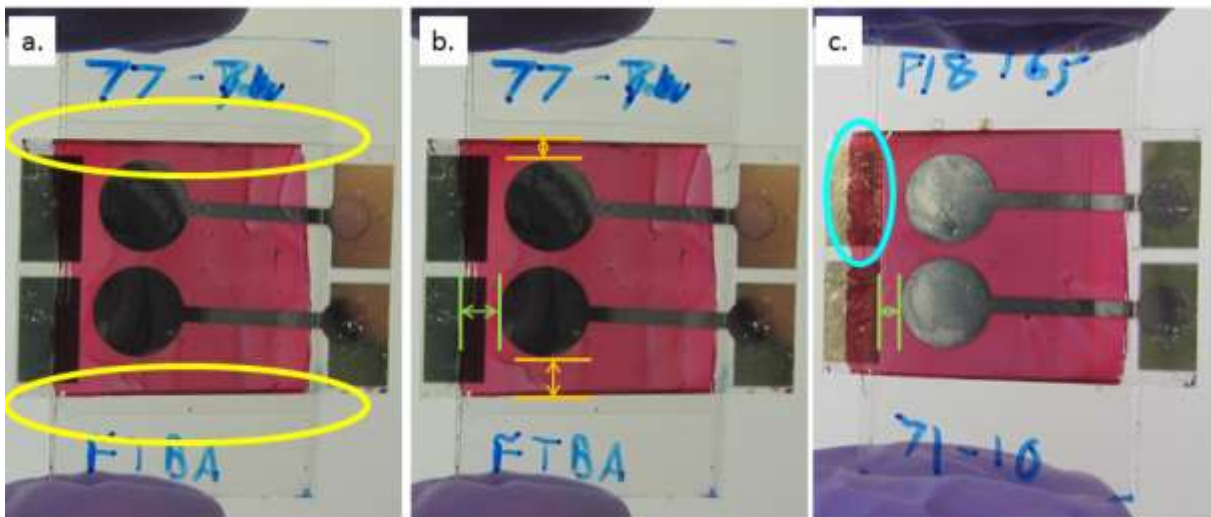


Figure 6.5 (a) Voids along the edges of the device are marked in yellow in this image of an OPV device encapsulated using a PSA (3M FTBA-25) in an open-electrode scheme. The voids come from the inability of the thin, solid adhesive (25 μ m thick per barrier film) to flow and completely enrobe the 175 μ m thick substrate of the OPV device. (b) The misalignment of the silver electrodes can be seen by the different distances marked in orange. This can be seen in the

other dimension by the different distances marked in green between images b and c. (c) A region where the OPV materials are outside the encapsulation is shown marked in blue on a device encapsulated with 150 μ m of neat F18.

The large differences in the rate of PCE loss likely come partially from the same type of variance within the cells seen in the study using one-shot encapsulation. However, the open-electrode encapsulation scheme also introduced another potentially large source of variance from the imperfect alignment of the cells in relation to the encapsulation. As the cells were fabricated, the exact placement of the silver electrodes was not carefully controlled. Since the regions underneath the electrodes are responsible for the vast majority of the measured current, varying the distance from the electrode to the edge of the substrate creates different permeation path-lengths. Some cells in this study showed a difference of a few millimeters in this distance as can be seen in Figure 6.5b. This variance is exacerbated by the relatively short distance to the edge of the encapsulation in this scheme, causing the variance in electrode placement to account for a larger percentage of the total permeation path-length. Additionally, the size and exact location of the regions coated by the other layers of the OPV device were not controlled. This poses a more significant problem for the open-electrode encapsulation scheme compared to other schemes as the distance between these regions and the edge of the encapsulation can be quite small. In fact, for some devices these regions extended past the edge of the barrier film as can be seen in Figure 6.5c. This creates additional permeation pathways directly into the device and can be particularly worrisome given the hygroscopic nature of some OPV materials such as PEDOT:PSS.

The large amount of variance between cells seen in this study makes it difficult to identify trends between the adhesives, especially for the F18 based adhesives. Nonetheless, some comparisons can be made, especially when comparing only the best performing cells for each test condition, as is done in Figure 6.6. Similar to the behavior seen in the study of one-shot encapsulated devices, the loss of PCE in all cells was closely mirrored by a loss in the short circuit current while the open circuit voltage and fill factor remained relatively stable. Some cells did show a gradual loss in their fill factor, though this was always less drastic than the loss in short circuit current and generally did not occur until the cell was already showing greatly decreased PCE. In comparison to the reference adhesive 3M 467MP, all F18 thicknesses and surface treatments had best performances that slower rates of PCE loss. This generally agrees with the results of water permeation seen in the optical calcium test where F18 displayed a lower apparent lateral water vapor permeation rate. Also agreeing with the general water vapor permeation trends seen in the optical calcium test was the relatively slow loss of PCE by cells encapsulated with FTBA-25. As a state-of-the-art adhesive designed as a water vapor barrier,

it displayed both the least water vapor permeation in optical calcium tests and the least loss of PCE in this study. Unlike the trends seen in the optical calcium test results shown in Chapters 4 and 5, the use of corona treatments did not limit the rate of PCE loss in these cells as the best performing cell of non-treated F18 showed a slower loss of PCE than those which had been corona treated. While the optical calcium did show less permeation for the corona treated samples, the improvement may not have been large enough to overcome the very large variance seen between OPV cells in this test.

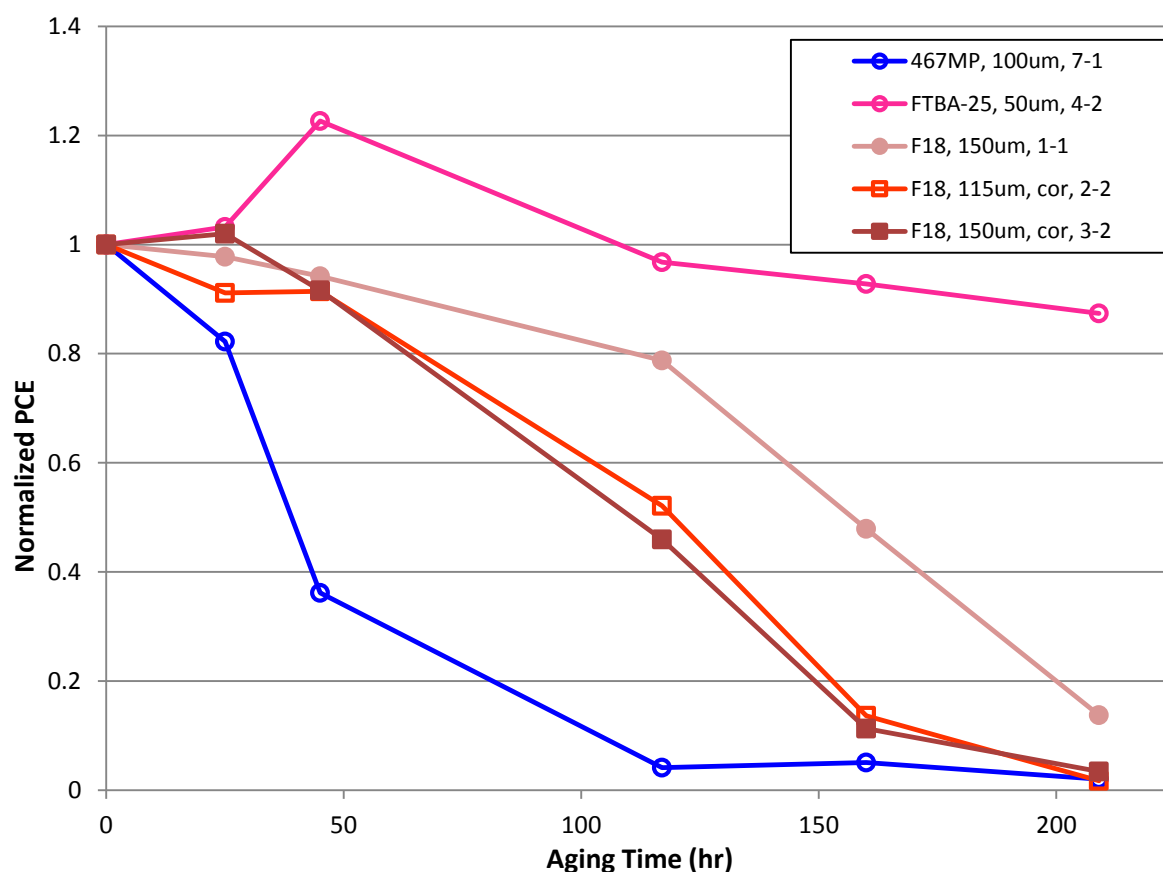


Figure 6.6 Plots of the power conversion efficiency of the best performing open-electrode encapsulated OPV cells using Oike VX 25T-2PO barrier films are shown after storage for various times at 65°C and 85% relative humidity without illumination. Square markers indicate the use of corona treated barrier films while open markers indicate voids in the encapsulation along the edge of the devices as seen in Figure 6.5.

UV Curing Nanocomposites

Given the large variation seen in the study of open-electrode encapsulated devices, a third study was performed using ribbon encapsulation. This study also included nanocomposites of F18 as a way to test the impact of adding nanoparticles to the adhesive on the aging of encapsulated OPV devices. The ribbon encapsulation scheme was chosen as it uses a larger distance from the edge of the device to the edge of the encapsulation, thus alleviating

some of the variance from the positioning of the cells and the exposure of the OPV materials outside of the encapsulation. In this study, this distance was set to 7.5mm as it corresponds to the distance used in the optical calcium test. Since the ribbon of bussing used to measure the device exits the encapsulation, care was taken to avoid creating the types of voids seen in Figure 6.5 along the edges of the bussing. This a particularly important issue as it would create a direct pathway to the device along which gas permeation would occur rapidly. For this reason, no PSAs were included in this study and only liquid adhesives which have the ability to flow and close these voids were tested. The geometry used for the placement of the ribbon of bussing also connected the two cells on each substrate in parallel, therefore creating a single device. This, combined with the impracticality of using a light blocking mask in this experimental set-up, led to each device being measured as a single entity instead of as individual cells. All samples in this study used corona treated Oike VX 25T-2PO barrier films.

The normalized PCE of the cells as a function of aging time at 65°C and 85% relative humidity in dark storage can be seen in Figure 6.7. Due to a malfunction with the J-V characterization equipment on the solar simulator located in ambient atmosphere, the initial measures ($t=0$) for all devices in this study were instead made using a different solar simulator located inside an inert atmosphere glove box. Though both simulators are well calibrated and were within their normal specifications, they do produce slightly different spectra of light. For absorber materials that have quantum efficiencies that are highly dependent on the wavelengths at which they are illuminated, such as P3HT, this change in spectra between solar simulators leads to a reduction in the measured photo-current produced, and thus also the PCE, when using the simulator in the inert atmosphere glove box. Though several attempts were made to quantify this difference and correct the measurements after testing, a reliable method was not found. Therefore, the initial values of PCE for this study appear to be lower than would otherwise have been measured using the same simulator as the other measurements. This effect is at least partially responsible for several cells showing immediate and sustained increases in PCE. All measures made after the initial test used the same simulator located in ambient atmosphere and are therefore directly comparable.

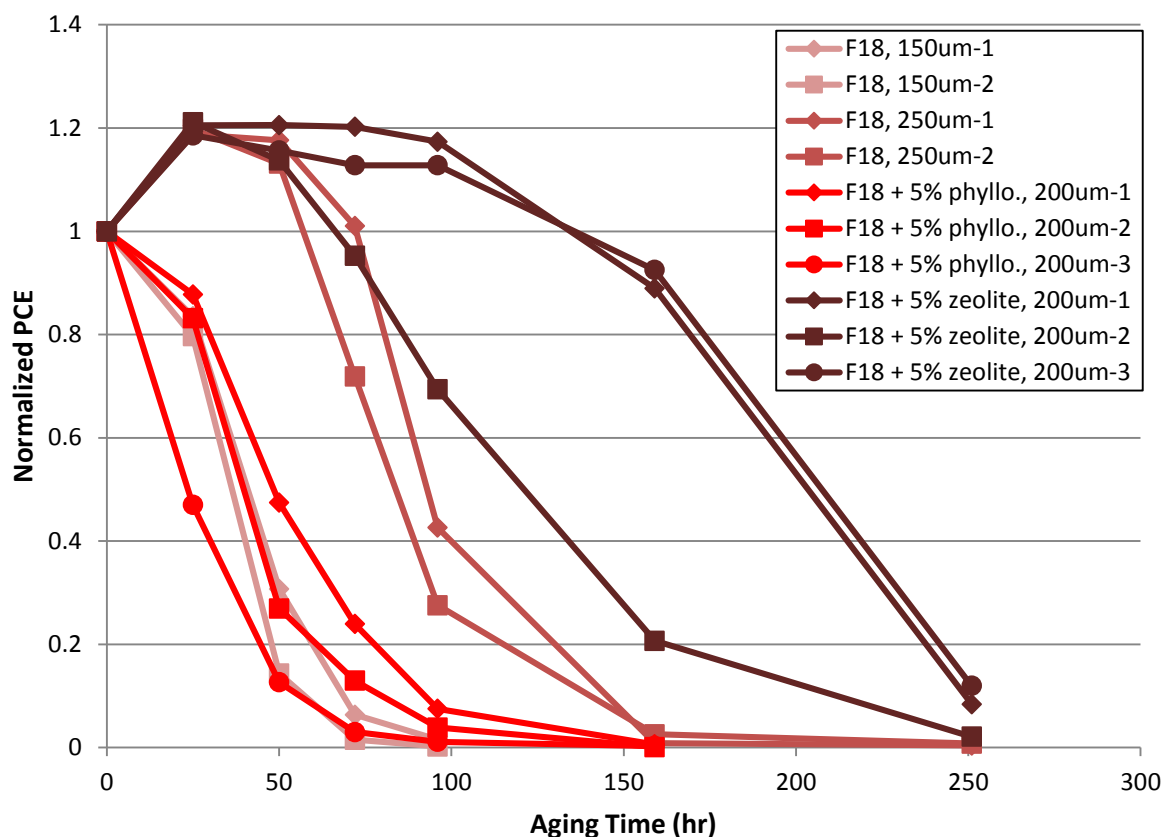


Figure 6.7 Plots of the power conversion efficiency of ribbon encapsulated OPV cells using Oike VX 25T-2PO barrier films are shown after storage for various times at 65°C and 85% relative humidity without illumination. The thickness of the adhesive layer is noted in the legend.

While all samples showed some formation of bubbles and voids near the edge of the device where the ribbon of bussing meets the device, the samples using neat F18 with a thickness of 150µm were especially poor in this respect. This was due to the adhesive layer being too thin to allow for complete coverage of a region with such large changes in topology. These voids are the likely source of why the devices encapsulated using thinner layers of neat F18 decreased in PCE more quickly than those with thicker layers. The phyllosilicate nanocomposites were not particularly poor with respect to voids but still showed a rapid loss of PCE compared to the thick coatings of neat F18. This result is somewhat surprising as this nanocomposite showed less water vapor permeation in optical calcium tests and little change in transparency compared to neat F18 as was discussed in Chapter 5. The results of this study indicate that the addition of phyllosilicates to this adhesive does not prolong the device lifetime. However, this nanocomposite does warrant further study to fully understand why the decreased water vapor permeation seen in optical calcium tests did not translate to increased device lifetime. It is possible that another as of yet unidentified factor could also have played a role, such as an interaction between the particles and the materials of the OPV cell or a change in

oxygen permeation. Interaction between the clay particles and the OPV materials is a particularly pertinent possibility as phyllosilicates frequently have impurities which could potentially impact OPV performance. On the other hand, active nanocomposites using zeolite nanoparticles showed slower losses of PCE compared to neat F18. The ability of the zeolites to adsorb permeating water before it can reach the device was evident by the very stable behavior of the devices encapsulated with this nanocomposite for the first 50-100 hours of storage in the very humid conditions of this study. Though nanocomposites of F18 with zeolite nanoparticles did not show a large difference in water vapor permeation in the optical calcium test, the results from encapsulating OPV devices imply that the zeolites are indeed effective at scavenging water in devices.

Conclusions

The accelerated aging of encapsulated OPV devices at 65°C and 85% relative humidity in dark storage has provided further insight into the barrier properties of F18 and its nanocomposites. Neat F18 generally showed slower losses of PCE than the reference material, 3M 467MP, which is a material that has been reported in the literature for encapsulating OPV devices. However, no variant of F18 slowed the loss of PCE more than the state-of-the-art gas barrier PSA, 3M FTBA-25. The performance of neat F18 in comparison to these two PSAs is also in agreement with the results seen in optical calcium tests. Neat F18 showed less water vapor permeation than 467MP but more than FTBA-25 in the optical calcium tests discussed in Chapter 5. The performance of F18, despite its varying results in OPV device aging, appears to be suitable for use in encapsulating flexible OPV devices based on the results of accelerated humidity aging in dark conditions. However, further manipulation of the formulation will be necessary in order to achieve the performance of state-of-the-art gas barrier adhesives. Aging under illumination must also be evaluated before implanting this nanocomposite for the encapsulation of OPV modules. The photo-stability of adhesives and nanocomposites will be discussed further in Chapter 7.

Phyllosilicate nanocomposites based on F18 did not show the same improved performance in OPV accelerated humidity aging as was seen in the optical calcium test. The addition of organically modified phyllosilicates did not improve the device lifetime and may have even caused faster loss of PCE. Based on the decreased water vapor permeation seen in the optical calcium test, this nanocomposite warrants further study to determine the cause of its

relatively poor performance in OPV accelerated humidity aging. It is likely that another source besides water vapor aided in accelerating the loss of PCE in OPV cells encapsulated using this adhesive, with the most likely culprit being contamination and impurities in the phyllosilicate particles.

Nanocomposites of F18 with zeolite nanoparticles were the best F18 based samples at preventing the loss of PCE in OPV devices. These active nanocomposites provided excellent stability for their encapsulated OPV devices for the first 50-100 hours of aging at 65°C and 85% relative humidity in dark storage. This was an improvement over neat F18 and demonstrates the advantages that active water scavengers can have for the performance of OPV devices in humid environments.

Chapter 7: Photostability

Introduction

As the goal of organic photovoltaic (OPV) modules is to convert light to electricity, they are by definition exposed to light, oftentimes in the form of intense sunlight. This makes the photostability of any material to be used in OPV devices critically important. For barrier adhesives, even materials with excellent physical properties are not good choices if those properties change overtime upon exposure to light. For this reason, the adhesives and nanocomposites studied in this thesis were also subjected to aging tests of their photostability using a SEPAP 12/24, which irradiates samples with large doses of ultraviolet (UV) radiation while maintaining an elevated temperature of 60°C. This chapter details the results of the various testing performed using these aging conditions to evaluate the suitability of the adhesives for use in OPV modules that may be exposed to years of intense sunlight. Tests were performed to determine both the chemical changes and the changes to some physical properties after exposure to the accelerated aging conditions. Much of the spectroscopy tests, chemical treatments, and some sample preparation of the samples presented in this chapter was performed by Diane Delbegue as part of her internship at the Institut de Chimie de Clermont-Ferrand (ICCF) under the guidance of Professor Jean-Luc Gardette and Dr. Sandrine Therias and in collaboration with the author.

MAM PSAs

Degradation Kinetics: Photo-oxidation and Photolysis

MAM PSAs were tested in transmission using both Fourier transform infrared spectroscopy (FTIR) and ultraviolet-visual spectroscopy (UV-Vis) with aging performed both in air (photo-oxidation testing) and sealed under vacuum in glass tubes (photolysis testing). The spectra during photo-oxidation testing of M65 and M85 can be seen in Figure 7.1. As they differ chemically only in their block ratios, it can be seen that both adhesives display changes to the

same absorption bands. It can also be determined that the poly(butyl acrylate) (PBA) block degrades more readily than the poly(methyl methacrylate) (PMMA) block since M85, which has a higher fraction of PBA, degrades faster than M65 which has less PBA. This is in agreement with the literature where it is well known that PMMA is a highly photo-stable polymer.^{160,163} For both adhesives, the growth of the bands with absorption maxima at 1790cm^{-1} (C=O), 3260cm^{-1} (-OH) and 3525cm^{-1} (-OH) indicated the formation of carbonyl and hydroxyl groups as a result of photo-oxidation. As these bands showed the greatest measurable changes, they were therefore used to plot the kinetics of the photo-degradation in the MAM PSAs.

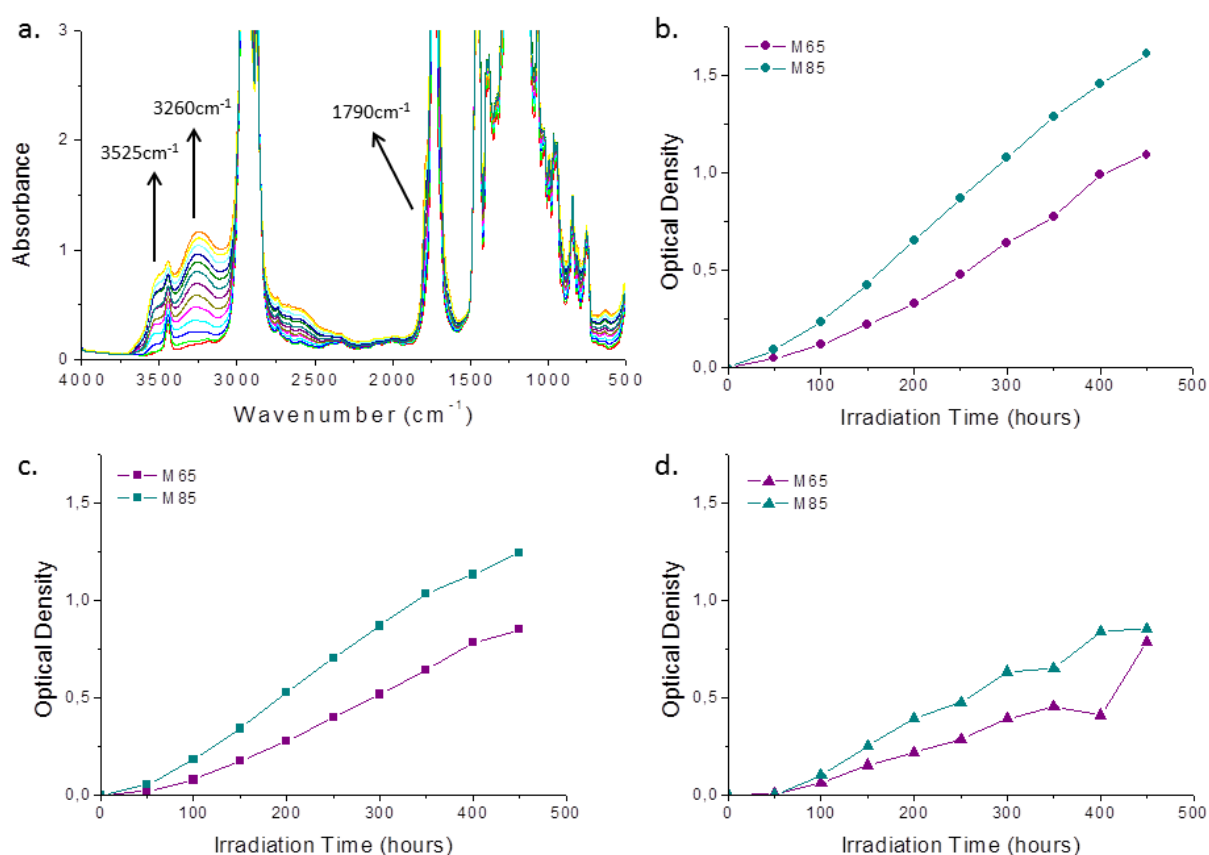


Figure 7.1 (a) FTIR spectra for M85 are shown after various aging times in a SEPAP 12/24 during photo-oxidation testing. The optical density at (b) 1790cm^{-1} , (c) 3260cm^{-1} , and (d) 3525cm^{-1} are plotted as a function of aging time during photo-oxidation testing are shown for both M65 and M85 with all points corrected for differences in sample thickness.

By treating the degraded samples with SF_4 , the presence of aliphatic acids was confirmed. This can be seen in Figure 7.2a from the shrinking of the absorption band at 3260cm^{-1} and the growth of the absorption band at 1840cm^{-1} . Further treatment with 2,4-dinitrophenylhydrazine (DNPH) showed the presence of aldehydes and/or ketones in the samples after aging. This can be seen in Figure 7.2b as the growth of the absorption bands at 1620cm^{-1} and 1600cm^{-1} . Using the schemes proposed by Liang et al, along with the combination of the absorption bands observed after photo-aging, after SF_4 treatments, and after DNPH treatments, led to the proposal of the photo-oxidation scheme shown in Scheme 7.1.

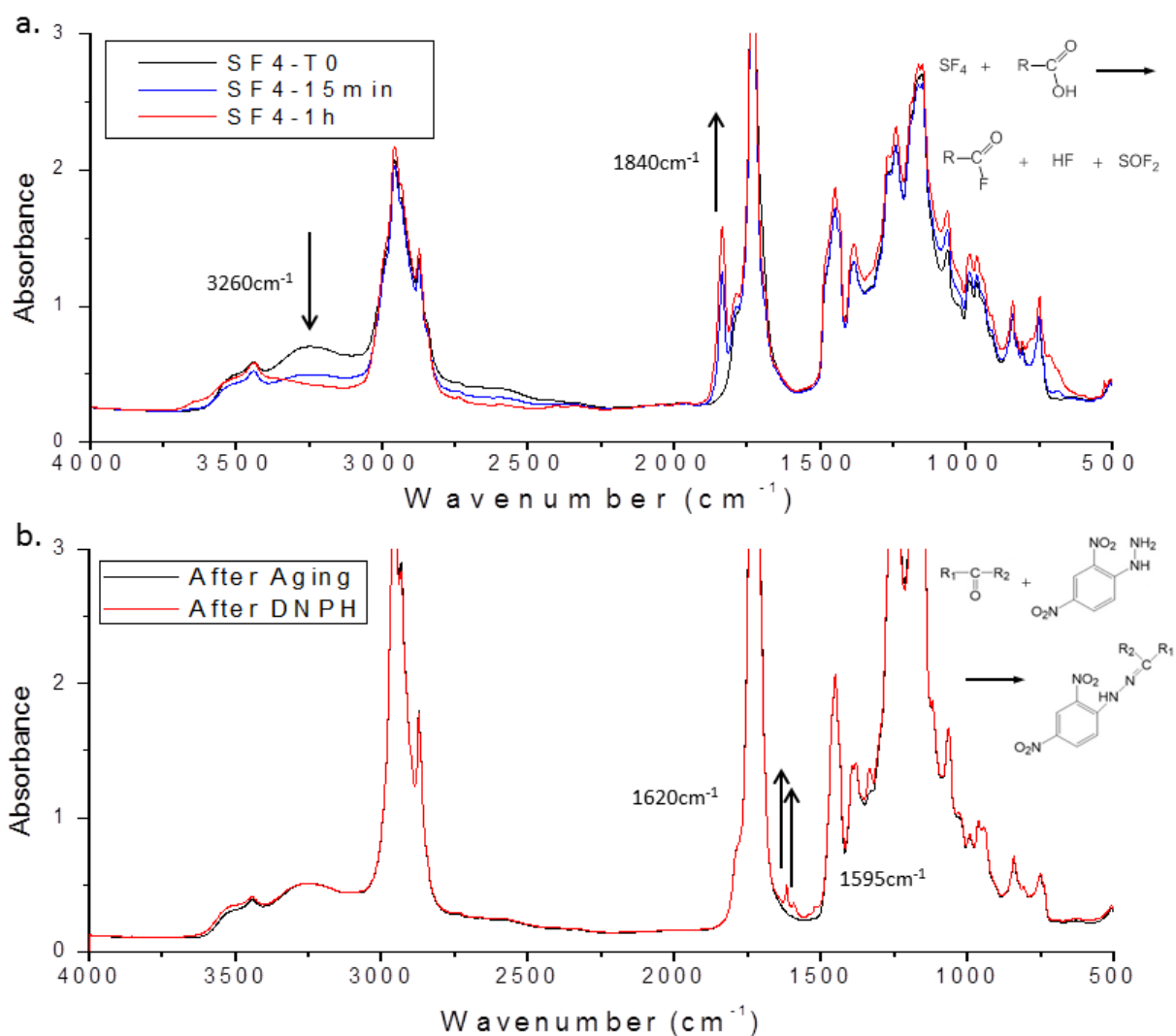
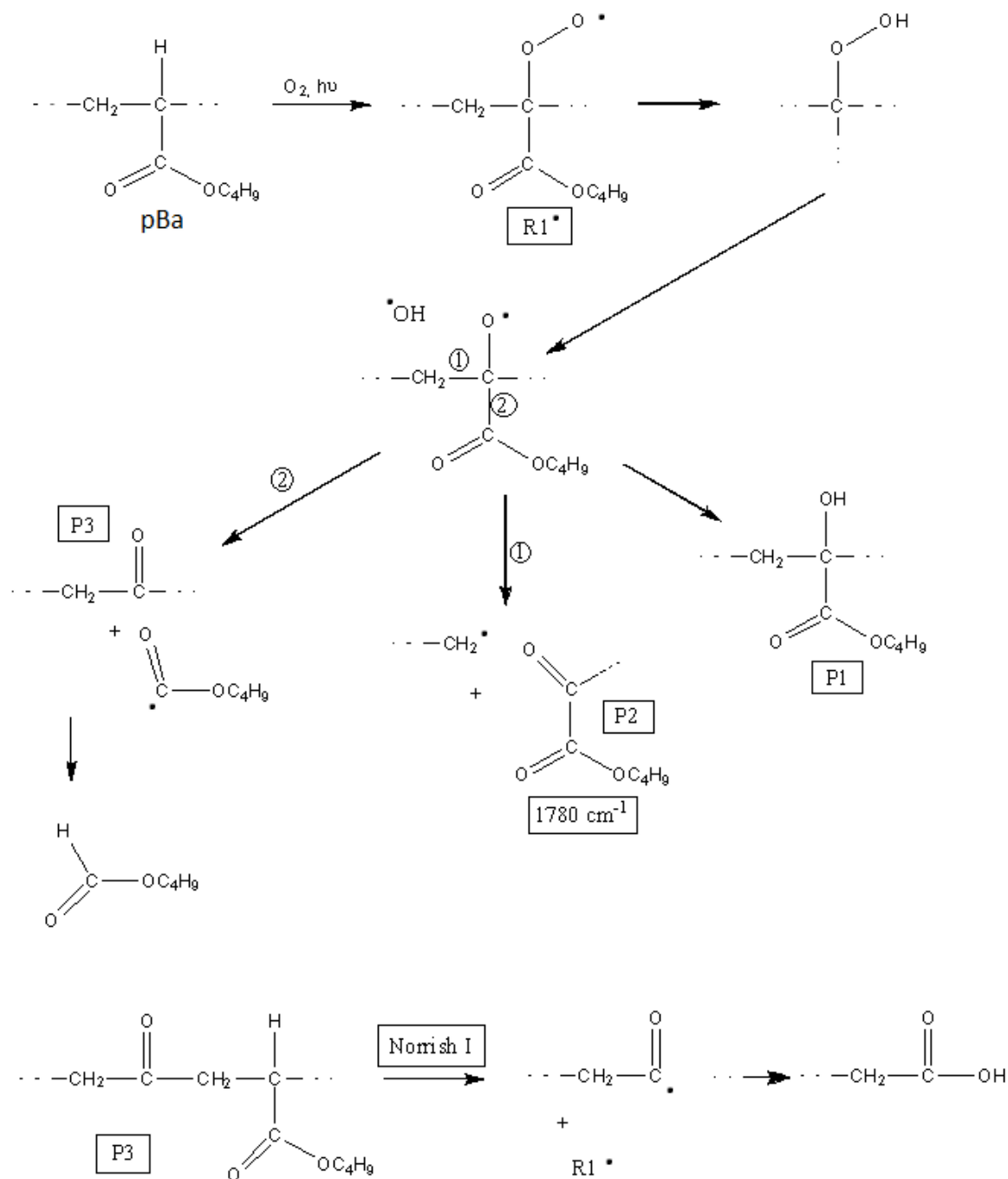


Figure 7.2 (a) FTIR spectra of M85 after photo-oxidation testing are shown for various treatment times with SF₄. The loss of -OH groups at 3260 cm⁻¹ and the shift of the C=O band to 1840 cm⁻¹ from R-COF indicate the presence of aliphatic acids in the photo-oxidation products. (b) FTIR spectra of M85 after photo-oxidation testing are shown before and after treatment with DNPH. The appearance of bands at 1595 cm⁻¹ and 1620 cm⁻¹ indicate the presence of aldehydes and/or ketones in the photo-oxidation products.



Scheme 7.1 The proposed mechanisms for the photo-oxidation of poly(n-butyl acrylate) are shown.

In the case of photolysis, where no molecular oxygen is present, the changes seen were so minimal that it was not possible to illuminate any particular reaction mechanisms for the MAM PSAs. Therefore, no scheme for the photolysis of these materials has been proposed in this thesis. As can be seen in Figure 7.3, little to no change was seen in the FTIR spectra after up to 300 hours of exposure in the SEPAP 12/24. This result is of particular importance as the barrier nature of both the adhesive itself and the barrier films which surround it greatly limit the presence of molecular oxygen in adhesive.

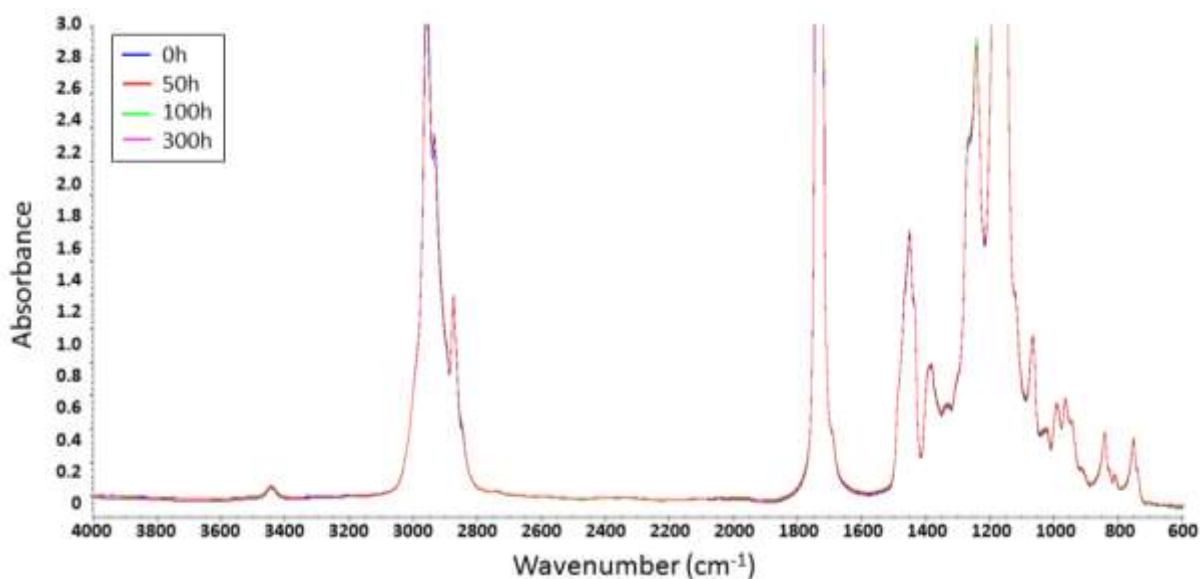


Figure 7.3 FTIR spectra of M85 after various aging times during photolysis testing are shown.

The same samples tested in FTIR were also measured via UV-Vis with the spectra shown in Figure 7.4. An immediate loss of the absorption band at 280nm was seen in photo-oxidation testing. As such a rapid loss of a band could be due to the evaporation of a solvent, subsequent testing with and without the presence of toluene in the polymer was performed. The same results were observed both with toluene present and in dried samples showing that this absorption band was not due to residual solvent but was indeed coming from the adhesive. Due to the proprietary nature of the polymerization process used with to synthesize the MAM PSAs it is unclear exactly what species is responsible for this reaction. After the disappearance of this band, the film then showed a very slight increase in absorption in the range of 250-290nm, though the absorption remained well below that seen before testing. In photolysis testing, the absorption band at 280nm did not disappear, indicating that the disappearance of this band under irradiation in presence of oxygen was due to the photo-oxidation of a species. Additionally, while the films were still clear and transparent to the naked eye, the MAM PSAs did lose some transparency at lower wavelengths during photolysis testing. However, this increase is rather small and would present only a minimal impact on the transparency of a film in an encapsulated OPV module.

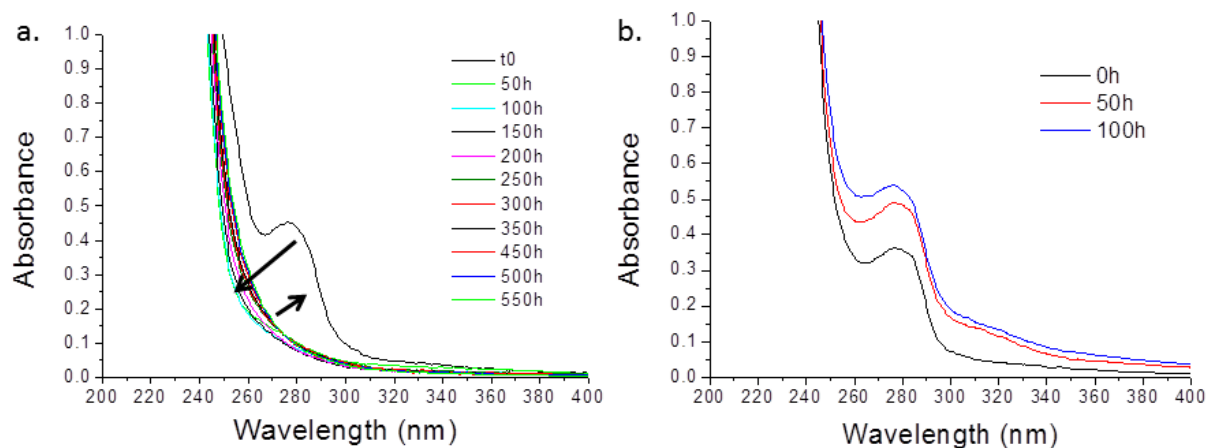


Figure 7.4 UV-Vis spectra for M85 after various aging times are shown for (a) photo-oxidation testing and (b) photolysis testing.

Effect of Nanoparticles

The impact of the addition of nanoparticles to the MAM PSAs was also studied. The losses and growths of the same absorption bands in the infrared spectra as the neat adhesive were seen for nanocomposites of 5wt% organically modified phyllosilicates in M65. The changes seen in FTIR over the course of photo-oxidation testing showed very similar results to that of neat M65 as can be seen in Figure 7.5, thus indicating similar reaction kinetics. In UV-Vis, the decreased transparency of this nanocomposite, as discussed in Chapter 5, prevented the observation of the absorption band seen at 280nm in the neat material. UV-Vis results did show an immediate, slight, change in the shape of the absorption spectrum during photo-oxidation testing, but all subsequent measures were similar with no evident trends as can be seen in Figure 7.5d. This immediate change in shape likely comes from the loss of the tail of the absorption band at 280nm seen for the neat material. However, its relative impact on the absorption spectrum of the less transparent nanocomposite was quite small.

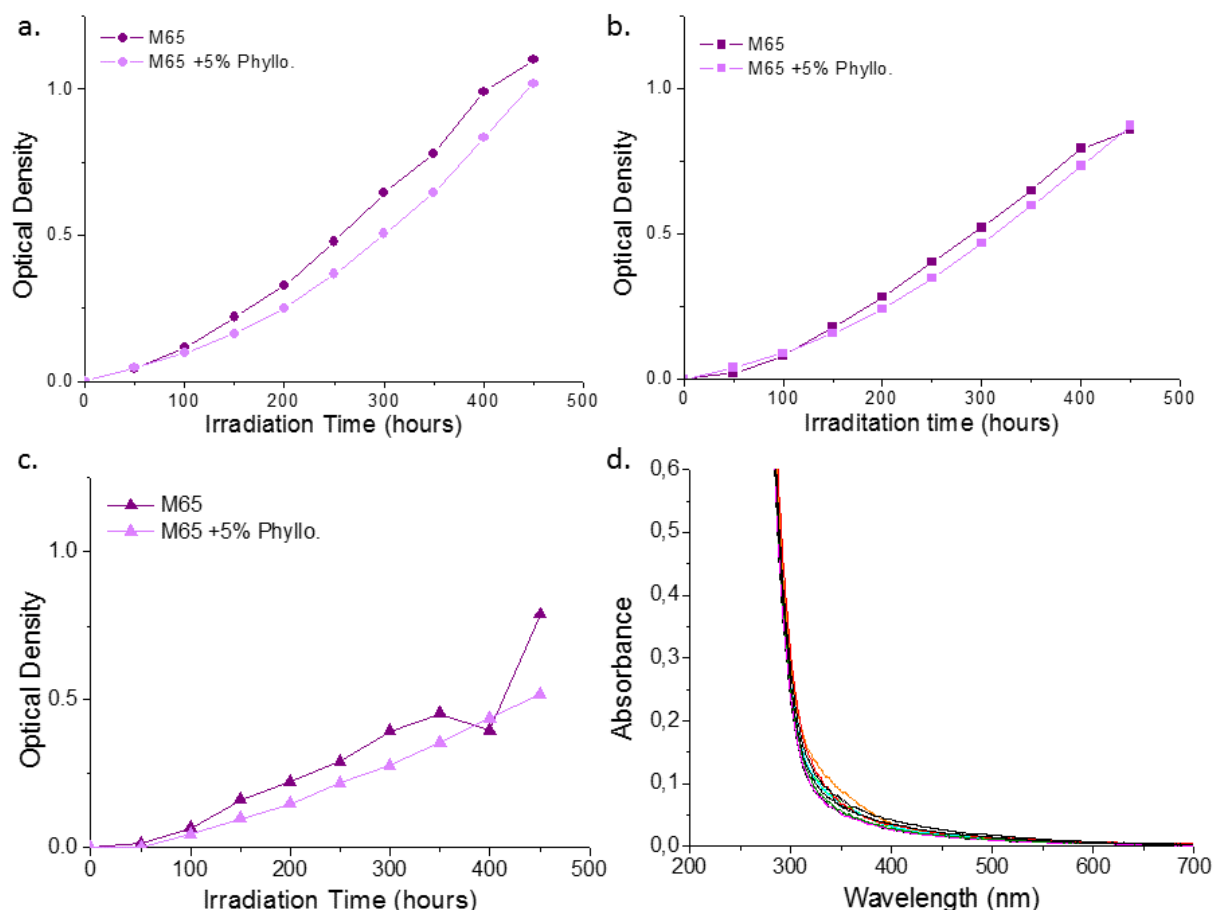


Figure 7.5 FTIR results, corrected for sample thickness, from photo-oxidation testing of M65 and the nanocomposite of M65 with 5wt% organically modified phyllosilicates are shown for the absorption bands at (a) 1790cm^{-1} , (b) 3260cm^{-1} , and (c) 3525cm^{-1} . (d) UV-Vis spectra for the nanocomposite of M65 with 5wt% organically modified phyllosilicates are also shown for various aging times during photo-oxidation testing. All UV-Vis measures after the initial measurement were quite similar with no evident trends related to aging time.

The addition of zeolite nanoparticles led to slightly greater changes in the FTIR spectra of the MAM PSAs than that for nanocomposites using organically modified phyllosilicates, but the changes remained fairly small. As a more extreme case, a nanocomposite of 20wt% zeolite nanoparticles in M85 was subjected to photo-oxidation testing. This nanocomposite produced changes to the same absorption bands in FTIR as the neat adhesive and the relative changes in the intensity of these bands can be seen in Figure 7.6. This nanocomposite did show a slight change in the ratio of the products compared to the neat adhesive with a slight reduction in –OH groups (3260cm^{-1} and 3525cm^{-1}) and slight increase in the C=O bond of P2 from Scheme 1 (1790cm^{-1}) in comparison to the neat adhesive. The UV-Vis spectra during photo-oxidation testing, seen in Figure 7.6d, showed a larger change than that seen for the neat adhesive. Despite this loss of transparency, the sample remained quite clear to the naked eye.

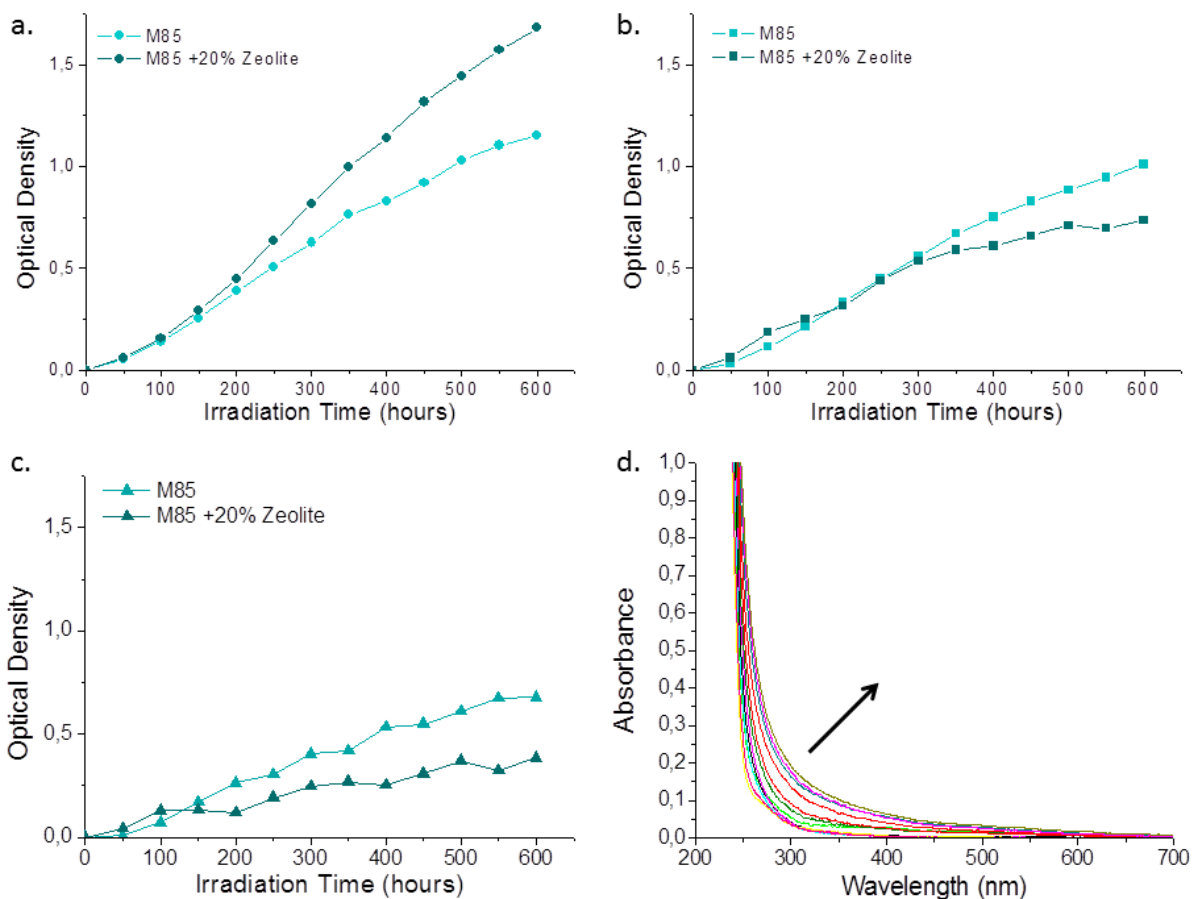


Figure 7.6 FTIR results, corrected for sample thickness, from photo-oxidation testing of M85 and the nanocomposite of M85 with 5wt% zeolite nanoparticles are shown for the absorption bands at (a)1790cm⁻¹, (b) 3260cm⁻¹, and (c) 3525cm⁻¹. (d) UV-Vis spectra for the nanocomposite of M85 with 5wt% zeolite nanoparticles show the loss of transparency with aging time.

The nanocomposite of 20wt% zeolite nanoparticles in M85 was also subjected to photolysis testing. The FTIR spectra from this testing can be seen in Figure 7.7. The only major changes in the observed absorption bands relate to those from the zeolite nanoparticles. These changes are likely related to the desorption of water from the zeolite nanoparticles as the nanocomposite was placed into vacuum at elevated temperatures during photolysis testing.

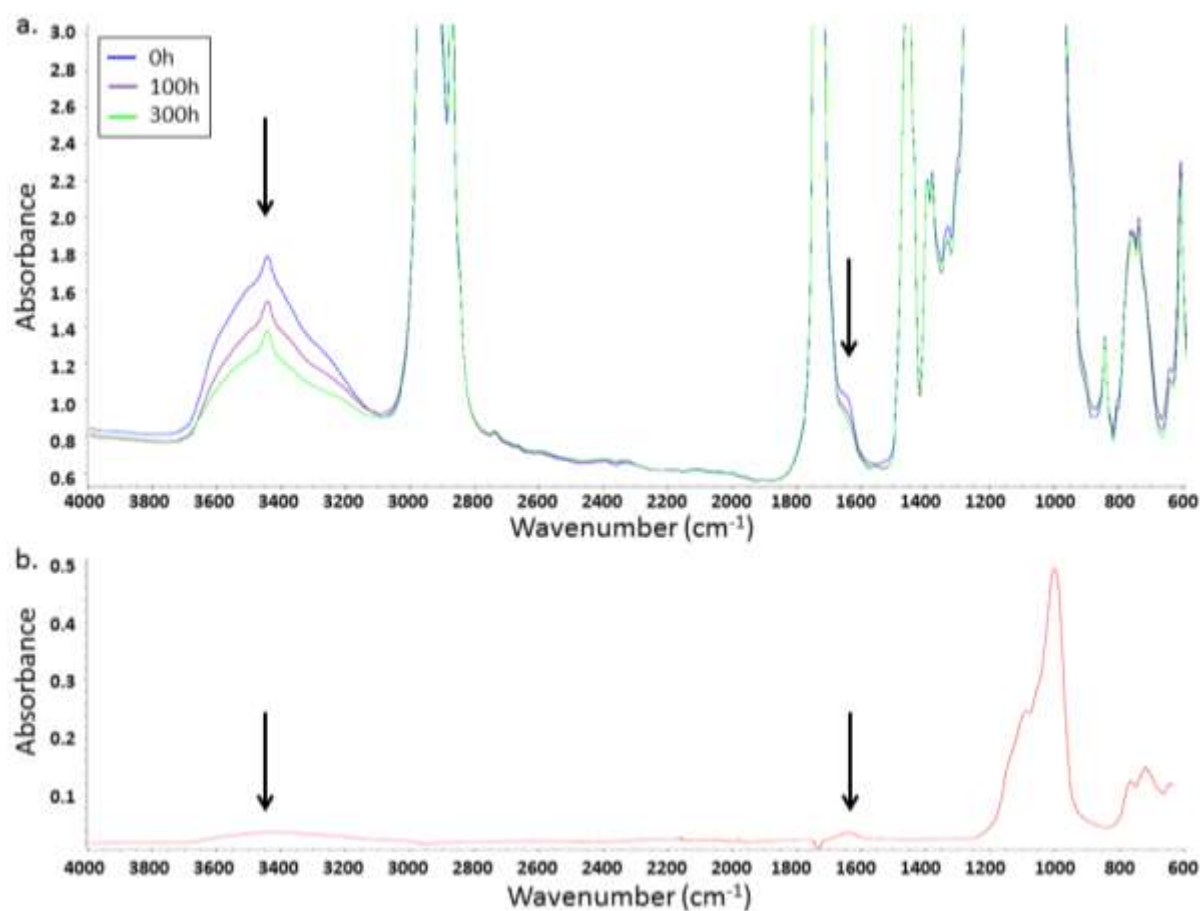


Figure 7.7 (a) FTIR spectra of M85 with 20wt% zeolite nanoparticles for various aging times during photolysis testing are shown. (b) A spectrum for a powder of zeolite nanoparticles as measured by FTIR in attenuated total reflection mode is shown for comparison with the spectra of the nanocomposite. It can be seen that the changes in the nanocomposite spectra correspond to absorption bands from the zeolite nanoparticles.

Changes to Properties

As the nanocomposite with zeolite nanoparticles provided a slightly more pronounced change in properties than the neat adhesive during accelerated photostability testing, the nanocomposite of M85 with 5wt% zeolite nanoparticles was tested in dynamic mechanical thermal analysis (DMTA) after photo-oxidation testing. The results as compared to the material without photo-oxidation testing can be seen in Figure 7.8. It can be seen that after photo-oxidation testing the T_g of the nanocomposite rose as evidenced by the peak of the loss modulus curve shifting from -39°C without photo-oxidation testing to -22°C after 125 hours of it. This increase in the T_g does lead to the material becoming more rigid in the temperature range for outdoor applications of OPV modules. However, even after this increased rigidity, the nanocomposite remains highly flexible over this range of temperatures.

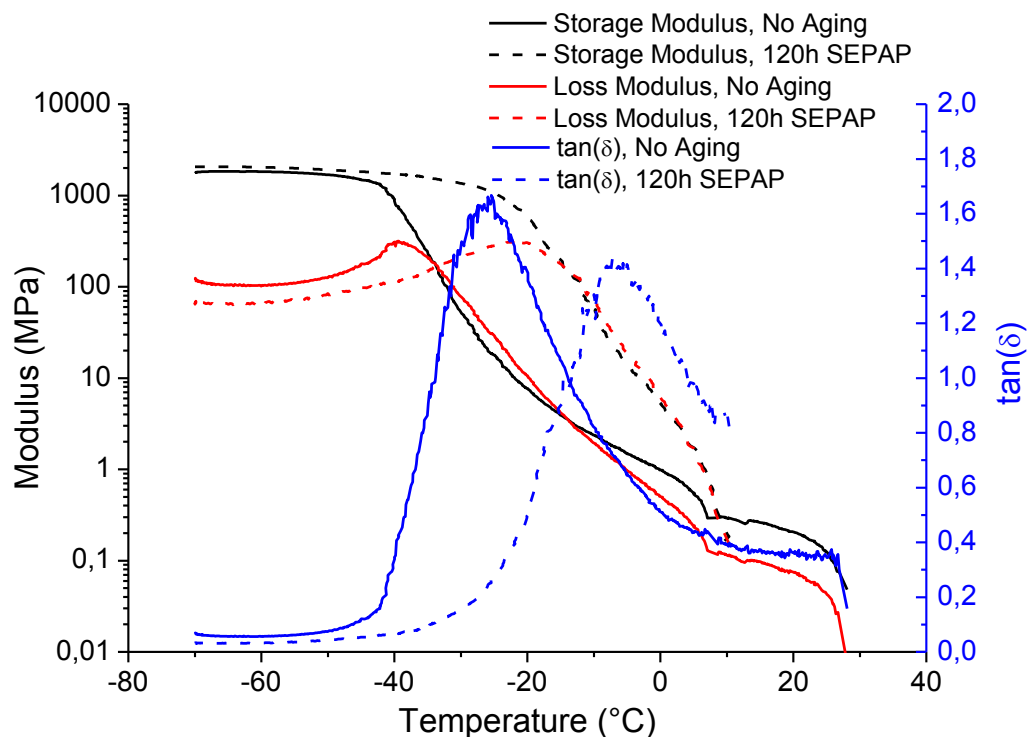


Figure 7.8 Tensile DMTA results for the nanocomposite of M85 with 5wt% zeolite nanoparticles are shown for both with and without exposure to in a SEPAP 12/24 in air for 120 hours. All DMTA tests were performed at 3°C/min, 1Hz and 0.1% strain.

The material was also subjected to T-peel adhesion tests, the results of which can be seen in Table 7.1. All samples were prepared using Oike VX 25T-2PO barrier films as substrates, which have a sharp decrease in transmission of light below about 380nm in wavelength. After 138 hours of photo-oxidation testing, the nanocomposite showed a slight increase in adhesion. This increase is quite small but could potentially be the result of the increased rigidity at room temperature seen in DMTA testing. However, the use of gas barrier films as substrates, in addition to their decreased transmission of UV wavelengths, may have also caused the aging of these samples to have a more limited presence of photo-oxidation, thus giving the degradation of the material more character of photolysis conditions that were shown to be more stable.

Table 7.1 The average adhesion strength from T-peel adhesion tests are shown for M85 with zeolite nanoparticles both without and after 138 hours of photo-oxidation testing. All samples used Oike VX 25T-2PO barrier films for substrates; had adhesive thicknesses of about 70µm; and displayed cohesive failure within the adhesive. Values in parentheses are the standard deviation.

Adhesive	No Aging	138h SEPAP	% Change
M85 +5wt% zeolite	8.10 N/cm (0.48 N/cm)	8.95 N/cm (1.04 N/cm)	10%

Calcium test samples for several adhesives and nanocomposites were prepared and placed in the SEPAP 12/24 in air for 125 hours. These samples were prepared in a dry nitrogen glove box at the Institut National de l'Énergie Solaire (INES) and then transported in desiccant filled thermo-sealed bags to the Institut de Chimie de Clermont-Ferrand (ICCF), where upon arrival they were immediately placed into a dry nitrogen glove box for storage prior to photo-oxidation testing. All samples also used a larger distance from the calcium to the edge of the barrier to prevent degradation of the calcium during transport and aging in the SEPAP 12/24. However, after 125 hours of exposure in the SEPAP 12/24, all samples except those using a nanocomposite of 5wt% zeolite nanoparticles in M85 showed complete degradation of the calcium layer. The samples for this nanocomposite, which did not show complete degradation of the calcium layer, were returned to INES where they were cut to the standard 6cm X 6cm size and subjected to the optical calcium test as described in Chapter 3. The results of this testing are shown in Figure 7.9 for the three samples aged in photo-oxidation testing and one control sample which was transported to and from ICCF but remained in a dry nitrogen glove box instead of being subjected to the SEPAP 12/24. All samples, including the control, showed large increases in lateral permeation in the optical calcium test as compared to the previously discussed results for this material. These results, along with the rapid loss of calcium upon removal from the dry nitrogen glove box seen in all other samples, appear to imply that the samples were damaged during transport. Unfortunately, time constraints prohibited the repetition of this experiment to confirm this hypothesis. However, the need for this experiment remains as it provides a method to predict the effect of sunlight in outdoor conditions on the ability of the adhesives and nanocomposites to prevent lateral gas permeation.

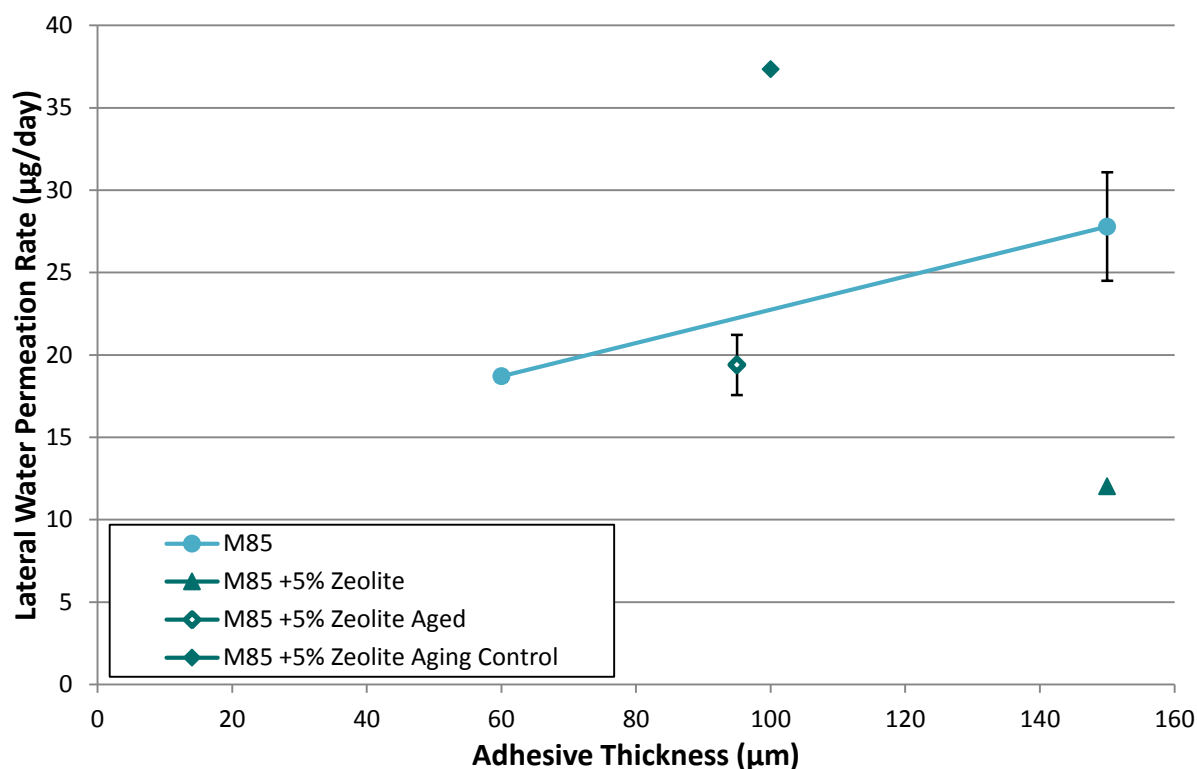


Figure 7.9 A plot of the average apparent lateral permeation rate as measured by the modified optical calcium test is shown for M85 and M85 nanocomposites with and without photo-oxidation testing. Aged samples were subjected to 125h in a SEPAP 12/24 in air. All values have been normalized to 45mm X 45mm calcium deposits to adjust for slight differences between samples. Error bars represent one standard deviation.

UV Curing Acrylates

Degradation Kinetics: Photo-oxidation and Photolysis

The photostability of F18 was also studied using both photo-oxidation and photolysis testing. The FTIR spectra of F18 films during photo-oxidation testing can be seen in Figure 7.10a. As this adhesive is a mix of several different oligomers and monomers, each with distinct chemical structures, it is difficult to identify the exact positions of many peaks as they were often highly convoluted. Nevertheless, a large amount of changes can be seen over the course of the 300 hours of photo-oxidation testing. The increases in the absorption bands in the broad range of $3700\text{-}3000\text{cm}^{-1}$ due to various -OH and -NH signals are commonly seen in the photo-oxidation of both epoxies and urethanes.^{141-144,153} Similar trends can be seen in Figure 7.10b for photolysis testing as well, though the changes in FTIR were not as strongly evident.

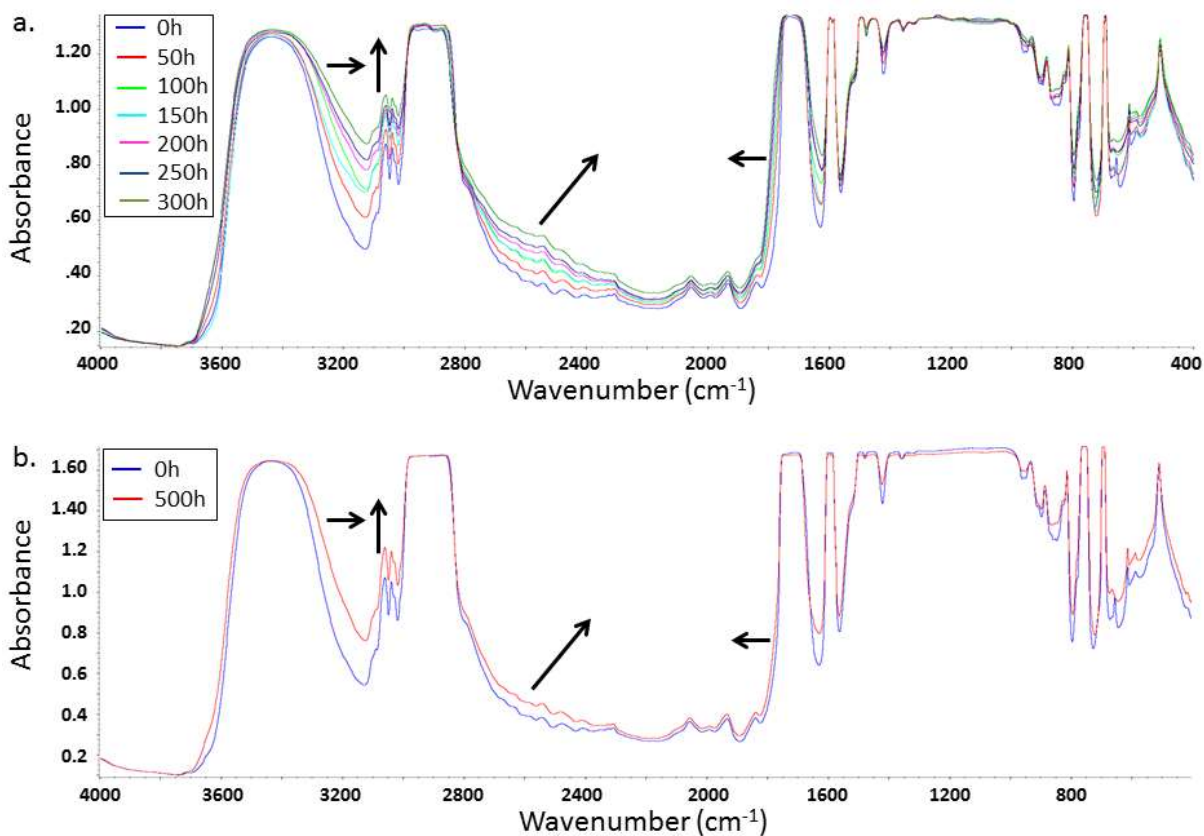


Figure 7.10 FTIR spectra of F18 after various aging times during (a) photo-oxidation testing and (b) photolysis testing are shown.

Even for very thin coatings on KBr substrates, all samples of F18 appeared very yellow to the naked eye after both photo-oxidation testing and photolysis testing. This can be seen in Figure 7.11 as the increased absorption of the samples at shorter wavelengths. An initial change in shape of the UV-Vis spectrum is seen as a result of the polymerization of residual un-cured acrylate groups, but the absorption then steadily increases with aging time for both photo-oxidation and photolysis testing. Photolysis testing in particular showed drastic changes in the transparency of the samples. This loss of transparency is of great concern for application to OPV modules as many active layer materials display high quantum efficiencies at the wavelengths being blocked after aging. This strong yellowing effect also helps to provide insight into the possible mechanisms of the degradation. Although its characteristic absorption band at about 1660cm^{-1} is not visible due to convolution, the evidence suggests the formation of quinone methide groups which are very strong absorbers at shorter wavelengths and are known to form with and without the presence of oxygen from the exposure of aromatic epoxies to UV radiation.¹⁴¹ This would indicate the oligomer CN9002 as the most likely source of the yellowing seen in F18 during photostability testing.

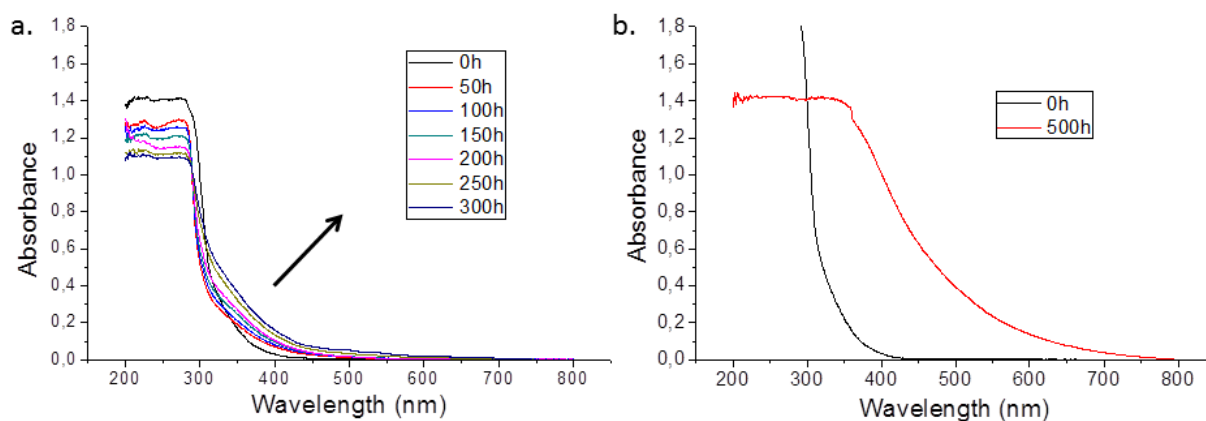


Figure 7.11 UV-Vis spectra of F18 after various aging times during (a) photo-oxidation testing and (b) photolysis testing are shown.

Changes to Properties

DMTA samples of F18 and its nanocomposites with 5wt% of organically modified phyllosilicates and 5wt% of zeolite nanoparticles respectively were also subjected to photo-oxidation testing. The storage modulus for each material both without and after photo-oxidation testing can be seen in Figure 7.12. All three materials showed similar behavior with larger transition regions and an increased T_g , which can be seen in Table 7.2 as calculated from the peak of the loss modulus curve. The larger transition region may come from the more varied segment length between cross-links caused by the combination of additional cross-linking and chain scission during photo-oxidation. The increased T_g is expected from an increase in cross-link density from the polymerization of residual acrylate groups, but may also come from additional cross-linking resulting from photo-oxidation. The further increase in rigidity is worrisome for these materials which were already relatively rigid in the operating temperature range of outdoor OPV modules.

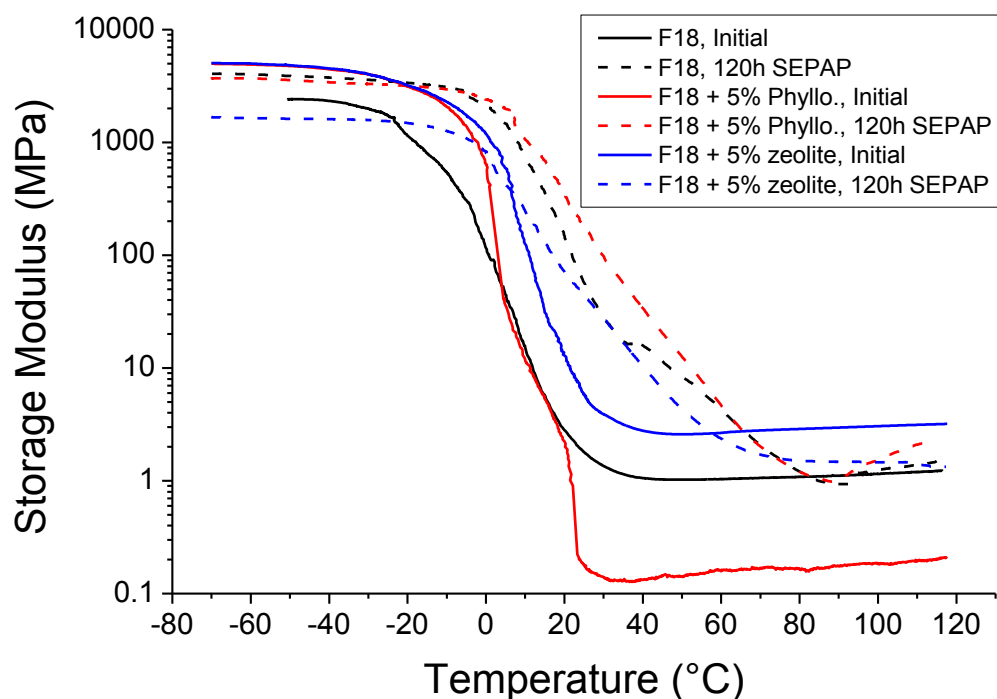


Figure 7.12 DMTA curves for F18 and its nanocomposites with organically modified phyllosilicates and zeolite nanoparticles respectively are shown for both without (solid lines) and after (dashed lines) photo-oxidation testing. All DMTA tests were performed at 3°C/min, 1Hz and 0.1% strain.

Table 7.2 As a measure of the T_g , the peak values of the loss modulus curves from DMTA testing are shown for F18 and its nanocomposites with organically modified phyllosilicates and zeolite nanoparticles respectively both without and after photo-oxidation testing. All DMTA tests were performed at 3°C/min, 1Hz and 0.1% strain.

	F18	F18 + 5wt% Phyllo.	F18 + 5wt% Zeolite
No Aging	-20°C	-9°C	-10°C
120h SEPAP	3°C	7°C	-2°C

The T-peel adhesion strength of neat F18 and the nanocomposite of F18 with 5wt% zeolite nanoparticles were evaluated after being subjected to photo-oxidation testing. All samples were prepared using Oike VX 25T-2PO barrier films as substrates, which have a sharp decrease in transmission of light below about 380nm in wavelength. After 138 hours of aging time, the neat adhesive showed a slight increase in adhesion, likely due to the additional cross-linking which occurred during aging. With the increase in rigidity after photo-oxidation testing, both materials showed at least some stick-slip behavior during adhesion tests. For the neat adhesive, it was possible to calculate the average T-peel adhesion strength without including regions of stick-slip, however, all samples for the zeolite nanocomposite displayed large regions of stick-slip behavior therefore necessitating the inclusion of these regions in the calculations. This behavior is the mostly likely cause of the calculated loss in adhesion for the zeolite

nanocomposite after photo-oxidation testing as the inclusion of “slips” in the calculation will cause an underestimation of the average adhesion strength.

Table 7.3 The average adhesion strength from T-peel adhesion tests are shown for F18 and its nanocomposite with 5wt% zeolite nanoparticles both without and after photo-oxidation testing. All samples used Oike VX 25T-2PO barrier films for substrates; had adhesive thicknesses of about 50µm; and displayed adhesive failure at the adhesive-to-barrier film interface. **All samples for F18 + 5wt% zeolite nanoparticles displayed large amounts of stick-slip behavior.*

	F18	% Change	F18 +5wt% zeolite	% Change
No Aging	1.32 N/cm (0.15 N/cm)	--	1.14 N/cm (0.06 N/cm)	--
138h SEPAP	1.55 N/cm (0.12 N/cm)	17%	0.72 N/cm* (0.18 N/cm)*	-37%*

Conclusions

The accelerated photostability testing of MAM PSAs, UV curing acrylates and various nanocomposites comprised of these respective adhesives provided insight into their applicability to OPV modules which are subjected to light over the course of their lifetimes. The MAM PSAs displayed very good stability, especially under photolysis conditions in the absence of molecular oxygen where almost no change in the materials could be seen in FTIR and only minimal changes were observed in UV-Vis. The photo-oxidation of these materials was dominated by the PBA block of the polymer for which a series of degradation mechanisms has been proposed. Despite these changes during photo-oxidation testing, the adhesives remained quite transparent and should be considered as excellent candidates to remain stable enough to not lose a large amount of performance over the course of the lifetime of an OPV module outdoors.

In comparison to the MAM PSAs, F18 showed relatively poor photostability in both photo-oxidation testing and photolysis testing. The strong yellowing, and therefore loss of transparency in the visible light range, along with the increased rigidity of both the neat adhesive and its nanocomposites present potential problems for use with OPV modules for outdoor applications. However, the relatively stable adhesion strength of F18 after photo-oxidation testing is important to note as the interface with the barrier film is the dominant permeation lateral pathway for water vapor as discussed in Chapter 4. As UV curing acrylate adhesives are known to be generally more photostable than epoxies or polyurethanes, the poor

performance of F18 in this study is somewhat surprising. However, replacing the aromatic epoxy backbone of the oligomer CN9002 in F18 provides a potentially facile approach to improving the photostability of this adhesive. As this is one of the changes to the formulation used to create S3, photostability studies of this adhesive should be performed to evaluate its use as a potentially more photo-stable alternative to F18.

Regardless of the polymer matrix used, the addition of nanoparticles to the adhesives had only minor effects on the photostability of the materials. The photostability of nanocomposite adhesives using organically modified phyllosilicates agrees well the literature as they had very little effect on the photostability of the adhesives. Nanocomposites of F18 with and without these particles showed similar trends for their mechanical properties in photo-oxidation testing. In addition, FTIR showed almost no difference in the degradation kinetics for composites of M65 with and without these particles.

The addition of zeolite nanoparticles to these adhesives has not been widely reported in the literature and was thus of particular interest in this thesis. Nanocomposites comprised of these materials showed very similar behavior to the neat adhesives during accelerated photostability testing with both M85 and F18 matrices. For nanocomposites of M85 with high concentrations of zeolite nanoparticles (20wt%), FTIR showed only a slight change in the ratios of the products produced during photo-oxidation testing while the same samples also displayed a small increase in the absorption of light in the UVA and blue light region of the spectrum in UV-Vis. However, these changes remained fairly small. An increase in the T_g was also seen for composites of these nanoparticles with both M85 and F18. For M85 this increase is not enough to directly affect the suitability for OPV modules of the nanocomposite, while for F18 the increase in T_g was similar to that seen for the neat adhesive. In photolysis testing, the only major visible change from the results of the neat adhesive can be linked to the desorption of water from the zeolites during irradiation. Overall, the presence of NZL-40 zeolite nanoparticles appears to have only a minor impact on the photo-stability of both the MAM PSAs and UV curing acrylates studied in this thesis.

Conclusions and Perspectives

Organic photovoltaic (OPV) devices, with their unique combination of properties, represent a promising source of renewable energy as an alternative to traditional silicon based photovoltaic devices. With the recent advancements in power conversion efficiency and in scale-up towards industrial production, OPV devices are in pressing need of more effective encapsulation technologies in order to limit and delay their degradation from oxygen and water vapor. While flexible, organic-inorganic, multi-layer films have been shown to be sufficient barriers for preventing orthogonal permeation into devices, the problem of lateral permeation, also known as side ingress, still remains as an important permeation pathway and thus limits the devices' operational lifetimes. This problem has created the opportunity for the work of this thesis to develop enhanced gas-barrier adhesives for encapsulation of OPV devices and methods to evaluate the lateral permeation in encapsulation schemes along multiple permeation pathways.

A very popular flexible encapsulation scheme for OPV devices is to laminate the device between two flexible barrier films using an adhesive to make the seal between the films. When evaluating the lateral permeation in this encapsulation scheme multiple pathways are present, namely permeation in the bulk adhesive and permeation along the interface between the adhesive and the flexible film. However, current permeation testing procedures mostly ignore the effect of interfacial permeation by not using flexible films, while also not allowing for the separation of the impact of the different permeation pathways. Therefore as part of this thesis, a modified version of the optical calcium test was developed in order to determine the relative impacts of the different water vapor permeation pathways present in an encapsulated flexible OPV device.

By using a sample geometry which closely resembles an actual OPV device, the optical calcium test that was developed was shown to be capable of distinguishing the relative contributions of orthogonal permeation, permeation in the bulk adhesive, and interfacial permeation for pairs of adhesives and barrier films. By defining a region which was not impacted by lateral permeation during the test, the orthogonal permeation across the barrier films can be accurately measured to evaluate their water vapor barrier properties. This information can then be used to perform a background subtraction and determine the total apparent lateral water vapor permeation. While not an exact quantitative measure of the

permeation, this value does provide an excellent relative comparison between samples, therefore allowing for the identification of the best encapsulation parameters. The results showed that lateral permeation accounts for a very large proportion of the overall permeation in samples of this size, often over 50% of the total water vapor permeation. By testing with the same materials but a different thickness of adhesive, it was also shown that the relative impacts of the water vapor permeation in the bulk adhesive and along the interfaces could be determined. The results showed that the ratio of permeation in the bulk adhesive and along the interface were very dependent on the adhesive-barrier film pair, with some combinations being overwhelmingly dominated by interfacial permeation – a pathway which has been largely ignored in other testing methods. The ability of this test to measure both the bulk adhesive and the interfaces while closely resembling an actual device has also allowed it to evaluate encapsulation design parameters such as surface treatments and the thickness of the adhesive layer. It can also be envisioned that other parameters could also be evaluated for their relative impact including the distance from the edge of the device to the edge of the encapsulation and the use of edge seal materials. While the inherent variability in the fabrication and performance of OPV devices, along with the additional impact of the design of the electrical connections, prevented a definitive link between the results of optical calcium tests and accelerated aging of encapsulated OPV devices in humid conditions, the modified version of the optical calcium test remains an effective tool for the evaluation of flexible OPV encapsulation.

With a test established to aid in the determination of the water vapor permeation of adhesives, two main classes of adhesives were then studied as part of this thesis. One class of adhesive was pressure sensitive adhesives (PSA) based on block copolymers of poly(methyl methacrylate)-*block*-(butyl acrylate)-*block*-(methyl methacrylate) (MAM). These adhesives, which were supplied by Arkema Group, are solid adhesives which are above the glass transition temperature of poly(butyl acrylate) (PBA), which was the majority block for all of the variants tested. These adhesives excelled in several key areas which are important for flexible OPV encapsulation materials including excellent transparency in the ultraviolet-A (UVA) and visible wavelengths, strong adhesion to flexible barrier films, and compatibility with solution processing and roll-to-roll manufacturing techniques. These materials were also found to have very good photostability, especially in photolysis where irradiations are performed in the absence of molecular oxygen. In photo-oxidation, some degradation of the PBA block was observed with the adhesives becoming slightly more rigid after aging, though this increased rigidity was not enough to affect their use as a flexible encapsulation material.

However, optical calcium tests with these materials showed relatively high water vapor permeation rates compared with commercial reference adhesives. It was also found that the water vapor permeation rate in these adhesives was not directly dependent on their mechanical properties nor their overall poly(methyl methacrylate) (PMMA) content, but instead on their morphology with the worm-like morphology being slightly less permeable than micelles of PMMA in a matrix of PBA. The MAM PSAs also showed a combination of permeation through both the bulk adhesive and along the interface despite their strong adhesion. Additionally, the most rigid of these materials had low tack and were difficult to laminate without the presence of bubbles at room temperature.

The other class of adhesives which were examined in this thesis were UV curing acrylates. These liquid adhesives are a mix of monomers and oligomers containing acrylic functionalities with photo-initiators which absorb UVA and/or visible wavelengths of light to generate radicals. The radicals generated upon exposure to a light source corresponding to the absorption bands of the photo-initiators causes the liquid adhesive to polymerize into a cross-linked network. One of these adhesives, F18, was formulated by the author using compatibility with OPV materials and adhesion to flexible polymer substrates as guiding parameters. A second adhesive, S3, was formulated by Sartomer of the Arkema Group which attempted to improve upon the adhesion to flexible polymer substrates compared to F18. These adhesives had relatively weak adhesion to flexible barrier films and were less transparent compared to the MAM PSAs. The use of a tackifying resin in S3 was able to increase the adhesion but at the same time caused a loss in transparency. S3 was also less rigid than F18, which is desirable as F18 was found to be rigid enough at low temperatures to be of concern for OPV modules operating in cold climates. Despite all these properties, both formulations were still able to meet the requirements of OPV encapsulation for those properties. However, F18 did exhibit low photostability compared to the MAM PSAs as it quickly became yellow and lost some transparency in both photo-oxidation and photolysis. This is likely due to the degradation of the epoxy backbone in one of the oligomers used in the formulation. Replacing this oligomer with one having a more stable backbone chemistry would likely greatly aid the photostability of this material.

Despite these issues, both F18 and S3 showed very good results in optical calcium tests where both formulations outperformed both the MAM PSAs and the reference adhesive. The UV curing acrylates showed very good bulk barrier properties with the lateral permeation being very much dominated by interfacial permeation. It was seen that low apparent lateral water

vapor permeation in these adhesives was closely correlated with stronger adhesion to the flexible barrier film, thus further indicating the importance of the interfacial permeation pathway. The low lateral water vapor permeation rate of F18 also translated well to aging studies of encapsulated OPV devices, where devices encapsulated with F18 showed much slower loss of performance than those encapsulated with the reference adhesive. These promising results warrant the further development of these adhesives to improve their overall performance in encapsulating OPV devices.

One such way to further develop both classes of adhesives is through the addition of nanoparticles. In this thesis, the modification of both classes of adhesives was examined using organically modified phyllosilicates and zeolite nanoparticles. Organically modified phyllosilicates were used as passive particles which created high aspect ratio, impermeable particles that result in a tortuous pathway for permeating gas molecules. On the other hand, the high surface area zeolite nanoparticles were used as active materials which bind permeating water molecules to their surfaces. Both types of particles were able to be dispersed into both classes of adhesive, though with different upper limits on the concentration of particles. Both types of particles showed only small changes in most properties, with some increased rigidity and decreased transparency compared to the neat adhesives. The most drastic change was the loss of adhesion strength for nanocomposites of F18 with organically modified phyllosilicates, though this was mostly recovered using corona treated substrates. However, the nanocomposites generally did not exhibit enough difference from the neat adhesive to change their applicability to OPV encapsulation. Of particular note is that the photostability of the adhesives also showed only minor changes with the addition of nanoparticles. This is especially noteworthy for zeolite nanoparticles which, to the knowledge of the author, have not been previously studied for their effect on the photostability of adhesives.

One property that did exhibit a large change after the addition of nanoparticles was the water vapor permeation. Optical calcium tests for nanocomposites based on the MAM PSAs showed large decreases in the apparent lateral water vapor permeation rate for all particle types and concentrations tested, with zeolite nanoparticles being the most effective at reducing the permeation. Though the dominance of the interfacial permeation pathway was expected to limit the effectiveness of the nanoparticles at reducing water vapor permeation in UV curing acrylates, nanocomposites based on F18 did show a decrease in the apparent lateral water vapor permeation rate with both types of particles showing similar performance. The ability of the organically modified phyllosilicates to perform as well as the zeolite nanoparticles is likely due

to the organically modified phyllosilicates having a higher concentration of particles immediately adjacent to the interface. This decreased permeation also manifested itself in aging tests of encapsulated OPV devices, as devices encapsulated using nanocomposites of F18 with zeolite nanoparticles showed the slowest loss of performance of any material developed in this thesis. However, organically modified phyllosilicates did not perform well in these tests, likely due to an interaction with the OPV materials that was possibly from contaminants in the particles.

In addition to the tests presented in this thesis, continued testing in several areas could help to further the efforts of this research. However, due to time constraints, this testing has not been performed. Outdoor aging tests of OPV devices would aid in determining the device lifetimes that could be expected using with these enhanced adhesives. Additionally, tests using industrial scale production methods such as roll-to-roll lamination, slot-die deposition, gravure printing or ink jetting for the deposition of the adhesives would be a next logical step for the implantation of the enhanced adhesives developed in this thesis.

Returning to the work presented in this thesis, there are several points which could benefit from further development. The formulation of the UV curing adhesives could use further development to increase their photostability and adhesion to flexible barrier films. This could be of particular interest given the results showing the dominance of interfacial permeation for these adhesives. Additionally, formulation work on both classes of adhesives could be carried out by combining both organically modified phyllosilicates and zeolite nanoparticles in the same adhesive. This combination of both passive and active particles represents an interesting approach given their respective successes at limiting water vapor permeation.

A final perspective for the work developed in this thesis is the continued development of the optical calcium test. The current method of manually removing samples from the climatic chamber and aligning them for imaging could potentially be automated. This type of system could be envisioned to have the camera and lamp inside a climatic chamber. A carousel could then be used to rotate different samples in front of the lamp for imaging automatically. This would greatly reduce the amount of work required to perform the test while simultaneously eliminating the large gaps in data from overnight periods where no one is present to manually capture the images. Further automation could also be added in the form of dedicated software to perform the image analysis and subsequent permeation calculations.

Overall, the research presented in this thesis has examined several different classes of adhesives with enhanced formulations for their applicability to encapsulation flexible OPV devices. After developing a test to characterize the relative importance of the various permeation pathways, the characterization of the developed adhesives has shown that the use of formulation and the creation of nanocomposites can meet the requirements of OPV encapsulation materials while limiting the permeation of water vapor into devices. Accelerated aging studies with OPV devices also showed that these enhanced adhesives are a promising technique for the prolongation of the device lifetime for flexible OPV modules.

References

1. Perez, R. & Perez, M. A Fundamental Look at Energy Reserves for the Planet. *IEA SHC Sol. Updat.* (2009).
2. Sawin, J. L. *et al.* *Renewables 2014: Global Status Report.* (2014).
3. Krebs, F. C. Fabrication and processing of polymer solar cells: A review of printing and coating techniques. *Sol. Energy Mater. Sol. Cells* **93**, 394–412 (2009).
4. Angmo, D. *et al.* Scalability and stability of very thin, roll-to-roll processed, large area, indium-tin-oxide free polymer solar cell modules. *Org. Electron. physics, Mater. Appl.* **14**, 984–994 (2013).
5. Sondergaard, R. R., Hosel, M. & Krebs, F. C. Roll-to-Roll fabrication of large area functional organic materials. *J. Polym. Sci. Part B Polym. Phys.* **51**, 16–34 (2013).
6. Steim, R. *et al.* Organic photovoltaics for low light applications. *Sol. Energy Mater. Sol. Cells* **95**, 3256–3261 (2011).
7. Janssen, R. a & Nelson, J. Factors limiting device efficiency in organic photovoltaics. *Adv. Mater.* **25**, 1847–58 (2013).
8. Jørgensen, M., Norrman, K. & Krebs, F. C. Stability/degradation of polymer solar cells. *Sol. Energy Mater. Sol. Cells* **92**, 686–714 (2008).
9. Jørgensen, M. *et al.* Stability of Polymer Solar Cells. *Adv. Mater.* **24**, 580–612 (2012).
10. *Stability and Degradation of Organic and Polymer Solar Cells.* (John Wiley and Sons, Ltd, 2012).
11. Heliatek GmbH Website. at <<http://www.heliatek.com/>>
12. Krebs, F. C., Tromholt, T. & Jørgensen, M. Upscaling of polymer solar cell fabrication using full roll-to-roll processing. *Nanoscale* **2**, 873–886 (2010).
13. Dhez, O. From Lab to Fab Scale-Up Requirements, Printed Large Area Photo Detectors. in *6th Int. Summit OPV Stab.* (2013).
14. Eight19 Website. at <<http://www.eight19.com/>>
15. Armor Group Website. at <<http://www.beautiful-light.eu/en>>
16. Disa Solar Website. at <<http://www.disasolar.fr/en/>>
17. Dracula Technologies Website. at <<http://www.dracula-technologies.com/>>
18. Belectric OPV GmbH Website. at <<http://www.belectric.com/en/organic-photovoltaics/>>
19. Solar Press Website. at <<http://www.solar-press.com/>>
20. Solar Window Technolgies Inc. Website. at <<http://solarwindow.com/>>
21. Solarmer Website. at <<http://solarmer.com/>>
22. Polyera Corporation Website. at <<http://www.polyera.com/>>
23. ISORG Website. at <<http://www.isorg.fr/>>
24. Wang, X., Xinxin Zhao, C., Xu, G., Chen, Z. K. & Zhu, F. Degradation mechanisms in organic solar cells: Localized moisture encroachment and cathode reaction. *Sol. Energy Mater. Sol. Cells* **104**, 1–6 (2012).
25. Cros, S. *et al.* Definition of encapsulation barrier requirements: A method applied to organic solar cells. *Sol. Energy Mater. Sol. Cells* **95**, S65–S69 (2011).
26. Ahmad, J., Bazaka, K., Anderson, L. J., White, R. D. & Jacob, M. V. Materials and methods for encapsulation of OPV: A review. *Renew. Sustain. Energy Rev.* **27**, 104–117 (2013).
27. Cao, W. & Xue, J. Recent progress in organic photovoltaics: device architecture and optical design. *Energy Environ. Sci.* **7**, 2123–2144 (2014).

28. Manceau, M. Impact de la lumiere sur la couche active des cellules photovoltaïques organiques. (2009).
29. Richard-Plouet, M. & Brohan, L. Insight on transition metal oxide layers in OPV , from the solid state chemistry point of view. in *6th Int. Summit OPV Stab.* (2013).
30. Lechene, B. *et al.* Design of intermediate layers for solution-processed tandem organic solar cells: Guidelines from a case study on TiO_x and ZnO. *Sol. Energy Mater. Sol. Cells* **120**, 709–715 (2014).
31. Angmo, D. *et al.* Outdoor operational stability of indium-free flexible polymer solar modules over 1 year studied in India, Holland, and Denmark. *Adv. Eng. Mater.* (2014). doi:10.1002/adem.201400002
32. Simonato, J. Transparent electrodes made of Ag nanowire networks: Fabrication, physical properties and intergration in OPV cells. in *6th Int. Summit OPV Stab.* (2013).
33. National Renewable Energy Laboratory - National Center for Photovoltaics Website. at <<http://www.nrel.gov/ncpv/>>
34. Rivaton, A. *et al.* Photostability of organic materials used in polymer solar cells. *Polym. Int.* **63**, 1335–1345 (2014).
35. Cao, H. & Ishikawa, K. Lateral oxygen diffusion dominated extrinsic degradation of small molecular organic solar cells. *Sol. Energy Mater. Sol. Cells* **109**, 215–219 (2013).
36. Dupont, S. R., Oliver, M., Krebs, F. C. & Dauskardt, R. H. Interlayer adhesion in roll-to-roll processed flexible inverted polymer solar cells. *Sol. Energy Mater. Sol. Cells* **97**, 171–175 (2012).
37. Dauskardt, R. Adhesion and Debonding Kinetics in OPV Devices Hybrid Organic Films in Device , Energy and Biomedical Technologies. in *6th Int. Summit OPV Stab.* (2013).
38. Schumann, S. *et al.* New Developments in PEDOT for OPVs. in *6th Int. Summit OPV Stab.* (2013).
39. Zemen, Y. *et al.* Comparison of new conductive adhesives based on silver and carbon nanotubes for solar cells interconnection. *Sol. Energy Mater. Sol. Cells* **109**, 155–159 (2013).
40. Muller-Meskamp, L. *et al.* Encapsulation of Small Molecule OPV Cells: Backelectrode Barrier Properties and its Influence on Device Degradation. in *6th Int. Summit OPV Stab.* (2013).
41. Han, S. H. *et al.* Lifetime of organic thin-film transistors with organic passivation layers. *Appl. Phys. Lett.* **88**, 2004–2007 (2006).
42. Jung, H. *et al.* Lifetime enhancement of organic thin-film transistors protected with organic layer. *Appl. Phys. Lett.* **92**, 1–4 (2008).
43. Kim, L. H. *et al.* Al₂O₃/TiO₂ nanolaminate thin film encapsulation for organic thin film transistors via plasma-enhanced atomic layer deposition. *ACS Appl. Mater. Interfaces* **6**, 6731–6738 (2014).
44. Cho, a. R., Kim, E. H., Park, S. Y. & Park, L. S. Flexible OLED encapsulated with gas barrier film and adhesive gasket. *Synth. Met.* **193**, 77–80 (2014).
45. Ghosh, a. P., Gerenser, L. J., Jarman, C. M. & Fornalick, J. E. Thin-film encapsulation of organic light-emitting devices. *Appl. Phys. Lett.* **86**, 1–3 (2005).
46. Meyer, J. *et al.* Reliable thin film encapsulation for organic light emitting diodes grown by low-temperature atomic layer deposition. *Appl. Phys. Lett.* **94**, (2009).
47. Park, J.-S., Chae, H., Chung, H. K. & Lee, S. I. Thin film encapsulation for flexible AM-OLED: a review. *Semicond. Sci. Technol.* **26**, 034001 (2011).
48. Park, J. H. & Oh, S. G. Preparation of CaO as OLED getter material through control of crystal growth of CaCO₃ by block copolymers in aqueous solution. *Mater. Res. Bull.* **44**, 110–118 (2009).

49. Wu, C. S., Liao, J. Y., Fang, S. Y. & Chiang, A. S. T. Flexible and transparent moisture getter film containing zeolite. *Adsorption* **16**, 69–74 (2010).
50. Greener, J., Ng, K. C., Vaeth, K. M. & Smith, T. M. Moisture permeability through multilayered barrier films as applied to flexible OLED display. *J. Appl. Polym. Sci.* **106**, 3534–3542 (2007).
51. Keibler, C., Hild, O., Muller-Meskamp, L. & Leo, K. Direct encapsulation of OLEDs with different thin film methods. in *Large Area Org. Print. Electron. Conv.* (2013).
52. Kempe, M. D., Dameron, A. A. & Moricone, T. J. EVALUATION AND MODELING OF EDGE-SEAL MATERIALS FOR PHOTOVOLTAIC APPLICATIONS. in *IEEE Photovolt. Spec. Conf.* (2010).
53. Kempe, M. D. Control of moisture ingress into photovoltaic modules. *Conf. Rec. Thirty-first IEEE Photovolt. Spec. Conf. 2005.* (2005).
54. Carcia, P. F., McLean, R. S. & Hegedus, S. Encapsulation of Cu(InGa)Se₂ solar cell with Al₂O₃ thin-film moisture barrier grown by atomic layer deposition. *Sol. Energy Mater. Sol. Cells* **94**, 2375–2378 (2010).
55. Coyle, D. J. Life prediction for CIGS solar modules part 1: Modeling moisture ingress and degradation. *Prog. Photovoltaics Res. Appl.* **21**, 156–172 (2013).
56. Coyle, D. J. *et al.* Life prediction for CIGS solar modules part 2: Degradation kinetics, accelerated testing, and encapsulant effects. *Prog. Photovoltaics Res. Appl.* **21**, 173–186 (2013).
57. Kim, N., Han, C., Baek, D. & Kim, D. Determination of Moisture Ingress through Various Encapsulants used in CIGS PV Module under Continuously Varying Environment. in *IEEE Photovolt. Spec. Conf.* 887–890 (2011).
58. Lee, D. W. *et al.* Effects of ZnO:Al films on CIGS PV modules degraded under accelerated damp heat. *Sol. Energy Mater. Sol. Cells* **105**, 15–20 (2012).
59. Selin Tosun, B. *et al.* Improving the damp-heat stability of copper indium gallium diselenide solar cells with a semicrystalline tin dioxide overlayer. *Sol. Energy Mater. Sol. Cells* **101**, 270–276 (2012).
60. Hardikar, K., Vitkavage, D., Sapruo, A. & Krajewski, T. A methodology for testing, characterization and prediction of edge seal performance in PV modules. *Photovoltaics Int.* 75–83 (2014).
61. Hodes, G. Applied physics. Perovskite-based solar cells. *Science* **342**, 317–8 (2013).
62. Liu, M., Johnston, M. B. & Snaith, H. J. Efficient planar heterojunction perovskite solar cells by vapour deposition. *Nature* **501**, 395–8 (2013).
63. Kim, J. H., Williams, S. T., Cho, N., Chueh, C. & Jen, A. K. Enhanced Environmental Stability of Planar Heterojunction Perovskite Solar Cells Based on Blade-Coating. *Adv. Eng. Mater.* 2–7 (2014). doi:10.1002/aenm.201401229
64. Smith, I. C., Hoke, E. T., Solis-ibarra, D., Mcgehee, M. D. & Karunadasa, H. I. Perovskite Solar Cells A Layered Hybrid Perovskite Solar-Cell Absorber with Enhanced Moisture Stability. *Angew. Chemie Int. Ed.* (2014). doi:10.1002/anie.201406466
65. Snaith, H. J. Perovskites : The Emergence of a New Era for Low-Cost , High-. *J. Phys. Chem. Lett.* (2013).
66. Crank, J. *THE MATHEMATICS OF DIFFUSION.* (1975).
67. Cros, S. *et al.* Relationship between encapsulation barrier performance and organic solar cell lifetime. in *SPIE* (Dhere, N. G.) **7048**, 70480U–70480U–12 (2008).
68. Graff, G. L., Williford, R. E. & Burrows, P. E. Mechanisms of vapor permeation through multilayer barrier films: Lag time versus equilibrium permeation. *J. Appl. Phys.* **96**, 1840–1849 (2004).

69. Michels, J. J., Peter, M., Salem, a., van Remoortere, B. & van den Brand, J. A combined experimental and theoretical study on the side ingress of water into barrier adhesives for organic electronics applications. *J. Mater. Chem. C* **2**, 5759 (2014).
70. Painter, P. C. & Coleman, M. M. *Essentials of Polymer Science and Engineering*. (DEStech Publications, 2009).
71. Boeffel, C., Fahlteich, J., Steiner, C., Amberg-Schwab, S. & Kuzukpinar, E. Ultra-high barrier substrates and ALD layers for the encapsulation of organic electronic devices. in *Int. Symp. Flex. Org. Electron.* (2014).
72. Doremus, R. H. *Glass Science*. (John Wiley and Sons, Ltd, 1994).
73. Corning Incorporated Willow Glass Website. at <<http://www.corning.com/displaytechnologies/en/products/flexible.aspx>>
74. SCHOTT Inc. Ultra-Thin Glass Website. at <http://www.us.schott.com/advanced_optics/english/products/wafers-and-thin-glass/glass-wafer-and-substrates/ultra-thin-glass/index.html>
75. Leterrier, Y. Durability of nanosized oxygen-barrier coatings on polymers. *Prog. Mater. Sci.* **48**, 1–55 (2003).
76. Roberts, a. P. *et al.* Gas permeation in silicon-oxide/polymer (SiO_x/PET) barrier films: Role of the oxide lattice, nano-defects and macro-defects. *J. Memb. Sci.* **208**, 75–88 (2002).
77. Howells, D. G. *et al.* Mechanical properties of SiO_x gas barrier coatings on polyester films. *Surf. Coatings Technol.* **202**, 3529–3537 (2008).
78. Kim, Y. *et al.* Experimental study of interfacial fracture toughness in a SiN(x)/PMMA barrier film. *ACS Appl. Mater. Interfaces* **4**, 6711–9 (2012).
79. Struller, C. F. *et al.* Aluminium oxide barrier films on polymeric web and their conversion for packaging applications. *Thin Solid Films* **553**, 153–156 (2014).
80. Yang, Y. H., Bolling, L., Priolo, M. a. & Grunlan, J. C. Super gas barrier and selectivity of graphene oxide-polymer multilayer thin films. *Adv. Mater.* **25**, 503–508 (2013).
81. Elrawemi, M. *et al.* Modelling water vapour permeability through atomic layer deposition coated photovoltaic barrier defects. *Thin Solid Films* **570**, 101–106 (2014).
82. Morlier, A., Cros, S., Garandet, J. P. & Alberola, N. Thin gas-barrier silica layers from perhydropolysilazane obtained through low temperature curings: A comparative study. *Thin Solid Films* **524**, 62–66 (2012).
83. Morlier, A., Cros, S., Garandet, J. P. & Alberola, N. Gas barrier properties of solution processed composite multilayer structures for organic solar cells encapsulation. *Sol. Energy Mater. Sol. Cells* **115**, 93–99 (2013).
84. Wang, K., Gu, M., Motz, G., Flinn, B. D. & Bordia, R. K. Control of Surface Energy of Silicon Oxynitride Films. *Langmuir* (2013).
85. Fahlteich, J., Steiner, C., Winkler, S., Fahland, M. & Schiller, N. Ultra-High Permeation Barrier Films for the Encapsulation of Flexible Electronic Devices. in *6th Int. Summit OPV Stab.* (2013).
86. Kools, J. High Throughput Atomic Layer Deposition of Al₂O₃ Ultrabarrier Encapsulation. in *Int. Conf. Org. Electron.* (2013).
87. George, S. M. Atomic layer deposition: An overview. *Chem. Rev.* **110**, 111–131 (2010).
88. Carcia, P. F., McLean, R. S., Reilly, M. H., Groner, M. D. & George, S. M. Ca test of Al₂O₃ gas diffusion barriers grown by atomic layer deposition on polymers. *Appl. Phys. Lett.* **89**, 031915 (2006).
89. Meyer, J., Schmidt, H., Kowalsky, W., Riedl, T. & Kahn, a. The origin of low water vapor transmission rates through Al₂O₃/ZrO₂ nanolaminate gas-

- diffusion barriers grown by atomic layer deposition. *Appl. Phys. Lett.* **96**, 243308 (2010).
90. Gaume, J. Etude du photovieillissement de matériaux nanocomposites pour l'encapsulation de cellules solaires organiques. (2011).
 91. Gaume, J. *et al.* Optimization of PVA clay nanocomposite for ultra-barrier multilayer encapsulation of organic solar cells. *Sol. Energy Mater. Sol. Cells* **99**, 240–249 (2012).
 92. Cros, S. & Morlier, A. GAS BARRIER MEASUREMENT : DEVICE & METHOD TO CONTROL RAPIDLY. in *Large Area Org. Print. Electron. Conv.* (2013).
 93. Lohwasser, W. Affordable Industrial Flexible High Barrier Materials for the Encapsulation of Organic Electronics. in *Large Area Org. Print. Electron. Conv.* (2013).
 94. McCormick, F. B. Barrier Films and Adhesives for OLED Solid State Lighting. in *US Dep. Energy Solid State Light. Work.* (2014).
 95. Gaume, J., Wong-Wah-Chung, P., Rivaton, A., Thérias, S. & Gardette, J.-L. Photochemical behavior of PVA as an oxygen-barrier polymer for solar cell encapsulation. *RSC Adv.* **1**, 1471 (2011).
 96. Kucukpinar, E., Kiese, S., Miesbauer, O. & Noller, K. Encapsulation Materials for OPVs : Integration of Novel Barrier Adhesives. in *6th Int. Summit OPV Stab.* (2013).
 97. Schmidt, M. *et al.* Adhesion and Barrier Performance of Novel Barrier Adhesives Used in Multilayered High-Barrier Laminates. *J. Adhes. Sci. Technol.* (2012). doi:10.1163/156856111X599535
 98. Harkema, S., Muelendijks-Kiggen, N. M. M. & Vanev, R. J. Nanocomposite, Method to Produce the Same, A Barrier Structure for an Electronic Device and an OLED Comprising the Same. (2014).
 99. Hösel, M., Søndergaard, R. R., Jørgensen, M. & Krebs, F. C. Comparison of UV-curing, hotmelt, and pressure sensitive adhesive as roll-to-roll encapsulation methods for polymer solar cells. *Adv. Eng. Mater.* **15**, 1068–1075 (2013).
 100. Lin, C.-C., Hsu, S.-H., Chang, Y.-L. & Su, W.-F. Transparent hydrophobic durable low moisture permeation poly(fluoroimide acrylate)/SiO₂ nanocomposite from solventless photocurable resin system. *J. Mater. Chem.* **20**, 3084 (2010).
 101. Ravichandran, J., Manoj, a G., Liu, J., Manna, I. & Carroll, D. L. A novel polymer nanotube composite for photovoltaic packaging applications. *Nanotechnology* **19**, 085712 (2008).
 102. Seethamraju, S., Ramamurthy, P. C. & Madras, G. Ionomer based blend as water vapor barrier material for organic device encapsulation. *ACS Appl. Mater. Interfaces* **5**, 4409–4416 (2013).
 103. *Handbook of Adhesives and Sealants.* (Elsevier Ltd, 2005).
 104. *Handbook of Adhesives and Surface Preparation.* (Elsevier Inc., 2011).
 105. Braun, T. *et al.* Enhancement of Barrier Properties of Encapsulants for Harsh Environment Applications. in *IEEE Trans. Components Packag. Technol.* 1418–1425 (2012).
 106. Braun, T. *et al.* Water diffusion in micro- and nano-particle filled encapsulants. *Electron. Syst. Integr. Technol. Conf. Proc.* **1**, (2010).
 107. Poppe, L., Paskevich, V., Hathaway, J. & Blackwood, D. *U. S. Geological Survey Open-File Report 01-041: A Laboratory Manual for X-Ray Powder Diffraction.* at <<http://pubs.usgs.gov/of/2001/of01-041/>>
 108. Drozdov, A. D., Christiansen, J., Gupta, R. K. & Shah, A. P. Model for Anomalous Moisture Diffusion through a Polymer – Clay Nanocomposite. *J. Polym. Sci. Part B Polym. Phys.* **41**, 476–492 (2002).

109. Kim, J. K., Hu, C., Woo, R. S. C. & Sham, M. L. Moisture barrier characteristics of organoclay-epoxy nanocomposites. *Compos. Sci. Technol.* **65**, 805–813 (2005).
110. Uhl, F. M., Davuluri, S. P., Wong, S. C. & Webster, D. C. Organically modified montmorillonites in UV curable urethane acrylate films. *Polymer (Guildf)*. **45**, 6175–6187 (2004).
111. Uhl, F. M., Webster, D. C., Davuluri, S. P. & Wong, S. C. UV curable epoxy acrylate-clay nanocomposites. *Eur. Polym. J.* **42**, 2596–2605 (2006).
112. Yano, K., Usuki, A. & Okada, A. Synthesis and Properties of Polyimide-Clay Hybrid Films. *J. Polym. Sci. Part A Polym. Chem.* 2289–2294 (2000).
113. Moller, M. W. *et al.* UV-cured, flexible, and transparent nanocomposite coating with remarkable oxygen barrier. *Adv. Mater.* **24**, 2142–2147 (2012).
114. Picard, E., Vermogen, a., G??rard, J. F. & Espuche, E. Barrier properties of nylon 6-montmorillonite nanocomposite membranes prepared by melt blending: Influence of the clay content and dispersion state. Consequences on modelling. *J. Memb. Sci.* **292**, 133–144 (2007).
115. Granstrom, J., Gällstedt, M., Villet, M., Moon, J. S. & Chatterjee, T. High performance encapsulation structures utilizing Russian Doll architectures. *Thin Solid Films* **518**, 5282–5287 (2010).
116. Bolis, V., Busco, C. & Ugliengo, P. Thermodynamic study of water adsorption in high-silica zeolites. *J. Phys. Chem. B* **110**, 14849–14859 (2006).
117. Ng, E. P. & Mintova, S. Nanoporous materials with enhanced hydrophilicity and high water sorption capacity. *Microporous Mesoporous Mater.* **114**, 1–26 (2008).
118. Valtchev, V. & Tosheva, L. Porous Nanosized Particles : Preparation , Properties , and Applications. *Chem. Rev.* (2013). doi:10.1021/cr300439k
119. Liljedahl, C. D. M., Crocombe, a. D., Gauntlett, F. E., Rihawy, M. S. & Clough, a. S. Characterising moisture ingress in adhesively bonded joints using nuclear reaction analysis. *Int. J. Adhes. Adhes.* **29**, 356–360 (2009).
120. Sanopoulou, M., Stamatialis, D. F. & Petropoulos, J. H. Investigation of case II diffusion behavior. 1. Theoretical studies based on the relaxation dependent solubility model. *Macromolecules* **35**, 1012–1020 (2002).
121. Zanni-Deffarges, M. P. & Shanahan, M. E. R. Diffusion of water into an epoxy adhesive: comparison between bulk behaviour and adhesive joints. *Int. J. Adhes. Adhes.* **15**, 137–142 (1995).
122. LaPlante, G., Ouriadov, A. V., Lee-Sullivan, P. & Balcom, B. J. Anomalous moisture diffusion in an epoxy adhesive detected by magnetic resonance imaging. *J. Appl. Polym. Sci.* **109**, 1350–1359 (2008).
123. O'Brien, E. P., White, C. C. & Vogt, B. D. Correlating Interfacial Moisture Content and Adhesive Fracture Energy of Polymer Coatings on Different Surfaces. *Adv. Eng. Mater.* **8**, 114–118 (2006).
124. Wapner, K., Stratmann, M. & Grundmeier, G. In situ infrared spectroscopic and scanning Kelvin probe measurements of water and ion transport at polymer/metal interfaces. *Electrochim. Acta* **51**, 3303–3315 (2006).
125. Baldan, A. Adhesion phenomena in bonded joints. *Int. J. Adhes. Adhes.* **38**, 95–116 (2012).
126. Lam, D. C. C., Yang, F. & Tong, P. Chemical kinetic model of interfacial degradation of adhesive joints. *IEEE Trans. Components Packag. Technol.* **22**, 215–220 (1999).
127. Leger, R., Roy, a. & Grandidier, J. C. A study of the impact of humid aging on the strength of industrial adhesive joints. *Int. J. Adhes. Adhes.* **44**, 66–77 (2013).

128. Mubashar, a., Ashcroft, I. a., Critchlow, G. W. & Crocombe, a. D. Moisture absorption-desorption effects in adhesive joints. *Int. J. Adhes. Adhes.* **29**, 751–760 (2009).
129. Mubashar, a., Ashcroft, I. a., Critchlow, G. W. & Crocombe, a. D. Strength prediction of adhesive joints after cyclic moisture conditioning using a cohesive zone model. *Eng. Fract. Mech.* **78**, 2746–2760 (2011).
130. Wapner, K. & Grundmeier, G. Spatially resolved measurements of the diffusion of water in a model adhesive/silicon lap joint using FTIR-transmission-microscopy. *Int. J. Adhes. Adhes.* **24**, 193–200 (2004).
131. Kapur, J., Proost, K. & Smith, C. A. Determination of moisture ingress through various encapsulants in glass/glass laminates. *Conf. Rec. IEEE Photovolt. Spec. Conf.* 001210–001214 (2009).
132. Tanenbaum, D. M. *et al.* Edge sealing for low cost stability enhancement of roll-to-roll processed flexible solar cell modules. *Sol. Energy Mater. Sol. Cells* **97**, 157–163 (2011).
133. Vitriflex Website. at <<http://www.vitriflex.com/>>
134. Kateeva Website. at <<http://kateeva.com/>>
135. Elkington, D., Cooling, N., Zhou, X. J., Belcher, W. J. & Dastoor, P. C. Single-step annealing and encapsulation for organic photovoltaics using an exothermally-setting encapsulant material. *Sol. Energy Mater. Sol. Cells* **124**, 75–78 (2014).
136. La Notte, L. *et al.* Influence of encapsulation materials on the optical properties and conversion efficiency of heat-sealed flexible polymer solar cells. *Surf. Coatings Technol.* **255**, 69–73 (2014).
137. Hülsmann, P., Weiß, K.-A. & Köhl, M. Temperature-dependent water vapour and oxygen permeation through different polymeric materials used in photovoltaic-modules. *Prog. Photovoltaics Res. Appl.* **22**, 415–421 (2014).
138. Gupta, S., Ramamurthy, P. C. & Madras, G. Synthesis and characterization of flexible epoxy nanocomposites reinforced with amine functionalized alumina nanoparticles: a potential encapsulant for organic devices. *Polym. Chem.* **2**, 221 (2011).
139. Osman, M. a., Mittal, V., Morbidelli, M. & Suter, U. W. Polyurethane adhesive nanocomposites as gas permeation barrier. *Macromolecules* **36**, 9851–9858 (2003).
140. Søndergaard, R. R. *et al.* The use of polyurethane as encapsulating method for polymer solar cells - An inter laboratory study on outdoor stability in 8 countries. *Sol. Energy Mater. Sol. Cells* **99**, 292–300 (2012).
141. Mailhot, B., Morlat-Thérias, S., Ouahioune, M. & Gardette, J. L. Study of the degradation of an epoxy/amine resin, 1 photo- and thermo-chemical mechanisms. *Macromol. Chem. Phys.* **206**, 575–584 (2005).
142. Mailhot, B., Morlat-Thérias, S., Bussière, P. O. & Gardette, J. L. Study of the degradation of an epoxy/amine resin, 2 kinetics and depth-profiles. *Macromol. Chem. Phys.* **206**, 585–591 (2005).
143. Rivaton, A., Moreau, L. & Gardette, J.-L. Photo-oxidation of phenoxy resins at long and short wavelengths—I. Identification of the photoproducts. *Polym. Degrad. Stab.* **58**, 321–332 (1997).
144. Rivaton, A., Moreau, L. & Gardette, J.-L. Photo-oxidation of phenoxy resins at long and short wavelengths—II. Mechanisms of formation of photoproducts. *Polym. Degrad. Stab.* **58**, 333–339 (1997).
145. Woo, R. S. C. *et al.* Environmental degradation of epoxy-organoclay nanocomposites due to UV exposure. Part I: Photo-degradation. *Compos. Sci. Technol.* **67**, 3448–3456 (2007).

146. Woo, R. S. C., Zhu, H., Leung, C. K. Y. & Kim, J. K. Environmental degradation of epoxy-organoclay nanocomposites due to UV exposure: Part II residual mechanical properties. *Compos. Sci. Technol.* **68**, 2149–2155 (2008).
147. Lin, S. H. *et al.* Synthesis of ultraviolet curable encapsulating adhesives and their package applications for organic optoelectronic devices. *Solid State Sci.* **13**, 1889–1895 (2011).
148. Chung, M.-H. *et al.* Preparation of organic/inorganic hybrid nanocomposites by ultraviolet irradiation and their packaging applications for organic optoelectronic devices. *Appl. Surf. Sci.* **257**, 9142–9151 (2011).
149. Hong, B. T., Shin, K. S. & Kim, D. S. Ultraviolet-curing behavior of an epoxy acrylate resin system. *J. Appl. Polym. Sci.* **98**, 1180–1185 (2005).
150. Hwang, J. S., Kim, M. H., Seo, D. S., Won, J. W. & Moon, D. K. Effects of soft segment mixtures with different molecular weight on the properties and reliability of UV curable adhesives for electrodes protection of plasma display panel (PDP). *Microelectron. Reliab.* **49**, 517–522 (2009).
151. Benard, F., Mailhot, B., Mallegol, J. & Gardette, J. L. Photoageing of an electron beam cured polyurethane acrylate resin. *Polym. Degrad. Stab.* **93**, 1122–1130 (2008).
152. Decker, C. & Zahouily, K. Photodegradation and photooxidation of thermoset and UV-cured acrylate polymers. *Polym. Degrad. Stab.* **64**, 293–304 (1999).
153. Larche, J. F., Bussire, P. O. & Gardette, J. L. Photo-oxidation of acrylic-urethane thermoset networks. Relating materials properties to changes of chemical structure. *Polym. Degrad. Stab.* **96**, 1438–1444 (2011).
154. Arajo, P. H. H., Sayer, C., Giudici, R. & Poo, J. G. R. Techniques for reducing residual monomer content in polymers: A review. *Polym. Eng. Sci.* **42**, 1442–1468 (2002).
155. Czech, Z. & Pelech, R. THERMAL DEGRADATION OF BUTYL ACRYLATE-METHYL ACRYLATE-ACRYLIC ACID-COPOLYMERS. *J. Therm. Anal. Calorim.* **96**, 583–586 (2009).
156. Lee, S. W. *et al.* Optical properties and UV-curing behaviors of optically clear semi-interpenetrated structured acrylic pressure sensitive adhesives. *Int. J. Adhes. Adhes.* **38**, 5–10 (2012).
157. Lee, S. W. *et al.* Optical properties and UV-curing behaviors of optically clear PSA-TiO₂ nano-composites. *Int. J. Adhes. Adhes.* **44**, 200–208 (2013).
158. Sun, S., Li, M. & Liu, A. A review on mechanical properties of pressure sensitive adhesives. *Int. J. Adhes. Adhes.* **41**, 98–106 (2013).
159. *Photochemistry and Photophysics of Polymeric Materials.* (John Wiley and Sons, Ltd, 2010).
160. Bennet, F., Barker, P. J., Davis, T. P., Soeriyadi, A. H. & Barner-kowollik, C. Degradation of Poly (butyl acrylate) and Poly (2- hydroxyethyl methacrylate) Model Compounds Under Extreme Environmental Conditions a. *Macromol. Chem. Phys.* **211**, 2034–2052 (2010).
161. Liang, R. R. H., Tsay, F.-D. & Gupta, A. Photodegradation of poly (n-butyl acrylate). Photochemical processes in polymeric systems. 8. *Macromolecules* **15**, 974–980 (1982).
162. McGill, W. & Ackerman, L. Photolysis of Poly (ethyl Acrylate) and Poly (n-butyl Acrylate) in Vacuo. *J. Polym. Sci.* **12**, 1541–1547 (1974).
163. Soeriyadi, A. H. *et al.* A detailed surface analytical study of degradation processes in (meth)acrylic polymers. *J. Polym. Sci. Part A Polym. Chem.* **50**, 1801–1811 (2012).
164. Forsthuber, B. & Grull, G. The effects of HALS in the prevention of photo-degradation of acrylic clear topcoats and wooden surfaces. *Polym. Degrad. Stab.* **95**, 746–755 (2010).

165. Krongauz, V. V. & Ling, M. T. K. Photo-crosslinked acrylates degradation kinetics. *J. Therm. Anal. Calorim.* **96**, 715–725 (2009).
166. Mocon Website. at <www.mocon.com>
167. Grahlert, W. *et al.* Reliable determination of the water vapor transmission rate of ultra-high barrier samples in the 10⁻⁴ to 10⁻⁶ g/m²/d range enabled by tunable diode laser spectroscopy. in *Large Area Org. Print. Electron. Conv.* (2013).
168. Nisato, G. *et al.* *Permeation Measurements Using the Calcium Tests.* (2012).
169. Reese, M. O., Dameron, A. a & Kempe, M. D. Quantitative calcium resistivity based method for accurate and scalable water vapor transmission rate measurement. *Rev. Sci. Instrum.* **82**, 085101 (2011).
170. Nisato, G. *et al.* Evaluating High Performance Diffusion Barriers: The Calcium Test. *Asia Disp.* (2001).
171. *ASTM D570 Standard Test Method for Water Absorption of Plastics.*
doi:10.1520/D0570-98R10E01
172. *ASTM D5229 / D5229M Standard Test Method for Moisture Absorption Properties and Equilibrium Conditioning of Polymer Matrix Composite Materials.*
doi:10.1520/D5229_D5229M-14
173. Nissen, D. a. The low-temperature oxidation of calcium by water vapor. *Oxid. Met.* **11**, 241–261 (1977).
174. Cros, S., Firon, M., Lenfant, S., Trouslard, P. & Beck, L. Study of thin calcium electrode degradation by ion beam analysis. *Nucl. Instruments Methods Phys. Res. Sect. B Beam Interact. with Mater. Atoms* **251**, 257–260 (2006).
175. Klumbies, H., Müller-Meskamp, L., Mönch, T., Schubert, S. & Leo, K. The influence of laterally inhomogeneous corrosion on electrical and optical calcium moisture barrier characterization. *Rev. Sci. Instrum.* **84**, 024103 (2013).
176. Paetzold, R., Winnacker, a., Henseler, D., Cesari, V. & Heuser, K. Permeation rate measurements by electrical analysis of calcium corrosion. *Rev. Sci. Instrum.* **74**, 5147–5150 (2003).
177. Schubert, S., Klumbies, H., Müller-Meskamp, L. & Leo, K. Electrical calcium test for moisture barrier evaluation for organic devices. *Rev. Sci. Instrum.* **82**, 094101 (2011).
178. Klumbies, H. *et al.* Water ingress into and climate dependent lifetime of organic photovoltaic cells investigated by calcium corrosion tests. *Sol. Energy Mater. Sol. Cells* **120**, 685–690 (2014).
179. Boutillier, J. Nanostrength Acrylic block copolymers for thermoplastic adhesive applications. in *Eur. Coatings Show* (2011).
180. *Zeomics.* (2014). at <<http://helios.princeton.edu/zeomics/>>